Ultrasonic Superharmonic Imaging

Financial support for the printing of this thesis was kindly provided by:

- Oldelft Ultrasound B.V.
- Lecoeur Electronique
- Erasmus MC

Cover design by Paul L.M.J. van Neer.
Printed in the Netherlands by Optima Grafische Communicatie, Rotterdam.
ISBN 978-90-8559-998-2

For a printed version please contact:
Secretary Biomedical Engineering (July 2010: room Ee. 23.02)
Erasmus Medical Center
P.O. Box 2040, NL-3000 CA
Rotterdam, the Netherlands

Ultrasonic Superharmonic Imaging

Ultrasone superharmonische beeldvorming

Proefschrift

ter verkrijging van de graad van doctor aan de
Erasmus Universiteit Rotterdam
op gezag van de
Rector Magnificus

Prof.dr. H.G. Schmidt

en volgens besluit van het College voor Promoties.

De openbare verdediging zal plaatsvinden op
donderdag 1 juli 2010 om 9:30 uur door

Paul Louis Maria Joseph van Neer
geboren te Heerlen

Promotiecommissie

Promotoren:	Prof.dr.ir. A.F.W. van der Steen Prof.dr.ir. N. de Jong
Overige Leden:	Prof.dr.ir. A.P.G. Hoeks Prof.dr.ir. A. Gisolf Prof.dr.ir. R. van Mastrigt

The research described in this thesis was financially supported by the Interuniversity Cardiology Institute of the Netherlands, an institute of the Royal Dutch Academia of Sciences. It was carried out at the department of Biomedical Engineering, Erasmus MC, Rotterdam, the Netherlands.

Contents

CHAPTER 1

Introduction

1.1 Medical ultrasound

Medical ultrasound is one of the most prevalent imaging techniques used for diagnosing patients. The technique allows for the visualization of tissues in the human body. Compared to competing imaging techniques such as CT or MRI, medical ultrasound has numerous advantages: it is real-time, safe (no radiation is involved), inexpensive and portable. Over the years medical ultrasound equipment has become smaller and the image quality has improved considerably (see Fig. 1.1). Similar to CT or MRI, contrast agents are also used in medical ultrasound. Their use comprises e.g. endocardial border delineation, the improvement of blood flow detection using Doppler methods in cardiology and radiology, and the visualization of malignant tumors (Emmer, 2009; Vos, 2010).
Ultrasound is also commonly used for therapeutic applications such as High Intensity Focused Ultrasound (HIFU), which is used for the noninvasive treatment of tumors by ablation, and extracorporeal shock wave lithotripsy, which is used for the noninvasive treatment of urinary calculosis and biliary calculi. The therapeutic applications for contrast agents are currently under research and range from the stimulated uptake of bioactive materials (van Wamel et al., 2006), to drug delivery (Kooiman et al., 2009) and the treatment of tumors by bloodvessel destruction (Skyba et al., 1998).
The start of high frequency echo-sounding techniques can be traced back to the discovery of the piezoelectric effect by the Curie brothers in the 1880s. They noted that an electric potential would be produced, if mechanical pressure was applied on a quartz crystal. From this key event onwards it was possible to generate and receive ultrasound in the MegaHertz range. The first practical application of the piezoelectric effect was the development of sound navigation and ranging (sonar) equipment. The first patent for an underwater echo ranging sonar was filed in 1914 by Lewis Richardson, one month after the Titanic sank. Unsurprisingly, it was intended for the detection of icebergs. Great strides were taken in sonar development in WO I due to a rather pressing need to detect submarines. The next significant event for the development of medical ultrasound was the invention of radar in

the 1920s and 1930s. Although not based on sound waves but on radio waves, the methods developed for data display and beamsteering were later applied on medical ultrasound. Equally important for ultrasonics was the invention of the pulse-echo ultrasonic metal flaw detector in the 1930s. The development of this was propelled by a need to check the integrity of metal hulls of ships and the armor plating of tanks (Woo, 2002; Cobbold, 2007). Ultrasound itself was first applied in medicine as a neuro-surgical tool in the 1930s and 1940s. It was used by researchers to destroy parts of the basal ganglia in patients with Parkinsonism. Others used ultrasound to ablate frontal lobe tissue for pain relief. It was also used for physical and rehabilitation medicine, for example for the treatment of rheumatic arthritis. In these early years wild claims were made on ultrasound effectiveness without much scientific evidence: it was reported to cure arthritis, eczema, asthma and angina pectoris. The idea to use ultrasound as a diagnostic tool was first coined in the early 1940s, with the first useful diagnostic images of biological structures reported in the scientific literature in the 1950s. Since that time advances in materials, transducer design, chip technology, electronics and signal processing have dramatically improved ultrasound image quality (Woo, 2002; Cobbold, 2007).

Figure 1.1: Improvements in image quality from 1985, 1990 to 1995 respectively. Image adapted from Woo (2002).

1.2 Echocardiography

Currently, ultrasonography is widely used in a diverse range of medical fields. In the case of clinical cardiology two-dimensional echocardiography is the main diagnostic technique (Galema et al., 2007). The modality is used to assess e.g. the left ventricular volume, the ejection fraction, valvular function (detection of valvular regurgitation) and ischemia (Chung, 2009).
Echocardiography remains technically challenging despite many advances in the recent years. A considerable subgroup of patients is considered difficult to image due to tough acoustic windows and inhomogeneous skin layers. Especially for obese patients or patients with lung disease the echo image quality can be insufficient for diagnosis. This group of patients comprises about 10-20% of routine echocardiographic examinations (Mulvagh et al., 2000). For these patients ultrasound contrast agents can be used to improve the diagnostic

accuracy of e.g. ventricular function quantification, regional wallmotion and the detection of thrombi (Chung, 2009).

1.3 Principles of medical ultrasound

Medical ultrasound is based on the principle that sound waves propagating through tissue are reflected at tissue boundaries or scattered by tissue inhomogeneities. Thus by observing the reflected waves (echoes) of an ultrasound wave traveling through tissue, information is obtained on tissue geometry and composition. The interference pattern of the reflections are specific for the type of tissue and by tracking the time-of-flight of an echo its axial depth can be determined. In a medical ultrasound system the waves are generated and received by a device called a transducer. A single transmission provides information on the tissue along the transducer's beam (an A-line). To create an image multiple transmissions are through the tissue either mechanically or electrically, thus producing many A-lines. By combining these A-lines a 2D cross section of the tissue can be obtained: a B-mode image. A 3D dataset can be obtained in a conceptually similar manner.

1.3.1 The acoustic field

The acoustic field produced by a transducer is affected by three phenomena: diffraction, attenuation and nonlinearity.
Diffraction affects all types of wave propagation in a bounded space. It is defined by Sommerfeld for light as (Cobbold, 2007): 'Any deviation of light rays from rectilinear paths which cannot be interpreted as reflection or refraction is called diffraction'. Perhaps a more insightful way to view diffraction is to depict the surface of the transducer as a collection of point sources spaced apart with much smaller distances than the acoustic wavelength. At any point in the propagation medium the signals produced by the point sources will interfere leading to maxima and minima in pressure at those points. The focus of the transducer is the final maximum where all contributions of the sources are in phase.
Next to diffraction, propagating sound waves are subject to energy loss through absorption and a redirection of some of its energy by scattering (Cobbold, 2007). Absorption is the process where ultrasound is converted into other energy forms such as heat. Scattering is the redirection of ultrasound energy by changes in compressibility and density on scales much smaller than the ultrasound wavelength. Most of the scattered ultrasound energy will be along paths that differ from the incident wave and will therefore not be detected by the transducer. As such, the attenuation of an ultrasound wave consists of both absorption and scattering effects (Cobbold, 2007).
The propagation of sound waves through a medium is nonlinear. This is caused by the fact that the medium is compressed during positive pressure peaks - relative to the ambient pressure - and rarefacted during negative pressure peaks. Since the propagation speed of the wave is related to the density of the medium, the propagation speed of the positive pressure peaks is higher than that of the negative peaks. This results in a distortion of the pressure wave.

The design of ultrasound systems and transducers aims to optimally exploit the above effects.

1.3.2 Transducers: single element

Most transducers used in medical sonography are based on the piezoelectric effect. Piezoelectricity is defined as an electrical polarization produced by mechanical strain. The polarization is proportional to the strain and changes sign with it (Cobbold, 2007). Thus the piezoelectric effect allows to convert energy in the electrical domain into energy in the mechanical domain and vise versa. The efficiency of the conversion depends on the frequency of the excitation; a slab of piezomaterial has a preferential frequency - the resonance frequency - at which the conversion of energy from one domain to the other is highest. The resonance frequency depends on the size and shape of the piece of piezomaterial. Since piezomaterial is anisotropic, the preferential frequency at which the piezomaterial vibrates differs from one direction to the next. A resonance mode in an unintended direction is called a 'spurious mode'.
Although the conversion of energy from one domain to the other is most efficient at the resonance frequency, frequencies near the resonance frequency of the transducer will also have a high conversion efficiency. The conversion efficiency of the transducer versus the excitation frequency is called the transfer function of the transducer. In transmission it is called the transmit transfer function and is usually expressed in Pa/V. In reception it is called the receive transfer function and is often expressed in V/Pa. The frequency range around the resonance frequency is called the bandwidth of the transducer.
A transducer usually consists of more components than only piezomaterial. One or more matching layers in combination with an acoustic backing are often fitted to a transducer to improve the energy transfer of the transducer into the tissue and to optimize its bandwidth. A schematic of a typical single element transducer is shown in Fig. 1.2.
The optimization of the transducer efficiency at the frequency band of interest and the suppression of spurious modes are very important in transducer design.

1.3.3 Transducers: arrays

The majority of transducers currently used in medical ultrasound are of the array type, instead of the single element type. An array transducer consists of many small transducer elements arranged in a line for 2D imaging or arranged in a 2D grid for 3D imaging. The array is called a 'linear array', if the elements are excited in successive groups. The array is called a 'phased array', if all the elements are excited by signals which are electronically phased to steer and to focus. Compared to (mechanically scanning) single element transducers arrays provide more flexibility (Szabo, 2004). Firstly, the beams can be automatically steered and focused at different depths. Secondly, the lateral resolution and beam shape can be altered through the adjustment of the length and apodization of the active aperture. And thirdly, dynamic focusing allows for perfect focusing throughout the scan depth instead of a fixed focal depth (Szabo, 2004).
The acoustic field of every transducer has sidelobes: the lobes of the far field radiation pattern that are not the main beam. A special kind of sidelobe associated with the periodic

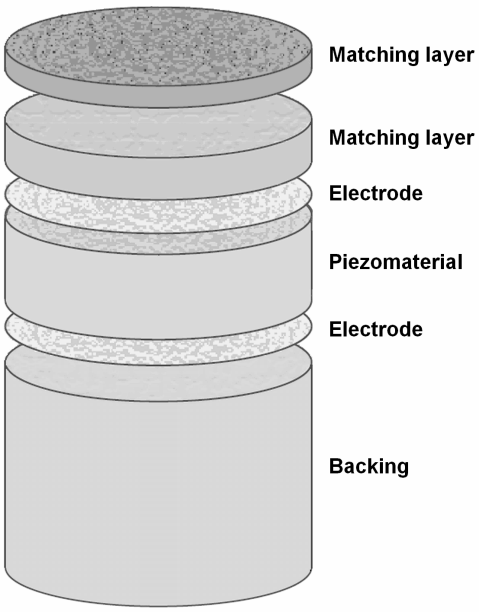

Figure 1.2: Schematic of the make-up of a typical single element transducer. Image adapted from Vos (2004), with permission.

array structure is called a grating lobe. Grating lobes are caused by constructive interference of the ultrasound beam between adjacent elements of the array (Barthez et al., 1997). The sidelobe and grating lobe levels relative to the main lobe are important for the design of arrays for medical ultrasound imaging, since these are one of the main factors determining the dynamic range of the ultrasound system (Cobbold, 2007).

1.3.4 Harmonic imaging

Up to the late 90s medical ultrasound was linear - the transmitted frequency was equal to the received frequency. Although medical ultrasound image quality had improved significantly during the previous years, a considerable subgroup of patients was still considered difficult to image due to tough windows, inhomogeneous skin layers and limited penetration (Averkiou et al., 1997). This was especially so in the case of echocardiography, where the ultrasound propagation paths are generally long and reflections from the skeletal structures occur often.

Second harmonic imaging

About a decade ago, it became possible to improve ultrasound image quality by exploiting the nonlinear nature of wave propagation. The technique is called 'tissue second harmonic imaging' and is based on the selective imaging of the second harmonic frequency (Averkiou et al., 1997; Thomas and Rubin, 1998). Compared to fundamental tissue imaging, second harmonic imaging has a number of advantages:

1. The second harmonic beam builds up progressively. Therefore, the effects of reverberation due to layers close to the transducer (e.g. the skin, subcutaneous fat) or due to strong reflectors in the near-field (e.g. the ribs) are greatly reduced. Thus, the progressive build-up reduces near-field artifacts (Tranquart et al., 1999; Bouakaz and de Jong, 2003).

2. The second harmonic beam has a narrower -6 dB width, which results in a higher lateral resolution.

3. The roll-off of the second harmonic beam is increased and the sidelobes are reduced. Therefore, a second harmonic image is less sensitive to clutter and off-axis scatterers (Ward et al., 1996; Shapiro et al., 1998; Tranquart et al., 1999; Humphrey, 2000; Bouakaz and de Jong, 2003).

4. The effective time length of the filtered second harmonic pulse is shorter in the case Gaussian apodized transmission pulses are used. This leads to a higher axial resolution.

These characteristics considerably improved ultrasound image quality, especially for the patient subgroup considered challenging to image (Bouakaz and de Jong, 2003). Fig. 1.3 shows example simulations of a fundamental and second harmonic beam illustrating the difference in characteristics. The main drawback of using the second harmonic band for imaging is the fact that it contains significantly less energy than the fundamental band. Thus to construct an ultrasound system capable of second harmonic imaging the following extra challenges have to be met compared to fundamental imaging:

1. Second harmonic imaging requires a system, which is both efficient in transmission on the fundamental band and sensitive in reception on the second harmonic band. In the case of a regular array design, the bandwidth of the transducer should be divided over both the transmit and receive bands. Since regular transducers have up to 80 % -6 dB bandwidth available, this translates into transmit pulses with limited bandwidth.

2. Transmission by the imaging system at the second harmonic frequency should be minimized.

3. The transducer should be efficient in transmission and be combined with waveform generators providing sufficient power. For optimal image quality the peak pressure at focus should be as high as possible without exceeding the regulatory limits.

4. The transducer should be sensitive in reception and be combined with a low noise receive system.

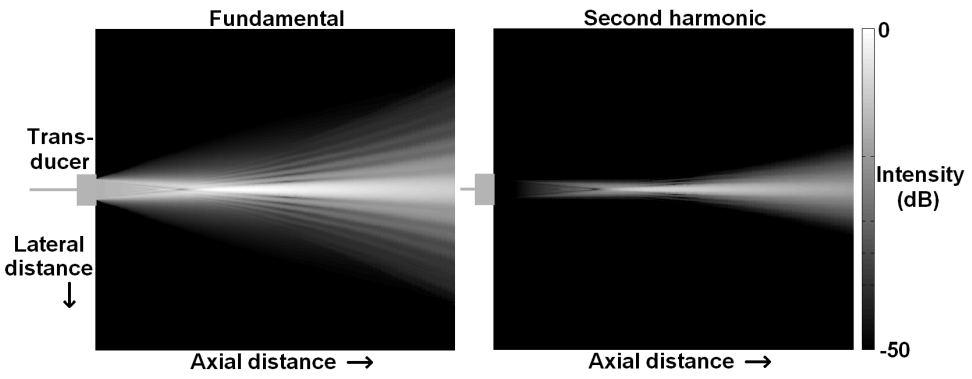

Figure 1.3: Example KZK simulations detailing the characteristics of the fundamental and second harmonic beams. The relative intensity is color coded using a dynamic range of 50 dB and normalized to the peak value of the fundamental.

Second harmonic imaging does provide a significant advantage for ultrasound system designers. In the case of transducers intended for fundamental imaging, the maximum distance between the element centers is approximately half the center frequency wavelength. However, this constraint can be relaxed in the design of transducers for second harmonic imaging. The second harmonic pressure is related quadratically to the overall pressure. Therefore, the ratio between the main beam and grating lobe pressures increases and the constraint on the distance between transducer element centers can be relaxed.

Imaging using higher harmonics - superharmonic imaging

Next to the selective imaging of the second harmonic band, also the higher harmonic bands - such as the third or fourth - could be used for imaging purposes. The beams of these higher harmonics have even more favorable characteristics compared to the second harmonic beam. The higher harmonics feature more narrow -6 dB beam widths (increased lateral resolution), a sharper lateral roll-off, increased reduction of sidelobes and a shorter length of the filtered harmonic time pulse (increased axial resolution). The drawback of using the higher harmonics in the context of imaging is that they contain even less energy than the second harmonic. Therefore, until now imaging based on harmonics higher than the second one has been hampered by signal-to-noise ratio (SNR) issues. Fig. 1.4 shows example simulations of the third, fourth and fifth harmonic beams corresponding to the fundamental and second harmonic beams of Fig. 1.3.
Recently, a new imaging modality dubbed tissue 'superharmonic imaging' (SHI) was proposed (Bouakaz et al., 2002). This modality combines the third to fifth harmonics arising from nonlinear wave propagation in an attempt to increase the received energy whilst retaining the advantages in beam shape provided by harmonics higher than the second one. The resulting images showed more details than those produced by second harmonic imaging (Bouakaz et al., 2002; Bouakaz and de Jong, 2003). Despite a promising start, there

are many hurdles to overcome in the quest for a practical superharmonic imaging system. To construct an ultrasound system capable of SHI the following challenges and questions have to be met:

1. The system should be efficient in transmission on the fundamental band and sensitive in reception from the third to fifth harmonic bands. This implies a -6 dB bandwidth $> 130\%$, a considerably larger bandwidth than that achievable with a conventional array configuration.

2. The transducer should be efficient in transmission and be combined with waveform generators providing sufficient power. For optimal image quality the peak pressure at focus should be as high as possible without exceeding the regulatory limits.

3. The transducer should be very sensitive in reception and be combined with a very low noise receive system.

4. It is critical that transmission at the third to fifth harmonic frequencies is minimized, thus ensuring that the energy in the third to fifth harmonic bands is produced by nonlinear propagation.

5. The optimal transmission frequency for SHI has to be determined.

6. Methods should be investigated to use and display the third to fifth harmonics in a single image, for example by using dedicated pulsing schemes and/or postprocessing techniques.

Harmonic imaging using ultrasound contrast agents

The selective imaging of harmonics is also used for ultrasound contrast agent (UCA) enhanced imaging. Two imaging strategies can be applied depending on the type of contrast agent. The first is used for rigid shelled contrast agents: high MI ultrasound pulses are transmitted to disrupt the agent. The destruction of the contrast agent then produces strongly nonlinear signals, which can be used to differentiate the contrast signal from tissue (Frinking et al., 1999; Bouakaz et al., 2005; Emmer, 2009). The second imaging strategy is used for contrast agents with more flexible shells. These agents are able to oscillate nonlinearly at low acoustic pressures ($\sim$100 kPa) producing higher harmonics, subharmonics and ultraharmonics (Schrope et al., 1992; Shi and Forsberg, 2000; Bouakaz et al., 2002; Chomas et al., 2002; Emmer, 2009; Vos, 2010). At these pressures the contribution of nonlinear wave propagation to the higher harmonics is low leading to a high contrast-to-tissue ratio (CTR) in the resulting ultrasound images. The advantages of selectively imaging the second harmonic frequency in combination with UCAs have been first described for pulse wave flow estimation by Schrope et al. (1992) (Schrope and Newhouse, 1993) and the technique is commonly implemented in commercial clinical ultrasound systems (Emmer, 2009). The quality of UCA enhanced images may still be increased by focusing on the superharmonics, as it has been shown by Bouakaz et al. (2002) that the CTR increases as a function of the order of the harmonic frequency.

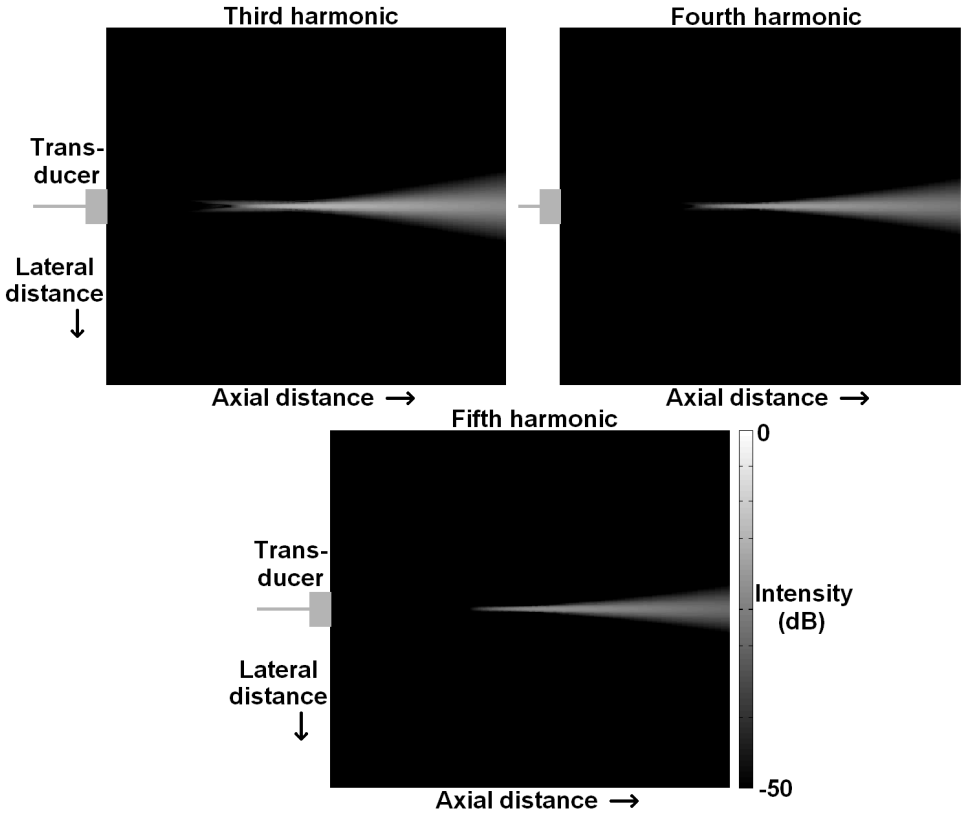

Figure 1.4: Example KZK simulations detailing the characteristics of the third, fourth and fifth harmonic beams. The relative intensity is color coded using a dynamic range of 50 dB and normalized to the peak value of the fundamental (shown in Fig. 1.3).

Next to the selective imaging of the harmonics, the subharmonic component could also be used for imaging purposes. The main advantage of using the subharmonic component is that the resulting image will not be contaminated by clutter from tissue signals, since nonlinear wave propagation through tissue does not produce subharmonics (Cobbold, 2007). Also, subharmonic imaging features an improved practical imaging depth compared to fundamental and harmonic imaging, as the attenuation of the subharmonic signal is lower. A disadvantage of subharmonic imaging is the reduced resolution compared to higher harmonic imaging (Shankar et al., 1998).
For an ultrasound system intended for UCA enhanced imaging the optimization of the sensitivity in reception and the minimization of noise in the receive chain is particularly important, since the pressure signals produced by single contrast microbubbles are generally low in amplitude.

1.4 Outline of the thesis

The first part of this thesis focuses on methods to characterize and model transducers. Methods to measure the absolute performance of a transducer as expressed in the amplitude and phase transfer functions are treated in chapters 2 and 3. The following chapters deal with the development of a FEM model (chapter 4) to design a transesophageal matrix probe for second harmonic imaging (chapter 5). Chapter 6 reports on the development of a single element transducer for bladder volume measurements using the second and third harmonics.
The second part of this work focuses on the development of hardware and signal processing methods for SHI. In chapters 7 and 8 the development of a dual frequency interleaved phased array transducer optimized for superharmonic echocardiography is reported. Chapter 9 presents a rigorous simulation study on the optimal transmission frequency for second harmonic and superharmonic imaging. The optimization of the interleaved design for receive sensitivity is also treated in this chapter. In chapter 10 the characteristics of the optimal fundamental, second harmonic and superharmonic beams are investigated in a simulation study. Chapters 11 - 14 detail the signal processing methods developed for superharmonic imaging. Standard postprocessing methods are treated in chapter 11, a dual pulse scheme is presented in chapters 12 and 13 and a chirp SHI method is demonstrated in chapter 14. The results of this thesis are further discussed in the final Discussion chapter.

Part 1: transducer characterization and modeling

CHAPTER 2

Transfer functions of US transducers for harmonic imaging and bubble responses[1]

Paul L.M.J. van Neer, Guillaume Matte, Jeroen Sijl, Jerome M.G. Borsboom, Nico de Jong

Abstract Current medical diagnostic echosystems are mostly based on harmonic imaging. This means that a fundamental frequency (e.g. 2 MHz) is transmitted and the reflected and scattered higher harmonics (e.g. 4 and 6 MHz), produced by nonlinear propagation, are recorded. The signal level of these harmonics is usually low and a well-defined transfer function of the receiving transducer is required. Studying the acoustic response of a single contrast bubble, which has an amplitude in the order of a few Pascal, is another area where an optimal receive transfer function is important. We have developed 3 methods to determine the absolute transfer function of a transducer. The first is based on a well-defined wave generated by a calibrated source in the far field. The receiving transducer receives the calibrated wave and from this the transfer functions can be calculated. The second and third methods are based on the reciprocity of the transducer. The second utilizes a calibrated hydrophone to measure the transmitted field. In the third method, a pulse is transmitted by the transducer, which impinges on a reflector and is received again by the same transducer. In both methods the response combined with the transducer impedance and beam profiles enables the calculation of the transfer function. The proposed methods are useful to select the optimal piezoelectric material (PZT, single crystal) for transducers used in reception only, such as in certain 3D scanning designs and superharmonic imaging, and for selected experiments like single bubble behavior. We tested and compared these methods on two unfocused single element transducers, one commercially available (radius 6.35 mm, center frequency 2.25 MHz) the other custom built (radius 0.75 mm, center frequency 4.3 MHz). The methods were accurate to within 15%.

[1]From Paul L.M.J. van Neer, Guillaume Matte, Jeroen Sijl, Jerome M.G. Borsboom, Nico de Jong, 'Transfer functions of US transducers for harmonic imaging and bubble responses', Ultrasonics, 2007, 46:336-340.

2.1 Introduction

Harmonic imaging is an established technique used in current medical diagnostic echo systems (Bouakaz and de Jong, 2003). A fundamental frequency (eg., 2 MHz) is transmitted into the human body and the reflected higher harmonics (eg., 4 and 6 MHz), produced by nonlinear propagation, are recorded. The signal level of these harmonics is low (Bouakaz and de Jong, 2003) and as such the efficiency in both transmission and reception and bandwidth of the transducer are critical. An area where an optimal transfer function in reception is important, is the study involving the acoustic response of single contrast bubbles, which are in the order of a few Pascal.
To assess the performance of a transducer, absolute measurements of its transfer functions are important. The functions of importance are the transmit, receive and pulse-echo transfer functions. In general, to characterize a transducer, the transmit transfer function is measured using a hydrophone. Also pulse-echo measurements are standard. Receive transfer functions are generally not considered. In this article we show that if one of the three transfer functions is measured the other two can be derived, if in addition the impedance of the transducer is measured.
We have adapted and tested three methods to determine absolute transfer functions, which are independent of the circuitry connected to the transducer. In the next section the necessary theory will be established.

2.2 Theory

The transducer transmit efficiency ($S_T(\omega, z)$) is defined by the International Electrotechnical Commission (IEC) as (Labuda et al., 2004)

$$S_T(\omega, z) = \frac{|p(\omega, z)|z}{|I_T(\omega)|}, \tag{2.1}$$

where $p(\omega, z)$ is the acoustical point pressure at an axial distance z of the transducer, ω is the angular frequency and $I_T(\omega)$ is the current through the transducer.
For unfocused transducers a reference transmit efficiency ($S_{ref}(\omega)$) can be defined as the transmit efficiency in the far field, whereas for focused transducers the reference transmit efficiency is defined to be the transmit efficiency at the focal point.

By rewriting expressions reported by Chen et al. (1993) $|p(\omega, z)|$ can be expressed as a function of $|p_0(\omega)|$ at the reference position

$$|p(\omega, z)| = \frac{A_T}{\lambda \cdot z}|p_0(\omega)|, \tag{2.2}$$

where A_T is the transducer surface area, λ the wave length and $|p_0(\omega)|$ the pressure at the transducer surface.
Combining (2.1) and (2.2) yields

$$|p_0(\omega)| = \frac{\lambda}{A_T} S_{ref}(\omega)|I_T(\omega)|. \tag{2.3}$$

The transducer transmit transfer function ($T_t(\omega)$) is defined to be

$$T_t(\omega) = \frac{|p_0(\omega)|}{|V_T(\omega)|}, \tag{2.4}$$

where $V_T(\omega)$ is the voltage over the transducer (see Fig. 2.1).

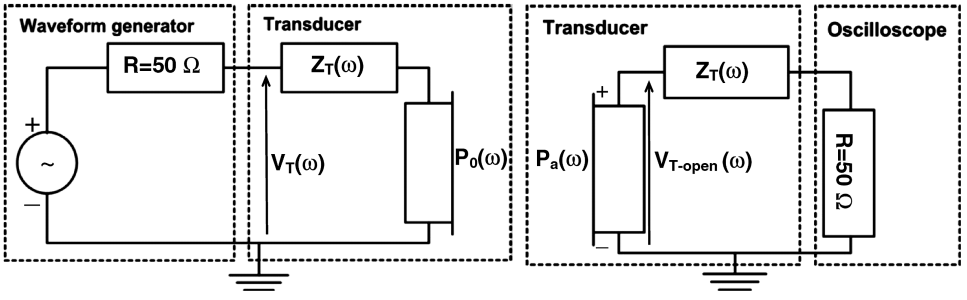

Figure 2.1: The essentials of the transmission and receive circuits are shown schematically on the left and right respectively.

Combining (2.3) and (2.4) produces

$$T_t(\omega) = \frac{1}{|Z_T(\omega)|}\frac{\lambda}{A_T}S_{ref}(\omega), \tag{2.5}$$

where $Z_T(\omega)$ is the complex impedance of the transducer.

The receive transfer function ($T_r(\omega)$) is defined to be similar to the sensitivity in reception ($M_T(\omega)$) as defined by the IEC (Labuda et al., 2004)

$$M_T(\omega) = T_r(\omega) = \frac{|V_{T-open}(\omega)|}{|p_a(\omega)|}, \tag{2.6}$$

where $V_{T-open}(\omega)$ is the open circuit voltage produced by the transducer (see Fig. 2.1) and $p_a(\omega)$ the received pressure averaged across the transducer surface.

Reciprocity

The spherical wave reciprocity parameter J for transducers of arbitrary shape and size is given by Bobber (1966)

$$J(\omega) = \frac{M_T(\omega)}{S_{ref}(\omega)} = \frac{2}{\rho_0 f}, \tag{2.7}$$

where ρ_0 is the ambient density of the medium in which the transducer is inserted and f the frequency.

A relation between $T_t(\omega)$ and $T_r(\omega)$ is obtained by combining (2.5), (2.6) and (2.7)

$$\frac{T_r(\omega)}{T_t(\omega)} = \frac{2|Z_T(\omega)|A_T}{\rho_0 c_0}, \tag{2.8}$$

where c_0 is the small signal acoustic wave speed of the medium in which the transducer is inserted.

2.3 Methods

2.3.1 Experimental setup

The experimental setup consisted of a tank filled with water with the transmitting transducer mounted in the sidewall and the receiving transducer, hydrophone or flat plate mounted in a holder controlled by an xyz-system (see Fig. 2.2).

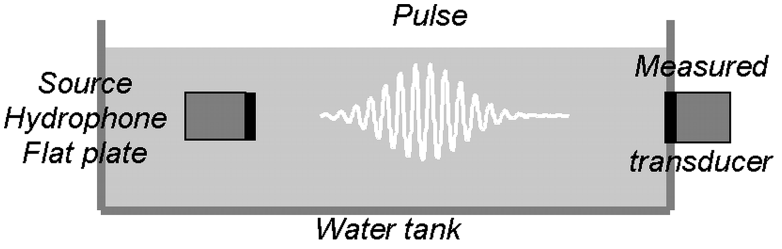

Figure 2.2: Schematic diagram of the experimental setup.

Care was taken to ensure that the transmitter output pressure was of such low magnitude that nonlinear propagation could be neglected. The influence of attenuation was neglected as well, as the propagation distance in water was small, in the order of centimetres. A correction for diffraction is necessary to recalculate the pressure at the transducer surface from a pressure measured some distance away. The exact diffraction correction function posted by Goldstein et al. (1998) is used to correct for the diffraction effects of a transmitting flat, circular piston transducer mounted in an infinite rigid baffle and the spatial averaging effects by a receiving flat circular piston transducer in a coaxial geometry. The expression given by Chen and Schwarz (1994) is used to correct for the diffraction of a flat plate transducer to a flat plate (perfect reflector) and back to the transducer. As a transmission pulse a spike was generally used.

2.3.2 Direct transmit transfer measurement

The transducer is mounted in the sidewall of the tank and used as a source transmitting a known pulse. A hydrophone is mounted in the holder of the xyz-system and measures the transmitted field. The transmit transfer function (T_t) of the transmitting transducer is

calculated by

$$T_t = \frac{V_h}{V_T} \cdot \frac{1}{T_h \cdot D_t}, \tag{2.9}$$

where V_h is the Fourier transformed voltage produced by the hydrophone, V_T the Fourier transformed voltage measured over the impedance of the transmitting transducer, T_h the hydrophone transfer function and D_t the diffraction correction function for the transmitting transducer.

2.3.3 Direct receive transfer measurement

A source with known transmit transfer function is mounted in the sidewall of the tank transmitting a known pulse. The transducer is mounted in the holder of an xyz-system and used as a receiver. Its receive transfer function (T_r) is calculated by

$$T_r = \frac{V_{T-open}}{V_T^s} \cdot \frac{1}{T_t^s \cdot D_t^s}, \tag{2.10}$$

where V_{T-open} is the Fourier transformed open circuit voltage produced by the receiving transducer, V_T^s the Fourier transformed voltage measured over the source impedance, T_t^s the transmit transfer function of the source and D_t^s the diffraction correction function for the source.

2.3.4 Pulse-echo

The transducer is mounted in the sidewall of the tank. It transmits a known pulse, which impinges on a thick aluminium plate reflector. The same transducer receives the reflected sound. The transmit and receive transfer functions of said transducer are related by

$$T_t \cdot T_r = \frac{V_{T-open}}{V_T} \cdot \frac{1}{D_{pe} \cdot R_I}, \tag{2.11}$$

where V_{T-open} is the Fourier transformed open circuit voltage produced in reception, V_T the Fourier transformed voltage measured over the transducer impedance in transmission, D_{pe} the diffraction correction function for the transmitting transducer to the flat plate and back and R_I the intensity reflection coefficient, for aluminium $\sqrt{0.84}$.

2.3.5 Equipment

Two transducers were investigated, both were of the unfocused single element type. The first was a commercially available transducer (PZT V306, Panametrics, Waltham, MA, USA, 2.25 MHz center frequency, diameter 12.7 mm), the other custom built (composite, 4.5 MHz center frequency, diameter 1.5 mm). An arbitrary waveform generator (33250A, Agilent, Loveland, Colorado) is used as a voltage source and connected directly to the transmitting transducer if necessary. The signal received by the transducer under scrutiny or hydrophone is attenuated by an attenuator (355D, Agilent, Santa Clara, CA, USA), amplified by a low noise amplifier (AU-3A-0110-BNC, Miteq, Hauppauge, NY, USA) and

digitized by an oscilloscope (9400A, LeCroy, Geneva, Switzerland). Both the waveform generator and oscilloscope are connected to a computer through GPIB.

2.4 Results

2.4.1 Panametrics V306

The left graph of Fig. 2.3 shows the transmit transfer functions of a Panametrics V306 determined by the various methods, the right graph presents its receive transfer function. The transfer functions determined by the different methods are similar and overlap. Except for the transfer spectra determined by the direct transmit experiment, which are significantly lower near 5 MHz. This is due to the presence of a low pass Butterworth filter with a cut-off point at 5 MHz in the measurement system. The accuracy is estimated at $\pm$ 15%, which is close to the accuracy of the hydrophone used. Notice the difference in shape between the transmit and receive transfer spectra, this is caused by the frequency dependency of the transducer's impedance.

2.4.2 Custom made 1.5 mm transducer

The left graph of Fig. 2.4 shows the transmit transfer functions of the custom 1.5 mm transducer determined by the various methods, the right graph presents its receive transfer function. The transfer functions determined by the different methods are similar. Below 2 MHz and above 7 MHz the SNR of the received signals was quite low. Between these frequencies the accuracy is estimated at $\pm$ 15%, which is close to the accuracy of the hydrophone used. Notice the difference in shape between the transmit and receive transfer spectra, this is caused by the frequency dependency of the transducer's impedance.

2.5 Conclusion

The specific definitions of the transmit and receive transfer functions ensure that these transfer functions and the reciprocity theorem relating them are transducer characteristics and circuit independent.
All methods described are sufficiently accurate for absolute transfer function measurements, the particular choice of method is based on practical considerations. A reciprocal transducer can be completely characterized using a pulse-echo measurement and a vector impedance measurement, without the need for a hydrophone or calibrated transducer.
Because of these reasons, the proposed methods are particularly suited to select the optimal piezoelectric material (PZT, single crystal) for arrays used in reception only (3D scanning, superharmonic imaging) or to judge the performance of alternative transducer designs. These methods are also important for selected experiments like single bubble behavior, where the complicated low pressure bubble response makes the precise absolute characterization of the measurement system mandatory.

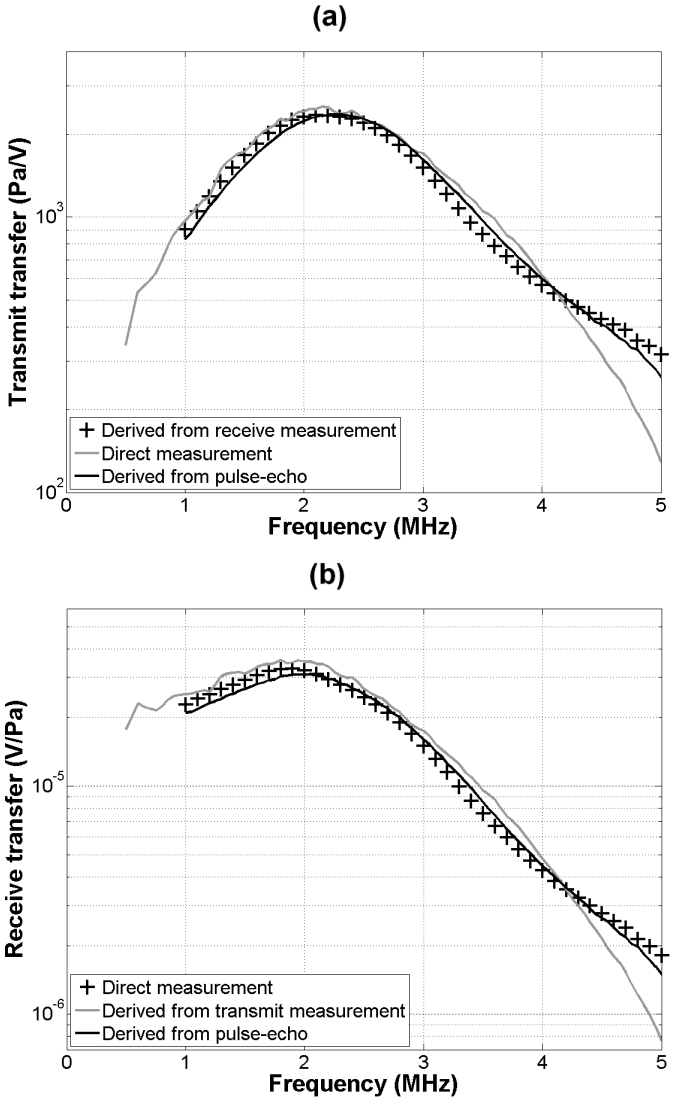

Figure 2.3: a) The transmit transfer function of a Panametrics V306 measured using the described methods. b) The receive transfer function of the same transducer.

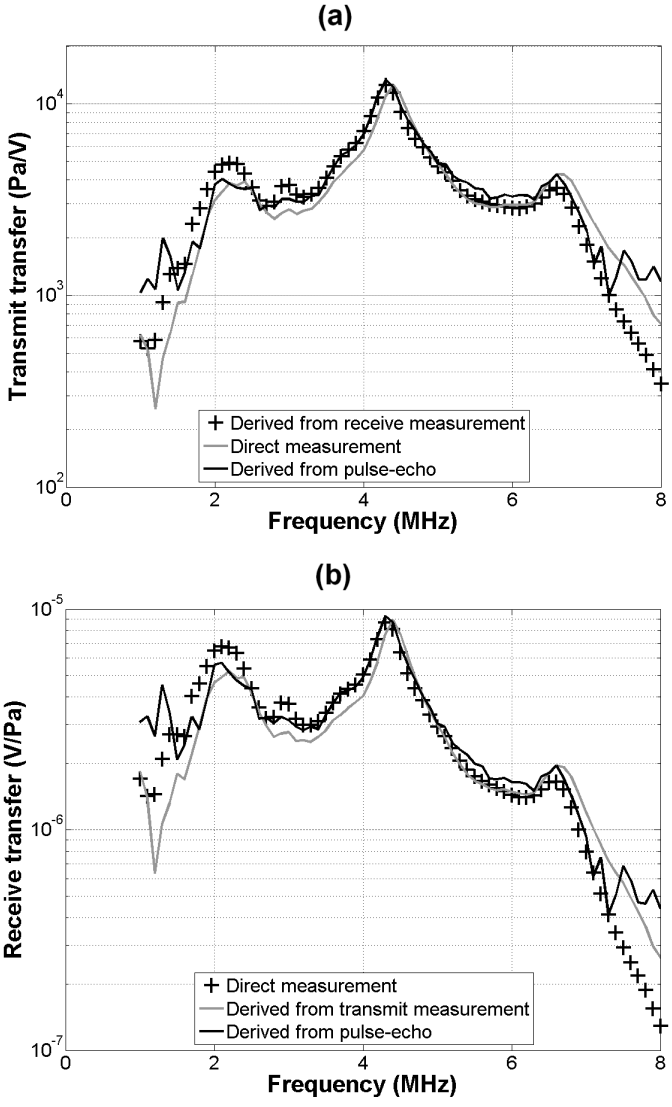

Figure 2.4: a) The transmit transfer function of the custom built 1.5 mm transducer measured using the described methods. b) The receive transfer function of the same transducer.

CHAPTER 3

Reflector-based phase calibration of ultrasound transducers[1]

Paul L.M.J. van Neer, Hendrik J. Vos, Nico de Jong

Abstract Recently, the measurement of phase transfer functions (PTFs) of piezoelectric transducers has received more attention. These PTFs are useful for e.g. coding and interference based imaging methods, and ultrasound contrast microbubble research. Several optical and acoustic methods to measure a transducer's PTF have been reported in literature. The optical methods require an expensive setup to which not all ultrasound laboratories have access to. The acoustic methods require accurate distance and acoustic wave speed measurements - small errors in these lead to large errors in phase. In this paper we present an acoustic pulse-echo method to measure the PTF of a transducer, which is based on linear wave propagation and does not require accurate knowledge of the wave travel distance and the acoustic wave speed. In our method the transducer is excited by a monofrequency sine burst with a rectangular envelope. The transducer initially vibrates at resonance (transient regime) prior to the forcing frequency response (steady state regime). The PTF value of the system is the difference between the phases deduced from the transient and the steady state regimes. Good agreement was obtained between KLM simulations and measurements on two transducers in a 1 - 8 MHz frequency range. The reproducibility of the method was $\pm 10^{\circ}$. This work demonstrates that the PTF of a transducer can be measured in a simple laboratory setting.

[1] Ultrasonics, accepted.

3.1 Introduction

The impulse response of a transducer can be represented in the frequency domain by its complex analogue, the transfer function. Methods to measure the amplitude transfer functions (ATFs) of ultrasound transducers and hydrophones are well developed (Ludwig and Brendel, 1988; Esward and Robinson, 1999; Radulescu et al., 2003; Matte et al., 2008; Umchid et al., 2009). Less developed are methods to measure the phase between the driving signal and the surface oscillation of the transducer as a function of the excitation frequency. However, a complete description of transducer behavior should consist of the phase transfer function (PTF) as well as the amplitude transfer function (ATF).
Several applications in medical ultrasound may benefit from information about the PTFs next to the ATFs of the transducers. For example, ultrasound contrast agent (UCA) enhanced medical imaging methods could be optimized. These techniques improve the contrast-to-tissue ratio in contrast harmonic imaging by reducing the level of tissue-generated harmonics without sacrificing frame rate (Krishnan et al., 1998; Christopher, 1999; Shen et al., 2007; Shen and Hsieh, 2008). The methods are based on transmitting a pulse with two frequency components, the fundamental and a high frequency component. Tissue second harmonics are either reduced by direct destructive interference by transmitting the high frequency component at the second harmonic frequency (Krishnan et al., 1998; Christopher, 1999), or by the nonlinear interaction between the fundamental and the high frequency component (Shen et al., 2007; Shen and Hsieh, 2008). Currently, iterative image calibration is used to optimally suppress the tissue harmonic (Shen and Hsieh, 2008). The number of iterations in this procedure could be reduced based on a measurement of the transmitting transducer's PTF, as this would enable the calculation of an initial estimate of the phase required for optimal suppression. Furthermore, coding-based imaging techniques - e.g. chirp based imaging - could be optimized by tailoring the emitted pressure pulse using an arbitrary waveform generator and the ATF and PTF (Misardis and Jensen, 2005a). Furthermore, in in-vitro studies involving the acoustic response of single UCA microbubbles, the ATFs and PTFs of the transducers used could be employed to dissociate the setup and microbubble responses - as their vibration is of considerable complexity (Sijl et al., 2008; Guidi et al., 2010).
In literature optical and acoustical methods are used to determine the PTF of transducers. Generally, for the optical methods an interferometer is used to measure the displacement of a pellicle and thus to calibrate the acoustic field. The pellicle is then replaced by the hydrophone under investigation (Koch and Molkenstruck, 1999; Wilkens and Koch, 2004). Good results of hydrophone calibrations with a frequency range of 1 - 70 MHz have been presented (Koch and Molkenstruck, 1999). However, the methods based on optical interferometry require a relatively expensive optical setup to which not all ultrasound laboratories have access to. For the acoustic methods several approaches have been described. Luker and van Buren (1981) extended the three-transducer reciprocity calibration for hydrophones to include phase for the 100 kHz range. Dang et al. (2002) derived a similar three-transducer reciprocity calibration method based on two-port network theory and presented results in the 100 kHz - 5 MHz range. A pulse-echo method was developed by Lopez-Sanchez and Schmerr (2006) for frequencies ranging from 1 - 20 MHz. Furthermore, a calibration method for hydrophones based on heterodyne and time-gated spec-

trometry was published by (Koch, 2003) for frequencies ranging from 1 - 20 MHz. In all these methods both the distance between the transmitter and receiver and the acoustic wave speed of the measurement medium needs to be accurately known. Small errors in either of them lead to large phase errors (Luker and van Buren, 1981). For example, an uncertainty of $\pm$0.1 m/s in the acoustic wave speed - a measurement accuracy of 0.007%, if water is the propagation medium (acoustic wave speed: $\sim$1490 m/s) - corresponds to an uncertainty in the PTF of $\pm 6.5^\circ$ at 4 MHz. The distance between the transmitter and receiver can be determined in practice with an uncertainty in the order of $\pm$0.1 mm - an accuracy of 0.1% at 10 cm - due to the issue of aligning the transmitter and receiver. The uncertainty in the PTF measurement at 4 MHz associated with the uncertainty of the axial distance is then $\pm 97^\circ$. Luker and van Buren (1981) addressed this issue with a specially constructed setup, where the distances between each transducer were known. Koch (2003) addressed the distance uncertainty by using a linear fitting procedure on the phase values in the 1 - 4 MHz range and subsequently subtracting the estimated values from the experimental data in the complete frequency range. The method was shown to work well on hydrophones, since monotone phase effects are unlikely at 1 - 4 MHz. However, this cannot be assumed for multilayered transducers - a constant slope component in the PTF of the transducer would be removed by the fitting procedure.
In this paper we present a novel acoustic method to measure the PTF without the necessity to measure wave travel distances and the acoustic wave speed of the medium. It is based on a pulse-echo measurement, where the driving pulse is a sine burst with a rectangular envelope. Initially the transducer will resonate at its natural resonance frequency followed by a forced vibration at the frequency of the burst. In this way phase relations as function of the frequency can be uniquely derived. In this technique linear wave propagation is assumed.
First we describe the theoretical background on which the method is based and continue with the implementation and setup details. The measurement results of two transducers are presented and compared with KLM model simulations. The discussion section then examines the advantages and limitations of the method.

3.2 Theory

The complex transducer transmit efficiency ($S(\omega, z)$) is defined as (Bobber, 1966; Luker and van Buren, 1981):

$$S(\omega, z) = \frac{p(\omega, z)}{I(\omega)}, \tag{3.1}$$

where $p(\omega, z)$ is the acoustical point pressure at an axial distance z of the transducer, ω is the angular frequency and $I(\omega)$ is the current through the transducer electrodes.
The complex transducer receive sensitivity ($M(\omega)$) is defined as (Bobber, 1966; Luker and van Buren, 1981):

$$M(\omega) = \frac{V_{open}(\omega)}{p_a(\omega)}, \tag{3.2}$$

where $V_{open}(\omega)$ is the open circuit voltage over the transducer and $p_a(\omega)$ the received pressure averaged across the transducer surface.

For reciprocal transducers (3.1) and (3.2) are related by the complex spherical wave reciprocity parameter (J), which is defined as (Luker and van Buren, 1981):

$$J(\omega) = \frac{M(\omega)}{S(\omega)} = \frac{4\pi z_{ref}}{i\omega\rho_0} e^{ikz_{ref}}, \tag{3.3}$$

where i is $\sqrt{-1}$, ρ_0 is the ambient density of the propagation medium, z_{ref} is the reference distance and k is the wave number - defined as $k = 2\pi/\lambda$ with λ the acoustic wavelength. The spherical wave reciprocity parameter (J) is valid in the far field of transducers of arbitrary shape and size, and assumes linear wave propagation.
We now define the complex transducer transmit transfer function ($T_t(\omega)$) to be independent of the acoustic field:

$$T_t(\omega) = \frac{p_0(\omega)}{V(\omega)}, \tag{3.4}$$

where $p_0(\omega)$ denotes the average pressure on the transducer surface and $V(\omega)$ is the voltage over the transducer electrodes.
The complex receive transfer function ($T_r(\omega)$) is defined to be equal to $M(\omega)$:

$$T_r(\omega) = M(\omega) = \frac{V_{open}(\omega)}{p_a(\omega)}, \tag{3.5}$$

An expression for the on-axis pressure distribution of a flat circular symmetric piston transducer excited by continuous wave excitation is (Chen et al., 1993):

$$p(\omega, z) = p_0(\omega) e^{-ikz} \left(1 - e^{-i\frac{ka^2}{2z}}\right), \tag{3.6}$$

where a is the radius of the active transducer element.
Equation (3.6) assumes $z > a$ and can be rewritten into:

$$p(\omega, z) = 2p_0(\omega) sin\left(\frac{ka^2}{4z}\right) e^{-ikz} e^{-i\left(\frac{ka^2}{4z} - \frac{\pi}{2}\right)}, \tag{3.7}$$

In the far field limit (3.7) can be approximated by:

$$p(\omega, z) = 2p_0(\omega) \frac{ka^2}{4z} e^{-ikz} i, \tag{3.8}$$

By combining (3.1), (3.3), (3.4), (3.5) and (3.8) and choosing $z = z_{ref}$ in (3.8) we obtain:

$$\frac{T_r(\omega)}{T_t(\omega)} = \frac{2Z(\omega)A}{\rho_0 c_0}, \tag{3.9}$$

Where $Z(\omega)$ is the electrical impedance of the transducer, A is defined as $A = \pi a^2$ and c_0 is the small-signal acoustic wave speed in the propagation medium.

3.2.1 Pulse-echo reflector measurement

Assuming linear propagation, the received signal in a pulse-echo experiment is described by:

$$V_{open}(\omega) = \alpha(\omega)D(\omega)e^{-ikz}S_p(\omega)R(\omega)T_t(\omega)V(\omega)T_r(\omega), \tag{3.10}$$

Where $\alpha(\omega)$ is the attenuation, $D(\omega)$ is the diffraction, e^{-ikz} is the phase change due to acoustic wave travel, $S_p(\omega)$ captures any spatial averaging effects by the transducer and $R(\omega)$ is the reflection coefficient of the reflector.

By combining (3.9) and (3.10) expressions for $T_t(\omega)$ and $T_r(\omega)$ can be derived:

$$T_t(\omega) = \sqrt{\frac{\rho_0 c_0 V_{open}(\omega)}{2Z(\omega)AV(\omega)} \cdot \frac{1}{\alpha(\omega)D(\omega)e^{-ikz}S_p(\omega)R(\omega)}}, \tag{3.11}$$

$$T_r(\omega) = \sqrt{\frac{2Z(\omega)AV_{open}(\omega)}{\rho_0 c_0 V(\omega)} \cdot \frac{1}{\alpha(\omega)D(\omega)e^{-ikz}S_p(\omega)R(\omega)}}, \tag{3.12}$$

From (3.11) and (3.12) the ATFs and PTFs ($\angle T_t(\omega)$ and $\angle T_r(\omega)$) can be calculated. Equations (3.11) and (3.12) simplify into (3.13) and (3.14) assuming that the attenuation of the propagation medium follows a square power law (eg. for water), the reflector is made from a material with low acoustic loss and located far away from the transducer, and sine bursts with a square envelope are used as transmission signals:

$$\angle(T_t(\omega)) = \frac{\angle(V_{open}(\omega) - V(\omega)) - \angle(Z(\omega)) - \pi/2}{2}, \tag{3.13}$$

$$\angle(T_r(\omega)) = \frac{\angle(V_{open}(\omega) - V(\omega)) + \angle(Z(\omega)) - \pi/2}{2}, \tag{3.14}$$

Equations (3.13) and (3.14) are only applicable assuming specific conditions for the attenuation of the medium and the acoustic wave propagation in the medium, the properties of the reflector and the diffraction characteristics of the transducer. The limitations for these parameters are discussed below:

Attenuation ($\alpha(\omega)$)

Ultrasound waves are attenuated by absorption and scattering. In the case of an unbounded homogeneous medium absorption causes dispersion: the change in the phase velocity with frequency of a propagating wave. The relation describing the phase velocity (c_ω) of waves propagating in media whose attenuation (α) can be modeled according to $\alpha = \alpha_0^{'}|\omega|^n$, is given by Cobbold (2007):

$$\frac{1}{c_\omega} = \frac{1}{c_0^{'}} + \alpha_0^{'} tan\left(\frac{\pi n}{2}\right)(|\omega|^{n-1} - |\omega_0^{'}|^{n-1}), \tag{3.15}$$

Where $c_0^{'}$ is the phase velocity at the reference angular frequency $\omega_0^{'}$ and $\alpha_0^{'}$ is the angular frequency attenuation factor. Equation (3.15) holds for $0 < n < 1$ and $1 < n < 3$.

If $n = 2$, (3.15) simplifies to $\frac{1}{c_\omega} = \frac{1}{c_0}$. The attenuation of pure water follows a square power law relation (Szabo, 2004). Therefore, dispersion effects may be neglected, if pure water is used as the propagation medium.

Reflection at normal incidence by a flat reflector ($R(\omega)$)

The reflection of a pressure wave, which travels at normal incidence to the reflector, by a flat reflector causes no phase change in the pressure signal, if both the propagation medium and the reflector are lossless (Leighton, 1994). These conditions can be approximated by using pure water (α = 2.17.10^{-3} dB/(MHz^2.cm) (Szabo, 2004)) as the propagation medium and a flat reflector made from aluminium (α = 2.6.10^{-2} - 6.2.10^{-2} dB/cm at 5 MHz (Mason and McSkimin, 1947)).

Diffraction ($D(\omega)$)

Diffraction is caused by the finite aperture size of the transmitting transducer. A pulse-echo experiment with a perfect reflector at axial distance z_R can be modeled by two identical and axially aligned transducers separated by a distance of $2z_R$. The on-axis pressure distribution of a flat piston transducer caused by diffraction is given by equation (3.7), showing that the contribution to the phase of a signal due to diffraction in the far field limit is $e^{i\frac{\pi}{2}}$. Therefore, if $\frac{ka^2}{8z_R} << \frac{\pi}{2}$, diffraction can be approximated by $e^{i\frac{\pi}{2}}$.

Spatial averaging ($S_p(\omega)$)

Spatial averaging occurs when a transducer of finite size receives a nonplanar pressure wave or a plane wave at an angle. In these cases the surface of the transducer is not excited equally and the electric field produced by the piezomaterial varies over the surface. This produces an extra phase shift, as the net voltage produced by a transducer at a specific point in time is related to the average of the electric field. In the case of a pulse-echo measurement spatial averaging is caused by diffraction. Generally, for transducers with sizes and frequencies typically used in the medical frequency range it holds that if diffraction can be approximated by $e^{i\frac{\pi}{2}}$, spatial averaging effects are low and can be neglected (the validity of neglecting spatial averaging was investigated by simulating the acoustic field of each measured transducer using Field II (Jensen and Svendsen, 1992; Jensen, 1996). The spatial averaging effects were then calculated using the expression reported by Radulescu et al. (2001)).

Acoustic wave travel (e^{-ikz})

The last term remaining to simplify (3.11) and (3.12) into (3.13) and (3.14) is e^{-ikz}, which is the phase change due to acoustic wave travel (Chen et al., 1993). To eliminate e^{-ikz}, we excited the electrodes of the transducer using a long sine burst with a square envelope (V). The start of the sine burst can be interpreted as the multiplication of a step function and a continuous sine. As transducers are damped resonance systems, the vibration induced by the step function at the start of the sine burst will be independent of the frequency of the

sine: the transducer starts vibrating at the same time point regardless of the forcing sine's frequency.

With reference to Fig. 3.1, let us consider the signal received by the transducer (V_{open}, the solid black line in Fig. 3.1) after the emitted pressure signal was reflected by a perfect reflector (e.g. an 8.5 cm thick aluminium slab) located in the transducer's far field (where $z_R >> \frac{ka^2}{4\pi}$). The starting point T_s of the signal (the star in Fig. 3.1) is constant regardless of the frequency of the forcing sine. A certain time after T_s the transient effect due to the step function has subsided and the transducer responds to the forcing frequency only (steady state regime). Next, a peak in the 'steady state' signal is selected, the time of which is denoted as T_p (the open circle in Fig. 3.1). As T_s is constant we may shift the excitation signal to T_s (the dashed gray line in Fig. 3.1). The phase difference between input and output signals is the relative phase difference between V_{open} and V at T_p (the open and filled circles in Fig. 3.1). Hence, this phase difference does not contain effects due to acoustic wave travel, but only due to transducer impedance, transfer functions and diffraction. The diffraction effects can be approximated in the very far field by $e^{i\frac{\pi}{2}}$ as shown in the paragraph on diffraction.

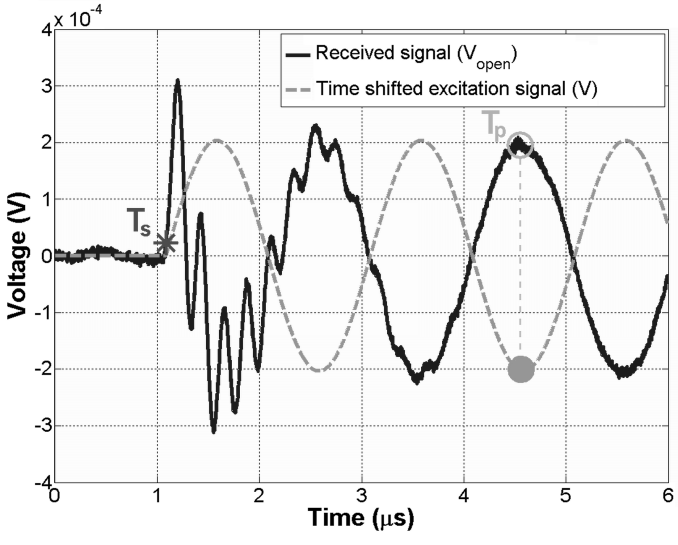

Figure 3.1: Pulse-echo response of a transducer excited by a monofrequency burst with a rectangular envelope. The solid black line is the signal received by the transducer (V_{open}). The dashed gray line is the time shifted excitation signal (V). The starting point (T_s) of the received signal is denoted by a star. The selected peak in the steady state part of the signal is denoted by the open circle (time point T_p). The phase difference between V_{open} and V is the relative difference between the open and filled circles. This phase difference contains effects due to the transducer transfer functions, impedance and diffraction.

3.3 Experimental setup and equipment

The experimental setup is shown in Fig. 3.2. The transducer was mounted in the sidewall of a water tank. The flat plate reflector was an 8.5 cm thick aluminium slab, which was located at an axial distance of ∼64 cm from the transducer.

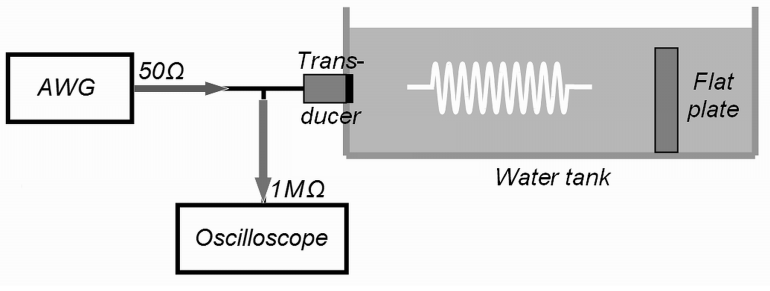

Figure 3.2: The experimental setup.

3.3.1 Equipment

Two custom built single element transducers were investigated. Custom transducer 1 was constructed using CTS 3203 HD piezomaterial (CTS Corporation, Bloomingdale, Illinois). It had neither matching layers nor a lens, and air backing. The transducer's radius was 6.5 mm and it had a 4 MHz center frequency. Custom transducer 2 was similar to transducer 1 but had in addition a front matching layer - its resonance frequency was 3.6 MHz. The properties of the materials are shown in Table 3.1. An arbitrary waveform generator (33250A, Agilent, Loveland, Colorado) drove the transducer with 300 cycle sine bursts with amplitude setting 5 V at a pulse repetition frequency of 250 Hz. The received signal was digitized by an oscilloscope (9400A, Lecroy, Geneva, Switzerland) at a sampling rate of 100 MHz. The input impedance of the oscilloscope was 1 MΩ. The electrical impedances of the equipment used were measured using a vector impedance meter (4193A, Hewlett Packard, Yokogawa, Japan).

3.3.2 Signal processing

Each pulse-echo measurement was repeated 128 times and the result was averaged and upsampled to 5 GHz. The starting point (the phase of the resonance frequency) of the signal (T_s in Fig. 3.1) was initially obtained by threshold detection. The threshold level was set equal to the noise floor, which was measured by averaging 128 time traces without signal and taking the maximum. The estimate of the starting point was refined by interpolating from the threshold voltage level to zero using the first order derivative of the initial section of the signal. The phase (φ) of the applied forcing frequency (at time T_p in Fig. 3.1) in the received signal relative to the starting point (T_s) was determined by fitting $Asin(\omega_d + \varphi)$ to

Table 3.1: Properties of the materials used in both example transducers

	Property	Variable	Unit	Transducer I	Transducer II
Piezo-material	Thickness	-	[m]	$5.07.10^{-4}$	$5.1.10^{-4}$
	Longitudinal wave speed	v_{33}	[m.s^{-1}]	4764	4764
	Density	ρ	[kg.m^{-3}]	7800	7800
	Coupling factor	k_t	-	0.536	0.536
	Dielectric constant	K_t^T	-	1197	1197
	Dielectric loss	$tan(\delta_e)$	-	0.028	0.028
	Mechanical quality factor	Q_m	-	65	65
Matching layer	Thickness	-	[m]	-	$1.15.10^{-4}$
	Longitudinal wave speed	v_{33}	[m.s^{-1}]	-	2440
	Density	ρ	[kg.m^{-3}]	-	2150
	Acoustic loss	α	[dB.m^{-1}.MHz^{-1}]	-	373

a window in the steady state regime (located $\sim$3 μs after T_s). Here A is the amplitude of the signal and ω_d the forcing frequency. In this way φ was determined for every applied forcing frequency. By compensation for the impedance effects of the transmission and reception circuits φ is recalculated into $\angle(V_{open}(\omega) - V(\omega))$, which can be directly inserted into (3.13) and (3.14) to obtain the PTFs.

3.3.3 KLM model

The PTFs of the custom built transducers were simulated using an in-house implementation of the KLM model (Leedom et al., 1971; Merks et al., 2006a,b). The material properties of the CTS 3203HD piezomaterial were based on the values reported by Sherrit et al. (1997) for the thickness extensional mode. The longitudinal wave velocity and attenuation of the matching layer used in custom transducer 2 were determined using the dual transducer method described by Wu (1996). A summary of the material properties used in the KLM model is given in Table 3.1.

3.4 Results

Two different transducers have been measured: one without a matching layer, the other with a matching layer.

3.4.1 Custom transducer 1

Fig. 3.3a shows the measured and KLM-simulated transmit PTFs of custom transducer 1. Fig. 3.3b presents its receive PTFs. The agreement between the simulations and the mea-

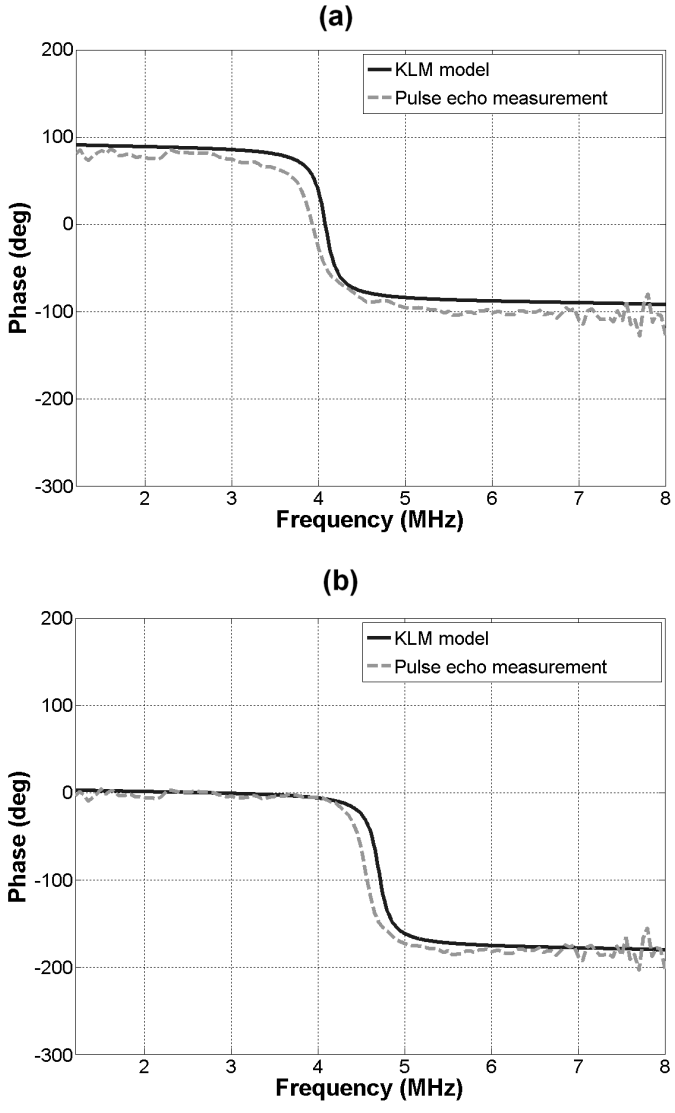

Figure 3.3: a) The modeled and measured transmit PTFs of custom transducer 1. The frequency where the transmit phase is 0° is the resonance frequency. b) The modeled and measured receive PTFs of custom transducer 1.

surements was good: the mean difference between the simulations and measurements was 13° and 7° for the transmit and receive PTFs respectively (Figs. 3.3a and 3.3b). There was an absolute difference of ∼90° and a frequency shift of ∼0.5 MHz between the transmit

and receive PTFs: this was in agreement with their different definitions as stated in equations (3.4) and (3.5). The resonance frequency of the transducer - the frequency where the transmit phase is 0° - was 3.93 MHz in the measurement and 4.07 MHz in the simulation (see Fig. 3.3a). The difference of 0.14 MHz between the measured and simulated resonance frequencies could be attributed to the variation of piezomaterial properties between batches. The steep slope around resonance is typical for a weakly damped, forced harmonic oscillator, as is the 180° difference between the phase at frequencies above and below resonance.

3.4.2 Custom transducer 2 with matching layer

Fig. 3.4a shows the measured and KLM-simulated transmit PTFs of custom transducer 2. Fig. 3.4b presents its receive PTFs. The simulations and the measurements differed considerably: the mean difference between the simulations and measurements was 73° and 76° for the transmit and receive PTFs respectively (Figs. 3.4a and 3.4b). The resonance frequency of the transducer - the frequency where the transmit phase is 0° - was 3.64 MHz in the measurement and 3.33 MHz in the simulation (see Fig. 3.4a). The difference between the measurements and the simulations could be attributed to the construction method used for custom transducer 2. The piezoelement and matching layer of transducer 2 were mounted in an indentation in the holder, to facilitate shaping the matching layer to its intended thickness (see Fig. 3.5b). The disadvantage of such a construction was that it restricted the vibration of the piezoelement at its edges. Therefore, the transducer deviated from the ideal piston resonator, which is modeled by the one dimensional KLM model. This was not the case for transducer 1, where the piezomaterial slab was glued on its edges on top of the holder resulting in an almost perfect piston transducer (see Fig. 3.5a).

3.5 Discussion

The main advantage of the proposed method for the measurement of PTFs is that a measurement of the acoustic wave travel distance or wave speed is not required. An estimate of the acoustic wave speed suffices to determine the minimum axial distance between the transducer and the reflector (see the paragraph on diffraction in the theory section). Furthermore, the method is robust in terms of alignment errors. The amplitude of the reflected signal is very sensitive to any deviations of the required perpendicular orientation of the reflector relative to the transducer. Thus the alignment of the reflector can be performed manually by searching for the maximum in the reflected signal. Therefore, a simple setup based on equipment commonly available in ultrasound labs, such as depicted in Fig. 3.2, suffices.

The proposed method only requires knowledge of the transducer diameter, the transmission frequency and an estimate of the acoustic wave speed. This is particularly useful for transducers where the piezomaterial is clamped on the sides, thus causing apodized surface movement instead of ideal piston behavior. In that case the phase bias due to diffraction calculable from (3.7) is actually an overestimation of the real phase bias (see paragraph on diffraction in the theory section).

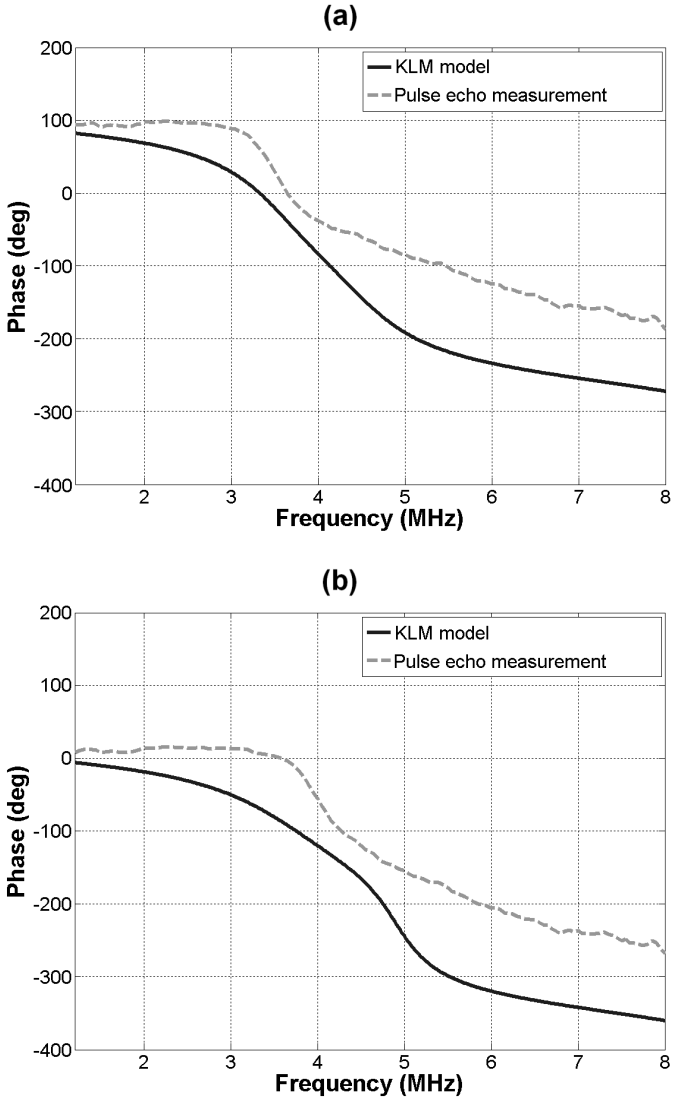

Figure 3.4: a) The modeled and measured transmit PTFs of custom transducer 2. The frequency where the transmit phase is 0° is the resonance frequency. b) The modeled and measured receive PTFs of custom transducer 2.

There is a trade-off between the distance of the reflector and the accuracy of the method. To limit the phase bias induced by diffraction the distance between the transducer and reflector should be large ($z_R >> \frac{ka^2}{4\pi}$ for a circular symmetric transducer). However, the

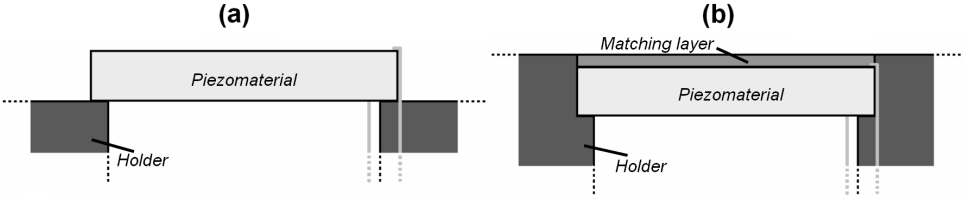

Figure 3.5: a) Schematic of custom transducer 1. b) Schematic of custom transducer 2.

signal-to-noise ratio (SNR) is limited at these distances due to diffraction and attenuation effects. At lower SNRs the accuracy of the method is reduced. From (3.7) it was calculated that the phase bias induced by diffraction varied from 2° to 16° for frequencies of 1 to 8 MHz at a distance of 0.64 m of the reflector.
The measurement reproducibility is estimated at $\pm 10°$ at high SNR (40 - 60 dB) and $\pm 20°$ at low SNR ($\sim$20 dB). These estimates were obtained by repeated measurements of the same transducer using different setups and equipment.
Transducers calibrated using the methodology presented in this work could be used as calibrated sources for the phase calibration of hydrophones. The hydrophone calibration would be performed similarly to the methodology presented here using multiple calibrated transducers to cover the entire frequency range of a hydrophone. Alternatively, the nonlinear propagation model based phase calibration method reported by Cooling and Humphrey (2008) for membrane hydrophones could be used. In this technique experimental measurements and numerical simulations of a nonlinearly distorted test field are compared, the idea being that the difference between these is the PTF of the hydrophone used to obtain the measurements. The advantage of the method of Cooling and Humphrey (2008) is that only a single calibrated transducer is needed to cover the frequency range of a hydrophone.
The proposed method could readily be extended to focused piston transducers. In this case the reflector would be located at the focal plane of the transducer. Equation (3.6) would change into the appropriate expression for the pressure of a focused piston transducer at focus as given by Chen et al. (1993). Also, the focal distance would be taken as the reference distance. The remainder of the derivation and methodology would remain the same.

3.6 Conclusion

This paper shows that the acoustic phase transfer of a transducer can be measured with a reproducibility of $\pm 10°$ using the presented methodology, with standard equipment based on a pulse-echo measurement.

Acknowledgements We would like to acknowledge the efforts of G. Springeling and M. Manten for the construction of the custom transducers and M.G. Danilouchkine, J.E.T. van Wamel and J.G. Bosch for their useful comments.

CHAPTER 4

A comparison of array element surface vibration calculated by finite element modeling and laser interferometer measurements[1]

Paul L.M.J. van Neer, Guillaume Matte, Philipp Gatta, Massimo Pappalardo, Nico de Jong

Abstract For several years the standard in ultrasound imaging has been second harmonic imaging. Recently, a new imaging modality dubbed superharmonic imaging (SHI) was proposed. SHI uses the higher - third to fifth - harmonics produced by either nonlinear propagation or contrast agent response. This modality requires a transducer with a high bandwidth (>130%), which was achieved by choosing different frequencies for the odd (4 MHz) and even (1 MHz) elements. For SHI it is important to minimize both crosstalk and the transmission of odd transducer harmonics. To determine the influence of geometry on these issues a 3D transducer model is necessary. In this paper we compare array element surface vibrations calculated by a finite element model (FEM) with measurements obtained using a laser interferometer system. A custom array was built (element size 13 mm x 0.2 mm, resonance frequency 1.6 MHz, no matching layer, backing 5.3 MRayl). Its elements were excited using continuous signals or impulses and its spatially and time dependant surface vibrations were measured in air using a laser interferometer setup. The array element (characterized by its dimensions, piezo parameters from the data sheet and measured bulk parameters of the backing) was modeled using the ANSYS 11 FEM package and subjected to the same excitation. The fundamental resonance, third harmonic, fifth harmonic and lateral resonance of the array elements were measured at 1.6, 6.2, 9.9 and 7.9 MHz and predicted by the FEM simulation at 1.7, 6.1, 9.9, and 8.0 MHz. The excursion during continuous wave excitation was measured at 27.6 nm and predicted by FEM at 26.4 nm. The ripple in the surface displacement over the elevation axis of the element had a 1.2 - 1.3 mm wavelength both in the measurements and in the FEM simulation. Good agreement was achieved between the FEM predicted surface vibrations and the laser interferometer results.

[1]From P.L.M.J. van Neer, G. Matte, P. Gatta, M. Pappalardo, N. de Jong, 'A comparison of array element surface vibration calculated by finite element modeling and laser interferometer measurements', Proc. IEEE Ultrasonic Symp., 2008, 788-791.

4.1 Introduction

For several years the standard in ultrasound imaging has been second harmonic imaging. Recently, a new imaging modality dubbed superharmonic imaging (SHI) was proposed (Bouakaz et al., 2002). SHI uses the higher - third to fifth - harmonics produced by either nonlinear propagation or contrast agent response. This modality requires a transducer with a high bandwidth (>130%), which was achieved by choosing different frequencies for the odd (4 MHz) and even (1 MHz) elements (Bouakaz et al., 2004b). For SHI it is important to minimize both the transmission of odd harmonics by the interleaved array and the inter-element crosstalk. The higher harmonic components used for SHI are low in amplitude, thus even low energy transmission of transducer harmonics reduces the image quality. Crosstalk limits the ring down of delayed signals from neighboring elements and the angular dispersion by increasing the effective element size (Guess et al., 1995). The influence of geometry on these issues can not be determined using 1D models (such as the KLM model) and requires a 3D approach. Traditionally, beam pattern measurements and electric measurements on the connections of neighboring elements (Guess et al., 1995) have been used to evaluate crosstalk. Recently, techniques such as laser interferometry and finite element modeling (FEM) have gained popularity in the modeling of complex vibration modes and crosstalk of phased arrays based on piezomaterial and cMUT's. Caronti et al. (2005) used both 3D FEM (Caronti et al., 2005) and laser interferometry (Caronti et al., 2003, 2005) to describe the acoustic coupling between cMUT array elements. Kondo and Kitatuji (2004) applied both FEM and laser interferometry to describe the effects of composite matching layers on mechanical crosstalk and Branca et al. (2004) used laser interferometry to study the effect of filling materials on inter-element coupling. Goldberg et al. (1997) used 3D FEM to predict the performance of multilayer transducers and to visualize their complex vibration modes.
In this paper we compare element surface vibration calculated by FEM with measured surface vibration obtained using a laser interferometer setup.

4.2 Methods

4.2.1 Custom array

A custom array was built based on CTS 3203HD piezomaterial, its backing had an acoustic impedance of 5.3 MRayl with an attenuation of 18 dB/cm at 1.6 MHz. No matching layer was applied. The array was cut into 18 elements using a diamond saw yielding an element size of 13 mm x 0.2 mm. The resonance frequency of the elements was 1.6 MHz. A picture of the array is displayed in Fig. 4.1.

4.2.2 Laser interferometer setup

An element of the array was excited by either a continuous sinusoidal signal at the array's resonance with amplitude 29 V_{pp} using a HP 8116A function generator (Agilent Technologies Inc., Englewood, CO, USA) or by an impulse with amplitude -69 V using a Pana-

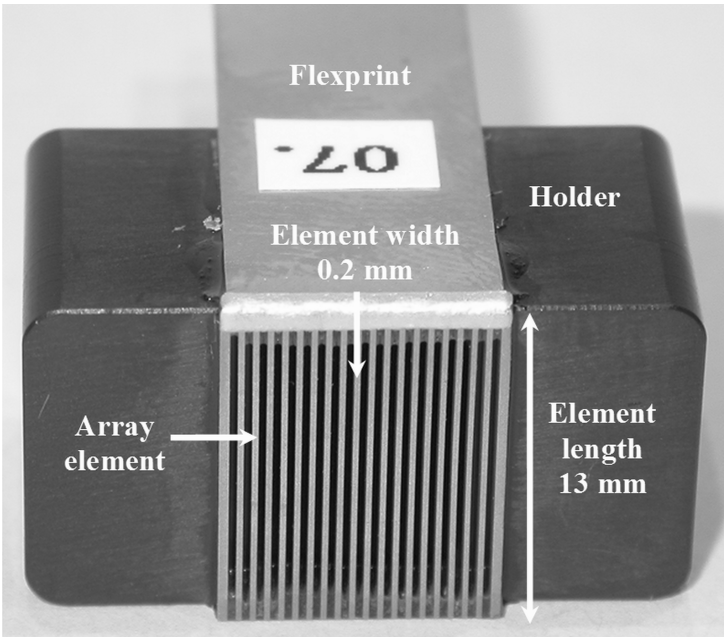

Figure 4.1: The custom built array.

metrics 5800 pulser/receiver (Panametrics, Waltham, MA, USA). The spatially and time dependant surface vibrations of the array elements in air were studied using a system originally realized by Gatta (2008) for the interferometric characterization of the vibrations of MEMS structures. The system was based on a Polytec MSV-300 laser scanning vibrometer system (Polytec GmbH, Waldbronn, Germany), similar to the one used by Caronti et al. [4, 5]. The laser interferometer consisted of a Polytec OFV 511 fiber interferometer connected to a Polytec MSV-Z-040 scanner controller and a Polytec OFV 2700-2 vibrometer controller. The interferometer equipment was mounted on a DMLM microscope (Leica Microsystems GmbH, Wetzlar, Germany) using a Polytec OFV 074 microscope adapter. The signals produced by the interferometer were digitized by a TDS 5034B oscilloscope (Tektronix Inc., Beaverton, OR, USA) at 100 MHz, which was triggered by the function generator. The oscilloscope was connected to a PC using an Ethernet connection. Labview 7.1 software (National Instruments, Austin, TX, USA) was used to control the xy-stage, laser interferometer and data acquisition. The array element surface vibration was studied using a laser spot diameter of 10 μm and a translation step size of 27 μm. In the case of continuous wave experiments the signal was averaged 8000 times for each measurement and filtered using an analogue filter with a cut off frequency of 2 MHz, in order to reduce the effects of variance in signal quality due to the variability of element surface reflectivity and surface roughness. In the case of impulse response experiments 128 traces were averaged per measurement with a pulse repetition frequency of 100 Hz.

4.2.3 Finite element model

An array element was modeled using the ANSYS 11 FEM package (ANSYS Inc., Canonsburg, PA, USA) and subjected to the same excitation used in the laser interferometer experiments. Only a quarter of the array element needed to be modeled due to symmetry. The piezomaterial geometry had dimensions 6.5 mm x 0.88 mm x 0.1 mm and was based on CTS 3203HD. Its material parameters were based on the values reported by Sherrit et al. (1997). The piezomaterial structure was meshed using the 20 node, 3D solid element SOLID226. The electrodes were assumed to be infinitesimally thin. The backing layer had dimensions 6.5 mm x 1.175 mm x 0.1 mm and was modeled using Maxwell viscoelasticity with a single time constant. The modeled backing was thin; the attenuation of the backing was set to ensure no reflections. The backing structure was meshed using the 20 node 3D viscoelastic elements VISCO89. The initial bulk modulus was taken to be 3.32 GPa and the initial shear modulus was 10.2 GPa. For both the associated time constant was 0.5 μs. The maximum frequency of interest was 10 MHz. The spatial sampling was chosen to be 12 points/wavelength at this frequency assuming the CTS 3203HD 33 direction wave speed of $\sim$3600 m/s. The sampling frequency was 25 MHz for the 'continuous' wave simulations and 100 MHz for the impulse simulations.
A schematic of the model is displayed in Fig. 4.2 and the material properties used in the simulations are listed in table 4.1.

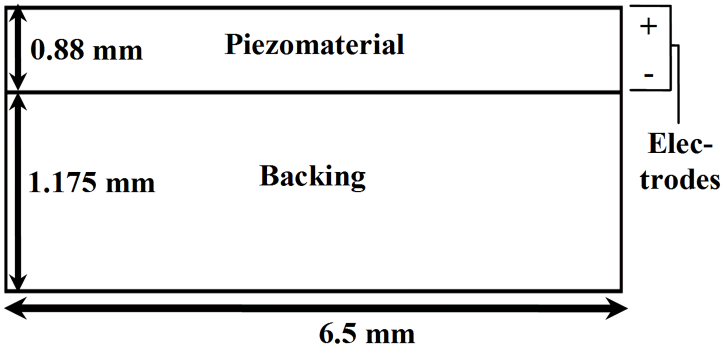

Figure 4.2: Array element geometry for FEM simulations.

4.3 Results

4.3.1 Continuous wave excitation

The mean element surface displacement versus time of the optical measurements and the FEM simulation are displayed in the top and bottom graph of Fig. 4.3 respectively.
The mean maximum excursion of the array element surface was 27.6 nm in the optical measurements versus a mean maximum excursion of 26.4 nm as predicted by the FEM si-

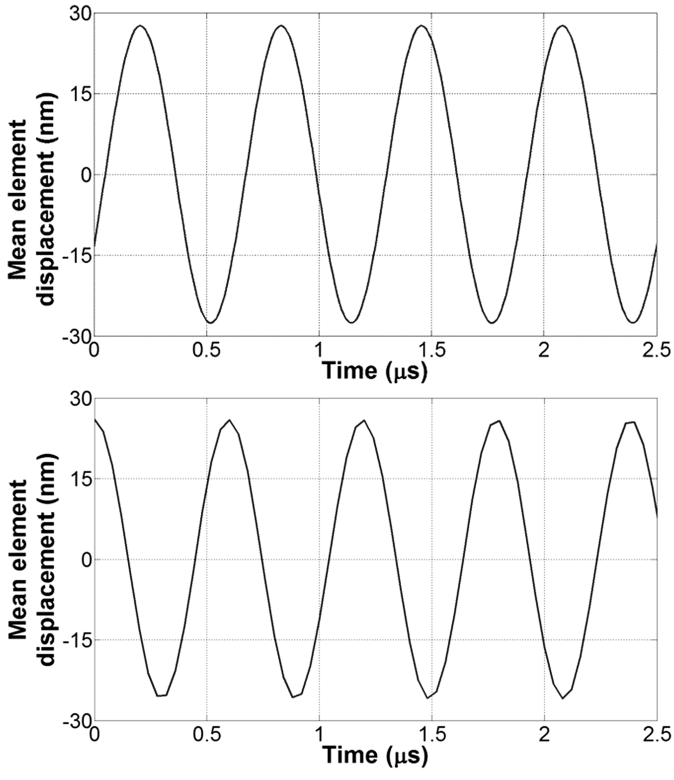

Figure 4.3: The mean element displacement versus time as optically measured on the top and as predicted by FEM simulations on the bottom.

mulation. The measured and the FEM predicted maximum excursion of the array element surface due to continuous wave excitation versus the location on the element elevation axis are shown in Fig. 4.4. The optical measurements did not start at the array element edge but a little distance away from the edge, due to poor reflectivity of the top electrode near the edge. Therefore, the measurements and the FEM simulation cannot be precisely superimposed: the apparent 180° phase shift between measurements and simulation is coincidental. The maximum excursion of the array element surface measured during continuous wave excitation was between 14.5 and 32 nm. The ripple in surface displacement over the elevation axis of the element had a wavelength between 1.2 and 1.3 mm and amplitude of $\sim$2 nm. Notice the apodization in the measured excursion as the measurement position was further away from the center. The maximum excursion of the array element surface predicted by the FEM model was between 13.6 and 35.1 nm. The ripple in surface displacement over the elevation axis of the element had a wavelength between 1.1 and 1.2 mm and amplitude $\sim$7 nm.

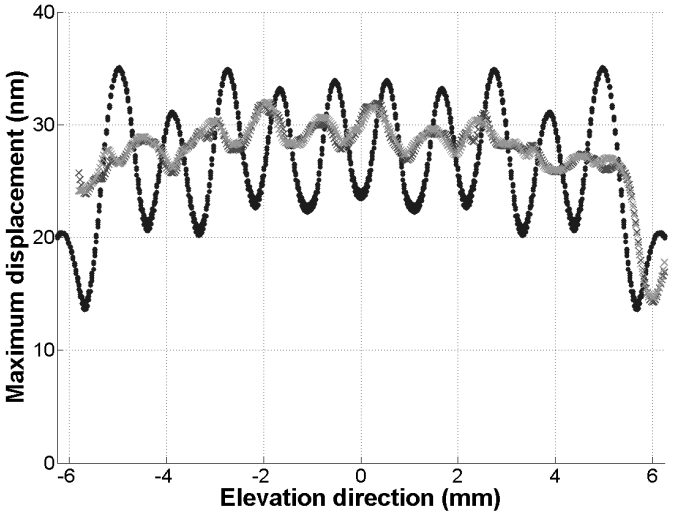

Figure 4.4: Optically measured and FEM simulation predicted maximum excursion of the array element surface, due to a continuous wave excitation with amplitude 29 V_{pp}, versus location on the element elevation axis. The FEM simulation predicted excursion is denoted by black dots, the optical measurements are denoted by light and dark grey crosses.

4.3.2 Impulse excitation

The measured and FEM predicted mean displacements of the array element surface due to impulse excitation are displayed in Fig. 4.5. The measured maximum mean displacement was ∼7.5 nm, and the FEM simulation predicted maximum mean displacement was ∼6.6 nm. After the initial peak the measured mean surface displacement decayed considerably faster than the FEM predicted mean surface displacement, except for a clear 130 kHz vibration trailing the initial excitation in the optical measurement. The absolute intensity of the Fourier transformed mean surface displacement of both the optical measurements and the FEM simulations as presented in Fig. 4.5 are displayed in Fig. 4.6. The optical measurements showed that the array had its fundamental resonance, third harmonic and fifth harmonic at 1.6, 6.2 and 9.9 MHz respectively. The FEM model predicts these resonances at 1.7, 6.1 and 9.9 MHz. A lateral mode was measured at 7.9 MHz, the FEM simulation put it at 8.0 MHz. Also, the FEM simulation yielded a resonance peak at 100 kHz.

4.4 Discussion

4.4.1 Continuous wave excitation

There is good agreement between the FEM predicted mean maximum surface vibration (26.4 nm) and the laser interferometer measurements (27.6 nm). The wavelength of the

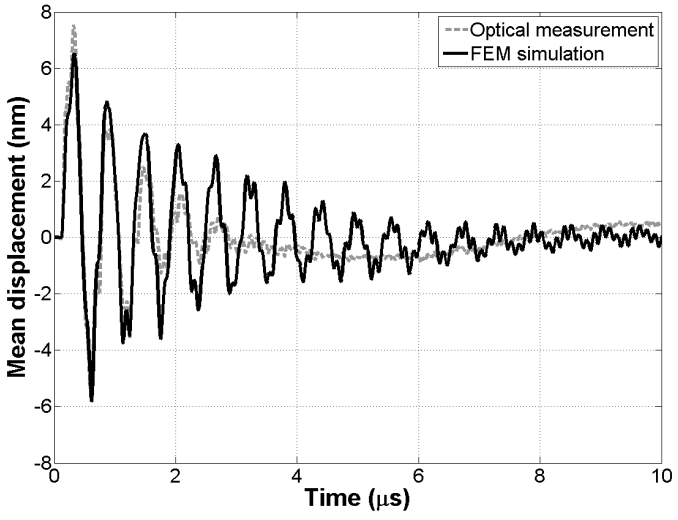

Figure 4.5: Optically measured and FEM simulation predicted mean excursion of the array element surface versus time, due to an impulse excitation with amplitude -69 V.

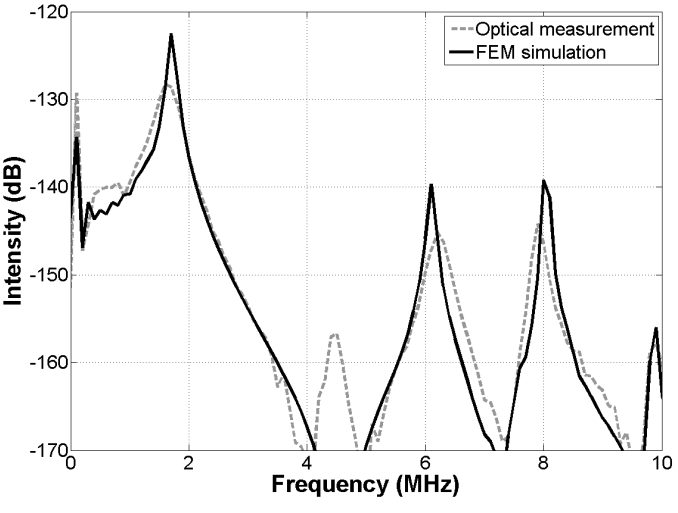

Figure 4.6: Absolute intensity of the Fourier transformed mean surface displacement, based on the time signal shown in Fig. 4.5.

ripple in surface displacement over the element elevation axis was the same in both the optical measurements and the simulation. The ripple originates from the interference of standing surface waves. The difference in ripple amplitude between experiment and simu-

lation may be explained by the fact that only a single array element was modeled in the FEM simulation. Thus there is no energy transfer from the excited element to other elements or to the holder, allowing the standing waves to reach higher amplitudes.
Notice the apodization in the optically measured displacement over the element elevation axis and the drop in maximum displacement ($\sim$50%) at the element edge (Fig. 4.4). These effects may be attributed to the glue present between the array elements. However, there is a drop in maximum displacement near the edges of the simulated array element as well (no glue is included in the simulation). This drop may be explained by the superposition of surface waves.

4.4.2 Impulse excitation

The optical measurements and FEM results showed similar initial maximum mean displacements of 7.5 nm and 6.6 nm respectively. The difference in decay after the initial peak between the simulation and measurements can be explained by the implemented viscoelastic backing model - it is suboptimal - and the damping effects of glue and holder, which are not modeled in the simulation.
There is good agreement in the thickness mode and lateral mode resonance frequencies predicted by the FEM simulation and those found in the optical measurements. The small differences are caused by the slightly different piezomaterial loading in the FEM simulation - the model does not incorporate glue or the holder of the custom array. Also, the precision with which the material properties can be measured plays a part. The optical measurements do show an unexplained peak on 4.5 MHz, which is absent in the FEM simulation results. The resonance at 100 kHz in the FEM model and 130 kHz in the optical measurements is likely the element elevation resonance.

4.5 Conclusion

Good agreement was achieved between the FEM predicted surface vibrations and the laser interferometer results.
Next steps include an improved implementation of viscoelastic backing, and the modeling of the matching layers, electrical connections and housing in order to obtain a model of the interleaved design.

Acknowledgements We gratefully acknowledge the efforts of Alessandro Caronti, Giosu Caliano, Jerome Borsboom, Wim van Alphen and Geert Springeling.

Table 4.1: Material properties used in the FEM simulations

Property	Unit	Piezomaterial	Property	Unit	Backing
Elastic compliance (s^E)	[m^2/N x 10^{-11}]	s^E_{11}=1.56, s^E_{12}=-0.420, s^E_{13}=-0.823, s^E_{33}=1.89, s^E_{55}=3.92, s^E_{66}=3.98	Bulk modulus (K)	[GPa]	Initial: 3.22, End: 0.5
Piezoelectric strain coefficient (d)	[C/N x 10^{-10}]	d_{13}=2.95, d_{33}=5.64, d_{15}=5.60	Bulk modulus time constant (τ_K)	[μs]	0.5
Relative permittivity (K^T)	-	K^T_{11}=2417, K^T_{33}=3331	Shear modulus (G)	[GPa]	Initial: 10.2, End: 0.5
Density (ρ)	[kg/m^3]	7800	Shear modulus time constant (τ_G)	[μs]	0.5
Dielectric loss ($tan\delta_e$)	-	0.028	Density (ρ)	[kg/m^3]	3100
Mechanical loss (Q_m)	-	66			

CHAPTER 5

Optimal geometry and element make-up for a transesophageal matrix transducer intended for second harmonic imaging[1]

Paul L.M.J. van Neer, Sandra Blaak, Johan G. Bosch, Charles T. Lancée, Christian Prins, Nico de Jong

Abstract Transesophageal echocardiography (TEE) uses the esophagus as an imaging window to the heart. This enables cardiac imaging without interference from ribs or lungs and allows for higher frequency ultrasound to be used compared to transthoracic echocardiography (TTE). TEE facilitates the successful imaging of obese or elderly patients, where TTE may be unsatisfactory. Recently, 3D TEE has been introduced, which improves TEE by adding an extra dimension. The current 3D TEE probes use fundamental imaging. However, the standard in TTE is second harmonic imaging, due to its increased resolution and reduced sensitivity for clutter and near-field artifacts compared to fundamental imaging. We expect that 3D TEE image quality may also benefit from second harmonic imaging. The aim of this paper is to find the optimal geometry and element make-up for a matrix probe intended for 3D second harmonic transesophageal echocardiography. The design features separated transmit and receive subarrays. The optimal element geometry was investigated using finite element modeling and a transmit subarray prototype was examined using laserinterferometry. The proposed design for the transmit subarray in combination with appropriate electrical tuning is expected to be very suitable for its role with a resonance frequency of $\sim$3 MHz and crosstalk levels $<$ -27 dB. The proposed design for the receive subarray fulfills or exceeds all of the requirements, with a center frequency of 5.6 MHz, a 50% -6 dB bandwidth and an acceptable number of elements in terms of cable related channel reduction.

[1] Submitted.

5.1 Introduction

Echocardiography is of large clinical significance in cardiology as a diagnostic modality to assess the physiological function of the heart and its disorders (Feigenbaum; Kisslo et al., 2006). Since its introduction in the mid-1950s, the field of echocardiography has been constantly evolving, leading to different modes such as M-mode imaging, 2D B-mode imaging and Doppler imaging (Kisslo et al., 2006). Most echocardiographic exams are performed using an imaging window between the ribs near the thorax, so called transthoracic (or precordial) echocardiography (TTE). An alternative technique uses the esophagus as an imaging window to the heart. This method is called transesophageal echocardiography (TEE). As the esophagus wall is located directly posterior to the heart, cardiac imaging can be performed without interference from the ribs or the lungs. Moreover, TEE allows for higher frequency ultrasound to be used compared to TTE - 5-6 MHz versus 3.5 MHz (Kasprzak et al., 1999) in fundamental mode -, because of the smaller distance between the array transducer and the structures of the heart (Lancée, 1987). This increase in transmission frequency directly translates into higher axial and lateral resolutions (Lancée, 1987; Seward, 1988) and improved sensitivity (Lancée, 1987) - crucial for imaging fine structures such as the mitral valve. The combination of these two advantages allows for the successful imaging of obese or elderly patients, where TTE may have unsatisfactory results (Lutz and Gharbi, 2006).
In the last 15 years 3D echocardiography has received considerable attention. The 3D visualization of organs offers a perspective closer to the real anatomy than 2D imaging. Moreover, the possibility of virtually removing structures to view inner parts of organs offers surgeons information on structure morphology and functionality helping in the preparation of surgical intervention (Roelandt, 2000). In addition, 3D imaging considerably increases the quantification accuracy of cardiac structures and parameters compared to 2D imaging (Krenning et al., 2003; Voormolen, 2007). 3D TEE cardiography could combine the advantages of 3D echocardiography with the high resolution and sensitivity of TEE imaging. Two 3D TEE methods have been reported in literature (Nathanail et al., 2008; Sugeng et al., 2008). The first is mechanical - 4D datasets (3D + time) are created by mechanically rotating a modified multiplane 2D TEE probe (Nathanail et al., 2008). Preliminary *in-vivo* results were presented showing valvular images with good diagnostic accuracy and high temporal and spatial resolution (Nathanail et al., 2008). The second method is based on a matrix array transducer, where 4D datasets are created by steering the ultrasound beam in two orthogonal directions (Sugeng et al., 2008). Sugeng et al. (2008) showed that this 3D TEE probe provided excellent real-time 3D visualization of the mitral valve, interatrial septum, left atrium and left ventricle. Matrix 3D TEE delivers equal image quality compared to mechanical 3D TEE but with simpler image reconstruction methods, since matrix 3D TEE does not produce irregularly distributed image data (Nathanail et al., 2008). The main drawback of the matrix approach is cost, as it requires a dedicated ultrasound system. The 3D TEE probes reported in literature operate in fundamental mode, i.e. the ultrasound received at the transmitted frequency is used to create an image. However, a decade ago it became possible to improve ultrasound image quality by exploiting the nonlinear nature of wave propagation. The technique is called tissue second harmonic imaging and is based on the selective imaging of the second harmonic frequency. Compared to fundamental ima-

ging, second harmonic imaging has a higher resolution and is less sensitive to near-field artifacts, clutter and off-axis scatterers (Bouakaz and de Jong, 2003). As a result second harmonic imaging has been the standard in transthoracic tissue imaging for several years. The main challenge for any design of a matrix array transducer optimized for 3D second harmonic TEE imaging is the size constraint associated with TEE operation. Since a TEE probe consists of a flexible endoscope with the array located at the tip, the whole device has to fit in the esophagus.
To obtain 3D images with sufficient resolution, a transducer consisting of several thousand elements is required (Blaak et al., 2009). This fact, combined with the frequency range at which TEE operates, means that the element size is such that these elements operate between 33-mode and plate mode. Also, lateral modes should be a point of attention. To achieve optimal image quality in second harmonic imaging the peak pressure produced by the array should be high. This fact in combination with a limited total array footprint means that the array should have very efficient elements and a minimized kerf width. The last affects the amount of crosstalk between the elements. Crosstalk limits the ring down of delayed signals from neighboring elements and the angular dispersion by increasing the effective element size (Guess et al., 1995). The influence of geometry on these issues cannot be determined using 1D models, such as the KLM model, and requires a 3D approach. Recently, techniques such as laser interferometry and 3D finite element modeling (FEM) have gained popularity in the understanding of these complex vibration modes and crosstalk of phased arrays based on piezomaterial and cMUT's (Goldberg et al., 1997; Caronti et al., 2003; Branca et al., 2004; Kondo and Kitatuji, 2004; Caronti et al., 2005).
The aim of this paper is to investigate the optimal geometry and element make-up for a matrix probe intended for 3D second harmonic transesophageal echocardiography, using finite element modeling and laserinterferometry.
First we derive an array design based on stated requirements, practical limitations and FEM simulations. The design features separate transmit and receive subarrays. Then, we analyze the performance of the transmit subarray design using FEM and laserinterferometry measurements of a prototype. The performance of the receive subarray design is explored using FEM modeling.

5.2 The array design

5.2.1 Array requirements

The requirements for the array can be listed as follows:

1. High efficiency in transmission. For optimal image quality in the case of tissue second harmonic imaging the peak pressure at focus should be as close as possible to the 1.9 Mechanical Index (MI) limit allowed by the Food and Drug Administration (FDA).

2. High sensitivity in reception. The amplitude of the reflected signal in the second harmonic band will be low for harmonics stemming from nonlinear propagation or

UCAs (minimum ∼10 Pa). The noise level of commercial TEE systems is generally in the order of 100 μV_{rms}, thus a sensitivity in the order of 10 μV/Pa is required.

3. Sufficient bandwidth to enable transmission at the fundamental frequency and reception at the second harmonic frequency. A total -6 dB bandwidth of 70 - 80% would suffice.

4. A good acoustic field with grating lobes of acceptably low amplitude. Cobbold (2007) states that the grating lobe levels should be 30 - 40 dB below the central lobe response at the receiving frequency of interest.

5. A small footprint in combination with a limited height of the element stack. Generally a TEE transducer has a footprint of ∼10 mm x 10 mm so that it fits in the esophagus.

6. Optimized for an imaging depth of 0.5 - 15 cm.

5.2.2 The design

The design features separated transmit and receive subarrays, the elements of which are optimized for their specific roles. The transmit subarray is located on one side of the array and the receive subarray on the other. Although the total footprint of the array is larger, the complete separation of the transmit and receive signal chains enables a more efficient layout of the acoustic stacks and electronics in the limited 3D space of the endoscope tip. Moreover, this choice of element layout allows for the use of low voltage circuitry in the receive array and minimizes the electromechanical coupling between the transmit and receive elements. A drawback of the design is the limited overlap of the acoustic beams of the transmit and receive arrays. The 70% - 80% -6 dB bandwidth requirement is now split: both the transmit and receive subarrays should have ∼50% -6 dB bandwidth.
The maximum number of coaxial cables that can be fitted in the shaft of the gastroscope is about 250, as the shaft has to remain sufficiently flexible for insertion into the esophagus. For the transmit subarray a 1.5D array topology is chosen. This design allows for electronic focusing in the lateral dimension, while a broad beam is produced in the elevation dimension. A full 2D array topology is chosen for the receive subarray allowing for receive focusing in both the lateral and elevation dimensions to construct a 3D dataset. Microbeamforming will be used to reduce the channel count from a few thousand (the number of receive elements) to a few hundred (the number of available coaxial cables) (Blaak et al., 2009).

5.2.3 Element geometry

Resonance frequencies

First the resonance frequencies of the arrays are chosen. The choice of these frequencies affects other characteristics of the array, such as the layer thicknesses and element dimensions.

TEE transducers based on the selective imaging of the fundamental band have been reported to use transmission frequencies of 5 MHz (Currie, 1989) - 5.6 MHz (Lancée, 1987; Lancée et al., 1988). The optimal transmission frequency for tissue second harmonic imaging depends on the level of the second harmonic at distances typical for TEE imaging. Consequently, the level of these harmonics is determined by two competing phenomena - nonlinear propagation and attenuation. In the case of transthoracic echocardiography the optimal transmission frequency for fundamental imaging is reported to be 3.5 MHz versus an optimal transmission frequency for second harmonic imaging of 1.6 - 1.8 MHz (Kasprzak et al., 1999). Analogous to TTE, we choose a $\sim$3 MHz transmission frequency so that the frequency of the second harmonic ($\sim$6 MHz) is close to the frequency used in fundamental imaging (5 - 5.6 MHz). The chosen resonance frequencies are $\sim$3 MHz and $\sim$6 MHz for the transmit and receive subarrays respectively.

Kerf

The spacing between the elements should be minimized to waste as little as possible of the limited footprint real estate. The lower kerf limit is determined by the requirement to produce the array reliably. Practical experience showed that a kerf of 40 μm was realistic. No kerf filler material was used.

Element dimensions: length/width

To find the optimal width and length of the elements of the transmit subarray three dimensional FEM simulations were performed. A single element was modeled: the mesh consisted of a piece of piezomaterial and a backing. The piezomaterial properties used were based on CTS 3203HD piezomaterial. The material of the backing was assumed to be isotropic and was modeled using linear elasticity. Both the piezomaterial and backing properties are given in table 5.1. The transducer was loaded by air and excited by an impulse of amplitude -70 V. The piezomaterial thickness was 0.47 mm. The thickness of the backing was 8 mm, such that reflections from the backing did not affect the displacement of the element surface during the simulation time. Only a quarter of the element needed to be modeled because of symmetry. The time sample frequency was 100 MHz. The width and length of the piezoelement were varied during the simulations. To ensure that the lateral mode resonance could always be sufficiently resolved, forty nodes were used in the width/length dimensions. Forty-one nodes were used in the thickness direction of the piezomaterial. The resonance frequencies of the fundamental and lateral modes as a function of the element width are plotted in Fig. 5.1. The chosen element width/length is 0.27 mm producing a fundamental resonance frequency at 2.7 MHz and a lateral mode resonance at 6 MHz. At this width/length the difference between the resonance frequency of the fundamental and lateral modes is sufficiently large to ensure that there is no significant interaction between the fundamental and lateral modes - even at the highest frequencies in the fundamental mode bandwidth (expected -6 dB bandwidth $\sim$50%). The transmit subarray will consist of 32 x 4 elements with a size of 0.27 mm x 0.27 mm x 0.47 mm yielding a subarray footprint of 9.9 mm x 1.2 mm.

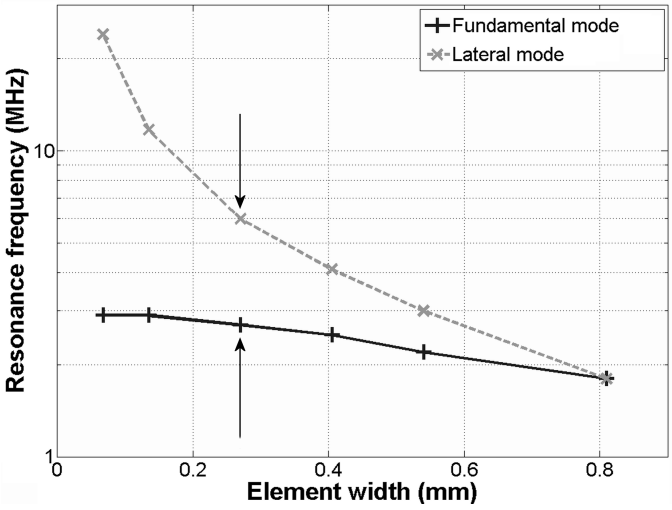

Figure 5.1: Graph detailing the relation between element width and resonance frequency of the fundamental mode (black plusses) and lateral mode (gray crosses) as modeled using FEM simulations in order to determine the optimal width and length for the elements of the transmit subarray. The piezoelement consisted of piezomaterial and a backing, see table 5.1 for their respective properties. The height of the piezomaterial and backing were 0.47 mm and 8 mm respectively. The width and length of the piezoelement were varied. Only a quarter of the element was modeled because of symmetry. The excitation was an impulse of -70 V. See table 5.2 for the relevant mesh properties.

The optimal width/length of the receive elements is determined by a compromise between the maximum possible channel reduction through microbeamforming and the desire to minimize the effects of lateral modes. To reduce the number of channels from the total number of elements to a few hundred, microbeamforming is used for the receive subarray. The concept of microbeamforming entails that the elements are arranged in groups, and that the delay is divided into a coarse delay common for all elements in the group and a fine delay for each individual element in the group. The signals of the N elements in a group are then summed reducing the number of required channels by a factor of N. The fine delays and the element summing are applied by use of a chip in the tip of the gastroscope (Blaak et al., 2009). To keep the effects of microbeamforming on the beam equal in the lateral and elevation directions, only square configurations (2x2, 3x3 and 4x4 elements) were investigated by Blaak et al. (2009). A 2x2 group configuration would provide an insufficient reduction in channels. A 9:1 channel reduction by a 3x3 group configuration has been shown to produce a sufficiently good acoustic field, with a peak grating lobe level of -27 dB relative to the main beam (Blaak et al., 2009). A 16:1 channel reduction by a 4x4 group configuration would produce unacceptably high grating lobe levels. A 3x3 group configuration limits the number of elements to a maximum of $\sim$2250.

To find the optimal width and length of the elements of the receive subarray three dimensional FEM simulations were performed. A single element was modeled, its geometry

consisted of a piece of piezomaterial and a backing. The geometry, materials and mesh properties were equal to those used in the simulations to find the optimal geometry of the transmit elements, except for the piezomaterial thickness, which was 0.29 mm. The width and length of the piezoelement were varied during the simulations. The resonance frequencies of the fundamental and lateral modes as a function of the element width are plotted in Fig. 5.2. The chosen element width/length is 0.17 mm producing a fundamental resonance frequency at 6.3 MHz and a lateral mode resonance at 9.4 MHz. At this width/length the difference between the resonance frequency of the fundamental and lateral modes is sufficiently large to ensure that there is no significant interaction between the fundamental and lateral modes - even at the higher frequencies of the fundamental mode bandwidth (expected -6 dB bandwidth $\sim$50%).
The combination of a receive element size of 0.17 mm x 0.17 mm x 0.29 mm and a 9:1 channel reduction leads to a receive array consisting of a grid of 45x45 receive elements (2025 in total). The footprint of the receive array is 9.4 mm x 9.4 mm. The footprint of the transmit and receive arrays combined amounts to 9.9 mm x 10.7 mm, which is comparable to the footprint of conventional TEE transducers.

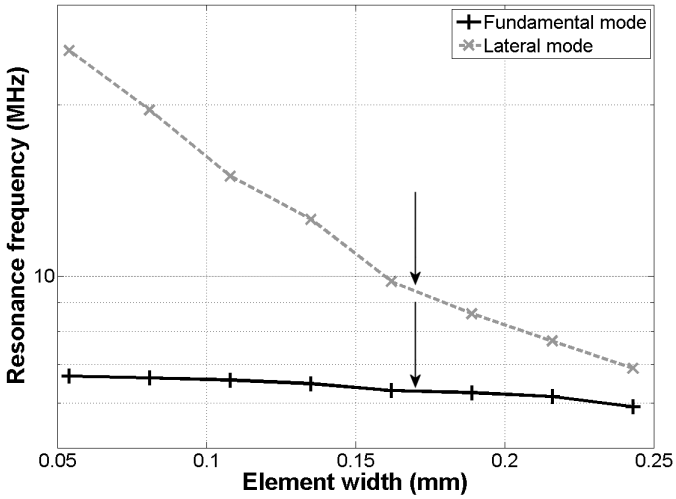

Figure 5.2: Graph detailing the relation between element width and resonance frequency of the fundamental mode (black plusses) and lateral mode (gray crosses) as modeled using FEM simulations in order to determine the optimal width and length for the elements of the receive subarray. The piezoelement consisted of piezomaterial and a backing, see table 5.1 for their respective properties. The height of the piezomaterial and backing were 0.29 mm and 8 mm respectively. The width and length of the piezoelement were varied. Only a quarter of the element was modeled because of symmetry. The excitation was an impulse of -70 V. See table 5.2 for the respective mesh properties.

5.3 Transmit subarray prototype

The transmit subarray consisted of four rows of 32 elements each, which resulted in 128 elements in total. The array was built using CTS 3203HD piezomaterial. The resonance frequency of the transmit array was ∼2.7 MHz. Each element had a matching layer of 6.5 MRayl at the 'front' and 'back' sides of the piezomaterial and a backing of 3.4 MRayl. Also, a 7 μm kapton/aluminum foil was glued on the front of the elements. No lens was mounted. The width and length of the elements were both 0.27 mm. The kerf was 40 μm. The total footprint of the transmit array was 9.9 mm x 1.2 mm. A picture of the array is displayed in Fig. 5.3 and an overview of the material properties used for the various layers in the array is given in table 5.1. The transducer was manufactured by Oldelft Ultrasound, Delft, the Netherlands.

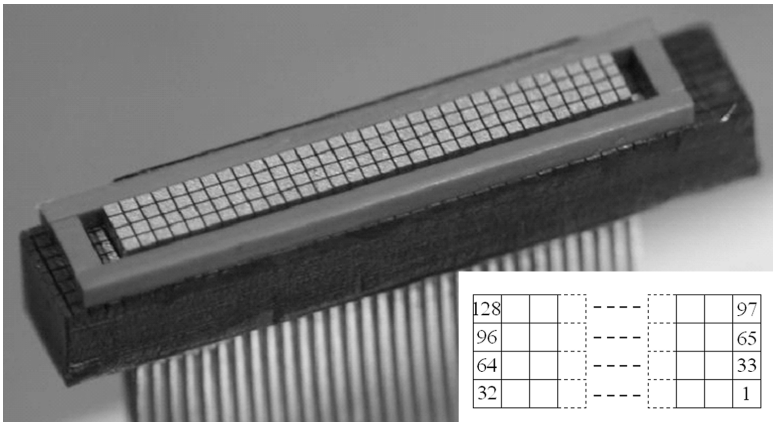

Figure 5.3: A picture of the transmit subarray prototype. The schematic on the bottom right shows the numbering of the elements.

5.4 Optical characterization and FEM model

5.4.1 Optical setup

The space and time dependant surface vibrations of the array were studied in air using a laser interferometer system. A schematic of the optical setup is displayed in Fig. 5.4. The system was based on a Polytec MSV-300 laser scanning vibrometer system (Polytec GmbH, Waldbronn, Germany). The laser interferometer consisted of a Polytec OFV 512 fiber interferometer connected to a Polytec OFV 5000 vibrometer controller equipped with a displacement decoder with an upper frequency limit of 20 MHz. The fiber interferometer was connected to the MSA-400 scan head, which functioned as a microscope. The continuous analog output produced by the vibrometer controller was captured by a digitizer card (DP235, Acqiris, Geneva, Switzerland) at a sampling rate of 100 MHz. The digitizer was

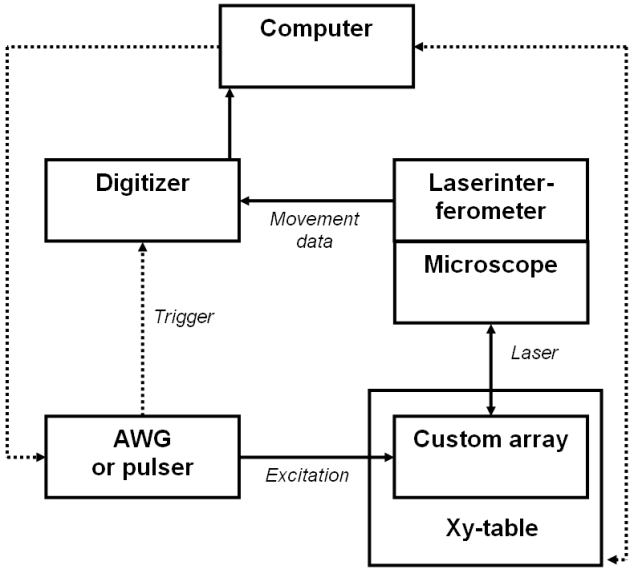

Figure 5.4: A schematic of the laser interferometer setup. Dotted arrows are either triggers or control signals.

triggered by either the arbitrary waveform generator or the pulser/receiver.
For amplitude transfer function measurements the array element was excited by 35 cycle sinusoids with amplitude 5 V generated by an arbitrary waveform generator (33250A, Agilent, Loveland, Colorado). For crosstalk measurements the element was excited by a pulser/receiver (5800, Panametrics, Waltham, MA, USA), which produced an impulse using amplitude setting -100 V and transducer frequency setting 3-4 MHz. The array was mounted on two orthogonal motorized translation stages (PT1-Z8, Thorlabs GmbH, Munich, Germany).
The out of plane surface vibrations of the array elements were studied using a laser spot diameter of 20 μm and a translation step size of 30 μm. The received signals were averaged 1000 times for each measurement position to reduce the effects of variance in signal quality due to the variability of element surface reflectivity and surface roughness. The pulse repetition frequency was set to 1 kHz.

5.4.2 Material properties

The properties of the CTS 3203HD piezomaterial used in both subarrays were based on the values reported by Sherrit et al. (1997). The passive materials used were assumed to be homogeneous and isotropic. The longitudinal wave speed (v_{33}) of these materials was determined using the method of Selfridge (1985). The density (ρ) was determined using Archimedes' method (Selfridge, 1985). Using v_{33} and ρ the axial modulus was calculated (Briggs, 1992; Cobbold, 2007). The Poisson ratio (ν) of the passive materials was estimated

Table 5.1: The properties of the materials used in the simulations and the prototype.

	Property	Unit	Value
Piezomaterial	Elastic compliance (s^E)	[m^2/N x 10^{-11}]	s^E_{11}=1.56, s^E_{12}=-0.420, s^E_{13}=-0.823, s^E_{33}=1.89, s^E_{55}=3.92, s^E_{66}=3.98
	Piezoelectric strain coefficient (d)	[C/N x 10^{-10}]	d_{13}=2.95, d_{33}=5.64, d_{15}=5.60
	Relative permittivity (K^T)	-	K^T_{11}=2417, K^T_{33}=3331
	Density (ρ)	[kg/m^3]	7800
	Dielectric loss ($tan\delta_e$)	-	0.028
	Mechanical quality factor (Q_m)	-	66
Matching	Longitudinal wave speed (v_{33})	[m.s^{-1}]	2066
layer	Poisson ratio (ν)	-	0.35
	Density (ρ)	[kg.m^{-3}]	3146
Backlayer	Longitudinal wave speed (v_{33})	[m.s^{-1}]	2066
	Poisson ratio (ν)	-	0.35
	Density (ρ)	[kg.m^{-3}]	3146
Backing	Longitudinal wave speed (v_{33})	[m.s^{-1}]	1818
	Poisson ratio (ν)	-	0.35
	Density (ρ)	[kg.m^{-3}]	1870

at 0.35. A summary of the material properties is given in table 5.1.

5.4.3 Finite element model

A single array element was modeled using the ANSYS 11 FEM package (ANSYS Inc., Canonsburg, PA, USA). Only a quarter of an array element needed to be modeled due to symmetry. An element of the transmit subarray consisted of four layers: a matching layer, the piezomaterial, a backlayer and the backing. An element of the receive subarray consisted of three layers: a matching layer, the piezomaterial and the backing. The electrodes were assumed to be infinitesimally thin. The kapton/aluminum foil was not modeled. The voltage over the transducer clamps due to the impulse excitation used in the laser interferometer experiments was recorded and used as a voltage boundary condition in the simulations (a -140 V impulse). The time sampling frequency was 100 MHz. If the element was loaded by air, the air was not modeled, since the energy transmission into air is almost zero. If the element was loaded by water, water was included in the model. The water domain was surrounded by an absorbing boundary layer. The longitudinal wavespeed (v_{33}) of the water was 1490 m/s and the density (ρ) 1000 kg/m^3. A schematic of the model is displayed in Fig. 5.5 and a summary of the mesh properties is given in table 5.2.

Table 5.2: Standard geometry and mesh parameter set used in the FEM simulations.

	Properties	Unit	Value
Piezomaterial	Width/length	[m]	135.10^{-6} *(transmit subarray)*
		[m]	85.10^{-6} *(receive subarray)*
	Height	[m]	467.10^{-6} *(transmit subarray)*
		[m]	292.10^{-6} *(receive subarray)*
	Element type	-	20 node, 3D element SOLID226
Matching layer	Width/length	[m]	135.10^{-6} *(transmit subarray)*
		[m]	85.10^{-6} *(receive subarray)*
	Height	[m]	120.10^{-6} *(transmit subarray)*
		[m]	80.10^{-6} *(receive subarray)*
	Element type	-	20 node, 3D element SOLID186
Backlayer	Width/length	[m]	135.10^{-6} *(transmit subarray)*
	Height	[m]	25.10^{-6} *(transmit subarray)*
	Element type	-	20 node, 3D element SOLID186
Backing	Width/length	[m]	135.10^{-6} *(transmit subarray)*
		[m]	85.10^{-6} *(receive subarray)*
	Height	[m]	2.10^{-3} (prototype) / 8.10^{-3} (FEM)
	Element type	-	20 node, 3D element SOLID186
Water	Radius	[m]	1.10^{-3}
	Element type	-	8 node, 3D element FLUID30
Nonreflecting boundary (around water)	Element type	-	4 node, 2D boundary element FLUID130

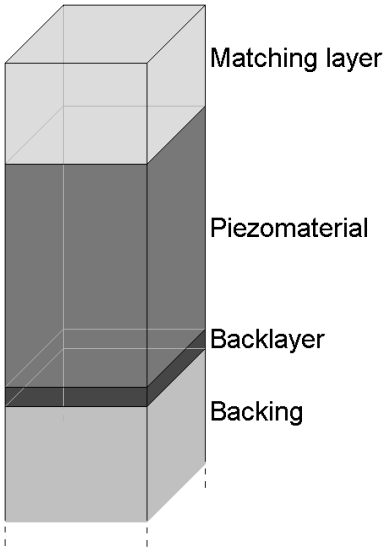

Figure 5.5: The geometry of a FEM modeled element of the transmit subarray.

5.5 Definitions

The transducer transmit transfer function ($T_t(\omega)$) was defined as:

$$T_t(\omega) = \frac{|p_0(\omega)|}{|V_T(\omega)|}, \tag{5.1}$$

with $p_0(\omega)$ the pressure at the transducer surface and $V_T(\omega)$ the voltage over the transducer electrodes.
The receive transfer function ($T_r(\omega)$) was defined as:

$$T_r(\omega) = \frac{|V_{T-open}(\omega)|}{|p_a(\omega)|}, \tag{5.2}$$

with $V_{T-open}(\omega)$ the open circuit voltage produced by the transducer and $p_a(\omega)$ the pressure received on the transducer surface.
The amplitude transmit transfer function of a transducer ($T_t^a(\omega)$) was defined as:

$$T_t^a(\omega) = \frac{|u_{33}^a(\omega)|}{|V_T(\omega)|}, \tag{5.3}$$

with u_{33}^a the mean out of plane displacement of the transducer surface.

5.6 Results

5.6.1 Transmit subarray

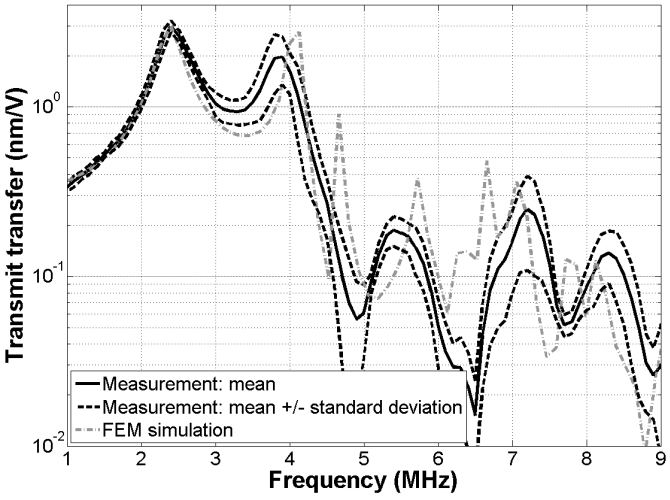

Figure 5.6: Amplitude transmit transfer function of the out of plane surface displacement of the transmit subarray vibrating in air. The laser interferometer results are indicated by the solid black line, which is the mean of the excursion of 4 elements. The standard deviation around the mean is indicated by the black dashed line. Each element was excited by a 10 V_{pp} sinusoidal signal of 35 cycles, which was swept over the frequency in steps of 100 kHz. The FEM simulation results are shown by a dashed gray line and were obtained by exciting the element by a -140 V impulse excitation.

The amplitude transmit transfer functions of transmit subarray elements produced by the optical measurements and FEM simulations are shown in Fig. 5.6. The elements were loaded by air. The experimental results were based on measurements of 4 elements. The maximum transmit transfer was 3 nm/V. Two peaks were visible in the spectra, the first - on 2.4 MHz - was the fundamental resonance of the piezomaterial, the second on 3.9 MHz (measurements) or 4.1 MHz (simulation) was caused by the matching layer. The experimental results showed a large spread around the second peak as indicated by the standard deviation of 0.7 nm/V versus a mean of 2 nm/V (see Fig. 5.6). This may have been caused by nonuniform adhesion between the matching layer and the piezomaterial, or by damage related to sawing. The agreement between the optical measurements and the FEM simulation was good, especially at frequencies below 5 MHz. The spikiness of the results above 5 MHz was caused by the lack of damping in the FEM model combined with the interaction of the out of plane surface displacement and a lateral mode at 6 MHz (see Fig. 5.6).
Fig. 5.7 shows the normalized maximum out of plane surface displacement of element 28 and element 93. The elements were excited by a -100 V impulse. Element 28 was located

Table 5.3: Normalized crosstalk level averaged over a frequency band of 1 - 5 MHz of excited element to neighboring element.

	Crosstalk in lateral direction (dB)	Crosstalk in elevation direction (dB)
Element 28	-18	-26
Element 85	-17	-38
Element 87	-20	-18
Element 93	-16	-28
Average	-18	-27

on the edge of the array and element 93 located in the middle. The peak out of plane displacement of elements 28 and 93 were 63.4 nm and 52.5 nm respectively. The peak displacements of the examined elements varied from 52 to 64 nm. The out of plane displacement pattern was checkered and corresponded to the element distribution. The out of plane displacement due to crosstalk in the lateral direction was higher than in the elevation direction. This was clearly visible in the displacement pattern produced by element 93 (Fig. 5.7b) and somewhat less obvious in the displacement pattern produced by element 28 (Fig. 5.7a). There was no discernible time delay in the time signals between the electrical or mechanical contributions to the crosstalk (time signals not shown).
The frequency dependency of the crosstalk from an excited element to a neighboring element is shown in Fig. 5.8 for elements 28 and 93. This was calculated by taking the Fourier transform of the mean surface displacement of an element neighboring the excited element and normalizing that by the Fourier transform of the mean surface displacement of the excited element. The crosstalk was higher in the lateral direction than in the elevation direction. In the case element 28 was excited the crosstalk averaged over 1 - 5 MHz was -18 dB and -26 dB in the lateral and elevation directions respectively. For element 93 this was -16 dB and -28 dB in the lateral and elevation directions respectively. The crosstalk showed a frequency dependency, being highest between 3 and 4 MHz (element 28: -8 and -14 dB for the lateral and elevation directions) and lowest between 1 and 2 MHz (element 28: -25 dB and -33 dB for the lateral and elevation directions).
These crosstalk measurements were performed for four excited elements. The average crosstalk over a 1 - 5 MHz band is summarized in table 5.3 for the lateral and elevation dimensions. The average crosstalk from the excited element to a neighboring element was -18 dB and -27 dB for the lateral and elevation directions respectively.

5.6.2 Receive subarray

The receive transfer function of an element of the receive subarray with the optimal width/ length of 0.17 mm x 0.17 mm as simulated using FEM modeling is displayed in Fig. 5.9. The thicknesses of the piezoelement and matching layer were 0.29 mm and 0.08 mm respectively. No backlayer was applied. The geometry and mesh parameters are given in table 5.2. The element was loaded by water. The receive transfer function had a maximum of 24.8 μV/Pa at 5.3 MHz. The center frequency of the element was 5.6 MHz. Its -6 dB

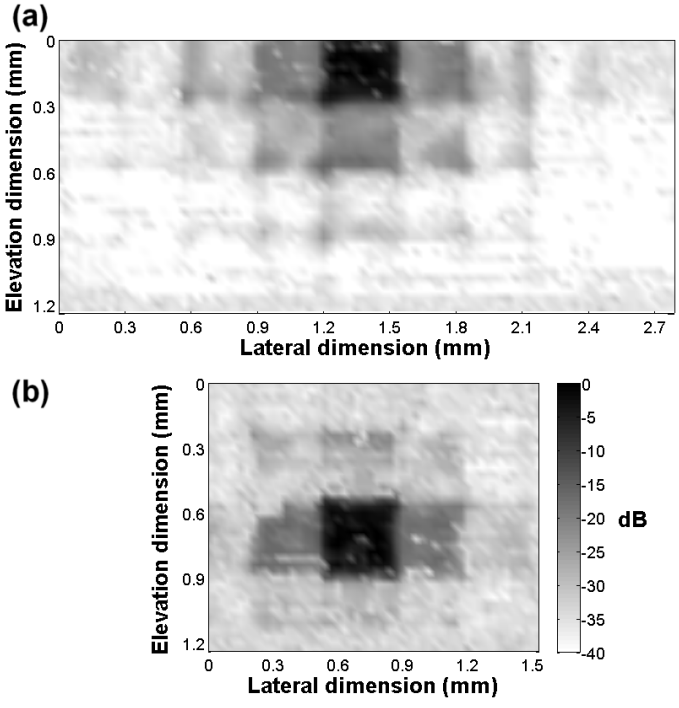

Figure 5.7: a) Normalized maximum out of plane displacement of array element 28. b) Normalized maximum out of plane displacement of array element 93. The normalized out of plane displacement in dB is encoded by gray values. The elements were excited by a -100 V impulse excitation and were vibrating in air.

bandwidth was 50% and stretched from 4.2 MHz to 7 MHz.

5.7 Discussion

5.7.1 Laser interferometer measurements

The signal-to-noise-ratio (SNR) of the laser interferometer measurements was determined mainly by the amount of light reflected back into the detector. The prototype array was covered by a highly reflective aluminum foil, which was stretched and smoothed as much as possible during production. Even so, the roughness of the top surface - e.g. due to folds in the aluminum - relative to the size of the laser spot (20 μm) occasionally caused very little light to be reflected back to the detector. This effect was visible in the maximum out of plane surface displacement plots of Fig. 5.7 as spots with an unexpectedly low displacement. During the total time of the measurements (two weeks) the smoothness of the aluminum foil deteriorated due to handling and temperature influences. This affected the

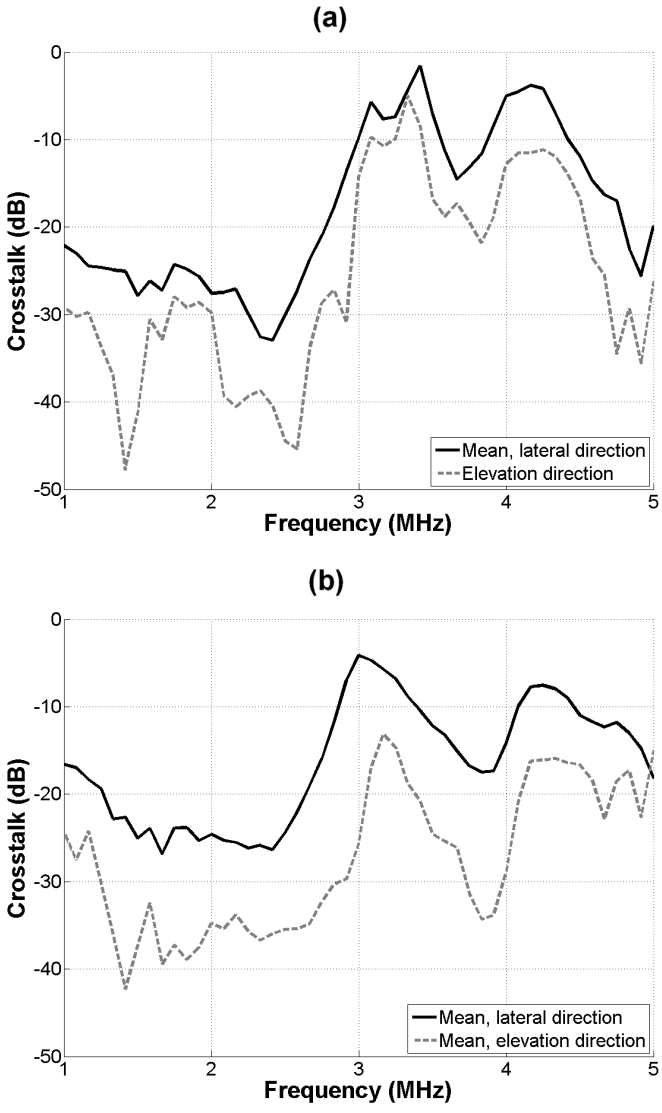

Figure 5.8: The surface displacement due to crosstalk from a neighboring element normalized to the surface displacement of the excited element plotted versus the frequency for elements 28 (a) and 93 (b). The mean crosstalk to a neighboring element in the lateral direction (black solid line) and to an element in the elevation direction (gray dashed line) are shown. The elements were vibrating in air.

reflectivity of the surface and thus the attainable SNR by a few dB.

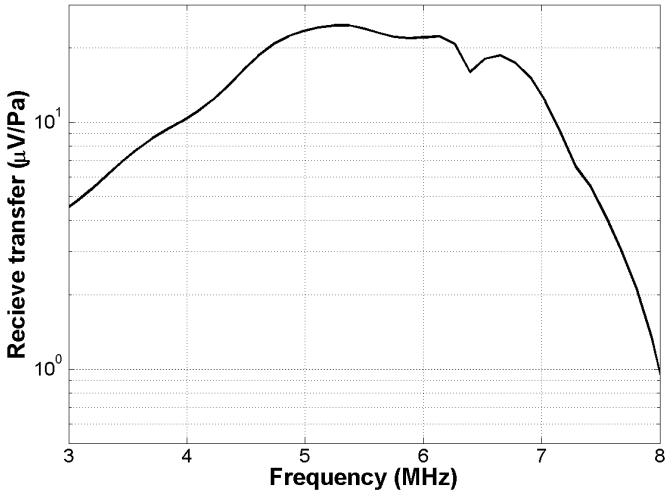

Figure 5.9: The receive transfer functions of the out of plane surface displacement of an element of the receive subarray, obtained using FEM simulations. The thicknesses of the piezoelement and matching layer were 0.29 mm and 0.08 mm respectively. No backlayer was applied. The geometry and mesh parameters are given in table 5.2. The element was loaded by water.

5.7.2 Transmit subarray

The amplitude transmit transfer function of the transmit subarray showed a considerable dip between the peak at 2.4 MHz (fundamental piezomaterial resonance) and the peak at 3.9 MHz (matching layer). However, it is expected that the peak at 3.9 MHz will be smoothed out and become considerably lower, when the array is loaded by water or tissue. Moreover, it is expected that the choice of a fundamental resonance at 2.4 MHz and the matching layer resonance at 3.9 MHz in combination with electrical matching to the transmitter by use of coils will ensure a sufficient 40% - 50% -6 dB bandwidth around a 3 MHz center frequency.
The crosstalk between the elements of the transmit subarray is important, because it has a detrimental effect on the transducer's ability to perform beam steering by effectively making the elements less omnidirectional. McKeighen (1998) reported that crosstalk values of -30 dB are considered acceptable for most imaging situations. Electrical crosstalk seems to be the largest contributor to the total crosstalk, as the out of plane displacement of neighboring elements starts at the same time as the displacement of the excited element. The out of plane displacement due to crosstalk in the lateral direction is higher than in the elevation direction. This corresponds to the direction of the flexprint. Since beam steering will only be applied in the lateral direction, it may be beneficial to connect the flexprint in the elevation direction to the elements. The crosstalk in the steering direction will be at -27 dB close to the requirement reported by McKeighen (1998).
A few remarks have to be made. The crosstalk levels reported in this paper were measured

in air and should be converted into their respective tissue loaded values. The relative value of the electrical crosstalk is expected to stay approximately similar, if the impedance of the waveform generators is very low compared to the (tissue loaded) impedance. This is however not the case for the mechanical crosstalk. If the element is loaded by air, almost all of the energy applied on the transducer is dissipated in the backing. However, in the case of a tissue load on the element, only part of the energy converted into a pressure wave is transmitted into the backing, the rest enters the tissue medium. Thus the mechanical crosstalk will be lower, the amount depending on the impedances of the matching layer in combination with the tissue load and the backing. In our case the reduction in mechanical crosstalk is estimated at $\sim$4 dB. Even so, the crosstalk along the flexprint is too high and efforts should be made to improve the electrical isolation of the elements. Acoustic measurements should be performed to investigate the effects of the crosstalk on the performance of the transducer. The crosstalk has a strong frequency dependency as shown in Fig. 5.8, with a shape similar to the element electrical impedance. For the typical 3 MHz imaging bursts with $\sim$50% -6 dB bandwidth, the crosstalk will be close to reported mean values. However, for applications requiring narrowband excitation - e.g. Doppler -, the 20 dB crosstalk variance due to the frequency should be taken into account. A 2.5 MHz excitation frequency would provide low crosstalk and a good transmission efficiency.

5.7.3 Receive subarray

The center frequency of 5.6 MHz found for the modeled element of the receive subarray is slightly lower than the intended 6 MHz, but still acceptable. The peak receive transfer of $\sim$25 μV/Pa reported by the FEM simulations is superior to the required value of 10μV/Pa. Moreover, the -6 dB bandwidth of 50% is on target for the bandwidth requirement of the receive subarray. This rather narrow bandwidth helps to maintain the dynamic range with which the second harmonic can be received by filtering out the fundamental. This effect could not be obtained otherwise, as no electrical tuning of the receive elements is possible in the chip design used for the receive chain.
Although the receive element and subarray design meets or exceeds all the stated requirements, the peak receive transfer could still be improved by adding a second matching layer.

5.8 Conclusion

The present design for the transmit subarray in combination with appropriate electrical tuning and a 90° turn of the flexprint is expected to be very suitable for its role, with a $\sim$3 MHz resonance frequency and $<$ -27 dB crosstalk levels in the lateral steering direction. The proposed design for the receive subarray fulfills or exceeds all of the requirements, with a center frequency of 5.6 MHz, a 50% -6 dB bandwidth and an acceptable number of elements in terms of the required channel reduction related to the available coaxial cables.

Acknowledgements We acknowledge the technical support of J. Ponte, G. Springeling and M. Manten. We thank S.L. Paalvast and Prof. D. Rixen from the faculty of Mechanical, Maritime and Materials Engineering, Delft University of Technology for providing the laser interferometer setup.

CHAPTER 6

Multilayer transducer for acoustic bladder volume assessment on the basis of nonlinear wave propagation[1]

Egon J.W. Merks, Paul van Neer, Nicolaas Bom, Antonius F.W. van der Steen, Nico de Jong

Abstract Catheterization remains the gold standard for bladder volume assessment, but it is invasive, uncomfortable to the patient, and introduces the risk of infections and traumas. Acoustic measurement of the bladder volume reduces the need for a urinary catheter. Recently, a new method to noninvasively measure the volume of liquid filled cavities *in-vivo* on the basis of nonlinear wave propagation has been introduced. To implement this method, two different multilayer ultrasound transducers were developed. Both transducers consisted of a piezoelectric layer of lead zirconate titanate (PZT) to transmit waves at a fundamental frequency (2 MHz) and a piezoelectric layer (copolymer) to receive a wide range of frequencies including the harmonics. In order to suppress the inherent susceptibility of the film to electromagnetic waves, one of the two transducers, i.e. an 'inverted' multilayer transducer, had the copolymer layer located inside the structure. The other multilayer transducer, i.e. a 'normal' multilayer transducer, had the copolymer film located on the outside. Both transducers were compared with a commercially available broadband piezocomposite transducer with respect to their transmit and receive transfer functions, their pulse-echo responses and their ElectroMagnetic Susceptibility (EMS) in reception. It was concluded that, in order to measure up to at least the third harmonic frequency component with good sensitivity in combination with high transmit efficiency at the fundamental frequency, a multilayer structure is preferred. To optimize for the EMS in reception, and hence also the signal-to-noise ratio, an inverted geometry, as proposed in this paper, was proven to be most effective.

[1]From Egon J. W. Merks, Paul van Neer, Nicolaas Bom, Nico de Jong, Antonius F. W. van der Steen, 'Multilayer Transducer for Acoustic Bladder Volume Assessment on the Basis of Nonlinear Wave Propagation', Ultrasound in Med. & Biol., 2009, 35(10):1690-1699.

6.1 Introduction

In several clinical situations it is important to accurately measure bladder volume. Catheterization remains the gold standard for bladder volume assessment, but it is invasive, uncomfortable to the patient, and introduces the risk of infections and traumas (Ord et al., 2003). Acoustic measurement of the bladder volume reduces the need for a urinary catheter (Hubert et al., 1998; Slappendel and Weber, 1999). As a result, noninvasive acoustic bladder volume measurement methods have gained interest within the last ten years. Because of the introduction of dedicated devices such as the BladderScan (Verathon Inc., Bothell, WA, USA), acoustic bladder volume measurements have become relatively easy and are valued more and more. These devices are as accurate as urinary catheterization and have proven to be important in clinical practice.
Recently, a new method for acoustic bladder volume assessment on the basis of nonlinear wave propagation has been introduced (McMorrow et al., 2002; Bouakaz et al., 2004a). It uses the medium-specific relationship between nonlinearity and attenuation in acoustic wave propagation, reflected in the so-called "Gol'dberg number" (Γ) (Bouakaz et al., 2004a), to differentiate between urine and tissue. Given a much stronger nonlinear behavior for urine (Γ = 104) than for tissue (Γ = 0.27), the amount of generated harmonics present within echoes received from a Region of Interest (ROI) behind the posterior bladder wall and the amount of urine present within the propagation path are highly correlated. The method uses a single element transducer with a diverging acoustic beam to capture the entire bladder (Fig. 6.1). In this way, the bladder volume can be estimated with only one pulse-echo acquisition. This new method is different from the devices currently available because it is instantaneous, and, because of its simplicity and low cost, is especially suitable for miniaturization and thus monitoring purposes and private use.

For this method a dedicated transducer is needed that has sufficient transmit efficiency at the fundamental frequency ($\sim$2 MHz) to induce significant nonlinear wave propagation, and has sufficient receive sensitivity and spectral bandwidth to measure up to the 3^{rd} harmonic frequency with sufficient signal bandwidth (1 MHz - 8 MHz). This frequency range was chosen as a trade-off between the volume measurement accuracy and the system's capability of measuring the acoustic signals with sufficient signal-to-noise ratio (SNR). The 3^{rd} harmonic needs more time to build up to measurable levels and is attenuated more than the 2nd harmonic component. Because the 3^{rd} harmonic is more sensitive to loss, i.e. the amount of tissue in the propagation path, it is also more sensitive to liquid volume variations. The 3^{rd} harmonic is therefore preferred over the 2^{nd} harmonic for volume estimation when the SNR of the pulse-echo data suffices. When the SNR at the 3^{rd} harmonic frequency is too low, the 2^{nd} harmonic is used instead. In practice, this means that larger volumes can be measured more accurately than smaller volumes. The same reasoning can be used for the 4^{th} and higher harmonics, but these higher harmonics are extremely difficult to measure due to the limited SNR. Therefore, the cut-off was set at the 3^{rd} harmonic. To obtain this dedicated transducer, three different transducer concepts, i.e. a multilayer transducer, a broadband piezocomposite transducer and a multi-element transducer, were compared (Merks et al., 2005). The multilayer transducer concept was previously introduced and its feasibility for bladder volume assessment was proven (Merks et al., 2006a,b). It consisted of a commercially available lead zirconate titanate (PZT) transducer for trans-

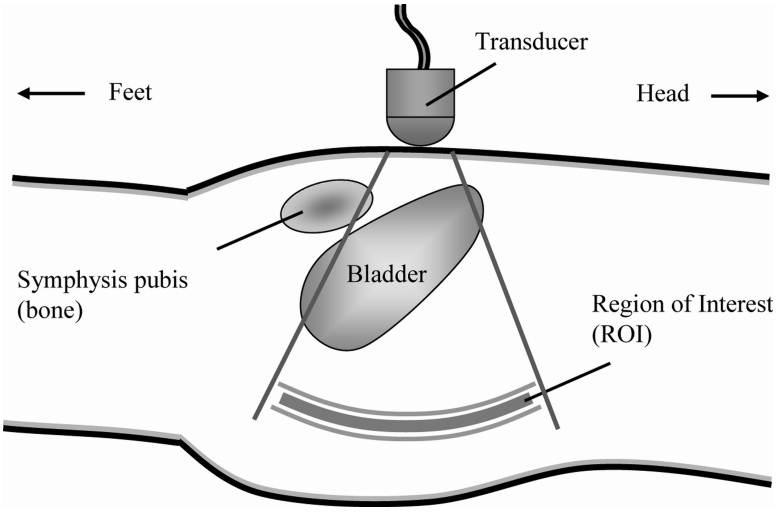

Figure 6.1: Setup for bladder volume measurements on the basis of nonlinear wave propagation.

mission, including backing and matching layer. A polyvinylidene flouride (PVDF) film was attached on top of the matching layer for broadband reception. The broadband single-element piezocomposite transducer was custom designed for transmission at the fundamental frequency and reception of the fundamental, second and third harmonic frequencies. The multi-element transducer consisted of an air-backed PZT ring-element for transmission and a broadband PZT inner-element for reception.

It must be noted that the mutual orientation of the transducer and the bladder walls affects the magnitude of the received signals. The signal magnitude is also affected by the different pressure distributions of the different receive frequencies. To reduce these effects a diverging acoustic beam was proposed, which could be created by application of an acoustic lens to the transducer surface.

The multi-element transducer had the highest transmit efficiency and receive sensitivity. However, applying an acoustic lens to the multi-element transducer resulted in a large on-axis efficiency, which is typical for a concentric ring element. This nonuniform acoustic beam would introduce an unwanted weighting of the volume present within the beam. Uniform pressure distributions were obtained with the other two concepts. The multilayer concept and the piezocomposite transducer where therefore preferred (Merks et al., 2005). However, the application of the acoustic lens does not generate a beam wide enough to encompass a full bladder. Hence, in the current setup, the bladder is manually scanned in search of the maximum harmonic-to-fundamental ratio to approximate the true bladder volume.

The multilayer concept had higher transmit efficiency at the fundamental frequency (1.9 MHz) than the piezocomposite transducer, but the receive sensitivity was relatively low. Additionally, the PVDF film suffered from a high ElectroMagnetic Susceptibility (EMS),

i.e. the sensitivity for electromagnetic distortion, which is inherent to the high electrical impedance and broadband characteristics of the PVDF. Hence, to obtain a sufficient SNR, averaging of at least 100 RF traces was required for each measurement. However, in contrast to the piezocomposite transducer, the design of the multilayer concept allowed for significant improvement with respect to sensitivity and noise behavior. Hence, the multilayer concept was preferred for bladder volume measurements above the other two concepts (Merks et al., 2005).
This paper describes the further development of the multilayer transducer concept. To improve on the SNR in reception and to improve on the transmit efficiency, a new multilayer transducer concept was developed and built. Measurements have been performed to obtain the transmit transfer function, the receive transfer function, the pulse-echo response and the EMS characteristics. The same measurements were performed with a new realization of the old multilayer concept and a broadband piezocomposite transducer for comparison.

6.2 Materials and methods

An inverted multilayer transducer was built and compared to a previously developed multilayer transducer and a commercially available piezocomposite transducer.

6.2.1 Inverted multilayer transducer concept

The design of the inverted multilayer design is shown in Fig. 6.2a. It consisted of a 1 mm thick PZT disc (PXE 5, Morgan Electro Ceramics, Southampton, UK) stacked with a 100 μm thick Copolymer film (Precision Acoustics Ltd., Dorchester, UK). Conductive adhesive (Emerson and Cuming, Westerlo, Belgium) was used for bonding the two piezoelectric layers and for ensuring the common ground. The complete stack had a diameter of 20 mm and was mounted in a stainless steel housing. Air-backing was used to achieve the highest transmit efficiency possible without considering bandwidth requirements. An acoustic matching layer was applied for the acoustic impedance mismatch between the PZT element and water. The PZT element will be used for the transmission of acoustic waves at the fundamental frequency (2.1 MHz) and the copolymer film will be used for the broadband reception of waves at the fundamental up to the 3^{rd} harmonic frequency including sufficient signal bandwidth (1 MHz - 8 MHz). As this geometry resembles an 'inverted' geometry of a previously developed transducer (as will be described next), it will be referred to as the 'Inverted Multilayer (IM-)transducer' throughout this paper.

6.2.2 Normal multilayer transducer concept

A second multilayer transducer was built based on a previously developed concept (Merks et al., 2006a,b). It had the same PZT and copolymer layers as the IM-transducer, but it had the copolymer layer mounted on the outside (Fig. 6.2b). A protective polyurethane coating was applied to protect the copolymer gold electrode. Again air-backing was used, but no matching layer was applied as the acoustic impedance of the copolymer film was

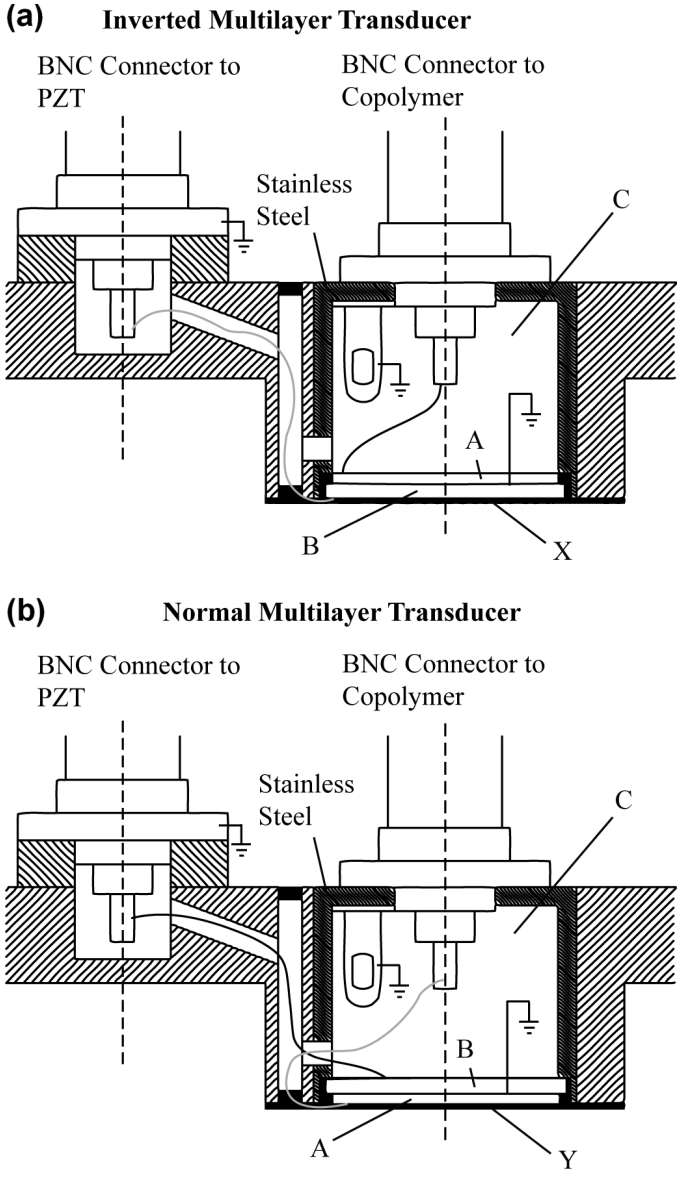

Figure 6.2: Schematics of an inverted multilayer transducer concept (a) and a normal multilayer transducer concept (b). The schematics show the copolymer layer for broadband reception (A), the PZT element for transmission (B), and the air-backing (C). The inverted multilayer transducer has a matching layer (X) and the normal multilayer transducer has a protective coating (Y). Separate BNC connectors are used for both active elements.

already close to that of water. This transducer will be referred to as the 'Normal Multilayer (NM-)transducer.'

6.2.3 Piezocomposite transducer

The third transducer used was an unfocussed broadband piezocomposite single element transducer (Vermon, Tours, France) with center frequency of 2.4 MHz, -6 dB bandwidth of 85% (as obtained from pulse-echo measurements) and an active diameter of 25 mm.

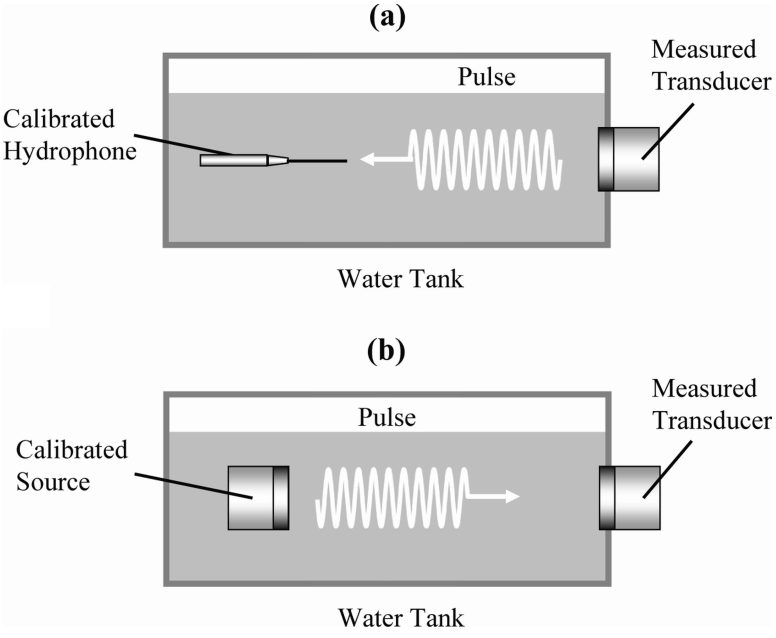

Figure 6.3: Experimental setup used to obtain the transfer functions. A calibrated hydrophone was used to obtain the transmit transfer function (a). A calibrated source was used to obtain the receive transfer function (b).

6.2.4 Transfer functions

The transmit transfer functions in Pascal per Volt (Pa/V) and the receive transfer functions in Volt per Pascal (V/Pa) of the IM-transducer, NM-transducer and the piezocomposite transducer were measured. The transfer functions were calculated by using the methods described in van Neer et al. (2007). For the multilayer transducers, only the transmit transfer functions of the PZT elements were measured. Accordingly, only the receive transfer functions of the copolymer layers were obtained.

Transmit transfer functions

The transducer transmit transfer function ($T_t(\omega)$) is defined as (van Neer et al., 2007):

$$T_t(\omega) = \frac{|p_0(\omega)|}{|V_T(\omega)|}, \tag{6.1}$$

where $V_T(\omega)$ is the voltage over the transducer clamps and $p_0(\omega)$ the pressure produced at the transducer surface. To obtain the transmit transfer functions, acoustic measurements with a calibrated hydrophone (Precision Acoustics Ltd., Dorchester, UK, active diameter: 200 μm) were performed. The experimental setup (Fig. 6.3a) consisted of a tank filled with saturated water and with the transducer under investigation mounted in the sidewall. The hydrophone was mounted in a holder and controlled by a custom built xyz-system. An arbitrary waveform generator (model 33250A, Agilent, Loveland, Colorado, USA) was used to drive the transmitting transducer with 300-cycle sine wave bursts. The waveform generator was controlled by a computer via a general purpose interface bus (GPIB) connection to generate a frequency sweep from 1 MHz till 8 MHz with steps of 50 kHz. The output pressures were kept below 20 kPa at the transducer surface such that nonlinear wave propagation could be neglected. The signals received by the hydrophone were digitized by a digitizer card (DP235, Acqiris, Geneva, Switzerland). In agreement with the method described in van Neer et al. (2007), the hydrophone transfer function was taken into account. The transmitting elements of both multilayer transducers were electronically tuned with a series inductor of 2.7 μH to increase the transmit efficiency. The piezocomposite transducer was electronically tuned by the manufacturer.

Receive transfer functions

The receive transfer function ($T_r(\omega)$) is defined as (van Neer et al., 2007):

$$T_r(\omega) = \frac{|V_{T-open}(\omega)|}{|p_a(\omega)|}, \tag{6.2}$$

with $V_{T-open}(\omega)$ the open circuit voltage produced by the transducer and $p_a(\omega)$ the received pressure averaged across the transducer surface. To obtain the receive transfer functions, direct receive measurements with a calibrated acoustic source were performed. A similar setup as previously described was used where the hydrophone was replaced by a single element transducer (model V310, Panametrics, Waltham, MA, USA) with center frequency of 5 MHz and active diameter of 6.35 mm (Fig. 6.3b). Again, 300-cycle sine wave bursts were used for transmission and output pressures were kept low. The transducer under investigation was used as a receiver and the received signals were digitized with the digitizer card. Again, the transducers were electronically tuned.

6.2.5 Electromagnetic susceptibility

The Electromagnetic susceptibility (EMS) of the IM-transducer, the NM-transducer and the piezocomposite transducer were measured. To mimic *in-vivo* measurement conditions with

the transducer applied to the abdominal wall, the transducers were placed against the palm of a hand using gel for acoustical and electrical coupling. The transducers were used in reception only. The signals were amplified with a broadband amplifier (model AU-1519-10289, Miteq Inc., Hauppauge, NY, USA) with about 60 dB signal gain and frequency bandwidth of 1 MHz - 300 MHz. Data-acquisition was performed with a PC oscilloscope (Handyscope 3, Tiepie Engineering, Sneek, the Netherlands) with sampling frequency of 50 MHz and 12-bit resolution. Data were transferred to a PC using a USB 2.0 interface. A low-pass filter with cutoff frequency at 22 MHz together with 20 dB attenuation was used between the amplifier and the oscilloscope to avoid aliasing and clipping. As a reference, the EMS of the complete acquisition system, without a load attached, was also measured.
In addition, *in-vitro* measurements were performed in a controlled setup. The three transducers were immersed in a water tank filled with tap water and were placed within 4 cm from each other. To ensure identical measurement conditions, the transducer responses were measured within 30 seconds. The measurement system was identical to the one used with the *in-vivo* EMS measurements, but without 20 dB attenuation.

6.2.6 *In-vitro* pulse-echo measurements

To obtain the responses to a bandwidth limited acoustic wave, two different pulse-echo measurements were performed with all three transducers. Measurements were performed in a water tank with a flat reflector at 2.7 cm distance. Another set of pulse-echo measurements was performed on a 500 ml bladder phantom (Zerdine^{TM}, Computerized Imaging Reference Systems, Inc., Norfolk, VA, USA). The PZT elements of the multilayer transducers and the piezocomposite transducer were excited with a Gaussian modulated 15-cycle sine wave burst with center frequency of 2.1 MHz and -6 dB bandwidth of 17%. A drive amplitude of 160 V_{pp}, resulting in peak pressures of approximately 800 kPa at the transducer surface for all three transducers, was used to induce strong nonlinear wave propagation. To prevent the transducers from transmitting harmonic frequency components, a passive 9^{th} order high-power Butterworth low-pass filter with cut-off frequency at 2.5 MHz was used (Merks et al., 2006b) between the power amplifier (model 150A-100B, Amplifier Research, EMV Benelux B.V., Hazerswoude Dorp, the Netherlands) and the transmitting elements. A high-impedance probe (1 MOhm, 1:10) was used to measure the copolymer and the piezocomposite responses. The transmitting elements of both multilayer transducers were electronically tuned with a series inductor of 2.7 μH to increase the transmit efficiency. The piezocomposite transducer was electronically tuned by the manufacturer. With the phantom measurements, an 8^{th} order low-pass Bessel filter with cut-off frequency of 12.5 MHz was used before digitalization. A custom built pre-amplifier with high-impedance input (2 kOhm) and 24 dB signal gain was used to measure the copolymer responses. With the piezocomposite transducer, a limiter-configuration, i.e. a series 50 Ohm resistor with a pair of anti-parallel diodes placed parallel to the receive circuitry, was used to protect the receiving pre-amplifier (model AU-1519-10289, Miteq Inc., Hauppauge, NY, USA). Attenuation of 40 dB was used to prevent the amplifier from clipping, leading to a net signal gain of 20 dB for the piezocomposite transducer.

6.3 Results

6.3.1 Transfer functions

Transmit transfer functions

The transmit transfer functions obtained for the piezocomposite transducer and the PZT elements of the IM-transducer and NM-transducer are shown in Fig. 6.4a. The transmit transfer function of the IM-transducer had a center frequency of 2.1 MHz and -6 dB bandwidth of 73%. The transmit efficiency at 2.1 MHz was measured to be 9.4 kPa/V. The transmit transfer function of the NM-transducer had a center frequency of 2.2 MHz, a -6 dB bandwidth of 87% and a transmit efficiency of 7.3 kPa/V at 2.1 MHz. The piezocomposite had the highest transmit efficiency of the three transducers at 2.1 MHz (11.4 kPa/V). Its transmit transfer function had a center frequency of 2.4 MHz and -6 dB bandwidth of 83%, which is in agreement with the specifications given previously. From these results the NM-transducer thus had the largest -6 dB bandwidth. However, from Fig. 6.4a, it can be seen that the transmit transfer function of the NM-transducer actually had two high-sensitivity peaks at 1.7 MHz and 2.7 MHz, with -6 dB bandwidths of 24% and 16%, respectively. This indicates that it is not possible to use the full 87% bandwidth in transmission without distorting the transmitted waves.

Receive transfer functions

The measured receive transfer functions of the piezocomposite transducer and the copolymer films of the IM-transducer and NM-transducer are shown in Fig. 6.4b. The IM-transducer and the NM-transducer had comparable receive sensitivity at the 2^{nd} harmonic frequency (15.4 μV/Pa), but the IM-transducer had much better sensitivity at the 3^{rd} harmonic frequency (13.2 μV/Pa). The transfer function of the IM-transducer also showed a moderate filtering at the fundamental frequency as the receive sensitivity at 2.1 MHz was measured to be 7.8 μV/Pa. This is advantageous to the dynamic range of the acquisition system, and enables measuring the fundamental frequency as well as the higher harmonics with sufficient SNR.
The transfer function of the NM-transducer showed sharp low-sensitivity peaks near the 2^{nd} and 3^{rd} harmonic frequencies, which could introduce distortion into the received signals. Since KLM-circuit model simulations also showed these peaks, they are considered specific to the design of the NM-transducer. The KLM-circuit model was adapted from the model used in Merks et al. (2006a). The peaks can be explained by considering the PZT element as a passive layer seen by the copolymer film. Because the media surrounding the PZT layer have much lower acoustic impedance, standing waves appear within the PZT layer at integer multiples of the fundamental frequency. Because of the specific geometry, the peaks observed within the receive transfer function of the NM-transducer are more pronounced than within the transfer function of the IM-Transducer.
The IM-transducer and the piezocomposite transducer both showed smooth transfer functions near the frequencies of interest. This indicates distortionless transfer of the received signals. The piezocomposite transducer had high receive sensitivity at the fundamental frequency (91.9 μV/Pa), but very low sensitivities at the harmonic frequencies, especially at

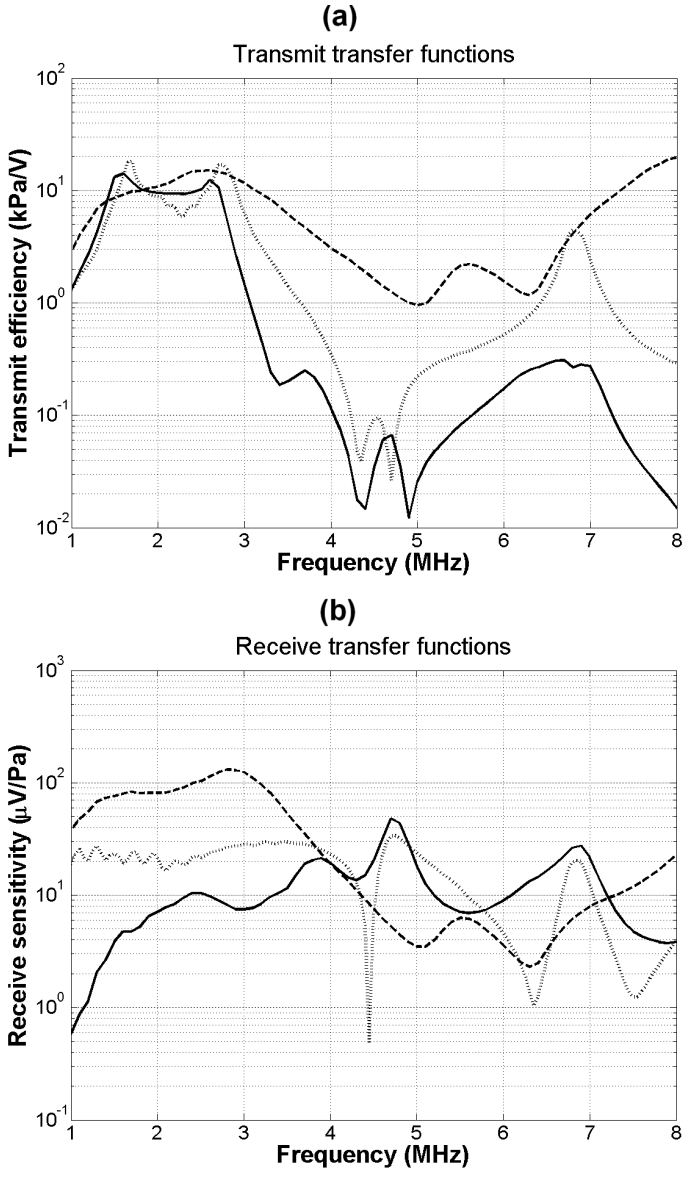

Figure 6.4: Transmit transfer functions (a) and Receive transfer functions (b) obtained for the IM-transducer (solid lines), the NM-transducer (dotted lines) and the piezocomposite transducer (dashed lines).

the 3^{rd} harmonic frequency (6.3 MHz).

6.3.2 Electromagnetic susceptibility

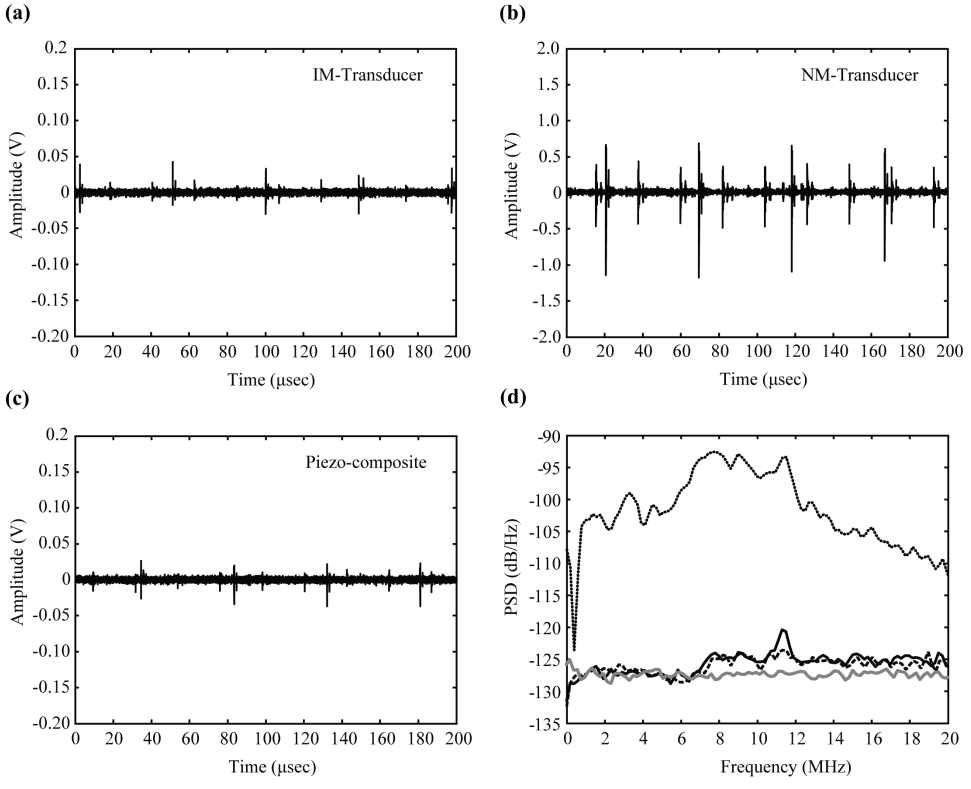

Figure 6.5: RF-recordings from the IM-transducer (a), the NM-transducer (b) and the piezocomposite transducer (c), while the acoustic interfaces were in contact with tissue. Notice the 10 times larger amplitude scaling for the NM-transducer with respect to the other two transducers. The corresponding Power Spectral Density estimates of the IM-transducer (solid black line), the NM-Transducer (dotted line) and the piezocomposite transducer (dashed) are shown at the lower right (d). The solid gray line represents the PSD of the acquisition system without load.

Fig. 6.5 shows the recorded RF-data from the IM-transducer, the NM-transducer and the piezocomposite transducer, while the front acoustic interfaces were in contact with tissue. The corresponding Power Spectral Density estimates (PSD) were computed from the RF-data using Welch's method and are shown at the lower right. The solid grey line represents the PSD of the acquisition system without load. Table 6.1 shows the Root-Mean-Square Voltages (V_{rms}), calculated from the time waveforms, and the measured maximum and minimum values of the received distortion. These values were calculated over a time period of 24 ms to approximate steady state EMS behavior.

Table 6.1: Results electromagnetic susceptibility measurements. The setup for the *in-vivo* measurements had 40 dB signal gain, whereas for the *in-vitro* measurements 60 dB gain was used. The SNR was calculated with 100 Pa acoustic pressure and average receive sensitivity of 10 μV/Pa.

	Setup	V_{rms}*(mV)*	*Max.(mV)*	*Min.(mV)*	*SNR (dB)*
	in-vivo	50.4	918.9	-1324.3	-22.4
NM-transducer	*in-vitro*	73.0	1093.7	-882.9	-0.8
	in-vivo	2.6	48.1	-36.8	6.4
IM-transducer	*in-vitro*	2.3	34.0	-34.8	29.2
	in-vivo	2.5	32.7	-45.7	6.8
Piezocomposite	*in-vitro*	2.4	29.2	-23.6	30.7
	in-vivo	2.1	10.2	-11.0	19.2
System reference	*in-vitro*	1.7	8.5	-7.9	41.4

The NM-transducer had a very high EMS, which was also the case with the PVDF layer of the previously introduced multilayer transducer. The time waveforms, especially the one from the NM-transducer, showed distortions with a clear repetitive pattern. The largest spikes had a time period of 50 μs and 20 μs, which correspond to switching frequencies of 20 kHz and 50 kHz, respectively. Most likely, this distortion originated from the switching electronic ballasts from fluorescent lamps. In contrast, the EMS of the IM-transducer was very low and could be compared with the EMS from the piezocomposite transducer, which is considered to be optimal. The measured EMS in the frequency range of interest (1 MHz - 8 MHz) was even limited by the system reference.
The controlled *in-vitro* measurements gave comparable results with respect to the *in-vivo* measurements and again showed the high EMS of the NM-transducer relative to the other two transducers (Table 6.1). Also, higher EMS was apparent *in-vivo* than *in-vitro*, which explains for the difference in signal attenuation used.
Table 6.1 also shows the estimated SNR when assuming harmonic peak pressures of at least 100 Pa with an average receive sensitivity of 10 μV/Pa. These ratios were calculated by taking the maximum absolute amplitude of the measured distortion, corrected for the applied signal gain. Both the piezocomposite transducer and the IM-Transducer have sufficient SNR ($>$ 6 dB), whereas the NM-transducer has not (-22 dB). Because the part with high EMS, i.e. the piezoelectric film, was shielded by the transducer housing and the electrodes of the PZT element, the large reduction of the EMS, and thus the increase in SNR, of the IM-transducer could be ascribed to the inverted geometry.

6.3.3 *In-vitro* pulse-echo measurements

The measured pulse-echo responses of the IM-transducer, the NM-transducer and the piezocomposite transducer, in a water tank with a flat reflector at 2.7 cm distance, are shown in Fig. 6.6. The PZT element was used for transmission and the copolymer layer was used for reception. The piezocomposite transducer was used for transmission as well as reception. In total 100 traces were averaged and a 3^{rd} order Butterworth filter with passband between

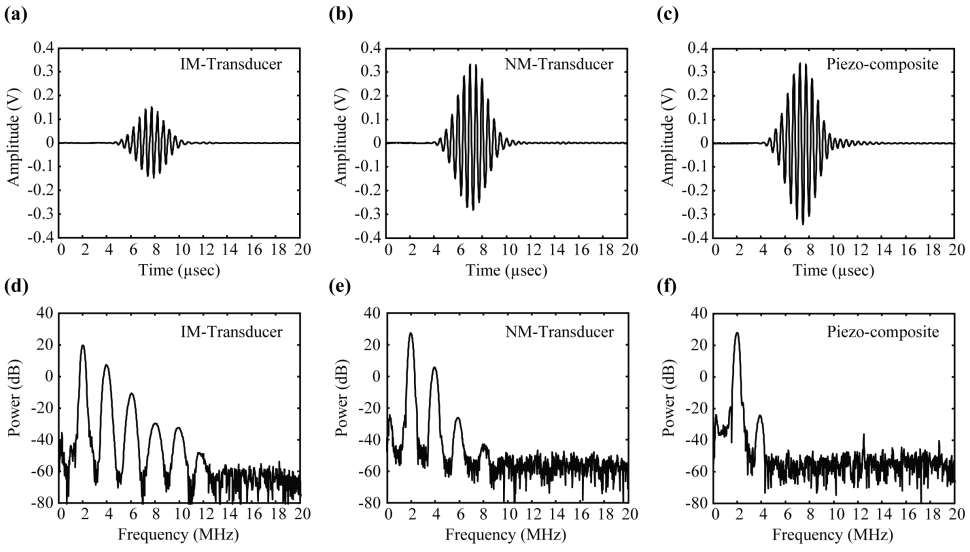

Figure 6.6: Time waveforms and corresponding spectra of the pulse-echo responses of the IM-transducer (a and d), the NM-transducer (b and e) and the piezocomposite transducer (c and f) measured in a water tank with a flat reflector at 2.7 cm distance. With the multilayer transducers, the PZT element was used for transmission and the copolymer layer was used for reception. The time scales represent retarded time.

200 kHz and 20 MHz was used before the spectra were calculated.
The IM-transducer had the best sensitivity at the harmonic frequencies compared to the other two transducers. The spectrum of the IM-transducer also showed the moderate filtering at the fundamental frequency with respect to the higher harmonics. The response of the IM-transducer showed a 3^{rd} harmonic level only 30 dB below the fundamental level. Even at the small reflector distance of 2.7 cm, but with averaging, a significant 6^{th} harmonic was apparent. The NM-transducer also showed a significant 3^{rd} harmonic component, but at 50 dB below the fundamental level. The piezocomposite transducer only showed a small 2^{nd} harmonic component, 50 dB below the fundamental level, and no higher harmonics. Both multilayer transducers are therefore better suited for harmonic pulse-echo applications.
The measured pulse-echo responses of the IM-transducer, the NM-transducer, and the piezocomposite transducer on the CIRS bladder phantom are shown in Fig. 6.7. Again, the RF-data were filtered with a 3^{rd} order Butterworth filter with passband between 200 kHz and 20 MHz before the spectra were calculated. No averaging was done. Also, the measurements were not corrected for the differences in receive circuitry between the copolymer and piezocomposite transducers. The spectra were computed from the filtered RF-signal present within a time segment from 140 tot 160 μs (see Fig. 6.7). This segment contained the echoes from the posterior bladder wall. A Hanning window with length equal to the time segment was used to obtain a smooth spectrum with sufficient frequency resolution.

Mainly due to the improved SNR and the moderate filtering at the fundamental frequency, the 3^{rd} harmonic frequency could still be measured with the IM-transducer at 45 dB below the fundamental level. The NM-transducer was capable of measuring only up to the 2^{nd} harmonic frequency with less SNR than the IM-transducer. The spectrum of the piezocomposite showed a very small 2^{nd} harmonic component, which may become apparent when averaging is applied. However, it is shown that the multilayer concepts, and especially the IM-transducer, outperformed the single-element piezocomposite transducer in the current application.

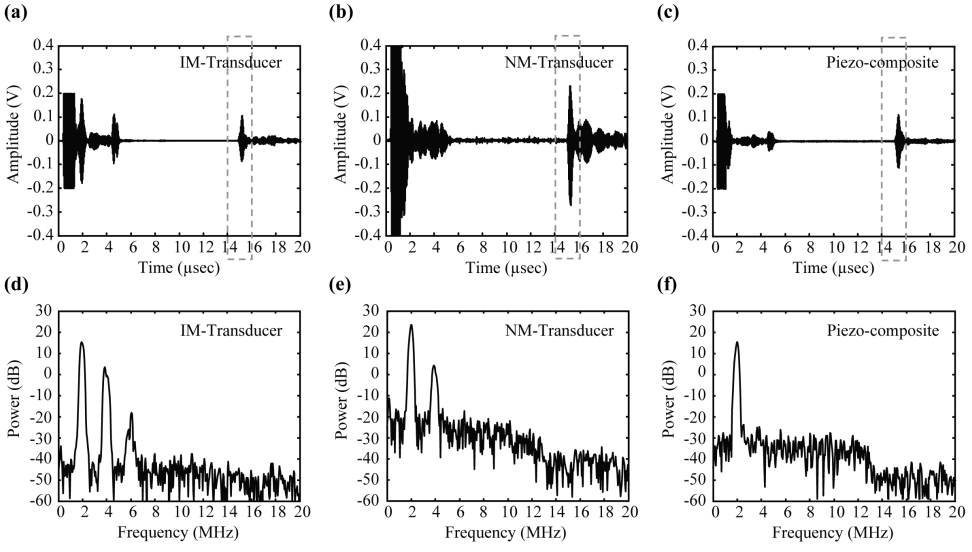

Figure 6.7: Time waveforms and corresponding spectra of the pulse-echo responses of the IM-transducer (a and d), the NM-transducer (b and e) and the piezocomposite transducer (c and f) measured on a 500 ml bladder test phantom. With the multilayer transducers, the PZT element was used for transmission and the copolymer layer was used for reception. The spectra were computed from the RF-signal present within the time segment indicated (dashed box).

6.4 Discussion and summary

An inverted multilayer transducer (IM-transducer) and a normal multilayer transducer (NM-transducer) were developed and built. The IM-transducer was designed to have a high transmit efficiency as well as broadband receive characteristics. This was achieved by using two separate layers; a PZT element for transmission at the fundamental frequency and a copolymer film for broadband reception. Copolymer was used instead of PVDF because of the higher coupling factor (k_t) and lower dielectric and mechanical losses ($tan\delta_e$ and $tan\delta_m$, respectively) (Lancée et al., 1985). The transmit efficiency was sufficient to cause significant nonlinear wave propagation. The receive sensitivity as well as the receive

bandwidth allowed for proper acquisition of the fundamental frequency up to at least the 3^{rd} harmonic frequency component in the reflected signals. The ElectroMagnetic Susceptibility (EMS) was reduced to a level comparable to commercially available PZT and piezocomposite transducers.
The NM-transducer, comparable with the previously introduced multilayer concept (Merks et al., 2006b), had the same PZT and copolymer film as the IM-transducer, but the copolymer layer was mounted on the outside and no matching layer was applied. The NM-transducer showed a very high EMS, which was approximately 20 times the EMS observed with the IM-transducer. The large reduction of the EMS was therefore ascribed to the inverted geometry of the IM-transducer.
Mounting the receiver at the back of the layer stack may raise questions with respect to receive sensitivity. This paper documents that, by comparing the IM-transducer with the NM-transducer, the receive sensitivity was only slightly reduced at the fundamental frequency and not at the higher harmonics. Consequently, it was shown that the IM-transducer concept had better signal-to-noise characteristics than the NM-transducer concept. Improvements with respect to previously published work have thus been the increased sensitivity in transmission and reception, and the significant decrease in EMS.
A broadband high sensitive piezocomposite transducer was also included in this study to show that the IM-Transducer had comparable EMS properties as the piezocomposite, which are considered to be optimal. The IM-Transducer and the piezocomposite had comparable transmit transfer functions (Fig. 6.4a), but differed in receive sensitivities. It must be noted that the piezocomposite transducer has a larger active surface (factor 1.56) than both multilayer transducers. This factor has not been corrected for.
From the measured receive transfer functions (Fig. 6.4b) it shows that the piezocomposite has the highest receive sensitivity up to 4 MHz, whereas the IM-transducer has a slightly higher sensitivity from 4.5 MHz to 7 MHz. The sensitivity at a frequency between 1.5 MHz and 2.5 MHz for the piezocomposite transducer is an order of magnitude higher than the sensitivities at the higher harmonics, whereas the IM-transducer has receive sensitivities at the same order of magnitude. The IM-transducer is therefore preferable when the dynamic range of the measurement system is limited. When the system dynamic range poses no problem, both the IM-transducer as well as the piezocomposite can be used for bladder volume assessment on the basis of nonlinear wave propagation.
A further advantage of using two separate layers is that the transmit and receive electronics can be optimized separately. This allows for dedicated transmit and receive circuitry, which are more efficient and, additionally, are more simple and less bulky than in the case of a single element broadband transducer. This was also the reason for the lower performance of the piezocomposite transducer in pulse-echo mode, where part of the transmit and receive energy were dissipated in the limiter configuration.
In addition, it was found that the receive transfer function was affected by electronically optimizing for the transmit layer, i.e. electrically tuning the PZT element. Hence, the transmit transfer functions and receive transfer functions of the IM-transducer, with and without electrically tuning the PZT element with a series inductor (2.7 μH), were obtained (see Fig. 6.8). Fig. 6.8a shows a significant increase in transmit efficiency and bandwidth when the PZT element is electrically tuned. The transmit efficiency was increased from 7

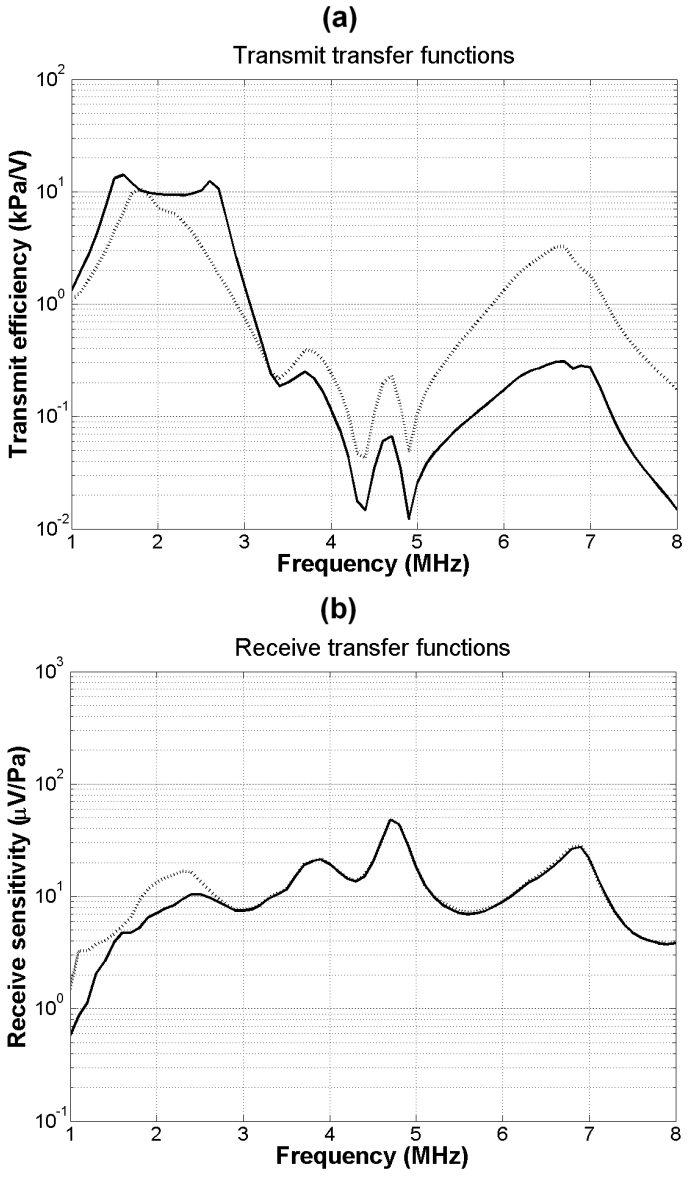

Figure 6.8: Transmit transfer functions (a) and receive transfer functions (b) obtained for the IM-transducer without the PZT element electrically tuned (dotted line) and with the PZT element electrically tuned (solid line) with a series inductor of $2.7\mu H$.

kPa/V to 9.4 kPa/V. The -6 dB bandwidth increased from 39% to 73%. Fig. 6.8b shows that the electrical tuning of the PZT element only affects the receive transfer at the funda-

mental frequency. The receive sensitivity at the fundamental frequency was reduced with 6 dB. This means that an electronically tuned IM-transducer shows a moderate filtering at the fundamental frequency with respect to the higher harmonics. This can be explained by the receive transfer function of the PZT, which has a preference for acoustic energy at the fundamental frequency. The PZT thus absorbs large part of the fundamental acoustic energy before the acoustic waves reach the copolymer layer. This is considered beneficial for the dynamic range of the receiving electronics, which has been increased with 6 dB.
Because of these benefits compared to single element implementations and because of the low lateral coupling of copolymer, the new multilayer concept could be beneficial for array transducer applications (Jeong et al., 2007). It is concluded that in order to measure at least up to the third harmonic frequency component with good sensitivity in combination with very high transmit efficiency at the fundamental frequency, a multilayer structure is optimal. To optimize for the EMS in reception, and hence also the signal-to-noise ratio, an inverted geometry as proposed in this paper has proven to be effective.

Acknowledgements The authors would like to thank Wim van Alphen en Geert Springeling for the transducer manufacturing. Many thanks to Oldelft (Delft, the Netherlands) for supplying the transducer materials. Also, many thanks to Verathon Medical Europe B.V. (IJsselstein, the Netherlands) for their constructive support.

Part 2: superharmonic imaging - transducer design and imaging methods

CHAPTER 7

Development of a phased array transducer for tissue and contrast superharmonic imaging[1]

Paul L.M.J. van Neer, Guillaume Matte, Jerome M.G. Borsboom, Martin D. Verweij, Nico de Jong

Abstract For several years the standard in ultrasound imaging is second harmonic imaging. Recently, a new imaging modality dubbed superharmonic imaging (SHI) has been proposed. SHI takes advantage of the higher - third to fifth - harmonics produced by either nonlinear propagation or contrast agent response. Tissue SHI shows a better suppression of near-field artifacts and improved lateral and axial resolutions, resulting in images with improved clarity compared to second harmonic imaging. In combination with contrast agents SHI produces a higher contrast-to-tissue ratio. To enable SHI with a high dynamic range an array sufficiently sensitive at the transmission frequency up to its fifth harmonic is necessary (bandwidth$>$130%). We present the results of custom built testarrays aiming specifically on receive sensitivity and SNR. The initial piezomaterial selection was done using the KLM model. From the selected materials testarrays were built (element size 13 mm x 0.2 mm, resonance frequency 4 MHz, no matching layer, backing 5.3 MRayl). A calibrated source generated a pressure pulse, while the testarray was located in the far field of the source. From the received pressure wave the element transfer functions and SNR were calculated, after compensation for diffraction and spatial averaging. The receive transfer function and SNR were evaluated on a per element basis. An element of the most sensitive testarray had an average peak receive sensitivity of 21 μV/Pa and could detect a long sinusoidal burst with amplitude 1 Pa with 22 dB SNR. Using these results a conservative estimate predicts a dynamic range for SHI of 55 dB. These results suggest *in-vivo* tissue and contrast SHI could be feasible using the current array configuration, which is based on interleaved low and high frequency elements.

[1]From P.L.M.J. van Neer, G. Matte, J.M.G. Borsboom, M.D. Verweij, N. de Jong, 'Development of a phased array for tissue and contrast super harmonic imaging', Proc. IEEE Ultrasonic Symp., 2007, 200-203.

7.1 Introduction

Classically, ultrasound images have been obtained using fundamental imaging. Since several years, the standard in ultrasound imaging has changed to second harmonic imaging. Recently, a new imaging modality dubbed superharmonic imaging (SHI) has been proposed. SHI takes advantage of the higher - third to fifth - harmonics produced by either nonlinear propagation or contrast agent response (Bouakaz et al., 2002). Tissue SHI shows a better suppression of near-field artifacts, reverberations and artifacts at the edges of the beam, next to improved lateral and axial resolution. The resulting images have improved clarity compared to second harmonic imaging (Bouakaz and de Jong, 2003). Recently, this was confirmed by simulations and *in-vitro* experiments conducted by Ma et al. (2006). As for ultrasound contrast agent (UCA) imaging, it has been demonstrated by Bouakaz et al. (2002) that the contrast-to-tissue ratio (CTR) increases as a function of the order of the harmonic frequency. As such, in combination with contrast agents SHI produces a higher CTR (Bouakaz et al., 2002) than second harmonic imaging while minimizing shadowing effects.
The primary requirements for a phased array transducer to be usable for SHI are bandwidth and sensitivity. The principle of transmission at the fundamental and receiving the third to fifth harmonic implies a traditional bandwidth of more than 130%. To meet this requirement an interleaved design was proposed (Bouakaz et al., 2002). In this design, the odd elements are used for reception and have a center frequency at 4 MHz, while the even elements are used in transmission and have a center frequency at 1 MHz.
This paper focuses on the issue of sensitivity. In both cases of harmonic generation - nonlinear wave propagation or nonlinear contrast response - the higher harmonic components will be much lower in energy than the fundamental or second harmonic. Although this issue is alleviated somewhat by combining the third to fifth harmonics, an optimally sensitive array is necessary. In this study, we investigate whether sufficient sensitivity can be achieved using the proposed array configuration for *in-vivo* SHI with a satisfactory dynamic range. We present the results of custom built testarrays aiming specifically on sensitivity. The sensitivity demand is split into two figures of merit: the absolute receive transfer function of each testarray element and the signal-to-noise-ratio (SNR) with which a single testarray element can detect a long sinusoidal wave train with an amplitude of 1 Pa.

7.2 Methods

The initial selection of piezomaterials to build testarrays from was performed by careful consideration of material properties and KLM-circuit model simulations (Leedom et al., 1971). From the selected materials (PZT5H like, high dielectric constant PZT and single crystal materials) testarrays were built. Each testarray had 16 elements with element size 13 mm x 0.2 mm and pitch 0.5 mm. The testarrays had resonance frequencies of 3 - 4 MHz, no matching layer and a backing with an acoustic impedance of 5.3 MRayl.

7.2.1 Experimental setup

The experimental setup as shown in Fig. 7.1 consisted of a tank filled with water with the testarrays mounted in the sidewall and a calibrated source mounted in a holder controlled by a custom built xyz-system.

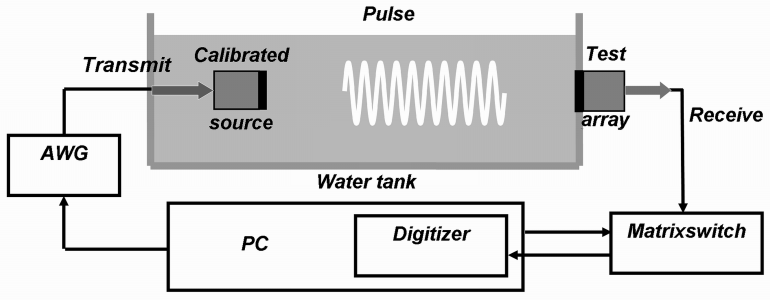

Figure 7.1: Schematic diagram of the experimental setup.

The source was a flat circular piston transducer, which produced sine bursts with length 300 cycles. Care was taken to ensure that the transmitter output pressure was of such low magnitude that nonlinear propagation could be neglected. The influence of attenuation was neglected as well, as the propagation distance in water was approximately 20 cm. The on-axis pressure at a certain distance from the source was calculated by means of a diffraction correction from the pressure produced at the surface of the source. For this purpose the exact diffraction correction function posted by Goldstein et al. (1998) was used. As the testarrays are 13 mm long in the elevation dimension, the on-axis pressure overestimates the actual pressure received by the testarrays. To account for this effect, a spatial averaging correction factor was calculated. This factor was calculated by simulating the complete wave over the relevant elevation range (-6.5 to 6.5 mm) produced by the calibrated source at the relevant axial distance for each frequency using Field II (Jensen and Svendsen, 1992; Jensen, 1996).

7.2.2 Equipment

Receive transfer measurements

An arbitrary waveform generator (33250A, Agilent, Loveland, Colorado) was used as a voltage source and was connected directly to the calibrated source transducer (V310, Panametrics, Waltham, MA, USA, 2.25 MHz center frequency, diameter 6.35 mm). The response of each element of the testarray under investigation was passed through a computer controlled matrix switch (custom built) and digitized by a digitizer card (DP235, Acqiris, Geneva, Switzerland). The waveform generator was connected to a computer through GPIB and the matrixswitch was controlled through an Ethernet connection. For a schematic overview see Fig. 7.1.

SNR measurements

For the SNR measurements an attenuator (355D, Agilent, Santa Clara, CA, USA) was placed between the arbitrary waveform generator and the calibrated source. Also, the matrix switch was replaced by a low noise amplifier (AU-3A-0110-BNC, Miteq, Hauppauge, NY, USA).

Calculating the element receive transfer function

The transducer transmit transfer function ($T_t(\omega)$) is defined as (van Neer et al., 2007)

$$T_t(\omega) = \frac{|p_0(\omega)|}{|V_T(\omega)|}, \tag{7.1}$$

where $V_T(\omega)$ is the voltage over the transducer (see Fig. 7.2) and $|p_0(\omega)|$ the pressure at the transducer surface.

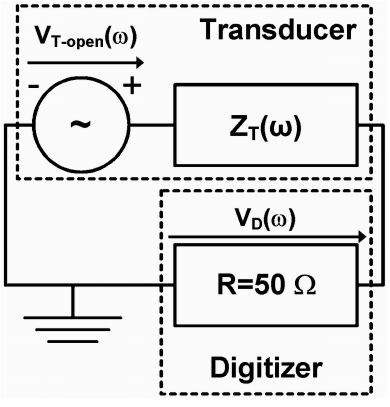

Figure 7.2: Essentials of the receive circuit.

The receive transfer function ($T_r(\omega)$) is defined as (van Neer et al., 2007)

$$T_r(\omega) = \frac{|V_{T-open}(\omega)|}{|p_a(\omega)|}, \tag{7.2}$$

with $V_{T-open}(\omega)$ the open circuit voltage over the transducer (see Fig. 7.2) and $p_a(\omega)$ the received pressure averaged across the transducer surface.

A source with known transmit transfer function is mounted in the holder of an xyz-system and transmits a known pulse. The testarray is mounted in the side of the tank and is used as a receiver. Its receive transfer function ($T_r(\omega)$) is calculated by

$$T_r = \frac{V_{T-open}}{V_t^s} \cdot \frac{1}{T_t^s \cdot D_t^s \cdot S_a}, \tag{7.3}$$

with V_{T-open} the Fourier transformed open circuit voltage produced by a testarray element, V_t^s the Fourier transformed voltage measured over the impedance of the source, T_t^s the transmit transfer function of the source, D_t^s the diffraction correction function for the source and S_a the spatial averaging correction factor.
In order to obtain V_{T-open} from V_D a compensation for the loss and impedance of the matrixswitch and coax cables is made.

Calculating the SNR

Using the experimental setup described earlier and by rewriting (7.3) the transmit amplitude (in volt) necessary to obtain a pressure of 1 Pa averaged over the testarray element surface was calculated. The testarray elements received the 1 Pa pressure wave and produced a potential over its electrodes. The low noise amplifier amplified the signal before passing it on to the digitizer and reduced the SNR by 1.2 dB (from specification sheet). Care was taken to minimize interference from other noise sources. As the testarray element was assumed to be the principal signal and noise source, the SNR calculated from the signal on the digitizer is the same as the SNR of the signal produced by the testarray element after compensation for the amplifier. The actual SNR value was calculated by taking the Fourier transform of a rectangular time window located in the middle of the sine burst.

7.3 Results

The receive transfer functions and SNR for a pressure of 1 Pa received by the transducer surface were evaluated on a per element basis. An example graph of a receive transfer function is shown in Fig. 7.3. This example is from testarray 05, built from CTS 3203 HD material. Each line represents the receive transfer function of an element. The average peak receive transfer (at the testarray's resonance frequency of 3.2 MHz) was 21 μV/Pa. As can be appreciated from the figure the variation between the curves of each array element was low. The standard deviation of the peak receive transfer was 0.8 μV/Pa. The -6 dB bandwidth was approximately 40%.
Key performance parameters characterizing testarray behavior are summarized in table 7.1. The resonance frequency of the testarrays was between 3.2 and 3.6 MHz, with the exception of testarray 11, which had a resonance frequency of 2.1 MHz. The average peak receive sensitivity generally lay between 13.7 and 15.6 μV/Pa. One exception was testarray 05, which had the highest average peak receive sensitivity of 21 μV/Pa. The other two exceptions were testarrays 12 and 13, which had average peak receive sensitivities between 5.5 and 7.6 μV/Pa. The standard deviation of the peak sensitivity, if comparing over elements, was between 0.5 - 1.3 μV/Pa. The exception was testarray 11, which had a standard deviation of 3.8 μV/Pa. The -6 dB bandwidth of the testarrays varied between 40 and 50%. The magnitude of the impedance at the resonance frequency of the testarrays varied between 350 and 800 Ohms. The phase of the impedance at the resonance frequency varied between -30° and -20°, except for testarrays 11 - 13, where it varied between -65° and -45°. The SNR, when receiving a sinusoidal pressure wave with amplitude 1 Pa (at the testarray's resonance frequency), varied between 11 and 22 dB.

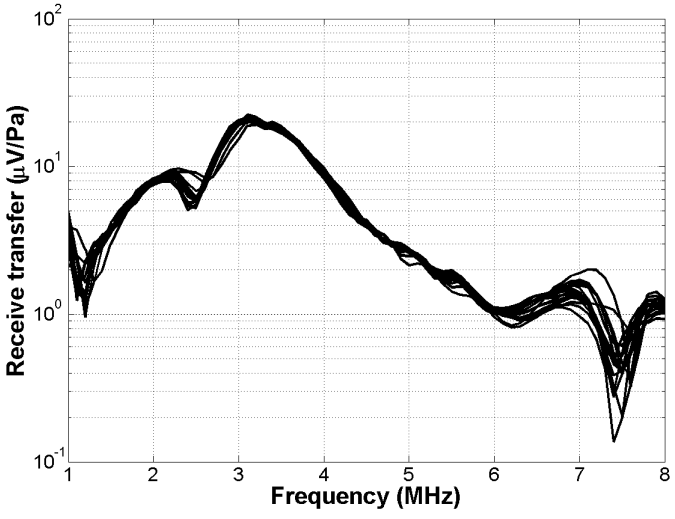

Figure 7.3: Receive transfer function of testarray 05, made from CTS 3203 HD material. Each line is the transfer function of an individual element.

7.4 Discussion

Testarray 05, based on PZT5H type material CTS 3203 HD, had the highest average peak receive sensitivity of 21 μV/Pa. It was also the best from a SNR perspective and could detect a long sinusoidal burst with amplitude 1 Pa at the testarray's resonance frequency with 22 dB SNR.

The relatively narrow -6 dB bandwidth of the testarrays was caused by the absence of a matching layer.

The testarrays built using single crystal material (testarrays 11, 12 and 13) showed either unexpectedly low average peak sensitivity (testarrays 12 and 13) or had a large standard deviation of the peak sensitivity (testarray 11) over the elements. These testarrays also showed an average per element phase at resonance of -45°, -58° and -65° for testarrays 11, 12 and 13 respectively, which was significantly lower than the -30° to -20° phase at resonance of the other testarrays. These effects were likely caused by dicing difficulties. The testarrays were diced using a diamond saw and the very brittle single crystal material has to be diced carefully. Visual inspection using a microscope of the testarray elements built from single crystal material revealed that chips had broken off the brittle single crystal material during sawing.

For SHI a typical frequency in transmission is 1 MHz and in reception 3-5 MHz. In the case of an MI of 1 (= 1 MPa at focus) the superharmonic component is conservatively estimated to be 30 dB lower compared to the fundamental (simulations performed by Bouakaz and de Jong (2003) showed that for an MI of 1.35 a superharmonic component about 5-15 dB lower than fundamental, depending on the axial distance). If an additional loss of 50 dB due to typical tissue reflection and attenuation is assumed, this results in a received

pressure wave with a maximum amplitude in the order of 100 Pa. Thus, based on the best performing testarray, the *in-vivo* dynamic range of a single array element is estimated to be 40 - 62 dB. By utilizing the full interleaved array (44 elements used in reception) the SNR will be improved by another 16 dB, which results in a dynamic range of 56 - 78 dB of the full array at superharmonic frequencies.

7.5 Conclusion

The best performing testarray had an average peak receive sensitivity of 21 μV/Pa. It was also the best from a SNR perspective and could detect a long sinusoidal burst at the testarray's resonance frequency with amplitude 1 Pa with 22 dB SNR. Using these results a conservative estimate predicts a dynamic range for SHI in excess of 55 dB. These results suggest that *in-vivo* tissue and contrast SHI is feasible using the current array configuration.

Acknowledgements We gratefully acknowledge the efforts of W. van Alphen, Roelof Hardenberg, G. Springeling and J.G. Bosch.

Table 7.1: Key testarray performance parameters

testarray ID	Material type	Resonance frequency (f_r)	$T_r(f_r)$: μ	$T_r(f_r)$: σ	Bandwidth at -6 dB	$\lvert Z(f_r)\rvert$	$\angle Z(f_r)$	SNR if receiving 1 Pa wave
		[MHz]	[μV/Pa]	[μV/Pa]	[%]	Ω	[$^\circ$]	[dB]
5	CTS 3203HD	3.2	21	0.8	40	350	-25	22
9	Morgan PZT5K1	3.4	13.7	1.3	41	350	-30	16
14	TRS PZT HK1HD	3.6	13.5	0.5	50	240	-25	16
15	TRS PZT HK1HD	3.6	14.3	0.5	47	250	-20	17
11	Omega PZNT	2.1	15.6	3.8	48	800	-45	11
12	TRS PMN-30%PT	3.4	5.5	0.8	47	300	-58	16.5
13	TRS PMN-30%PT	3.5	7.6	0.9	46	300	-65	13

CHAPTER 8

Superharmonic imaging: development of an interleaved phased array transducer[1]

Paul L.M.J. van Neer, Guillaume Matte, Mikhail G. Danilouchkine, Christian Prins, Franc van den Adel, Nico de Jong

Abstract For several years the standard in ultrasound imaging has been second harmonic imaging. A new imaging technique dubbed 'superharmonic imaging' (SHI) was recently proposed. It takes advantage of the higher - third to fifth - harmonics arising from nonlinear propagation or ultrasound contrast agent (UCA) response. Next to its better suppression of near-field artifacts, tissue SHI is expected to improve axial and lateral resolutions resulting in clearer images than second harmonic imaging. When SHI is used in combination with UCAs, a better contrast-to-tissue ratio can be obtained. The use of SHI implies a large dynamic range and requires a sufficiently sensitive array over a frequency range from the transmission frequency up to its fifth harmonic (bandwidth $>$ 130%). In this paper, we present the characteristics and performance of a new interleaved dual frequency array built chiefly for SHI. We report the rationale behind the design choice, frequencies, aperture and piezomaterials used. The array is efficient both in transmission and reception with well behaved transfer functions and a combined -6 dB bandwidth of 144%. Moreover, there is virtually no contamination of the harmonic components by spurious transducer transmission, due to low element-to-element crosstalk ($<$ 30 dB) and a low transmission efficiency of the odd harmonics ($<$ 46 dB). The interleaved array presented in this article possesses ideal characteristics for SHI, and is suitable for other methods like second harmonic, subharmonic and second order ultrasound field (SURF) imaging.

[1]From Paul L.M.J. van Neer, Guillaume Matte, Mikhail G. Danilouchkine, Christian Prins, Franc van den Adel, Nico de Jong, 'Super harmonic imaging: development of an interleaved phased array transducer', IEEE Trans. Ultrason. Ferroelectr. Freq. Control, 2010, 57(2):455-468.

8.1 Introduction

A decade ago it became possible to improve ultrasound image quality by exploiting the nonlinear nature of wave propagation. The technique is called tissue second harmonic imaging and is based on the selective imaging of the second harmonic frequency. Compared to fundamental imaging second harmonic imaging has a higher resolution and is less sensitive to near-field artifacts, clutter and off-axis scatterers (Bouakaz and de Jong, 2003). As a result second harmonic imaging has been the standard in tissue imaging for several years. Nonlinear effects are not just exploited in tissue imaging. In fact the selective imaging of the second harmonic band was originally intended for ultrasound contrast agent (UCA) enhanced imaging (Bouakaz and de Jong, 2003). Used in this way the technique improved the contrast-to-tissue ratio (CTR) compared to fundamental imaging, thus enabling better imaging of blood flow (Bouakaz et al., 2002).
Several other methods have been proposed to exploit the nonlinear behavior of UCAs. A new and promising imaging modality for the nondestructive imaging of UCAs is subharmonic imaging (Shi and Forsberg, 2000; Chomas et al., 2002; Forsberg et al., 2004; Biagi et al., 2007). This imaging method is primarily intended to estimate blood perfusion by accurately quantifying the refresh of UCAs in a vascular bed after UCA destruction (Chomas et al., 2002). The principal advantage of UCA subharmonic imaging compared to UCA (second) harmonic imaging is that subharmonic signals are not generated in tissue at diagnostic pressures and frequencies maintaining a high CTR (Forsberg et al., 2004). The optimal subharmonic imaging technique described in literature insonifies the UCA using a low pressure excitation pulse - but still higher than the UCA pressure threshold for subharmonics - at twice the UCAs resonance frequency (Chomas et al., 2002).
Another promising UCA imaging modality utilizing nonlinear UCA behavior is second order ultrasound field (SURF) imaging or radial modulation imaging. In this method a low frequency low pressure pulse is transmitted (0.5 - 2 MHz), which manipulates the contrast agent around resonance by altering its scattering properties. In conjunction with the low frequency pulse a high frequency pulse (3 - 14 MHz) is transmitted to detect the changes in scattering (Shariff et al., 2006; Masoy et al., 2008). The main advantage of this imaging technique is that it allows for UCA detection at clinically high frequencies - higher frequencies than the resonant frequencies of the UCAs. Example *in-vivo* B-mode results were presented by (Masoy et al., 2008), who obtained contrast enhanced images of pig kidneys with a CTR of 15 - 40 dB.
Recently, a new imaging modality dubbed 'superharmonic imaging' (SHI) was proposed. The modality improves on second harmonic imaging by combining the third to fifth harmonics arising from nonlinear wave propagation or contrast-agent response (Bouakaz et al., 2002). Tissue SHI efficiently suppresses near-field artifacts, reverberations, and off-axis artifacts in addition to the enhanced lateral and axial resolution. The resulting images showed more details than those produced by second harmonic imaging (Bouakaz and de Jong, 2003). Recently, this was confirmed by simulations and *in-vitro* experiments conducted by Ma et al. (2006). SHI is also promising for UCA enhanced imaging. It has been demonstrated by Bouakaz et al. (2002) that the CTR increases as a function of the order of the harmonic frequency. Thus, SHI in combination with contrast agents produces a higher CTR than second harmonic imaging, while at the same time minimizing shadowing effects. Until

now, imaging with harmonics higher than the second one has been hampered by signal-to-noise ratio (SNR) issues, due to the progressively lower energy content of these harmonics. A traditional phased array design is inadequate for the implementation of the above imaging modalities. In the case of SHI the principle of transmission at the fundamental and receiving the third to fifth harmonic implies a -6 dB bandwidth $> 130\%$, a considerably larger bandwidth than that achievable with a conventional array configuration. Although -6 dB bandwidths as high as 140% are reported in the literature for single element transducers made from a 1-3 single crystal-epoxy composite, the actual peak bandwidth at -6 dB reported for single crystal arrays are in the order of 95% (Rehrig et al., 2003; Zipparo et al., 2004; Li et al., 2007) - not sufficient for SHI. Next to the bandwidth demand, the implementation of SHI requires an array to be efficient in transmission - to generate significant higher harmonics - and sensitive in reception - the reflected harmonic energy will be low.

This paper presents the rationale behind, construction of and performance measurements of a very broadband array primarily intended for both tissue and UCA enhanced cardiac medical imaging. The array is mainly optimized for SHI, but is also capable of regular second harmonic imaging. Furthermore, the suitability of the array for UCA techniques, such as subharmonic and SURF imaging, is discussed.

8.2 Materials and methods

8.2.1 Requirements

The requirements for the new array can be listed as follows:

1. Very broad bandwidth. For SHI, the principle of transmission at the fundamental and receiving the third to fifth harmonic implies a -6 dB bandwidth $> 130\%$.

2. High efficiency in transmission. For optimal image quality in the cases of tissue SHI and second harmonic imaging the peak pressure at focus should be as close as possible to the 1.9 MI limit allowed by the FDA.

3. High sensitivity in reception. In the case of the imaging modalities based on harmonics the amplitude of the reflected signal at higher harmonic frequencies will be low for both nonlinear propagation and UCA produced harmonics. Noise levels of ultrasound imaging systems are generally in the order of 10 μV_{rms}, thus a receive sensitivity of $\sim$10 μV/Pa is required.

4. Have a good acoustic field with grating lobes of acceptably low amplitude. Cobbold (2007) states that grating lobe levels should be 30 - 40 dB below the central lobe response at the receiving frequency of interest.

The main application of the array will be echocardiography, which adds the following extra requirements:

1. A small enough footprint to facilitate imaging through the ribs. Generally cardiac transducers have a footprint of about 15 mm x 15 mm.

2. Be optimized for an imaging depth of 0.5-15 cm.

8.2.2 Design options

Several designs meet the bandwidth requirement for SHI (Hossack and Auld, 1993; Hossack et al., 2000; Bouakaz et al., 2002; Zhou and Hossack, 2002; Bouakaz et al., 2004b; Mills, 2004; Zhou et al., 2005; Akiyama et al., 2006; Yaralioglu et al., 2006; Ferin et al., 2007). In the following paragraphs we list these alternatives and consider their advantages and disadvantages.
The first option is to stack two active layers (usually PZT or a PZT composite) with different resonance frequencies on top of each other for each array element (Hossack and Auld, 1993; Hossack et al., 2000; Zhou and Hossack, 2002; Akiyama et al., 2006). Advantages of this configuration are a limited total footprint of the array and ease of manufacture. Its main disadvantage is the electromechanical coupling between both active layers. This causes troughs in the frequency response of the transducer, if the resonance frequencies of both active elements are close to each other. Hossack and Auld (1993) presented a study on a transducer design consisting of a piezoelectric layer and an active (piezoelectric) matching layer. A proper adjustment of the phase response of the active matching layer and the subsequent addition of the responses of both active layers yielded a well behaved broadband transfer function. Zhou and Hossack (2002) showed in a finite element analysis study that the transfer function of a dual active layer transducer can be further improved with matched filtering. However, fairly complicated electronics (Hossack and Auld, 1993; Hossack et al., 2000) and knowledge of the phase transfer function of each element are required for successful implementation. Also, the choice of matching layer characteristics is not straightforward, as the active layer used in transmission has a significantly different resonance frequency than the layer used in reception.
A second alternative was reported by Akiyama et al. (2006). They presented an ultra broadband transducer used in a mechanical sector scanner. The design features a PZT layer for transmission and a PVDF layer for reception. The PVDF layer functions well below its resonance frequency, to guarantee electromechanical decoupling. However, the absolute sensitivity of PVDF applied in this manner is generally low.
The third option is a horizontal stack topology, where two low frequency arrays are positioned laterally on both sides of a central high frequency array (Ferin et al., 2007). The main advantage of this design is that the initial performance of each subarray is not modified. Disadvantages are the limited overlap of both acoustic beams and the increased footprint in the elevation dimension relative to a regular array design.
The fourth alternative is an interleaved configuration as proposed by Bouakaz et al. (2002, 2004b), where the even elements are used in transmission and the odd elements are used in reception. The main advantages of this design are the full overlap of the transmission and receive beams and a small footprint. Disadvantages are its relatively complicated manufacture and its intrinsically reduced sensitivity as only half the elements are used in reception - necessary to keep the footprint size limited.

A final option is capacitive micro machined ultrasound transducers (cMUT's). cMUT transducers with -6 dB bandwidths of 130% have been reported in literature (Mills, 2004; Zhou et al., 2005). However, cMUTs are held back by challenges such as achieving high output pressures (Yaralioglu et al., 2006), their inherent nonlinearity and relatively high crosstalk (Zhou et al., 2005). One of the most important difficulties of cMUT technology is the contradicting requirement regarding the gap height to get both a high sensitivity in reception and a high output pressure in transmission (Yaralioglu et al., 2006). Mills (2004) reported pulse-echo gains of cMUT transducers, which were between 10 and 20 dB less than a comparative PZT transducer.

After careful consideration of the advantages and disadvantages of each option the interleaved design was chosen. Next to obvious advantages, such as fully overlapping beams and a low foot print, there are no fundamental problems associated with this design. There is no direct electromechanical coupling between the elements, because the acoustic stacks for transmission and reception, including the associated circuitry, are fully separated. Also, the use of piezoceramics - PZT, single crystal or piezocomposites - ensures operation in the linear regime, even at high output pressures. In this way any transmission of harmonics due to device nonlinearity, which considerably reduces the dynamic range of the imaging system, can be prevented. This fact is particularly important for SHI, as the level of higher harmonics generated by either nonlinear propagation or UCA response will be low.
The design does have an intrinsically reduced sensitivity in reception. However, this is alleviated by the fact that - like all designs with completely separate active elements for transmission and reception - each element can be acoustically matched and electrically tuned for its specific role.

8.2.3 Frequency

After selecting a design the transmission frequency has to be chosen. This frequency influences other characteristics of the array, such as the receive frequency, layer thicknesses and element dimensions.
For fundamental imaging the transmission frequency used in clinical echocardiography is $\sim$3.5 MHz (Kasprzak et al., 1999). For both tissue and UCA enhanced second harmonic imaging the fundamental transmission frequency used in clinical echocardiography ranges between 1.6 - 1.8 MHz (Kasprzak et al., 1999). It is expected that for tissue SHI the transmission frequencies will be lower still. The optimal transmission frequency for tissue SHI is intrinsically dependent on the level of the third to fifth harmonics at distances typical for cardiac imaging. Consequently, the level of these harmonics is determined by two competing phenomena - nonlinear propagation and attenuation. In order to find the optimal transmission frequency for SHI we used a combination of nonlinear and linear simulations. Forward propagation was simulated using the Burgers equation, which describes the propagation of finite-amplitude plane progressive waves. The solution was found as a complex Fourier series using the iterative computation scheme given by Cobbold (2007). The back propagation was assumed to be linear. The acoustic nonlinearity parameter (B/A) was taken to be 5.8 and the attenuation was modeled as $\alpha = a.f^b$ with a = 0.52 dB.cm^{-1}.MHz^{-b} and $b = 1$. Furthermore, a density of 1060 kg/m^3 and an acoustic

wavespeed of 1529 m/s were used. These values were reported for human fetal or dog cardiac tissue (Duck, 1990). Calculations were performed for transmit frequencies between 0.5 - 1.8 MHz. The initial MI was kept at 1.5. The imaging depth was taken between 0.5 - 15 cm. The intensities of the first five harmonics and the superharmonic versus the transmission frequency are shown in Fig. 8.1 for an imaging depth of 10 cm. The simulations showed that the frequency giving the optimal compromise between the rapidity of the build-up of harmonics at short distances and the attenuation of the harmonics at large distances was $\sim$1 MHz. This frequency was chosen as the resonance frequency of the low frequency subarray. Correspondingly, a resonance frequency of $\sim$4 MHz was opted for the high frequency subarray.

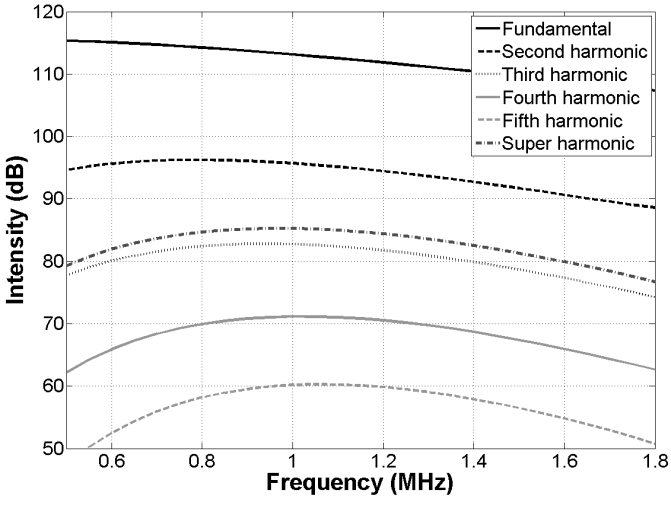

Figure 8.1: The intensity of the first five harmonics and the superharmonic versus the transmission frequency at an image depth of 10 cm. The intensity values are relative to 1 Pa. The forward propagation was modeled using the Burgers equation, the back propagation was assumed to be linear. The acoustic nonlinearity parameter (B/A) was 5.8 and the attenuation was modeled as $\alpha = a.f^b$ with a = 0.52 dB.cm^{-1}.MHz^{-b} and $b = 1$. The density was 1060 kg/m^3 and the acoustic wavespeed 1529 m/s. The initial MI was 1.5.

The optimal frequency for tissue SHI generally agrees with the requirements for UCA enhanced SHI, as the UCAs used for cardiac applications are resonant at 1 - 5 MHz (Dawson et al., 1999). More specifically, Sonevue® and Definity®/Luminity® have reported resonance frequencies in the range of 1.5 - 3.1 MHz (Masoy et al., 2008).

8.2.4 Element geometry

The next feature to be established is the geometry of the two subarrays. The number and size of the array elements has a profound effect on the acoustic wave field, but also affects

the ease of manufacture.

Elevation dimension

The elevation dimension of the low frequency subarray was chosen to be 16 mm. This value was small enough for the ultrasound beam to pass unimpeded between the ribs, but is still as high as possible to optimize the energy transferred into the medium. Due to the method used to interleave the elements, the elevation size of the high frequency subarray was 13 mm.

Lateral dimension: kerf/pitch

The spacing between the elements of the final interleaved array is a compromise between the desire to waste as little as possible of the footprint real estate and the ability to reliably merge both subarrays - a critical step in the production process. If the elements of improperly merged subarrays touch each other, the element transmit efficiency and receive sensitivity are suboptimal. Moreover, crosstalk levels are increased. Practical experience showed that an inter-element spacing of 50 μm was optimal.

The width of the elements for both subarrays was the same in order to facilitate the array production process. The principal compromise for the lateral element size/pitch is the desire to have an as high as possible pitch-to-kerf ratio, whilst still having acceptable grating lobe levels at the highest intended transmitting frequency for the tissue imaging modalities (which is 1.6 - 1.8 MHz for tissue second harmonic imaging). The effects of grating lobes are less important for UCA imaging, as UCAs exhibit a very nonlinear pressure dependent response at pressures above 50 - 100 kPa (Emmer, 2009). The FIELD II simulation program (Jensen and Svendsen, 1992; Jensen, 1996) was used to evaluate the peak intensities of the fundamental grating lobe relative to the main beam versus the subarray pitch at transmission frequencies of 1.7 - 1.8 MHz and a steering angle of 35°. The element elevation size was 13 mm and the geometric elevation focus was 6 cm. No lateral focus was applied. The simulations were performed using 3 cycle sine bursts, which were Gaussian apodized. The propagation medium was assumed to be lossless. The peak intensities of the second harmonic grating lobe relative to the main second harmonic beam were estimated from the fundamental levels using the Fubini solution for weakly shocked plane waves produced by a monofrequency source (Cobbold, 2007). A graph detailing the peak intensities of the simulated grating lobe versus the subarray pitch is shown in Fig. 8.2. Note that the subarray pitch was twice the element width plus twice the 50 μm element spacing of the final interleaved array. A subarray pitch of 0.5 mm yields a lateral element size of 0.2 mm (Fig. 8.2). For this chosen pitch the second harmonic levels in the grating lobe were $\sim$-45 dB at 1.7 MHz, $\sim$-38 dB at 1.75 MHz and $\sim$-33 dB at 1.8 MHz relative to the second harmonic of the main bundle. The positions of the grating lobes in these cases were -83°, -79° and -77° respectively. The obtained characteristics match the requirements for grating lobe levels, which should be at least 30 - 40 dB below the central lobe response (Cobbold, 2007).

To keep the total footprint size practical, the final interleaved array consisted of a total

of 88 elements, 44 of which were used in transmission and 44 were used in reception. This yielded a total footprint of 16 mm x 22 mm.

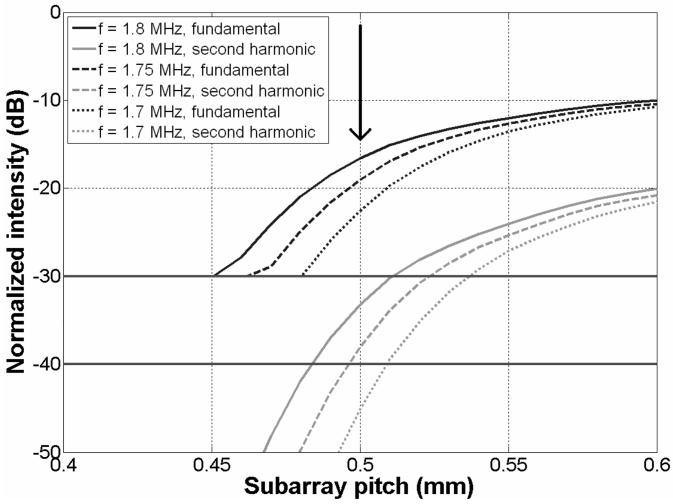

Figure 8.2: The relation between the fundamental peak grating lobe intensity versus the subarray pitch, simulated using Field II. The grating lobe intensity was normalized by the main beam peak intensity. Note that the subarray pitch was double the element width plus double the 50 μm element spacing of the interleaved array. The peak second harmonic intensity of the grating lobe was estimated from the fundamental using the Fubini solution. The simulations were performed using Gaussian apodized 3 cycle sine bursts at center frequencies of 1.7, 1.75 and 1.8 MHz. The element elevation size was 13 mm and the geometric elevation focus was 6 cm. The beam was unfocused in the lateral direction and steered 35°, the propagation medium was assumed to be lossless. The horizontal lines are at the intensity levels at which the grating lobe levels are low enough for high quality imaging (Cobbold, 2007). The subarray pitch used in the final interleaved array is indicated by the black arrow.

8.2.5 Choice of piezomaterial

To optimize the receive sensitivity research was conducted to select the optimal piezomaterial for an array with the selected frequency and aperture. After the piezomaterial was selected, the matching and backing materials were chosen in order to optimize each subarray for bandwidth.

A preselection of commercially available piezomaterials was made by careful consideration of their datasheet properties and by using the KLM model (Leedom et al., 1971). Of these selected piezomaterials custom arrays (18 elements, element size 13 mm x 0.2 mm, pitch 0.5 mm, resonance frequencies 3 - 4 MHz, backing 5.3 MRayl, no matching layers) were constructed in order to compare their performance in both transmission and reception. Columns 1 and 2 of Table 8.1 provide a summary of custom array characteristics. The

Table 8.1: Custom array and final interleaved array characteristics

	Custom array	Interleaved array low frequency subarray	Interleaved array high frequency subarray
Nr. of elements	18	44	44
Resonance frequency [MHz]	3 - 4	1	3.7
Element size [mm x mm]	13 x 0.2	16 x 0.2	13 x 0.2
Pitch [mm]	0.5	0.5	0.5
Piezomaterial	Various	CTS 3203HD	CTS 3203HD
Matching layers	-	1	2
Backing [MRayl]	5.3	3.2	3.2
Lens	-	Elevation, focus 6 cm	Elevation, focus 6 cm

arrays with large element variance were repoled in an attempt to improve performance. A voltage of 300 V DC was applied over the element electrodes for about 30 minutes. This voltage was chosen to prevent over-poling of single crystal material and corresponds to an electric field strength of $\sim$700 V/mm.

The performance of the custom arrays was evaluated in terms of:

1. the maximal peak of the receive transfer function (shortened in this article as sensitivity) and the maximal peak of the transmit transfer function (shortened in this article as efficiency) of each element.

2. The SNR. The SNR was determined for continuous ultrasound at the element's resonance frequency and a pressure of 1 Pa.

Table 8.2 summarizes the performance results of all 8 custom arrays. We considered the essential characteristics of each array, such as the resonance frequency, the mean and standard deviation of the sensitivity and efficiency, the -6 dB bandwidth, the impedance and the SNR while receiving a 1 Pa pressure wave.

The custom array constructed of CTS 3203HD PZT was the most sensitive in our study and this piezomaterial was used for the interleaved array.

A few remarks have to be made. In this study no correction for differences in piezomaterial acoustic impedance was made, as preliminary calculations indicated that the correction factors were small compared to actual sensitivity differences - even when comparing composite piezomaterial to PZT. Also, the sensitivity as expressed in μV/Pa is influenced by the resonance frequency of each array element. The resonance frequencies of the undiced slabs of piezomaterial lay between 4.0 to 4.9 MHz. However, KLM model simulations established that the effect of variation of the resonance frequency was less than 1 dB. Therefore, no correction was made for this effect.

The custom arrays based on composite piezomaterial had a somewhat low sensitivity. A retrospective investigation using an optical microscope showed damaged elements due to

the dicing process. The arrays built using single crystal material had low mean sensitivities with high standard deviations and similar -6 dB bandwidths compared to PZT based arrays - even after repoling. This was different from earlier studies, in which single crystal material was found to be superior in performance to PZT (Rehrig et al., 2003; Rhim et al., 2005; Li et al., 2007; Rhim and Jung, 2007). Part of the explanation is that the array element height-to-width ratio was ∼2:1, which is not ideal for 33-mode vibrations. Also, the effects may be related to dicing difficulties. The custom arrays were diced using a diamond saw. A visual inspection using a microscope of the array elements showed that small chips had broken off the brittle single crystal material during dicing. Temperature dependent degradation of the single crystal properties could not have been the cause, as the custom array production process takes place at low temperatures (below 70°C).

8.3 Array prototype

The transducer consisted of two interleaved subarrays with 88 transducer elements in total. The low and high frequency elements were mechanically separated and electrically decoupled. That enabled the optimization of each element (eg., matching layers, electrical tuning) for its specific role. Both the low and high frequency subarrays were built using CTS 3203HD piezomaterial. The subarray optimized for transmission had a resonance frequency of 1.0 MHz and consisted of 44 elements. The low frequency elements had a single matching layer and a backing of 3.2 MRayl. The low frequency element size was 16 mm x 0.2 mm and the subarray had a pitch of 0.5 mm. The subarray optimized for reception had a resonance frequency of 3.7 MHz and was composed of 44 elements. The high frequency elements had two matching layers on the front and a backing with an impedance of 3.2 MRayl. The high frequency element size was 13 mm x 0.2 mm and the subarray had a pitch of 0.5 mm. A lens with a geometric elevation focus at an axial distance of 6 cm was attached to the final interleaved transducer. The total footprint of the interleaved transducer was 16 mm x 22 mm. The electrical tuning of the final interleaved transducer to the imaging machine was optimized for SHI. A coil was mounted in series with each element of the low frequency subarray and a coil was fitted in parallel to each element of the high frequency subarray.
Each subarray was constructed separately and cut with a diamond saw. The kerf between the elements was 0.3 mm for both subarrays. After cutting of the two subarrays, special tooling was used to merge the two subarrays, ensuring that the adjacent elements did not touch each other and aligning the front of both subarrays on the same plane.
The final interleaved transducer is shown schematically in Fig. 8.3. A summary of its characteristics is given in columns 3 and 4 of Table 8.1. The transducer was manufactured by Oldelft Ultrasound, Delft, the Netherlands.

8.4 Acoustic characterization

The final interleaved array transducer was characterized by measuring its efficiency in transmission as well as its sensitivity in reception. For that, we determine the transmit

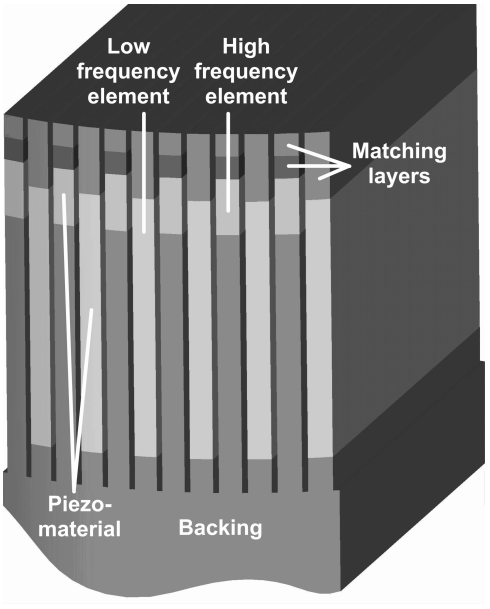

Figure 8.3: Schematic showing the various parts of the final interleaved array transducer.

and receive transfer functions of all the elements. Also, lateral and elevation beam profiles were measured at high pressure ultrasound. Finally, the array's electrical and mechanical crosstalk was measured.

8.4.1 Transfer functions

Definitions

The transducer transmit transfer function ($T_t(\omega)$) is defined as

$$T_t(\omega) = \frac{|p_0(\omega)|}{|V_T(\omega)|}, \tag{8.1}$$

with $p_0(\omega)$ the pressure at the transducer surface and $V_T(\omega)$ the voltage over the transducer electrodes.
The receive transfer function $T_r(\omega)$) is defined as

$$T_r(\omega) = \frac{|V_{T-open}(\omega)|}{|p_a(\omega)|}, \tag{8.2}$$

with $V_{T-open}(\omega)$ the open circuit voltage produced by the transducer and $p_a(\omega)$ the pressure received on the transducer surface.

The transfer functions are calculated using the methods described by van Neer et al. (2007).

Setup

The experimental setup consisted of a water-filled tank. The array was attached to its sidewall. A calibrated source was mounted in a holder controlled by an xyz-system (see Fig. 8.4a). The source was a flat circular piston transducer (V310, Panametrics, Waltham, MA, USA, 2.25 MHz center frequency, diameter 6.35 mm).

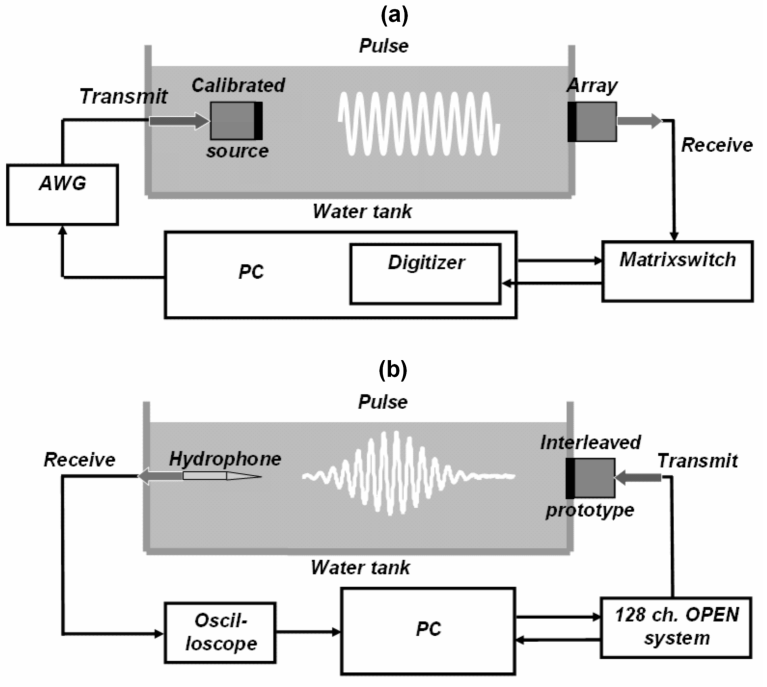

Figure 8.4: a) Setup to obtain transfer functions and SNR measurements. b) Setup to obtain beam profiles and crosstalk measurements.

For the transfer function measurements the source was excited by an arbitrary waveform generator (33250A, Agilent, Loveland, Colorado), which produced 600 cycle sine bursts with an amplitude of 5 V. Each array element was connected to a computer controlled matrix switch (custom built). The received signal was digitized by a digitizer card (DP235, Acqiris, Geneva, Switzerland) at a sampling rate of 100 MHz. The waveform generator was connected to a computer through GPIB, and the matrix switch was controlled using an Ethernet connection.

The acoustic pressures were low, so nonlinear propagation could be disregarded. Also attenuation was neglected, as the propagation distance in water was only $\sim$20 cm. The exact diffraction correction function posted by Goldstein et al. (1998) was used to calculate on-axis pressures from the pressure produced at the source's surface. The elements of the high frequency subarray were 13 mm long in the elevation direction. The spatial averaging cor-

rection factor ($S(\omega)$) was calculated by simulating the complete wave over the elevation range (-6.5 to 6.5 mm) produced by the calibrated source at the axial distance ($\sim$23 cm) using Field II (Jensen and Svendsen, 1992; Jensen, 1996) and calculating the mean pressure. $S(\omega)$ was recalculated for the elements of the low frequency subarray, as their size was 16 mm x 0.2 mm.

8.4.2 Beam profiles and crosstalk measurements

Beam profiles of the final interleaved array transducer were measured with a hydrophone (diameter 0.2 mm, Precision Acoustics, Dorchester, UK) mounted in a xyz-system (see Fig. 8.4b). The elements of the low frequency subarray were excited by an eight cycle Gaussian apodized sine burst at 1 MHz and amplitude of 30 V, which was produced by a multi channel programmable ultrasound system (OPEN system, Lecoeur Electronique, Chuelles, France, first reported by Vignon et al. (2005)). The signals received by the hydrophone were digitized by an oscilloscope (9400A, Lecroy, Geneva, Switzerland) with a sampling frequency of 100 MHz and transferred to a computer for further processing.
The electrical and mechanical crosstalk was measured by exciting an element of either the low frequency or the high frequency subarray by a 3 cycle Gaussian apodized sine burst at the element's resonance with an amplitude of 12 V_{pp}. The responses of all the elements were measured and recalculated for the open circuit case (V_{resp}^{open}). The crosstalk was defined as:

$$Crosstalk = 20\log(\frac{V_{resp}^{open}}{V_e}) \tag{8.3}$$

where V_e is the excitation voltage, which is measured over the electrodes of the excited element.

8.5 Results: interleaved array characteristics

8.5.1 Low frequency subarray

The transmit and receive transfer functions of both the low and high frequency subarrays are shown in Fig. 8.5. The average efficiency (defined in this article as the maximum of the transmit transfer function) of the elements of the low frequency subarray was $\sim$22 kPa/V (Fig. 8.5a). The average -10 dB bandwidth was 86%. After electrical tuning the average efficiency increased to $\sim$98 kPa/V (Fig. 8.5a). The -10 dB bandwidth was lowered from 86% to 55%. The transmit transfer function of the tuned elements shows that the efficiency of the third and fifth harmonics was respectively $\sim$46 dB and $\sim$55 dB below that of the fundamental.
Fig. 8.6 details the variation in element behavior by showing the normalized efficiency of the elements at resonance. The standard deviation of the normalized efficiency at resonance of the low frequency subarray was $\sim$1.9 dB (Fig. 8.6). The peak negative pressure reached $\sim$1.6 MPa at a focal distance of 6 cm, if the elements of the low frequency subarray were excited with a 2 cycle 1 MHz Gaussian apodized sine burst of amplitude 120 V_{pp}. The

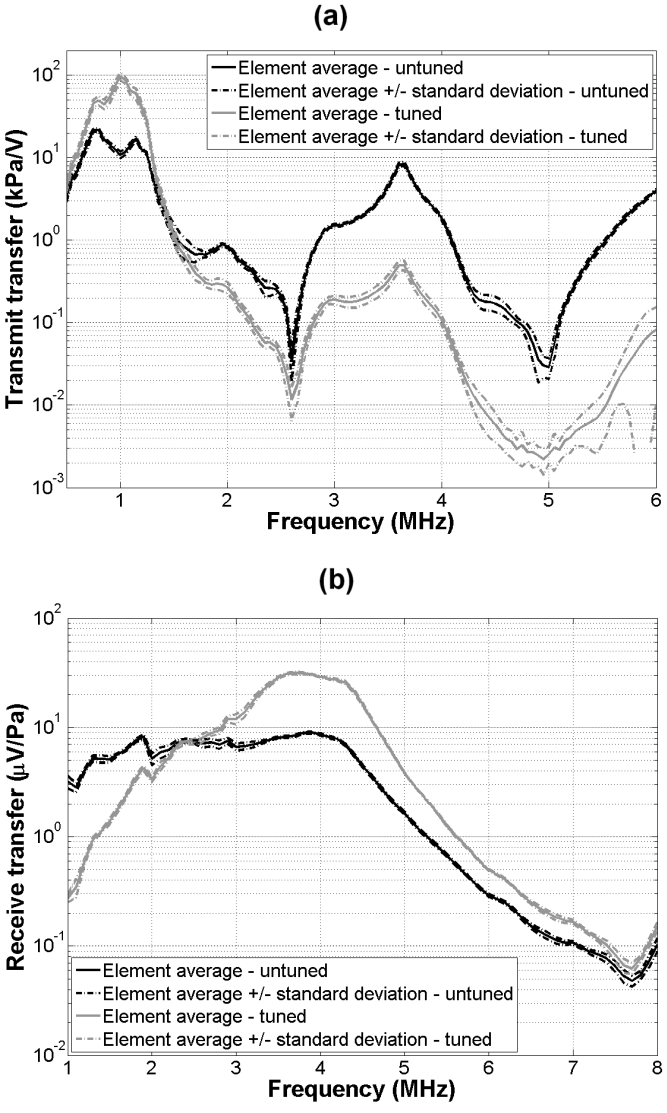

Figure 8.5: a) Transmit transfer function of the low frequency subarray, the mean and standard deviations are based on measurements of 8 elements. b) Receive transfer function of the high frequency subarray, the mean and standard deviations are based on measurements of 8 elements.

peak negative pressure reached 2.0 MPa, if a similar excitation signal 3 cycles in length was applied.

In Fig. 8.7 the normalized time pulse at focus is displayed, which was produced by exciting

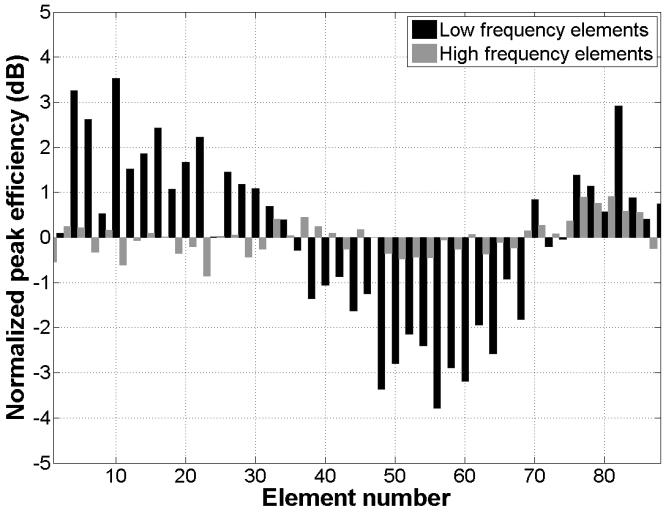

Figure 8.6: The element variation of both subarrays by showing the efficiency (defined as the maximum of the transmit transfer function). The efficiency was normalized to the mean efficiency of either the low or high frequency subarray.

the elements of the low frequency subarray with a 2 cycle 1 MHz Gaussian apodized sine burst of amplitude 120 V_{pp}. The lateral focus of 6 cm was equal to the geometric elevation focus. The top panels show the fundamental and third harmonic components, the lower panels detail the fourth and fifth harmonics. The fundamental -6 dB pressure pulse length was $\sim$2.9 μs at focus, and it decreased to 1.7 μs, 1.4 μs and 1.3 μs for the third, fourth and fifth harmonics respectively. In Fig. 8.8a the lateral beam profiles of the fundamental up to the fifth harmonic recorded at a lateral focal distance of 6 cm (is equal to the geometric elevation focus) are presented. The lateral -6 dB beam width was 4.6 mm, 2.6 mm, 2.1 mm, 1.7 mm and 1.5 mm for the fundamental, second, third, fourth and fifth harmonic respectively. In Fig. 8.8b lateral beam profiles of the second, third and superharmonic components are displayed. The superharmonic component is defined as the combination of the third, fourth and fifth harmonics. The -6 dB beam width of the superharmonic was 1.9 mm.

8.5.2 High frequency subarray

The elements of the high frequency subarray had an average sensitivity (defined in this article as the maximum of the receive transfer function) of $\sim$9 μV/Pa, with a -10 dB bandwidth of 93% (Fig. 8.5b). After electrical tuning the average sensitivity increased to $\sim$31 μV/Pa. The -10 dB bandwidth of the elements was lowered from 93% to 50%. The standard deviation of the normalized efficiency at resonance of the high frequency part was $\sim$0.4 dB (Fig. 8.6). In transmission the untuned elements of the high frequency subarray had an

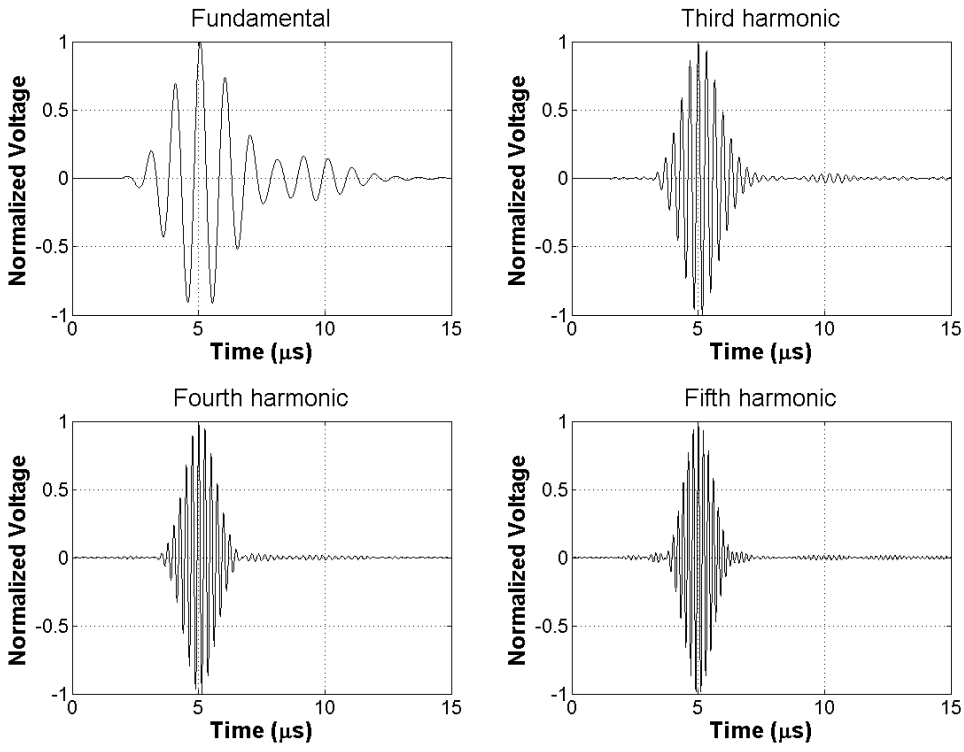

Figure 8.7: The normalized fundamental, third, fourth and fifth harmonic components of a pressure signal recorded at focus. The lateral focus of 6 cm was equal to the geometric elevation focus. The elements of the low frequency subarray were excited using a 2 cycle Gaussian apodized sine burst at 1 MHz with amplitude 120 V_{pp}.

average efficiency of $\sim$20 kPa/V.

8.5.3 Crosstalk

The inter-element crosstalk is shown in Fig. 8.9. Fig. 8.9a displays the crosstalk versus the element position relative to the excited element. The peak crosstalk amplitude was normalized by the excitation voltage. Fig. 8.9b shows the corresponding time delay. The mechanical crosstalk between the elements of the low frequency subarray ranged from -53 to -31 dB relative to the transmitted signal, depending on the distance between the active element and the element of interest (Fig. 8.9a). Notice the local minimum in the mechanical crosstalk 3 elements away from the excited element; this was caused by diffraction effects in the backing. The large standard deviations of the 4 elements closest to the excited element in Figs. 8.9a and 8.9b were caused by overlap and interference of electrical and mechanical crosstalk. The large standard deviation in time delay of the excited element in

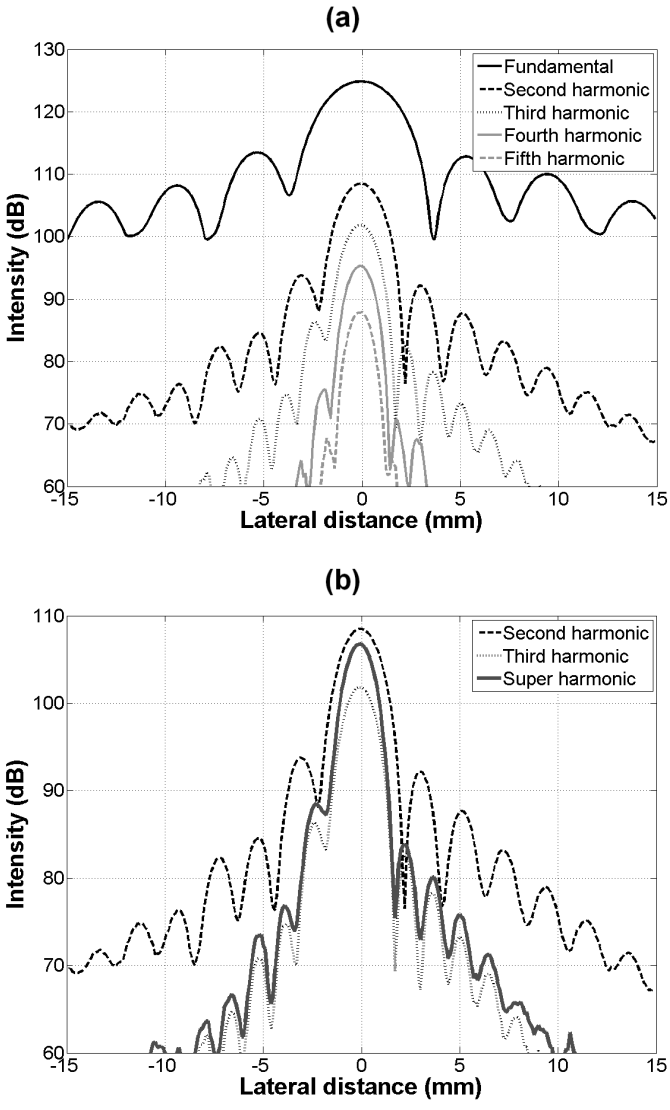

Figure 8.8: a) Lateral beam profiles of the fundamental up to the fifth harmonic at focus. The lateral focus of 6 cm was equal to the geometric elevation focus. The intensity values are relative to 1 Pa. The elements of the low frequency subarray were excited using an eight cycle Gaussian apodized sine burst at 1 MHz with amplitude 60 V_{pp}. b) Zoomed lateral beam profiles of the second, third and superharmonic component at focus. The lateral focus of 6 cm was equal to the geometric elevation focus.

Fig. 8.9b was caused by clipping of the receive circuitry. The mean element-to-element travel distance of the pressure wave was 0.8 mm, as was calculated from the mean relative time delay of 0.47 μs between the peak values of the mechanical crosstalk of each element (Fig. 8.9b). The crosstalk between the elements of the low frequency subarray was not significant ($<$ -60 dB) for elements further away than 10, except for elements at a distance of 16. In this case the crosstalk was $\sim$-37 dB with a standard deviation of 5.0 dB compared to the excitation signal. The time delay between this element and the excited element was 0 μs implying purely electrical crosstalk. This crosstalk was explained by the wiring configuration.
Peak crosstalk from the low to the high frequency elements was $\sim$-60 dB relative to the transmitted signal with a standard deviation of 3.7 dB.

8.6 Discussion

8.6.1 Performance of the interleaved array for SHI

The frequency response of the final interleaved array is shown in Fig. 8.10. Its combined -6 dB bandwidth exceeds 144%, whereas traditional arrays generally have 80% - 90% bandwidth. The graph summarizes the key characteristics of the implemented concept for the interleaved array in terms of bandwidth and efficiency.
The interleaved array consists of two separate subarrays, which are merged during manufacture. This is a critical step and improperly merged arrays suffer from high crosstalk levels.

The low frequency subarray used in transmission

The resolution of a B-mode picture is determined by such transmission beam characteristics as the length of the imaging pulse and the bundle profile. The effect of imaging schemes on the (axial) resolution is not treated, as it is considered to be out of the scope of this article. The axial resolution is related to the time duration of the pressure pulses produced by the transducer (Fig. 8.7). Two main observations can be made. Firstly, the pulse lengths of the third, fourth and fifth harmonic are progressively shorter than the one of the fundamental. Secondly, the time trace of the fundamental is relatively long. This stems from the rather narrow bandwidth of the transmit transfer function of the tuned low frequency subarray (55% at -10 dB). Because of the intrinsic relation between the length of the fundamental pulse and the axial image resolution, it is highly desirable to increase the bandwidth. This goal can be achieved by either electrically tuning the low frequency subarray off resonance or by use of a multiple resonance circuit. Both methods exchange transmit efficiency for bandwidth, resulting in a lower peak pressure at focus - and, consequently, less energy in the higher harmonics - at the same excitation voltage. However, with the limited output voltage of our imaging system and a short excitation pulse of 2 cycles, the final interleaved array produced a maximum peak negative pressure of 1.6 MPa at focus. As this is below the MI limit of 1.9, the electrical tuning was not optimized further for bandwidth.
The lateral resolution is best investigated using lateral beam profiles (Fig. 8.8a). The pro-

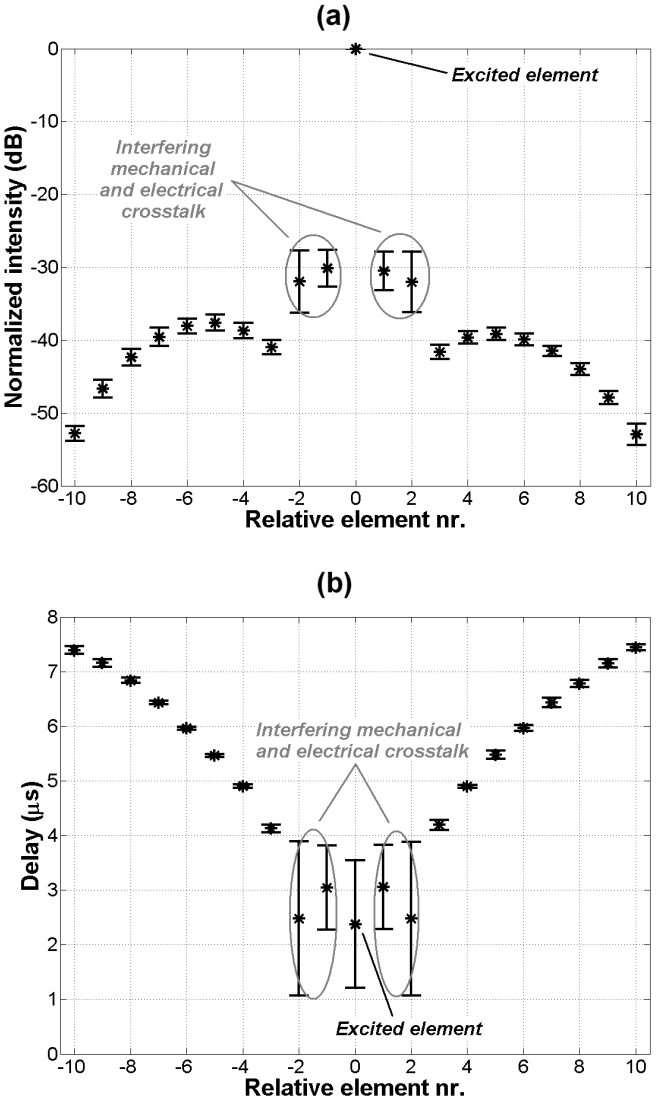

Figure 8.9: a) Peak element-to-element mechanical crosstalk of the low frequency subarray relative to the excited element. The average and standard deviation are based on measurements of 9 elements. b) Time delay of peak mechanical crosstalk of the low frequency subarray relative to the excited element. The average and standard deviation are based on measurements of 9 elements.

files show the progressively smaller -6 dB beam width of the higher harmonics. The most striking is the superharmonic component shown in Fig. 8.8b: its on-axis intensity is al-

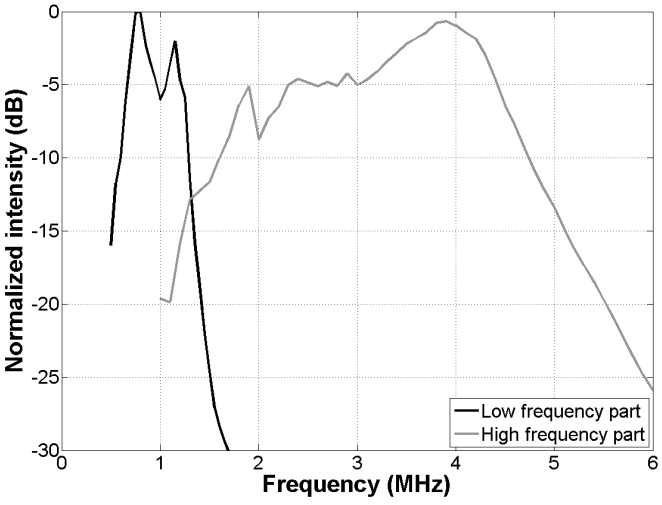

Figure 8.10: The transmission transfer functions of the untuned low and high frequency subarrays combined in order to illustrate the interleaved array concept. The transfer functions are normalized by the peak transmission transfer of the low frequency subarray.

most equal to the second harmonic, but it has an off-axis energy distribution similar to the third harmonic. This decreases the so called haze in an image and by that improves the 2D image quality. The -6 dB superharmonic beam width is 59% smaller than the fundamental and 37% smaller than the second harmonic beam width. Similar values were reported by Bouakaz and de Jong (2003), who found the -6 dB beam width of the superharmonic component to be 50% smaller than the fundamental and 30% smaller than the second harmonic in nonlinear wave propagation simulations of circular symmetric transducers. However, this comparison is not completely suitable. It would be more appropriate to compare superharmonic beam profiles to the optimal second harmonic beam profiles produced using a transmission frequency of 1.6 - 1.8 MHz (Kasprzak et al., 1999). But the graph does demonstrate the potential of SHI, not only from a beam width perspective but also because of the lower off-axis energy of the superharmonic component at almost-equal-to-second-harmonic on-axis pressure intensity.

The high frequency subarray used in reception

Next to the characteristics of the transmission beam, the image quality is further affected by the sensitivity of the subarray used in reception and the noise characteristics of the imaging system. The untuned elements of the high frequency subarray had an average sensitivity of 9 μV/Pa, which is more than 50% less than that of the custom array made of the same piezomaterial (see Table 8.2). This is caused by the extra attenuation of the lens on the array and the optimization for very wide bandwidth. The final interleaved array in combination with the OPEN system can detect a pressure as low as 3 Pa with 10 dB SNR. By far

the largest noise contribution (17 μV_{rms} over a 20 MHz band) originates from the OPEN system. To improve total system SNR, preamplifiers for each high frequency element could be added in the handle. The necessary circuitry will be relatively simple, as no high voltage protection circuitry is needed for the elements in SHI mode.
Currently, the electrical tuning of the final interleaved array is optimized for SHI. The high frequency subarray is tuned on a single resonance, making the transducer plus circuitry quite narrowband (its -10 dB bandwidth is lowered from 93% to 50%). For SHI broadband electrical tuning is preferable, such as using a matching circuit with multiple resonances distributed over the required pass band of 2.5 to 5.5 MHz. In both cases the phase response of the matching circuit should be taken into account as well. In the future programmable electrical tuning will be installed yielding a transducer capable of efficient second harmonic imaging and SHI.

Transducer generated SHI contaminants

As the energy of the superharmonics generated by either nonlinear propagation or UCA response is quite low, the contamination of the SHI component by transducer produced signals at these frequencies should be minimized. For this two transducer characteristics are essential. Firstly, the low frequency subarray should have a low efficiency at the superharmonic frequencies. Secondly, the crosstalk between the low and high frequency subarrays should be minimized.
The transmit transfer function of the tuned low frequency subarray showed that the third harmonic efficiency was $\sim$46 dB below its fundamental (Fig. 8.4a). The subarray's fifth harmonic efficiency was more than 55 dB lower than its efficiency at the fundamental. By using a Gaussian modulated sine burst with a center frequency at the low frequency elements' resonance with a -6 dB bandwidth similar to or slightly larger than the elements' fundamental band, the energy produced by the transducer at the third or fifth harmonic frequency can be kept $<$ -100 dB. Thus, although the energy of the third and fifth harmonic components due to either nonlinear propagation or UCA response is quite low, the energy content of spuriously transmitted odd harmonics by the array is negligibly low.
Crosstalk from the low to the high frequency elements was $\sim$-60 dB, due to the fact that the low and high frequency parts are in essence completely separate arrays. The high frequency elements are quite insensitive at the frequencies generated by the low frequency part during SHI and possible crosstalk artifacts in B-mode images are kept to a minimum.
The crosstalk between the low frequency elements is important, because it has a detrimental influence on the transducer's ability to perform beam steering by effectively making the elements less omnidirectional. McKeighen (1998) reported that crosstalk values of -30 dB are considered acceptable for most imaging situations. Crosstalk between low frequency elements was $<$ -31 dB, so the interleaved array performed superior to this value.

Abdominal SHI

SHI is also suitable for abdominal imaging. As there is no size constraint on the array footprint in this application, the number of elements could be increased to 128; 64 elements used in transmission and 64 used in reception. In this case the footprint size would be 16

mm x 32 mm instead of the current 16 mm x 22 mm. Advantages of this modification would be an increased maximum lateral focal distance ($\sim$10 cm instead of the current $\sim$6 cm) and higher peak pressures at focus using equal excitation voltages. As the current interleaved array in conjunction with regular ultrasound equipment is already capable of reaching the 1.9 MI limit using a 3 cycle imaging burst, this means that the array's fundamental compromise between efficiency and bandwidth would shift more to bandwidth.

8.6.2 Potential imaging methods

The final interleaved array is suitable for new UCA imaging techniques such as subharmonic imaging or SURF imaging due to its broad bandwidth. The role of each subarray changes for these imaging techniques. For subharmonic imaging, the high frequency elements are used in transmission and the low frequency elements in reception. In the case of SURF imaging, both element types are used in transmission and reception. To facilitate these different roles, the electrical tuning has to be changed and optimized for each application. A possible problem is the existence of grating lobes produced when transmitting using the high frequency elements. These grating lobes are caused by the fact that the subarray pitch of 0.5 mm is large relative to ultrasound wavelengths of 0.3 - 0.5 mm. For example, if a 4 MHz square wave is transmitted, a grating lobe of -10 dB relative to the main beam is located 45° off the main beam.
The following sections treat subharmonic and SURF imaging in combination with the final interleaved array, with the emphasis on usable imaging frequencies and grating lobes.

Subharmonic imaging

First of all, the frequencies necessary for subharmonic imaging in cardiac applications are discussed in relation to the transfer function of the final interleaved array. Chomas et al. (2002) reported that the best subharmonic response is produced - while minimizing bubble instability - by using a transmission frequency which is twice the UCAs resonant frequency. UCAs used for cardiac applications are resonant at 1 - 5 MHz (Dawson et al., 1999). The final interleaved array is suitable for subharmonic imaging of UCAs with resonance frequencies between 1 - 2.4 MHz, as the high frequency subarray is efficient up to $\sim$4.8 MHz (see Fig. 8.10). Depending on the frequency of the subharmonic component either the low or high frequency subarray should be used in reception.
The other topic of discussion is the influence of grating lobes. There exists an onset pressure threshold for the production of subharmonics by UCA. Below this threshold no subharmonic component can be detected. Chomas et al. (2002) reported a pressure threshold of 200 kPa. By keeping the peak pressure in the grating lobe below this threshold, only the UCA in the main beam will produce significant subharmonic response. In this case, the existence of grating lobes can be disregarded. This implies that there is a frequency dependent maximum of the peak pressure in the main beam. To study the aforementioned relation we investigated the appearance of grating lobes in the acoustic field produced by the final interleaved array at varying transmission frequencies using the FIELD II simulation program (Jensen and Svendsen, 1992; Jensen, 1996). The element size was 13 mm x 0.2 mm with a subarray pitch of 0.5 mm. The simulations were performed using 3 cycle

sine bursts, which were Gaussian apodized. The geometric elevation focus of the beam was 6 cm, but no lateral focus was applied. The beam was steered 35° and the propagation medium was assumed to be lossless. In Fig. 8.11a a graph is shown detailing the peak intensities of the simulated grating lobe versus the transmission frequency and in Fig. 8.11b the angle of the grating lobe is shown versus the transmission frequency. From Fig. 8.11a can be deduced that the maximum peak pressures of the main beam for subharmonic imaging reduce from 600 kPa at 2.5 MHz to 360 kPa at 4.5 MHz. These pressures are common for nondestructive UCA imaging. The actual pressure threshold value for the generation of subharmonics depends on the bubble type and the excitation frequency. Typical threshold values for free gas bubbles are around 60 kPa, if excited at twice the bubbles' resonance frequency (Eller and Flynn, 1969). For UCAs, such as Levovist®, Optison®, Definity® and Sonazoid®, threshold values around 300 kPa were reported (Frinking et al., 2009). For SonoVue® the subharmonic pressure threshold was found to be 40 kPa (Biagi et al., 2007).

SURF imaging

Firstly, the frequencies necessary for SURF imaging in cardiac applications in relation to the transfer function of the final interleaved array are discussed. Masoy et al. (2008) state that the difference between the low and high frequency bursts should be on the order of 7 - 10 times for SURF imaging. In the case of echocardiography this would imply a low frequency pulse of $\sim$0.6 MHz and a high frequency pulse of $\sim$4 - 5 MHz. The combined bandwidth of the interleaved array is sufficient for SURF imaging, albeit at relatively low frequencies. For example, if a manipulation pulse of 0.6 MHz is used, an imaging pulse of $\sim$4.2 MHz could be used. As the manipulation pulse pressures are usually in the order of 50 - 100 kPa (Masoy et al., 2008), the normalized -10 dB transmit efficiency of the untuned low frequency subarray at 0.6 MHz (Fig. 8.10) is sufficient.
Secondly, the effect of grating lobes on SURF imaging is discussed. It turns out that grating lobes caused by transmitting at higher frequencies are of minor importance for SURF imaging. Although the high frequency imaging pulse ($\sim$5 MHz) used in SURF would produce significant grating lobes, the low frequency manipulation pulse ($\sim$0.7 MHz) used to alter UCA scattering properties would not. Therefore, the final image subtraction step used in SURF imaging removes the UCA response from the grating lobes of the high frequency imaging pulse.

Other possibilities

Although the details are not covered in this article, the interleaved array is also suitable for other advanced imaging techniques. Examples are source prebiasing to reduce tissue harmonics in UCA imaging (Christopher, 1999) or third harmonic transmit phasing to either enhance the tissue second harmonic - in tissue imaging - or reduce the tissue second harmonic - in UCA imaging - (Shen et al., 2007).

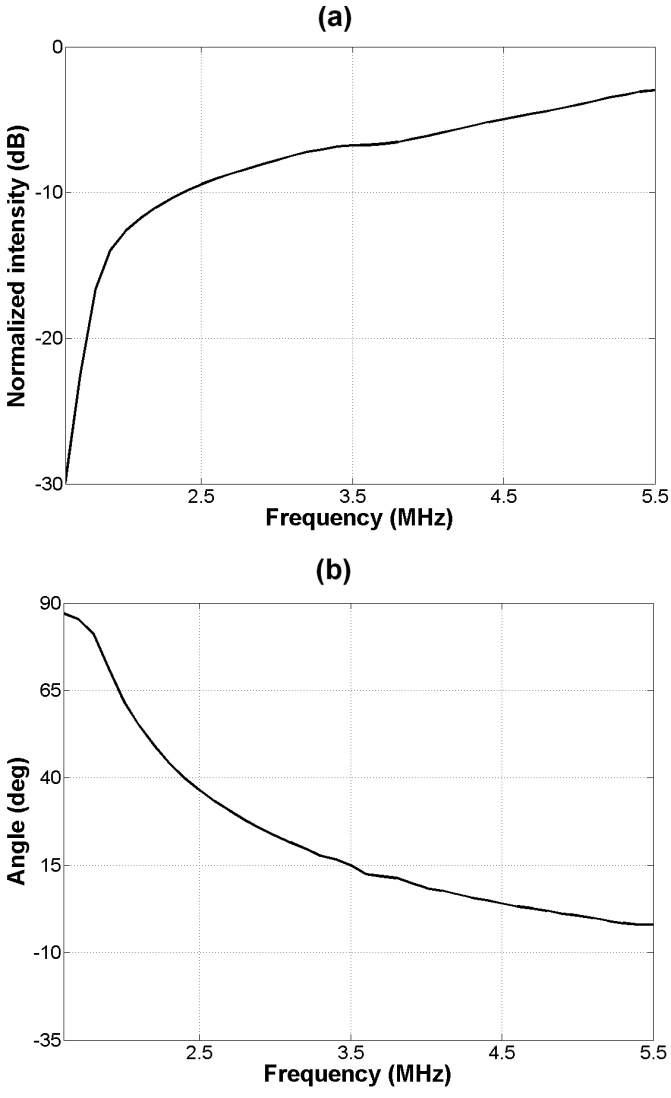

Figure 8.11: a) The relation between the fundamental peak grating lobe intensity versus the transmission frequency, simulated for the final interleaved array using Field II. The grating lobe intensity was normalized by the main fundamental beam peak intensity. The element size was 13 mm x 0.2 mm with a subarray pitch of 0.5 mm. The simulations were performed using 3 cycle sine bursts, which were Gaussian apodized. The geometric elevation focus of the beam was 6 cm, no lateral focus was applied. The beam was steered 35° and the propagation medium was assumed to be lossless. b) The angle of the grating lobe versus transmission frequency.

8.7 Conclusion

The interleaved array presented in this article possesses optimal characteristics for tissue and UCA enhanced SHI. Moreover, this array is suitable for a wide range of other experimental and clinical imaging modalities, such as second harmonic, subharmonic, and SURF imaging.
With considerably less variation in response over the elements, much lower element-to-element crosstalk, a higher fundamental transmission efficiency, reduced third and fifth harmonic transmission efficiency, and improved sensitivity in reception, the interleaved array described in this article is a large improvement over the array reported by Bouakaz et al. (2004b).

Acknowledgements We would like to thank W. van Alphen, G. Springeling, J.M.G. Borsboom, C. Pakvis, J.E.T. van Wamel, J.G. Bosch and T.R. Shrout for their efforts.

Table 8.2: Custom array performance parameters

Custom array ID	Material type	Resonance frequency (f_r)	$T_r(f_r)$: μ	$T_r(f_r)$: σ	Bandwidth at -6 dB	$T_t(f_r)$: μ	$T_t(f_r)$: σ	$\lvert Z(f_r)\rvert$	$\angle Z(f_r)$	SNR if receiving 1 Pa wave
		[MHz]	[μV/Pa]	[μV/Pa]	[%]	[kPa/V]	[kPa/V]	Ω	[°]	[dB]
1	CTS 3203HD	3.2	21	0.8	41	32.5	1	440	-18	24
2	Ferroperm Pz29	3.1	10.6	1.1	43	15.8	1.3	530	-36	16
3	Morgan PZT5K1	3.4	13.7	1.3	41	20.5	2.1	450	-22	17
4	TRS PZT HK1HD	3.6	14.4	0.4	47	31.1	1.1	330	-17	18
5	CTS 50-50 composite	3.3	7	1.2	51	4.6	0.8	440	-77	14
6	CTS 60-40 composite	3.3	3.3	0.6	68	1.8	0.3	470	-86	3
7	Omega PZNT	1.6	15.6	3.8	48	5.5	1.8	850	-45	11
	after repoling	2.0	15.6	3.7	45	7	2	800	-38	1
8	TRS PMN-30%PT	3.4	5.5	0.8	46	5.9	1.1	340	-50	18
	after repoling	3.4	12.6	0.7	47	16	1.2	380	-35	15

CHAPTER 9

Frequency and topology simulation study of a phased array transducer for multiple harmonic imaging in medical applications[1]

G.M Matte, P.L.M.J. Van Neer, M. G. Danilouchkine, J. Huijssen, M.D. Verweij, N. de Jong

Abstract Second harmonic imaging is currently one of the standards in commercial echographic systems for diagnosis because of its high spatial resolution and low sensitivity to clutter and near-field artifacts. The use of nonlinear phenomena mirrors a great set of solutions to improve echographic image resolution. To further enhance the resolution and image quality the combination of the third to fifth harmonics - dubbed the superharmonics - could be used. However, this requires a bandwidth exceeding that of conventional transducers. A promising solution features a phased array design with interleaved low and high frequency elements for transmission and reception respectively. As the amplitude of the backscattered higher harmonics at the transducer surface is relatively low, it is highly desirable to increase the sensitivity in reception. Therefore, we investigated the optimization of the number of elements in the receiving aperture as well as their arrangement (topology). A variety of configurations was considered, including one transmit element for each receive element (1/2) up to one transmit for 7 receive elements (1/8). The topologies are assessed based on the ratio of the harmonic peak pressures in the main and grating lobes. Further, the higher harmonic level is maximized by optimization of the center frequency of the transmitted pulse. The achievable signal-to-noise-ratio (SNR) for a specific application is a compromise between the frequency dependent attenuation and nonlinearity at a required penetration depth. To calculate the SNR of the complete imaging chain, we use an approach analogous to the SONAR equation used in underwater acoustics. The generated harmonic pressure fields due to nonlinear wave propagation were modeled with the Iterative Nonlinear Contrast Source (INCS) method, the KZK or the Burger's equation. The optimal topology for superharmonic imaging was an interleaved design with 1 transmit element per 7 receive elements. It improves the SNR by $\sim$5 dB compared to the interleaved (1/2) design reported by Bouakaz et al. (2004b) and van Neer et al. (2010). The optimal transmission frequency for superharmonic echocardiography was found to be 1.0 - 1.2 MHz. For superharmonic abdominal imaging this frequency

[1] Submitted.

was found to be 1.7 - 1.9 MHz. For second harmonic echocardiography the optimal transmission frequency of 1.8 MHz reported in the literature was corroborated with our simulation results.

9.1 Introduction

Since its introduction in the late 90s, tissue second harmonic imaging of biological tissue has become the de-facto standard in commercial echographic systems for medical diagnosis. The method is based on the selective imaging of the second harmonic frequency (Averkiou et al., 1997; Thomas and Rubin, 1998). Compared to fundamental tissue imaging, tissue second harmonic imaging has a higher lateral resolution and lower sidelobes, and is, therefore, less sensitive to clutter and off-axis scatterers (Ward et al., 1996; Shapiro et al., 1998; Tranquart et al., 1999; Humphrey, 2000; Bouakaz and de Jong, 2003). Also, since the second harmonic field builds up progressively, the effects of reverberation and near-field artifacts are greatly reduced (Tranquart et al., 1999; Bouakaz and de Jong, 2003). Recently, Bouakaz et al. (2002) introduced a novel ultrasonic tissue imaging method dubbed superharmonic imaging (SHI) (Bouakaz and de Jong, 2003). This technique combines the third to fifth harmonics to construct an image. Tissue SHI efficiently suppresses near-field artifacts, reverberations, and off-axis artifacts in addition to the enhanced lateral and axial resolution. The resulting images showed more details than those produced by second harmonic imaging (Bouakaz and de Jong, 2003). However, one of the challenges in SHI is the very wide bandwidth requirement ($> 130\%$) for the array used to transmit at the fundamental and receive the third to fifth harmonic signals.

An approach for having such a very wideband transducer is to use capacitive Micromachined Ultrasound Transducers (cMUT's). CMUT's having a -6 dB bandwidth of 130% have been reported (Mills, 2004; Zhou et al., 2005). However, cMUTs are held back by challenges such as achieving high output pressures (Yaralioglu et al., 2006), their inherent nonlinearity and relatively high crosstalk (Zhou et al., 2005). The most important drawback of cMUT's for tissue SHI is their nonlinearity at high output pressures. The level of the higher harmonics generated by nonlinear propagation is low, thus any transmission of harmonics due to device nonlinearity will considerably reduce the dynamic range of the imaging system.

The other way to obtain a transducer with sufficient bandwidth is to further improve the current transducer technology. However, the 130% bandwidth necessary for SHI is considerably larger than that achievable with conventional arrays. Although -6 dB bandwidths as high as 140% are reported in the literature for single element transducers made from a 1-3 single crystal-epoxy composite, the actual peak bandwidth at -6 dB reported for single crystal arrays are in the order of 95% (Rehrig et al., 2003; Zipparo et al., 2004; Li et al., 2007) - not sufficient for SHI. Thus, in order to accommodate the bandwidth requirement for SHI, the transmit and receive elements need to be separated. Such an approach has been proven to be viable and has been intensively treated in the scientific literature (Hossack and Auld, 1993; Hossack et al., 2000; Zhou and Hossack, 2002; Bouakaz and de Jong, 2003; Bouakaz et al., 2004b; Akiyama et al., 2006; Ferin et al., 2007; van Neer et al., 2010). A short overview of the earlier proposed solutions is given in the following paragraphs.

The first solution comprises a stacked topology. In this design two active PZT layers with different resonance frequencies are placed on top of each other (Hossack and Auld, 1993; Hossack et al., 2000; Zhou and Hossack, 2002). Thus the total surface used for transmission and reception remains the same as in a conventional phased array. Advantages of this configuration are the limited total footprint of the array and the ease of manufacturing. The

difficulty of using such a configuration comes from the electromechanical and acoustical coupling between the active layers. This causes troughs in the frequency response of the transducer due to destructive interference in the active layers, if the resonance frequencies of both layers are close to each other. Although solutions have been presented in literature, they require either fairly complicated electronics or knowledge of the phase transfer function of each element (Hossack and Auld, 1993; Zhou and Hossack, 2002). Moreover, the matching layer characteristic is compromised, since it should match for two different resonance frequencies.

A stacked topology for a single element has been described by Akiyama et al. (2006). Their design comprises an ultra wideband transducer used in a mechanical sector scanner. It features a PZT layer for transmission and a PVDF layer for reception. To obtain very wide bandwidth the PVDF layer functions below its resonance frequency. This has the added benefit of guaranteeing electromechanical decoupling between the active layers. However, the sensitivity of PVDF used in this manner is generally low.

Another option is to use a horizontal stack topology, where two low frequency arrays are positioned in the elevation direction on both sides of a central high frequency array (Ferin et al., 2007). The main advantage of this approach is that the initial performance of both arrays is not modified, thus facilitating manufacture. Disadvantages are the limited overlap of the acoustic beams constricting the imaging range and the increased footprint in elevation direction.

A final possibility is to arrange the transmit and receive elements in the lateral direction. Bouakaz and de Jong (2003) proposed to interleave two arrays distributing the transmit and receive elements alternately (Bouakaz et al., 2004b). With this configuration the transmit and receive beams overlap fully. Also, its footprint remains small and the transmit and receive elements can be optimized for their specific roles. Drawbacks are the relatively complicated manufacturing process and the intrinsically reduced sensitivity as only half the elements are used in reception and transmission. For transmission the reduced sensitivity can be compensated by increasing the amplitude.

The interleaved design is chosen in our project. It has fully overlapping beams and a low foot print. Also, there is no direct electromechanical coupling between the elements, since the acoustic stacks for transmission and reception including the associated circuitry are fully separated. Next to the initial interleaved array design reported by Bouakaz et al. (2004b), a follow-up interleaved array intended primarily for SHI and optimized for echocardiography was reported by van Neer et al. (2010). In the paper the rationale behind the element geometry, frequency and material choice was reported and performance measurements were provided (van Neer et al., 2010). However, in the current paper the interleaved design of alternate transmit and receive elements is further investigated. Redistributing the transmit and receive elements in groups or changing the ratio of transmit-to-receive elements may considerably improve the receive efficiency whilst a high quality beam is retained. This is important for tissue SHI, as the level of the higher harmonics generated by nonlinear propagation is low. Moreover, the paper by van Neer et al. (2010) only basically covers the choice for the 1 MHz transmit frequency used for the interleaved array optimized for superharmonic echocardiography. The optimal transmit frequency for tissue SHI depends on the level of the third to fifth harmonics at the distances determined

by the application. Consequently, the level of these harmonics is determined by two competing phenomena - nonlinear propagation and attenuation. To the authors' knowledge no systematic study of the optimal transmit frequency for SHI versus the imaging distance determined by the application has been conducted.
The first aim of the manuscript is to investigate the optimal transmit frequency for second harmonic imaging and SHI depending on the imaging application domain. The second aim of this paper is to optimize the distribution of the transmit and receive elements in order to maximize the receive sensitivity whilst retaining a high quality ultrasound beam.

9.2 Research directions

9.2.1 Transmission frequency optimization

The first part of the paper focuses on the optimization of the transmission frequency for multiple harmonics imaging, initially for echocardiography but also extended to the different imaging ranges associated with other applications. In order to study the best possible compromise between the level of the third to fifth harmonics received and the penetration depths associated with different applications the transmit frequency has to be optimized. For this we modify the SONAR equation widely used in underwater acoustics for transducer design (Lurton, 2002) to medical imaging purposes. This equation describes the whole pulse-echo imaging chain including transmit equipment, nonlinear wave propagation, backscattering and receive equipment. The levels of harmonics generated during the propagation of sound through tissue are calculated by two analogous methods described later.

9.2.2 Topology optimization

The other part of the paper focuses on the optimization of the lateral distribution of the transmit and receive elements in order to improve the receive efficiency whilst retaining a high quality ultrasound beam.
First we analyze an array where the ratio of transmit and receive elements is 1. The array with N elements is then divided in 2, 3 or N groups. So each group has $N/2$, $N/3$ or 1 elements. The former cases are referred to as group topologies, and the latter case is referred to as the interleaved or mixed topology. After this the effects of lowering the ratio of transmit-to-receive elements is studied in order to increase the receive sensitivity. The decrease in sensitivity in transmission can be compensated by a higher electrical transmission amplitude. For the analyses we used simulations based on Field II (Jensen and Svendsen, 1992; Jensen, 1996) in combination with the Burgers equation (Cobbold, 2007) and the INCS method (Huijssen et al., 2006; Huijssen, 2008; Verweij and Huijssen, 2009; Huijssen and Verweij, 2010).

9.2.3 Group topology

In the first configuration of the group topology class the array is constituted of two equal groups of elements distributed laterally (see Fig. 9.4a). The transmit elements (tuned on the fundamental frequency) are on one side of the array, while the receive elements (tuned on higher frequency components) are on the other side. The origin of the coordinate system of the probe is located in between both groups of elements.
The second type of the group topology defines an array consisting of three parts in a lateral distribution (see Fig. 9.4b). A group of transmit elements is located in the middle and two groups of receive elements are laterally arranged on each side of the transmit elements. The total number of receive elements is twice the amount of transmit elements. This configuration is analogous to the one described by Ferin et al. (2007), except in our case the lateral arrangement of the elements enables electronic focusing instead of a fixed focus. The transmit and receive elements are distributed symmetrically, thus the convolved transmit and receive beams are expected to be symmetric.

9.2.4 Interleaved topology

The interleaved topology is an array configuration where single transmit elements are equidistantly placed over the footprint (see Figs. 9.4c-e). The successive transmit elements are interleaved by a group of n receive elements ($n = 1$ to N). We further refer to $1/k$ interleaved topologies to make the distinction between each particular combination of a single transmit element and ($n = k - 1$) receive elements. The main difference between the introduced topology classes lies in the fact that transmit elements are grouped together to form the transmit aperture in the group topology class. The perceived advantage of the interleaved over the group topology is the possibility of increased sensitivity in reception whilst having the best distribution of the elements from a beam quality perspective. According to the nomenclature established in the current paper, the transducer design described by Bouakaz et al. (2004b) and van Neer et al. (2010) belongs to the 1/2 interleaved topology.

9.2.5 Criteria for topology evaluation

Of major importance in the design of phased arrays for medical ultrasound is the system dynamic range. It is limited by the relative energy difference between the main and the grating lobes and by the signal-to-noise ratio (SNR). A grating lobe is the result of constructive interference of the acoustic waves produced by the array at a sideways direction. The backscattered echoes originating from a grating lobe pollute the signal of the main beam. The grating lobes are caused by the under-sampling of the physical aperture. Considering a phased array as a sampled aperture and taking into account the Nyquist theorem, it is easy to deduce that a grating lobe would occur when the distance between neighboring elements of the array exceeds half of the wavelength of the emitted pulse. Thus, the presence of a grating lobe and its intensity depend on the wavelength and the pitch. Obviously to avoid the occurrence of grating lobes, the inter-element spacing should be equal to or less than the aforementioned distance. In case of harmonic imaging this requirement can

be weakened, as the production of the n'th harmonic is related to the pressure in the beam to the power n - the peak pressure in the main beam will be considerably higher than the pressure in the grating lobe. The pressure in the grating lobe relative to the pressure in the main beam at the frequency used to construct an image sets a limit on the dynamic range of that image. Cobbold (2007) states that the grating lobe pressure should be 40 dB below the pressure in the main beam.
To evaluate the effect of the varying distance between elements for each topology, the levels of a harmonic in the main and grating lobes have to be calculated and compared with each other. All further analyses will be backed by simulations based on Field II (Jensen and Svendsen, 1992; Jensen, 1996) in combination with the Burgers equation (Cobbold, 2007), the KZK equation (Lee and Hamilton, 1995) and the INCS method (Huijssen et al., 2006; Huijssen, 2008; Verweij and Huijssen, 2009; Huijssen and Verweij, 2010).

9.3 Theory

9.3.1 Expression of the SNR

The SNR can be expressed as a logarithmic sum of transfer functions, each representing a phenomenon of the imaging process:

$$SNR = V_T + T_t + H_{FRWD} - Bs - H_{BKWD} + T_r - Ns, \tag{9.1}$$

with V_T the excitation voltage amplitude on the transducer clamps, T_t the transmit transfer of the transducer (analogous to TVR (Transmitting Voltage Response) in underwater acoustics), H_{FRWD} the function describing the pressure wave during forward propagation - it includes diffraction, attenuation and nonlinearity -, Bs the power loss during the backscattering process (analogous to the target strength in underwater acoustics), H_{BKWD} the function describing the pressure wave during back propagation - linear back propagation is assumed, thus it includes only attenuation (A_{back}) -, T_r the receive transfer of the transducer and Ns the noise of the imaging system.
This expression is analogous to the SONAR equation, widely used in underwater acoustics for transducer design (Lurton, 2002).

The combination of V_T, T_t and H_{FRWD} is the incoming pressure at the scatterer location. Thus, (9.1) can be rewritten into:

$$SNR = P - Bs - A_{back} + T_r - Ns, \tag{9.2}$$

with P the incoming pressure at the scatterer location due to forward propagation of the ultrasound produced by the transducer and A_{back} the ultrasound attenuation during linear back propagation to the transducer.

All of the factors in (9.1) and (9.2) are expressed in dB.
Fig. 9.1 provides a schematic for the concept of the SNR expression. The terms in (9.1) and (9.2) are explained in more detail in the following paragraphs.

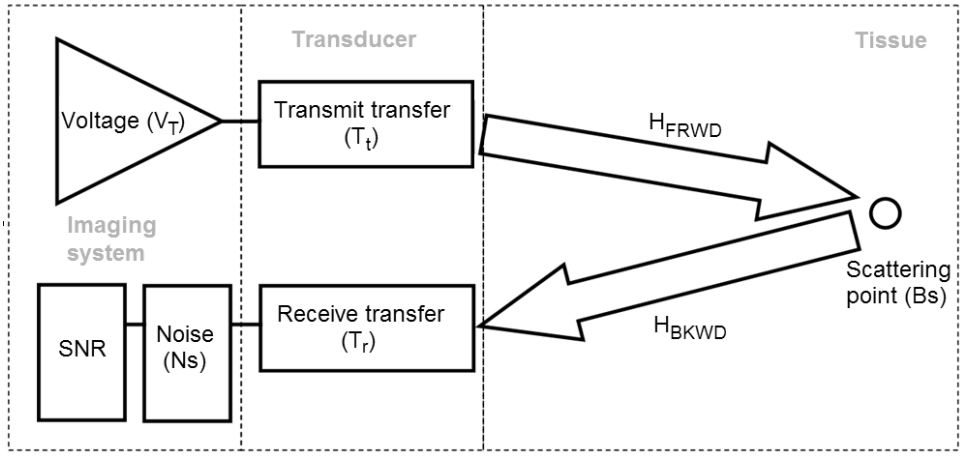

Figure 9.1: Schematic description of the expression of the SNR shown in (9.1) and (9.2).

The incoming pressure at the scatterer location (P)

For nonlinear propagation the acoustic wave at the transducer surface has to be propagated towards the scatterer location. We use two simulations models: the KZK equation (Hart and Hamilton, 1988; Lee and Hamilton, 1995; Hamilton and Blackstock, 1998) and the INCS approach (Huijssen et al., 2006, 2007, 2008; Huijssen, 2008; Verweij and Huijssen, 2009; Huijssen and Verweij, 2010). These models include the attenuation of the medium. P is expressed in dB relative to 1 Pa.

The excitation voltage (V_T)

The excitation voltage (V_T) over the clamps of the transmitting part of the transducer is expressed in dB relative to 1 volt.

The transmit transfer (T_t)

The transmit transfer (T_t) is defined as (van Neer et al., 2007):

$$T_t = \frac{|p_0|}{|V_T|}, \tag{9.3}$$

with p_0 the pressure at the transducer surface and V_T the voltage over the transducer electrodes. T_t is expressed in dB relative to 1 Pa/V.

The backscattered signal (Bs)

The total backscattered intensity (Bs) is defined as:

$$Bs = \Omega \mu_t L, \tag{9.4}$$

where Ω is the solid angle, impinging the receive aperture of the transducer for a given observation point. The area of the receive aperture is simply determined as a product of an element area and the number of elements in reception. L defines the scattering distance, which is equal to the distance between the observation point and the transducer, and μ_t is the backscattering cross-section, which is modeled as (Duck, 1990):

$$\mu_t = \mu_a f^{\mu_b}, \tag{9.5}$$

with f the frequency, μ_a in cm^{-1}.Sr^{-1} (described in (Duck, 1990) as a) and μ_b associated with the frequency dependency (described in (Duck, 1990) as b).
Bs is expressed in dB.

Attenuation of backscattered signal during backpropagation (A_{back})

The amplitude of the backscattered signal is generally low, thus the backward propagation can be considered to be linear. The attenuation of the backscattered signal during linear propagation from the tissue target back to the transducer (A_{back}) was modeled as:

$$A_{back} = L \cdot \alpha_0^f \cdot f^b, \tag{9.6}$$

with α_0^f the frequency attenuation factor.
A_{back} is defined per harmonic n in dB.

The receive transfer (T_r)

The receive transfer (T_r) is defined as (van Neer et al., 2007):

$$T_r = \frac{|V_{T-open}|}{|p_a|}, \tag{9.7}$$

with V_{T-open} the open circuit voltage over the transducer and p_a the pressure received on the transducer surface.
T_r is expressed in dB relative to 1 V/Pa.

Transducer and system noise (Ns)

The transducer and system noise (Ns) is expressed in dB relative to 1 V_{RMS}. The noise is assumed to be white. As the SNR is considered after beamforming, the noise level is divided by $\sqrt{N_{el}}$.

9.3.2 The KZK equation

The cumulative effects of diffraction, absorption and nonlinearity in directive sound beams are modeled by the KZK nonlinear wave equation (Averkiou et al., 1997; Cobbold, 2007). The KZK equation uses the parabolic approximation and is therefore only valid for 15° around the direction of wave propagation:

$$\frac{\partial^2 p}{\partial z \partial t'} = \frac{c_0}{2}\left(\frac{\partial^2 p}{\partial r^2} + \frac{1}{r}\frac{\partial p}{\partial r}\right) + \frac{\alpha_0}{\omega_0^2}\frac{\partial^3 p}{\partial t'^3} + \frac{\beta}{2\rho_0 c_0^3}\frac{\partial^2 p}{\partial t'^2}, \tag{9.8}$$

with p the sound pressure at an axial location z, t' the retarded time defined as $t' = t - \frac{z}{c_0}$, c_0 the small-signal acoustic wave velocity, r the transverse radial coordinate, α_0 the thermoviscous attenuation coefficient, ω_0 the angular frequency of the fundamental, β the coefficient of nonlinearity and with ρ_0 the ambient density.
The first term on the right-hand side of (9.8) accounts for diffraction, the second term accounts for absorption and the third term accounts for quadratic nonlinearity. To mimic tissue absorption the absorption term was replaced with an attenuation term, which depended linearly on the frequency (Bouakaz and de Jong, 2003). Equation (9.8) is written using cylindrical coordinates, assumes axisymmetry - also in the source - and uses a paraxial approximation. The well known time domain approach proposed by Lee and Hamilton was implemented (Hart and Hamilton, 1988; Lee and Hamilton, 1995; Hamilton and Blackstock, 1998).
The KZK equation has been utilized by many researchers and is in excellent agreement with experiments (Tjotta et al., 1990, 1991).

9.3.3 The INCS method

A full wave description of the nonlinear propagation of acoustic waves in a homogeneous medium is given by the Westervelt equation (Hamilton and Blackstock, 1998). The INCS method provides a numerical solution for this equation and is not dependent on the direction of the wave propagation:

$$\frac{1}{c_0^2}\frac{\partial^2}{\partial t^2}\left(\chi(t) *_t p\right) - \nabla^2 p = S + \frac{\beta}{\rho_0 c_0^4}\frac{\partial^2 p^2}{\partial t^2}, \tag{9.9}$$

with $\chi(t)$ a normalized compressibility relaxation function, $*_t$ the convolution with respect to time and S the primary source term. The usual prescription of a pressure $P(x, y, t)$ at the boundary $z = 0$ can be accounted for by using $S = -\partial\left(F(x, y, t)\delta(z)\right)/\partial z$, where $F = 2P(x, y, t)$ is the surface force density in the positive z-direction and $\delta(z)$ is the Dirac delta function. The details about the theoretical background of the method can be found in the works of Huijssen et al. (2006) (Huijssen et al., 2007, 2008; Huijssen, 2008; Verweij and Huijssen, 2009; Huijssen and Verweij, 2010). The strategy to solve this equation is to consider the nonlinear pressure field as a sum of the linear field solution and a nonlinear correction. The linear field solution can be obtained from the homogeneous lossless and linear background medium with external source S. The nonlinear field correction arises from the solution of equation (9.9) with the single second term on the right hand side.

Those solutions are numerically refined in an iterative manner until convergence (Huijssen, 2008). The nonquadratic attenuation of lossy media such as tissue was incorporated (Huijssen et al., 2008).
In contrast to the KZK simulations the INCS method does not require a paraxial approximation. As such it is more precise for steered beams, but requires considerably more computation time and memory resources.

9.3.4 Linear acoustic modeling using Field II

The FIELD II simulation program (Jensen and Svendsen, 1992; Jensen, 1996) was used to calculate the fundamental acoustic fields of the various group configurations and mixed configurations. The Burgers equation was used in order to estimate the harmonic level in the grating lobes.

9.3.5 The Burgers equation

The Burgers equation describes the propagation of finite-amplitude plane progressive waves in a medium with thermoviscous losses. The solution was found as a complex Fourier series using the iterative computation scheme given by Cobbold (2007).

9.4 Material and Methods

9.4.1 Transmission frequency optimization

Nonlinear propagation is frequency dependent. In general the higher the frequency the more nonlinear the wave propagation is and therefore the more harmonics are generated. On the other hand the higher the frequency the higher the attenuation is in the propagation medium, which counterbalances the generated harmonics. The SNR of the harmonics depends on the transducer configuration and the characteristics of the propagation medium.
The SNR as a function of the frequency is given by (9.1) and (9.2). We used liver as the propagation medium (c_0 = 1580 m/s, ρ_0 = 1050 kg/m^3 and β = 4.4, μ_a = 2.7 10^{-4} m^{-1}.Sr^{-1}.MHz$^{\mu_b}$ and μ_b = 1.2, α_0^f = 5.2 Np.m^{-1}.MHz^{-b} and b = 1.05 (Duck, 1990)). The transducer was the interleaved array reported by van Neer et al. (2010). This phased array transducer had a low frequency subarray consisting of 44 elements (16 mm x 0.2 mm, center frequency of 1 MHz) interleaved with a high frequency subarray also consisting of 44 elements (13 mm x 0.2 mm, center frequency of 3.7 MHz). The pitch was 0.5 mm and so the lateral dimension of the array was 22 mm. The elevation focus was fixed and set to 60 mm. In the lateral direction the steering angle was set to zero and the focal distance to 60 mm. The transmit transfer (T_t) was taken to be 32.5 kPa/V and for the receive transfer (T_r) 21 μV/Pa was taken (see (van Neer et al., 2010)). The transducer and system noise was measured and equal to 7 μV_{RMS} over a 3.5 MHz band. This measurement was performed on a commercial programmable ultrasound system (OPEN system, Lecoeur Electronique, Chuelles, France) including the above mentioned transducer. The excitation amplitude on the transducer was chosen to get a resulting MI in focus of 1.5 (note: MI is equal to the

derated peak negative pressure divided by the square root of the frequency).
The value of every individual harmonic of P was computed using either the KZK equation or the INCS method. The KZK equation for an axi-symmetric lightly focused source was solved in the time domain according to the algorithm described by Lee and Hamilton (1995). The algorithm was implemented in C and an interface was written in Matlab to extract the data (Matte et al., 2008).
The solver of the INCS method has been implemented in parallel and ran on an IBM clustered symmetric multiprocessing system (Huygens system, Amsterdam, the Netherlands). The entire system consists of 1664 dual core processors (IBM Power6, 4.7 GHz), 128 Gbytes / 256 Gbytes of memory per node. The total peak performance is 60 Teraflop/sec. Depending on the frequency, a single run takes 2 to 30 hours on 32 processors for a complete 3D nonlinear beam profile.
For an overview of the parameters used see Table 9.2.

9.4.2 Topology optimization

For the topology the discriminating feature is the grating lobe level. Simulations have been carried out to calculate the fundamental and harmonic main beam together with the sidelobes and grating lobes. For the simulations we used a Gaussian apodized transmission signal of 3 cycles with a frequency of 1.2 MHz. This frequency corresponds to the optimal transmission frequency for SHI and echocardiography (see Fig. 9.3). For the propagation medium we used the properties of liver - c_0 = 1580 m/s, ρ_0 = 1050 kg/m^3. The linear simulations were lossless, for the nonlinear simulations β = 4.4, α_0^f = 5.2 Np.m^{-1}.MHz^{-b} and b = 1.05 (Duck, 1990). The excitation amplitude was set such to get an MI of 1.5 in focus. The used apertures with different transmit-to-receive element ratio's are shown in Fig. 9.4. The beam steering angle was 35° and the lateral and elevation foci were set to 60 mm.
A two step approach was used to calculate the grating lobe levels. Firstly, the fundamental acoustic field was calculated using the FIELD II simulation program (Jensen and Svendsen, 1992; Jensen, 1996). Secondly, the harmonic grating lobes were estimated from the fundamental grating lobe levels using the Burgers equation. For that the fundamental peak pressure in the grating lobe was used as the starting pressure for the Burgers equation. The wave was then propagated over a distance of 60 mm. Acoustic attenuation was included. The harmonic levels of the grating lobes were compared to the harmonic levels in the main beam as calculated using INCS simulations for the same apertures shown in Fig. 9.4c - 3.
For an overview of the parameters used see Table 9.2.

9.5 Results

9.5.1 Transmission frequency optimization

In Fig. 9.2a the SNR of the system as function of the transmission frequency is plotted for the fundamental up to the 5th harmonic. The curves are calculated at a depth of 6 cm. The MI is kept constant at 1.5. As seen in the figure the SNR of the fundamental ranges between 62 and 79 dB for the transmit frequency range of 0.5 - 2.5 MHz. The second

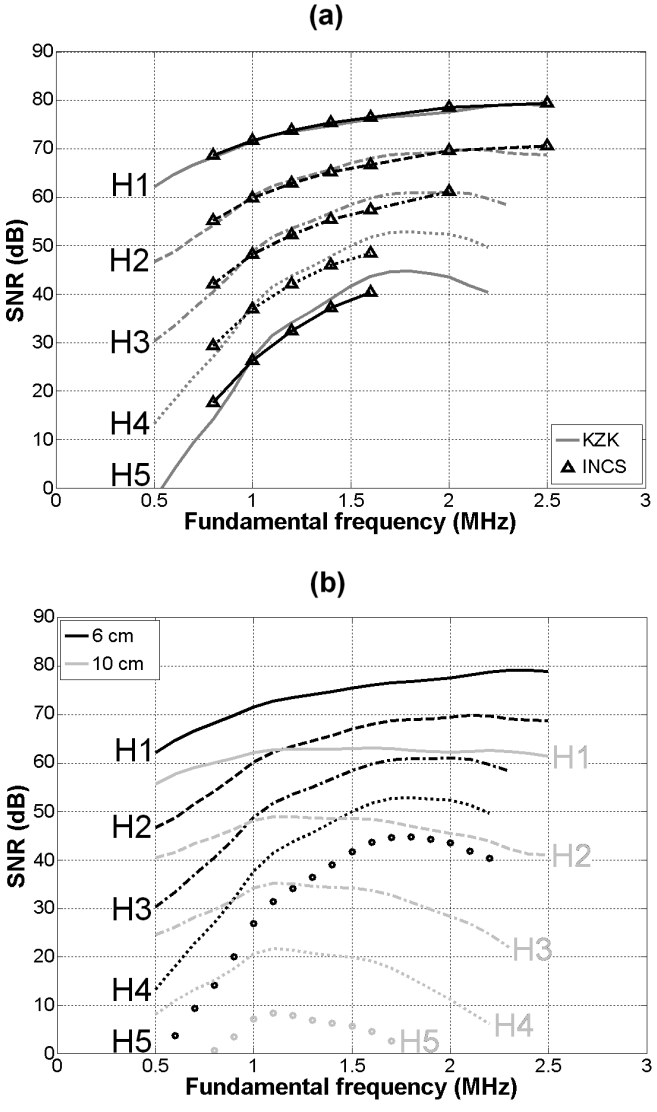

Figure 9.2: a) The SNR as calculated by the INCS method (black triangles) and the KZK model (gray lines) using the same input parameters. The curves were calculated for a propagation distance of 60 mm using the transducer described in the materials and methods as a source and the material properties of liver. The corresponding harmonics are indicated next to each curve. b) The SNR as calculated using the KZK model for a propagation distance of 6 cm (black lines) and 10 cm (gray lines). The corresponding harmonics are indicated next to each curve.

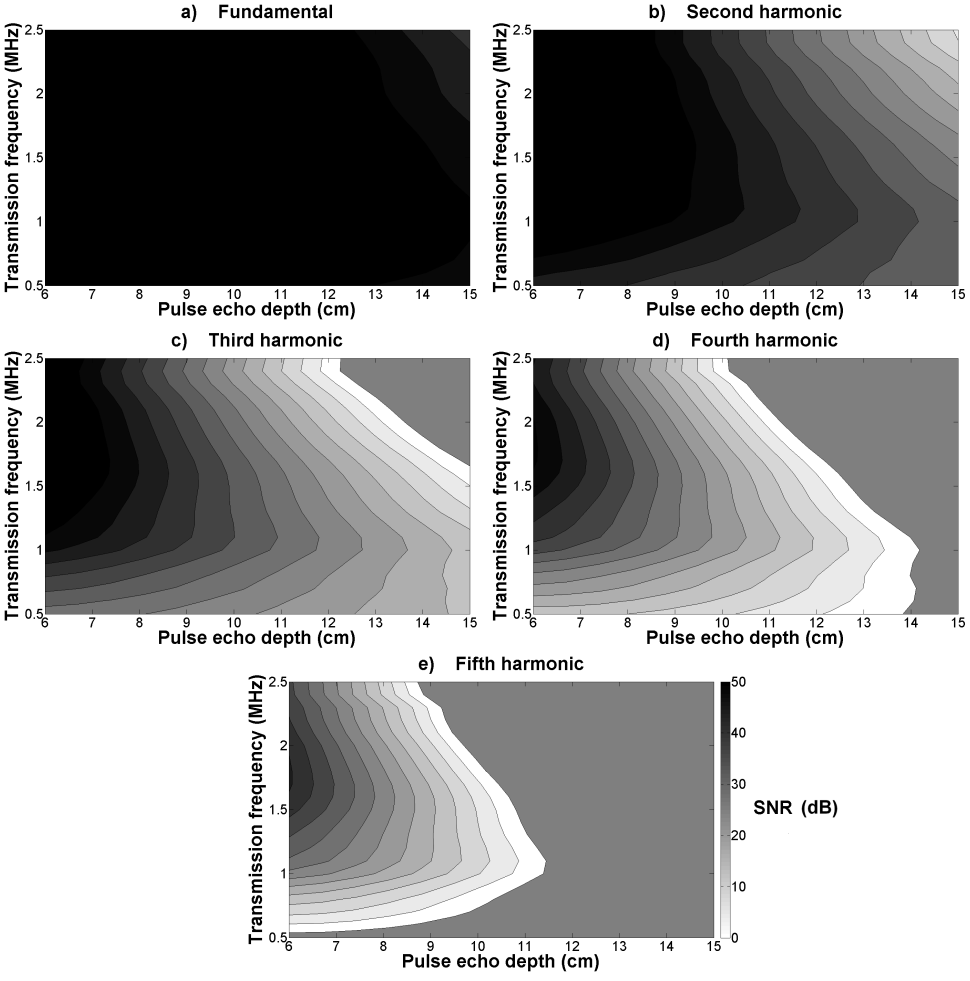

Figure 9.3: The SNR depending on the transmission frequency and depth. Panel A shows the fundamental, panel B shows the second harmonic, panel C shows the third harmonic, panel D shows the fourth harmonic and panel E shows the fifth harmonic. The SNR is encoded by an inverted gray scale using a 50 dB dynamic range, the uniform gray area at large depths indicates the area where the SNR is below 0 dB.

harmonic SNR ranges between 47 and 70 dB, the third harmonic SNR between 30 and 61 dB, the fourth harmonic SNR between 13 and 53 dB and the fifth harmonic SNR between -2 and 45 dB. For H1 there is no maximum observed for the frequencies between 0.5 and 2.5 MHz. The optimal transmitting frequency is higher than 2.5 MHz. There is a maximum observed for the second, the third, fourth and fifth harmonics. For H2 the maximum occurs at 2.1MHz, for H3 around 1.9 MHz, for H4 around 1.85 MHz and for H5

around 1.75 MHz.
In the figure the results of the KZK as well as the INCS simulations methods are plotted. In the frequency range from 0.8 up to 1.4 MHz the two methods differ only by ± 1 dB for the fundamental up to the third harmonic, while this is slightly more for the fourth and fifth harmonic (± 2 dB). The maximum difference between the INCS method and the KZK method is ± 3 dB. These slight differences are as expected for an unsteered beam. The KZK method is used for most of the remainder of this article.
For an imaging depth of 10 cm the SNR for each harmonic is given in Fig. 9.2b. Two effects can be seen when comparing these results with those obtained at a 6 cm imaging depth. First, the level of the curve is lower over the whole frequency band and secondly the maximum of the curves shifts towards lower frequencies. Since the foci of all the harmonics are at or around 6 cm, both phenomena can be explained by the increased propagation path and consequently the increased attenuation. The fundamental has an SNR of 62 dB and is flat for frequencies above 1 MHz, so for fundamental imaging the preferred frequency is 2.5 MHz or higher. All of the harmonics show a maximum around 1.2 MHz. H2 and H3 have an SNR above 30 dB, while the SNR of H4 is still above 20 dB. For the fifth harmonic the level is further decreased and is less than 10 dB above the noise level.
In diagnostic ultrasound the transmission frequency used depends on the application and by that on the scanning depth. If the scanning depth increases, the transmission frequency is lower. In Fig. 9.3 intensity plots show the SNR levels in dB as a function of the transmitting frequency and the scanning depth. Panel A shows the fundamental frequency, panel B the second harmonic, panel C the third harmonic, panel D the fourth harmonic and panel E the fifth harmonic. The colour gives the level of the SNR and ranges from 50 dB (black) till 0 dB (white). From the figure it can be seen that for the second harmonic the optimal frequency for a maximum scanning depth of 9 cm is 2.5 MHz. However, at a maximum scanning depth of 12 cm the highest SNR occurs using a transmission frequency of 1.1 MHz. For the third harmonic and a scanning depth of for example 12 cm a transmission frequency of 1 MHz results in a SNR of more than 25 dB (gray), but is close to 0 dB for a transmitting frequency of 2.5 MHz (light gray-whitish). The fourth and fifth harmonics only have an acceptable SNR at scanning depths smaller than 8 cm.

9.5.2 Topology optimization

The investigated topologies of the array transducer are plotted in the first column of Fig. 9.4. The transmitting elements are colored black, while the receiving elements are colored gray. The transmitting elements always transmit at the fundamental frequency (1.2 MHz). In the middle column the transmit-receive beam profiles for the fundamental frequency are shown. In this case the transmit elements are also used in reception. The right column in Fig. 9.4 shows the convolution of the transmit ultrasound field at the fundamental frequency and the receive ultrasound field at the second harmonic frequency. The steering angle is 35°. Of importance are the main beam size and the off-beam energy, mostly reflected in the side lobes and grating lobes.

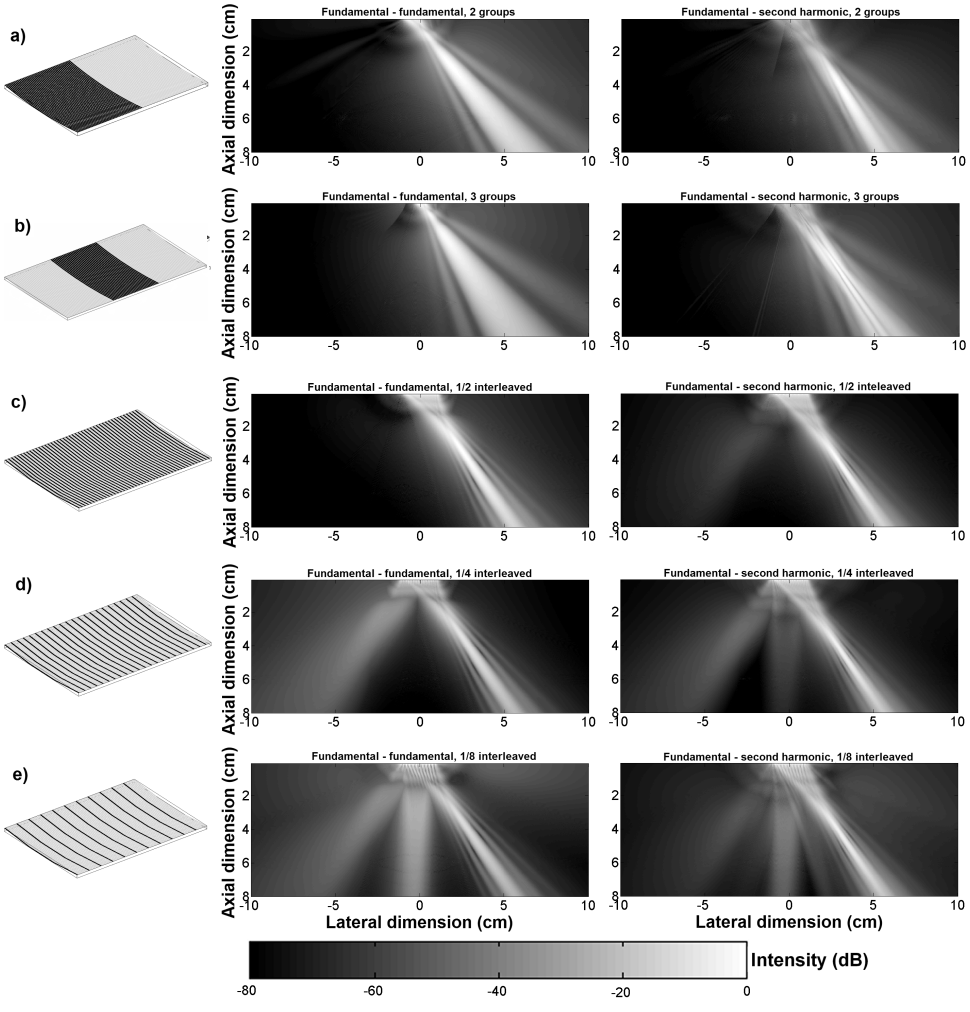

Figure 9.4: a) Two group topology. b) Three group topology. c) Interleaved 1/2 topology. d) Interleaved 1/4 topology. e) Interleaved 1/8 topology. The black elements are used in transmission, the gray elements are used in reception. The middle column shows the convolved fundamental transmit - receive beam using the darkly colored aperture only. The right column shows the convolved fundamental - second harmonic beams using the complete aperture. The intensity in dB is denoted by the grayscale color using an 80 dB dynamic range.

Two subarray topology

The two-subarray topology is shown in Fig. 9.4a. The transmitting elements are on one side of the array (black color), while the receiving elements are on the other side (gray

color). The middle panel shows the convolved transmit - receive beam at the fundamental frequency. The fundamental beam width at focus is 8.7 mm and the second harmonic beam width is 4.4 mm. Notice that the convolved transmit (fundamental)-receive (second harmonic) beam is curved. This effect becomes stronger when looking at beams of higher harmonics.

Three subarray topology

The three-subarray topology is detailed in Fig. 9.4b. The transmitting part is in the center and the two receive parts are located on each side of the transmit array. The fundamental transmit-receive beam is displayed in the middle panel, while the convolved fundamental transmit and second harmonic receive beam is displayed on the right. The fundamental beam is much wider (11.2 mm) than the previous configuration as a result of the smaller aperture. The second harmonic beam on the right measures 7.3 mm at focus. However, at the location of the focal point, the beam splits and has a very high level of side lobes (up to -2dB relative to its center).

Mixed topology

The mixed or interleaved topologies of the array are further shown in Figs. 9.4c, d and e. The interleaving ratio varies from one transmit element for each receive element (denominated as 1/2, see Fig. 9.4c), up to a ratio of one transmit element for every seven receive elements (denominated as 1/8, see Fig. 9.4e).
For the 1/2 configuration there are no grating lobes visible for the fundamental beam and consequently also the second harmonic beam is free of grating lobes. This changes for the 1/4 configuration in Fig. 9.4d. There is a clear grating lobe in the fundamental beam plot located at about -35°. In the second harmonic beam profile the grating lobe level is greatly diminished and just above the noise level. For the 1/8 configuration in Fig. 9.4e there are two grating lobes, one at -35° and the other one at zero degrees. The one at 0° is only -10 dB below the main beam intensity. For the second harmonic beam the grating lobe is still there, but the level is now $\sim$-20 dB. The main beam in the mixed topologies is more or less independent of the interleaving ratio, since the aperture remains the same. The fundamental beam width at focus is 7.8 mm.
Table 9.1 summarizes the results of the grating lobe level of the fundamental and second harmonic as discussed above and includes an extension for the third - fifth harmonic components. According to Cobbold (2007) an imaging system should have a grating lobe to main lobe level of less than -40 dB. From Table 9.1 it can be read that for the fundamental mode the maximum interleaving ratio of the transmit-receive elements is 1/2. For the second harmonic the maximum ratio is 1/4, while for the third harmonic a ratio of 1/7 still provides a grating lobe to main lobe level below -40 dB. For the fourth and fifth harmonics the grating lobe levels stay below -40 dB in all configurations.

Table 9.1: Peak grating lobe intensity relative to peak main beam intensity of the mixed topologies

f_0	Pitch	Nbr. of receivers	Fundamental	H2	H3	H4	H5
[MHz]	-	-	[dB]	[dB]	[dB]	[dB]	[dB]
1.2	1/2	44	-	-	-	-	-
	1/3	59	-23	-56	-83	-107	-130
	1/4	66	-15	-41	-59	-76	-92
	1/5	70	-13	-36	-50	-64	-77
	1/6	73	-11	-32	-46	-57	-69
	1/7	75	-9	-30	-42	-53	-62
	1/8	77	-8	-27	-37	-47	-55

9.6 Discussion

9.6.1 Transmission frequency optimization

The results presented in this paper allow for validation of the findings on the optimal transmission frequency for second harmonic imaging but also for prediction of the same parameter for imaging based on higher harmonics. Kasprzak et al. (1999) investigated experimentally the optimal transmission frequency for second harmonic imaging. Their methodology consisted of comparing the quality of the images produced by several commercial echographic systems on the frequency range of 1.6 - 1.8 MHz and 2.1 - 2.4 MHz. Kasprzak et al. (1999) found that a relatively low 1.6 - 1.8 MHz transmission frequency is necessary to visualize the whole heart including the parts furthest away from the transducer. We translate the qualitative criteria used by Kasprzak et al. (1999) into an explicit demand for the dynamic range at the maximum imaging depth depending on the transmit frequency. In the case of echocardiography we analyze our results at 12 - 15 cm requiring a dynamic range of at least 30 dB at this distance. Indeed our simulation results confirm the initial findings of Kasprzak et al. (1999) and show that the optimal transmission frequency is 1.7 - 1.8 MHz for second harmonic echocardiography (see Fig. 9.3) - this provides an SNR of $\sim$32 dB at 13 cm. The optimal transmission frequency for the selective imaging of the third harmonic is 1.0 - 1.2 MHz (see Fig. 9.3). However, with a third harmonic SNR of $\sim$22 dB at 13 cm it is below the 30 dB dynamic range criterion. Both the fourth and fifth harmonics would not provide sufficient dynamic range at 13 - 15 cm for the selective imaging using either. As the third harmonic contains the most energy of the components in the superharmonic band, the optimal transmission frequency for superharmonic echocardiography is concluded to be 1.0 - 1.2 MHz (see Fig. 9.3). Although the fourth and fifth harmonics are below the noise floor at 14 - 15 cm, they still contribute to the superharmonic image at shallower depths. The optimal transmission frequency found for SHI is in agreement with the 1.0 MHz reported by van Neer et al. (2010).

The maximum imaging depth for imaging of the kidneys, the gallbladder or the abdominal aorta is at 9 - 10 cm lower than that for echocardiography. Therefore, the optimal trans-

mission frequency for second harmonic imaging is higher at ∼2.5 MHz (see Fig. 9.3). For third harmonic imaging the optimal transmission frequency becomes ∼1.7 - 1.9 MHz. For imaging based on the fourth harmonic the optimal transmission frequency is ∼1.6 MHz, but the harmonic level remains below the required 30 dB dynamic range threshold with an SNR of 22 dB at 10 cm (see Fig. 9.3). The optimal transmission frequency for SHI is ∼1.8 MHz, since the third harmonic component contains the most energy of the components in the superharmonic band. Both the fourth and fifth harmonics are above the noise floor and contribute to the superharmonic image.
The simulations reported here were performed for a homogeneous medium using the material properties reported for liver. However, the human body has a heterogeneous structure with considerable variation in tissue material properties and interfaces in between different tissue types, where the acoustic impedances vary strongly. For example in the case of echocardiography, most of the propagation medium consists of blood and cardiac tissue. Although the range of reported B/A and attenuation values for cardiac tissue are similar to those reported for liver, the attenuation values reported for blood are four times lower than that of liver tissue at similar B/A values (Duck, 1990). Therefore, the SNR levels reported here should be interpreted as a worst case scenario.
Also, the element geometry used for the simulations was based on the geometry reported for a transducer intended for echocardiography. In this modality the height and width of the transducer are limited by the space between the ribs. However, in abdominal imaging there is no such constraint and the element dimensions and number of elements can be increased. This would increase SNR but the reported trends would remain similar.

9.6.2 Topology optimization

The convolved transmit(fundamental)-receive(harmonic) beam is curved in the case of the two-groups topology. This is caused by the fact that the centers of the transmit and receive apertures do not spatially coincide. The contribution of the farthest elements to the focal point is overestimated, which misplaces the effective backscattered signal at an incorrect position in space. The solution requires modified element delays for steering in transmission and an extra postprocessing step to correct for the aberrated point spread functions in reception. The three group topology does not have the aforementioned problems, but the convolved transmit-receive beam is wide. At the limit of the large group topology is the interleaved topology. Its convolved transmit-receive beam is the most narrow and well defined. Therefore, the fully interleaved design is preferred over topologies consisting of a lower amount of groups.
The mixed topologies combine the well defined beams of the interleaved design with an increase in surface area dedicated for receiving. The dynamic range of an ultrasound system is limited by the grating lobe to main lobe ratio and the maximum SNR, where the lower of the two is the main determinant. Cobbold (2007) states that the grating lobe pressure should be 40 dB below the pressure in the main beam. Focusing on the third harmonic, our simulations show that the 1/7 configuration provides the maximum number of receive elements while still providing a grating lobe level less than -40 dB compared to the main beam (see Table 9.1). For the fourth and fifth harmonics all configurations provide sufficiently low grating lobe levels. As the third harmonic has the highest intensity overall of

the superharmonics (third to fifth harmonics), the 1/7 configuration is optimal for superharmonic echocardiography.
The optimal 1/7 configuration uses 75 elements for reception, compared to the 44 elements used in reception by the interleaved (1/2) configuration reported by Bouakaz et al. (2004b) and van Neer et al. (2010). The increased number of receive elements improves the total SNR by $\sim$5 dB, because of the reception of an increased amount of backscattered energy and the reduction of the effective noise level after beamforming. Although a 5 dB improvement in SNR may seem like a modest improvement, it is an SNR improvement over the entire imaging depth.
The main assumption here is that the voltage over the transducer clamps - or the transmit efficiency of the transmit elements - can be increased sufficiently to compensate for the reduced number of transmit elements. By exciting their 1/2 transducer using signals 60 V in amplitude van Neer et al. (2010) reported reaching an MI of 1.9. Thus to reach the same peak pressures using the 1/7 configuration the amplifier output should be increased to 210 V. This voltage level should pose no problem to the integrity of the piezomaterial at the thicknesses associated with $\sim$1 MHz resonance frequencies.
Although the pressure at focus will be within regulatory limits, the pressure near the element surface of the optimal 1/7 configuration will exceed it. The generated pressure drops rapidly further along the axial dimension, because of the small size of the elements in the lateral dimension. Therefore, this issue could be solved by mounting a thin slab of low loss material with an acoustic impedance close to that of tissue on the front of the transducer.

9.7 Conclusion

The optimal transmission frequency for superharmonic echocardiography was found to be 1.0 - 1.2 MHz. For superharmonic abdominal imaging this frequency was found to be 1.7 - 1.9 MHz. For second harmonic echocardiography the optimal transmission frequency of 1.8 MHz reported in literature was corroborated and for second harmonic abdominal imaging a frequency of 2.5 MHz was found.
The optimal topology for superharmonic echocardiography was the mixed transducer configuration with 1 transmit element per 6 receive elements. This configuration improves the SNR by $\sim$5 dB compared to the interleaved (1/2) design reported by Bouakaz et al. (2004b) and van Neer et al. (2010).

Acknowledgements This work was supported by the Dutch Technology Foundation (STW) and by the Dutch National Computing Facilities Foundation (NCF).

Table 9.2: Aperture characteristics and acoustic properties of the simulated signals

Simulation type	Element length [mm]	Element width [mm]	Nbr. of elements	c_0 [m/s]	ρ_0 [kg/m^3]	Kerf [mm]	Steering angle [°]	Pulse length	Absorption (α_0^f) [Np.m^{-1}.MHz^{-b}]	Absorption (b) [Np.m^{-1}.MHz^{-b}]	Scattering (μ_a) [cm^{-1}.Sr^{-1}.MHz$^{\mu_b}$]	Scattering (μ_b) [cm^{-1}.Sr^{-1}.MHz$^{\mu_b}$]	β
Frequency (SNR calculation)	16	0.2	44	1580	1050	0.05	0	3	5.2	1.05	$2.7.10^{-4}$	1.2	4.4
Topology (INCS - main beam)	16	0.2	varies	1580	1050	0.05	-	3	5.2	1.05	-	-	4.4
Topology (Field II - grating lobe)	16	0.2	varies	1490	1000	0.05	35	3	0	-	-	-	3.5
Topology (Burgers - grating lobe)	16	0.2	varies	1580	1050	0.05	-	3	5.2	1.05	-	-	4.4

CHAPTER 10

Comparison of fundamental, second harmonic and superharmonic imaging: a simulation study[1]

Paul L.M.J. van Neer, Mikhail G. Danilouchkine, Marco M. Voormolen and Nico de Jong

Abstract Initially medical ultrasound imaging was linear - the frequency transmitted was also received and used to construct an image. The trade-off between the transmission frequency and the required penetration depth defines the attainable spatial resolution. About a decade ago ultrasound image quality was improved by exploiting the nonlinear nature of wave propagation. The method, called second harmonic imaging, selectively images the second harmonic frequency improving the lateral resolution and lowering sidelobe levels compared to fundamental imaging. Recently, a new modality dubbed 'superharmonic imaging' (SHI) was proposed. The level of the harmonics is determined by two competing phenomena - nonlinear propagation and attenuation. Thus the optimal trade-off between the spatial resolution, the penetration depth and the transmission frequency changes for second and superharmonic imaging. This paper quantitatively compares the concepts of fundamental, second harmonic and superharmonic echocardiography at their optimal transmission frequencies (3.5 MHz vs 1.8 MHz vs 1.2 MHz). For this a 3D implementation of the KZK approximation for nonlinear wave propagation was used for forward propagation. The backpropagation was assumed to be linear. The lateral -6 dB beam width is the most narrow around focus for optimal fundamental imaging. In the far field the superharmonic beam is considerably more narrow than the optimal fundamental and second harmonic beams (46% and 34% at 10 cm respectively). Also, the roll-off of the superharmonic beam is superior to that of the fundamental and second harmonic beams. The superharmonic pulse-echo peak intensity in the far field (15 cm) is equal to that of the second harmonic and only 8 dB below that of the fundamental. Thus, *in-vivo* superharmonic imaging is not only feasible but is expected to improve the image quality of echocardiography compared to the current standard of second harmonic imaging.

[1] In preparation.

10.1 Introduction

Over the last decades, medical ultrasound has greatly improved due to numerous technological advances (Tranquart et al., 1999). However, until the late 90's most of these improvements mainly impacted the technically satisfactory patient subgroup (Averkiou et al., 1997; Tranquart et al., 1999). A considerable subgroup of patients was considered difficult to image due to tough windows, inhomogeneous skin layers and limited penetration (Averkiou et al., 1997). This was especially so in the case of echocardiography, where the ultrasound propagation paths are generally long and reflections from the skeletal structures occur often. In this early period ultrasound imaging was linear - the frequency transmitted (the fundamental frequency) was also received and used to construct an image. The spatial resolution attainable is a trade-off between the transmission frequency and the required penetration depth (Ward et al., 1996). For the 15 cm imaging depth needed for echocardiography the optimal transmission frequency was found to be 3.5 MHz (Kasprzak et al., 1999).
About a decade ago it became possible to improve ultrasound image quality by exploiting the nonlinear nature of wave propagation. The technique is called tissue second harmonic imaging and is based on the selective imaging of the second harmonic frequency (Averkiou et al., 1997; Thomas and Rubin, 1998). Compared to fundamental imaging second harmonic imaging has a higher lateral resolution and lower sidelobes, and is therefore less sensitive to clutter and off-axis scatterers (Ward et al., 1996; Shapiro et al., 1998; Tranquart et al., 1999; Humphrey, 2000; Bouakaz and de Jong, 2003). Also, since the second harmonic field builds up progressively, the effects of reverberation and near-field artifacts are greatly reduced (Tranquart et al., 1999; Bouakaz and de Jong, 2003). This is particularly important for echocardiography, due to the proximity of the ribs to the available imaging windows and the intermediate skin and fat layers. Ultrasound image quality improved considerably due to these characteristics, especially for the patient subgroup considered challenging to image (Bouakaz and de Jong, 2003).
Even though the nonlinear nature of wave propagation in tissue was already used in the late 1970s for acoustic microscopy (Kompfner and Lemons, 1976) and shown to be relevant in the context of medical applications in the early to mid 1980s by Muir and Carstensen (1980) and Starritt et al. (1986), it took until the late 1990s for second harmonic imaging to take off. Reasons for this were the necessary improvements in dynamic range and signal processing, but also the widely held assumption that nonlinear distortion was not a significant factor in medical diagnostic imaging, since the frequency dependent thermoviscous absorption rapidly dissipates the generated harmonic energy (Averkiou et al., 1997). The level of the harmonics is determined by two competing phenomena - pressure dependent nonlinear propagation and attenuation. Therefore, compared to fundamental imaging, second harmonic imaging requires a different trade-off between the obtainable spatial resolution, the required penetration depth and the transmission frequency. In the case of echocardiography the optimal transmission frequency for second harmonic imaging was found to be 1.6 - 1.8 MHz (Kasprzak et al., 1999), this in contrast to the 3.5 MHz found for fundamental imaging (Kasprzak et al., 1999).
Recently, a new imaging modality dubbed tissue 'superharmonic imaging' (SHI) was proposed. The modality improves on second harmonic imaging by combining the third to fifth harmonics arising from nonlinear wave propagation (Bouakaz et al., 2002). Tissue SHI

efficiently suppresses near-field artifacts, reverberations, and off-axis artifacts in addition to the enhanced lateral and axial resolution. The resulting images showed more details than those produced by second harmonic imaging (Bouakaz and de Jong, 2003). Recently, this was confirmed in simulations and in-vitro experiments conducted by Ma et al. (2006). As SHI uses the third to fifth harmonics for imaging instead of the second harmonic, a different transmission frequency is expected to yield the optimum trade-off between spatial resolution and penetration depth. This was confirmed by van Neer et al. (2010) and Matte et al. (2010) who found optimal SHI transmission frequencies of 1.0 - 1.2 MHz for echocardiography.
Although the physical principles of the aforementioned imaging methods are different, there exists a property those methods share. The frequency ranges used to create an image in the three imaging methods - fundamental, second harmonic and superharmonic imaging -, are very similar at 3.5 MHz, 3.4 - 3.6 MHz and 3 - 4.5 MHz respectively. The question thus arises which method is the best, if they are compared under their optimal conditions. Although Zemp et al. (2003) compared the second harmonic beam produced by a 2 MHz array with the fundamental beam produced by a 4 MHz, these results were normalized. Next to the beam shape the signal intensity versus the imaging distance plays a major role in the proper comparison of each imaging method. This is especially the case for the methods based on nonlinear propagation, due to their inherent exploitation of the balance between nonlinear propagation and attenuation.

The aim of this paper is to quantitatively compare the concepts of fundamental, second harmonic and superharmonic imaging at their optimal frequencies in terms of acoustic field and energy content, applied to echocardiography.

10.2 Method

A large variety of approaches for simulating nonlinear ultrasound wave propagation in an attenuating medium has been developed during the past three decades. A model, based on the Khokhlov-Zabolotskaya-Kuznetsov (KZK) parabolic approximation, seems to be best suited to the study of weakly focused beams and is widely used for these purposes (Zabolotskaya and Khokhlov, 1969; Kuznetsov, 1971). It accounts for a number of physical phenomena including the effect of nonlinearity, diffraction and absorption. Diffraction is modeled in the KZK model via the parabolic approximation. The latter assumes that the propagating beam resembles a plane wave and advances in the preferred direction. In general, the KZK model produces a rather accurate distribution of the acoustic pressure field due to a directional sound source in the far-field (at a distance beyond a few characteristic sizes of the source). The accurate solution is also limited to the paraxial region. More details on the accuracy and validity of the KZK model can be found in the excellent papers by Tjotta et al. (1990) (Tjotta et al., 1991).

The classical wave equation for ultrasound propagation in fluids is attributed to Stokes and was modified to include the effect of thermal and viscous conduction losses (Blackstock, 1965) and nonlinearity (Kuznetsov, 1971). In the Cartesian coordinate system (x, y, z)

where z coincides with the direction of wave propagation and (x, y) the in-plane coordinates perpendicular to z, it has a form of:

$$\frac{\partial^2\Phi}{\partial t^2} - c_0^2\nabla^2\Phi = \frac{\partial}{\partial t}\left[\frac{1}{\rho_0}\left(\mu_B + \frac{4}{3}\mu\right)\nabla^2\Phi + (\nabla\Phi)^2 + \frac{\beta-1}{c_0^2}\left(\frac{\partial\Phi}{\partial t}\right)^2\right], \quad (10.1)$$

where Φ is the velocity potential of the particle due to ultrasound insonation, ρ_0 is the particle density, μ and μ_B are the shear and bulk viscosities, respectively, c_0 is the phase velocity and β is the coefficient of tissue nonlinearity. Using the Gallilean transformation, (Kuznetsov, 1971) derived the lossy wave equation in the temporal coordinate system of the propagating wave, frequently referred to as the retarded time $t' = t - z/c_0$:

$$\frac{\partial^2\Phi}{\partial t'\partial z} - \frac{c_0^2}{2}\nabla_\perp^2\Phi = \frac{\partial}{\partial t'}\left[\frac{1}{2c_0^3\rho_0}\left(\mu_B + \frac{4}{3}\mu\right)\frac{\partial^2\Phi}{\partial t'^2} + \frac{\beta}{2c_0^3}\left(\frac{\partial\Phi}{\partial t'}\right)^2\right], \quad (10.2)$$

where $\nabla_\perp^2$ is the transverse Laplacian that operates in a plane normal to the direction of propagation. To derive the equation in terms of the pressure distribution p rather than the velocity potential, $p \approx \rho_0\frac{\partial\Phi}{\partial\tau'}$, which is consistent with the adopted order of approximation:

$$\frac{\partial^2 p}{\partial t'\partial z} - \frac{c_0^2}{2}\nabla_\perp^2 p = \frac{1}{2c_0^3\rho_0}\frac{\partial}{\partial t'}\left[\left(\mu_B + \frac{4}{3}\mu\right)\frac{\partial^2 p}{\partial t'^2} + \beta\frac{\partial p^2}{\partial t'}\right]. \quad (10.3)$$

To obtain the numerical solution to (10.3) the approach of Lee and Hamilton (1995) will be further adhered to. They transform the wave equation into a non-dimensional form on the retarded Cartesian coordinated system, using the following relations:

$$\sigma = \frac{z}{d}; \qquad X = \frac{x}{a}; \qquad Y = \frac{y}{b}; \qquad \tau = \omega_0 t'; \qquad P = \frac{p}{p_0}, \quad (10.4)$$

where d is the characteristic length in the direction of propagation (e.g. a focal distance), a and b are the in-plane characteristic size of the sound source, ω_0 is the characteristic angular frequency (e.g. the center frequency of the emitted pulse) and p_0 is the peak pressure of the initial sound wave. That yields the following equation:

$$\frac{\partial P}{\partial\sigma} = \frac{1}{4}\int_{-\infty}^{\tau}\left(\frac{1}{G_x}\frac{\partial^2 P}{\partial X^2} + \frac{1}{G_y}\frac{\partial^2 P}{\partial Y^2}\right)d\tau' + NP\frac{\partial P}{\partial\tau} + A\frac{\partial^2 P}{\partial\tau^2} \quad (10.5)$$

where the dimensionless coordinates are expressed as,

$$G_x = \frac{k_0 a^2}{2d}; \quad G_y = \tfrac{k_0 b^2}{2d}; \quad N = \frac{d}{\bar{z}};$$
$$A = \alpha_0\omega_0^2 d; \quad k_0 = \tfrac{\omega_0}{c_0}; \quad \bar{z} = \frac{\rho_0 c_0^3}{\beta\omega_0 p_0};$$
$$\alpha_0 = \tfrac{\mu_B + \frac{4}{3}\mu}{2c_0^3\rho_0} \quad ,$$

with $k_0 = \omega_0/c_0$ is the wave number, $\bar{z}$ is the shock formation distance and α_0 is the absorption coefficient. It is important to mention that the viscous loss model adopted in

the KZK model simulates the propagation of ultrasound waves in fluids and assumes a quadratic-frequency dependence. However, applied to medical ultrasound such a model turns out to be inadequate, as the soft biological tissue exhibits the power-frequency dependency $\alpha_0 f^{\alpha_1}$, with the factor α_1 being equal or slightly larger than unity. The formalism proposed by Szabo (1994) allows for the generalization of the thermoviscous absorption term obeying a power-law form. It was proved that the casual convolutional propagation operator $L_{\alpha_0,\alpha_1,\tau}$ can adequately describe the sound wave dissipation in the time domain:

$$L_{\alpha_0,\alpha_1,\tau} * P = \frac{2h}{\alpha_1 + 1} \int_{-\infty}^{\tau} \frac{P(\tau')}{|\tau - \tau'|^{\alpha_1+1}} d\tau', \tag{10.6}$$

where the constant $h = -\alpha_0 \Gamma(\alpha_1 + 2) cos\left[(\alpha_1 + 1)\pi/2\right]/\pi$ with Γ being the gamma function. Equation (10.5) with the modified attenuation term of (10.6) is iteratively solved by advancing in the direction of the wave propagation σ. The traditional operator splitting scheme was employed to separately account for the effects of diffraction (the left most term on the right hand side of (10.5)), nonlinearity (the middle term on the right hand side of (10.5)) and attenuation (10.6) (Lee and Hamilton, 1995). The finite difference scheme of the Alternating Direction Implicit (ADI) algorithm was employed to solve the diffraction term. In the ADI method each step is divided into two half-steps: the differentiation is applied first in the lateral direction followed by the elevation direction. The nonlinearity was numerically solved via the classical Poisson scheme. A complete description of the algorithms can be found in the PhD-thesis of Voormolen (2007). The discrete form of the attenuation contribution is expressed via a finite sum for each in-plane coordinate (x, y):

$$\sum_{n=0}^{T} L_{\alpha_0,\alpha_1}(n\triangle t) \cdot P(x, y, (k-n)\triangle t)\triangle t, \tag{10.7}$$

where $T = k\triangle t$ is the temporal length of the emitted wave, $\triangle t$ is the discrete time step and discrete representation of the casual convolutional propagation operator has the following form:

$$L_{\alpha_0,\alpha_1}(n\triangle t) = -2H_+(n\triangle t) \cdot \mathbf{IFT}\left[\alpha_0 |\omega|^{\alpha_1}\right], \tag{10.8}$$

where **ITF** is the inverse Fourier transformation, H_+ represents the step function:

$$H_+(n\triangle t) = \begin{cases} 0 & \text{if } n < 0, \\ 0.5 & \text{if } n = 0, \\ 1 & \text{if } n > 0. \end{cases} \tag{10.9}$$

10.3 Simulation settings

In this paper three imaging modalities applied to echocardiography are compared: fundamental, second and superharmonic imaging. The acoustic beams produced in each modality were calculated using a full 3D implementation of the KZK equation up to an axial depth of 15 cm. To estimate the energy received by the transducer in the pulse-echo mode for each of the imaging modalities, linear back propagation was assumed. It was assumed

Table 10.1: The array geometries used for the simulations

	Transmit frequency (MHz)	p_0 (kPa)	Footprint (mm^2)	Nbr. of elements -	Element size (mm^2)	Kerf (mm)
Fundamental imaging	3.5	800	16 x 22	128	16 x 0.12	0.05
Second harmonic imaging	1.8	580	16 x 22	88	16 x 0.2	0.05
Superharmonic imaging	1.2	1280	16 x 22	44	16 x 0.2	0.3

that all energy was backscattered. The transmission pressure amplitude at the element surface was taken such that an MI of 1.9 was produced in the lossless case.
For fundamental imaging the optimal transmission frequency of 3.5 MHz as reported by Kasprzak et al. (1999) was used. The transducer geometry consisted out of 128 elements with size 16 mm x 0.12 mm. The kerf was 0.05 mm. The transmission pressure amplitude at the element surface (p_0) was 800 kPa. For second harmonic imaging the optimal transmission frequency of 1.8 MHz as reported by Kasprzak et al. (1999) was used. The transducer geometry consisted out of 88 elements with size 16 mm x 0.2 mm. The kerf was 0.05 mm. The transmission pressure amplitude at the element surface (p_0) was 580 kPa. For superharmonic imaging the optimal transmission frequency of 1.2 MHz as reported by Matte et al. (2010) was used. The transducer geometry was based on the interleaved array reported by van Neer et al. (2010). The low frequency subarray of this transducer is used in transmission and consists of 44 elements (16 mm x 0.2 mm). The kerf was 0.3 mm and so the lateral dimension of the array was 22 mm. The transmission pressure amplitude at the element surface (p_0) was 1280 kPa. The settings used to simulate each imaging modality are described in Table 10.1. Notice that the footprint is equal for each array at 16 mm x 22 mm. In all cases both the elevation and the lateral foci were set to 60 mm. No beam steering was applied. Three cycle Gaussian apodized sine bursts were used as transmission signals.
The acoustic nonlinearity parameter (B/A) was taken to be 5.8, based on values reported for human fetal cardiac tissue (Duck, 1990). The attenuation was modeled as $a = \alpha_0.f^{\alpha_1}$ with α_0 = 0.52 dB cm^{-1} $MHz^{-\alpha_1}$ and α_1 = 1, based on properties reported for cardiac muscle from dog (Duck, 1990). Also, a density of 1060 kg/m^3 reported for cardiac muscle was used, as well as an acoustic wave speed of 1529 m/s reported for human fetal cardiac tissue (Duck, 1990).

10.4 Results

The lateral intensity profiles of the fundamental at 3.5 MHz (solid line), the second harmonic at 3.6 MHz (dashed line) and the superharmonic at 3.6 - 6 MHz (dotted line) at a depth of 6 cm are displayed in Fig. 10.1. The lateral -6 dB beam width was 1.44 mm, 1.67 mm and 1.95 mm for the fundamental, second harmonic and superharmonic respectively. The intensity level 10 mm off the beam-axis relative to the on-axis intensity was -33 dB, -47 dB and -49 dB for the fundamental, second harmonic and superharmonic respectively.

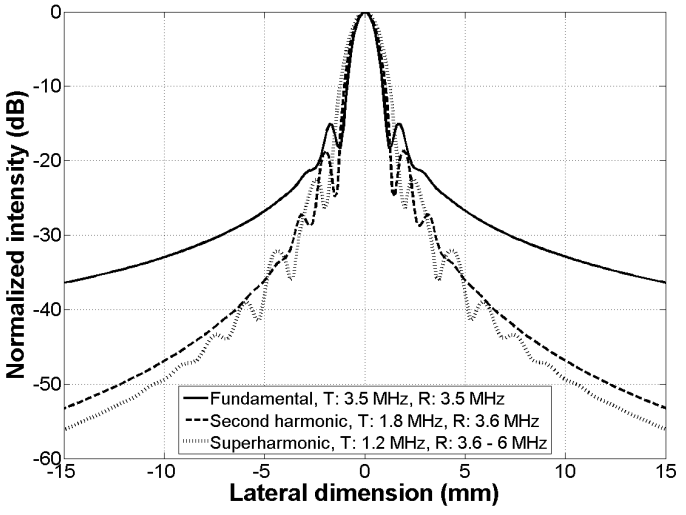

Figure 10.1: The lateral intensity profiles of the fundamental at 3.5 MHz (solid line), the second harmonic at 3.6 MHz (dashed line) and the superharmonic at 3.6 - 6 MHz (dotted line) at a depth of 6 cm. The intensity values are relative to 1 Pa.

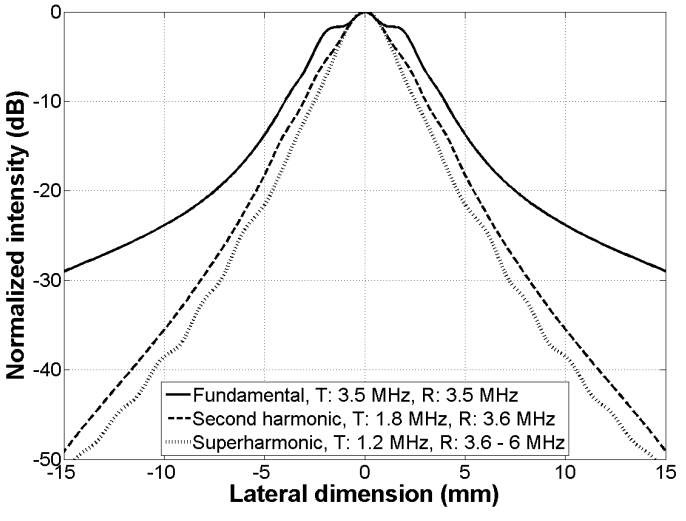

Figure 10.2: The lateral intensity profiles of the fundamental at 3.5 MHz (solid line), the second harmonic at 3.6 MHz (dashed line) and the superharmonic at 3.6 - 6 MHz (dotted line) at a depth of 8 cm. The intensity values are relative to 1 Pa.

The lateral intensity profiles of the fundamental at 3.5 MHz (solid line), the second harmonic at 3.6 MHz (dashed line) and the superharmonic at 3.6 - 6 MHz (dotted line) at a depth of 8 cm are displayed in Fig. 10.2. The lateral -6 dB beam width was 5.7 mm, 4.3 mm and 3.4 mm for the fundamental, second harmonic and superharmonic respectively. The intensity level 10 mm off the beam axis relative to the on-axis intensity was -24 dB, -36 dB and -39 dB for the fundamental, second harmonic and superharmonic respectively. The lateral intensity profiles of the fundamental at 3.5 MHz (solid line), the second harmonic at 3.6 MHz (dashed line) and the superharmonic at 3.6 - 6 MHz (dotted line) at a depth of 10 cm are displayed in Fig. 10.3. The lateral -6 dB beam width was 12.4 mm, 10.3 mm and 6.8 mm for the fundamental, second harmonic and superharmonic respectively. The intensity level 10 mm off the beam axis relative to the on-axis intensity was -14 dB, -20 dB and -25 dB for the fundamental, second harmonic and superharmonic respectively. The pulse-echo axial intensity profiles of the fundamental at 3.5 MHz (solid line), the second harmonic at 3.6 MHz (dashed line) and the superharmonic at 3.6 - 6 MHz (dotted line) are displayed in Fig. 10.4. The peak intensity of 116 dB for the fundamental occurred at 54.2 mm, while the peak intensity of 103 dB for the second harmonic occurred at 52.9 mm. For the superharmonic the peak intensity was 96 dB and occurred at 51.0 mm. The intensities at a pulse-echo axial depth of 5 cm were 115 dB, 102 dB and 96 dB for the fundamental, second harmonic and superharmonic respectively. At a pulse-echo depth of 10 cm the intensities became 82 dB, 76 dB and 74 dB respectively and at a pulse-echo depth of 15 cm the intensities became 57 dB, 49 dB and 49 dB for the fundamental, second harmonic and superharmonic respectively.

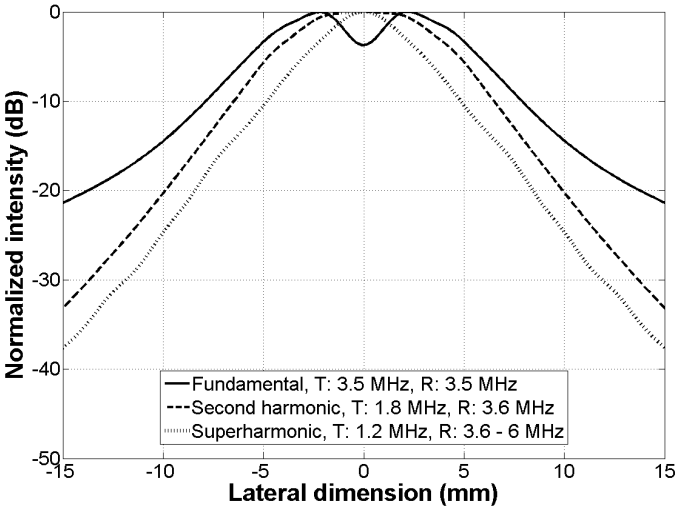

Figure 10.3: The lateral intensity profiles of the fundamental at 3.5 MHz (solid line), the second harmonic at 3.6 MHz (dashed line) and the superharmonic at 3.6 - 6 MHz (dotted line) at a depth of 10 cm. The intensity values are relative to 1 Pa.

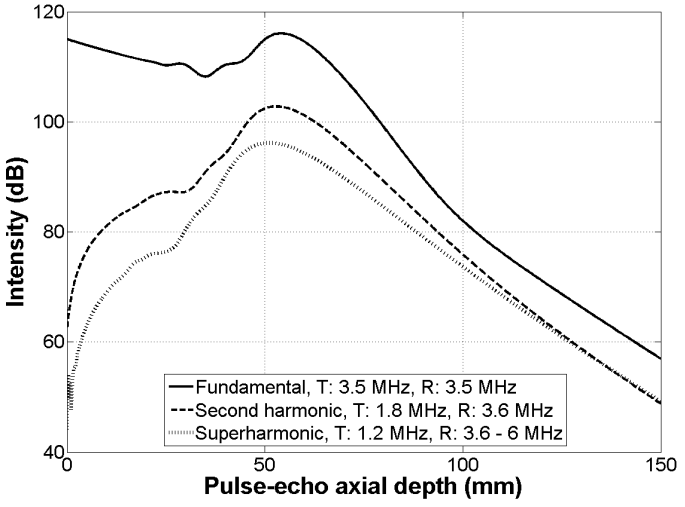

Figure 10.4: The pulse-echo axial intensity profiles of the fundamental at 3.5 MHz (solid line), the second harmonic at 3.6 MHz (dashed line) and the superharmonic at 3.6 - 6 MHz (dotted line). The intensity values are relative to 1 Pa.

10.5 Discussion

To the authors knowledge the comparison between the fundamental, second harmonic and superharmonic imaging modalities at their respective optimal frequencies is the first one of its kind reported in the literature. The -6 dB lateral beam widths of the second and superharmonic are 14% and 26% wider than the fundamental at 6 cm. Next to that the focal points of the fundamental and second harmonic beams are located slightly further away from the transducer and closer to 60 mm than that of the superharmonic beam. At larger distances (10 cm) the superharmonic beam has a -6 dB lateral beam width which is 46% and 34% narrower than the fundamental and second harmonic beams respectively. These characteristics are due to the fact that the superharmonic beam is hardly focused, as the natural focus of the aperture is close to the lateral and elevation foci of 60 mm. Therefore, the focal zone is elongated and the ultrasound beam spreads slowly. The superharmonic beamshape is thus largely determined by the autofocusing effect caused by nonlinear propagation. This in contrast to the fundamental and second harmonic beams, which are considerably more focused due to the higher transmission frequencies at equal aperture dimensions. Therefore, these beams spread more rapidly after focus compared to the superharmonic beam. The roll-off of the second and superharmonic beams is considerably higher than that of the fundamental beam. Interestingly enough, the roll-off of the second and superharmonic beams is similar in shape, but the latter has a 2 - 5 dB advantage.
It is the increased roll-off in combination with the progressive build-up of the harmonic beams, which leads to less clutter and a better suppression of near-field artifacts and reverberation in harmonic images compared to a fundamental image - despite the increased

beam widths around focus. The superharmonic beam has a considerably narrower beam width away from the focus and an increased roll-off compared to the second harmonic beam. Also, 62% shorter pulse lengths have been reported for superharmonic beams compared to second harmonic beams (Bouakaz and de Jong, 2003). Therefore, it is expected that the superharmonic image will improve on the second harmonic image - especially in the far field.

The peak intensity of the superharmonic beam is 20 dB and 7 dB lower than those of the fundamental and second harmonic beams respectively. However, the intensity loss associated with the imaging of larger depths is lower for superharmonic imaging compared to fundamental and second harmonic imaging. At 150 mm the superharmonic pulse-echo intensity is slightly higher than that of the second harmonic and only 8 dB lower than that of the fundamental. This indicates that *in-vivo* superharmonic imaging using its optimal frequency should be equally feasible as second harmonic imaging - the current standard. Because the results of the KZK model are inaccurate in the near-field, no conclusions are drawn on possible differences in build-up of the second and superharmonic beams.

The simulations performed here assumed a homogeneous propagation medium and used the material properties reported for cardiac tissue. However, in the case of echocardiography a propagating sound wave encounters a mix of cardiac tissue and blood. Although the B/A values of blood (6.0) and cardiac tissue (5.8) are similar, the attenuation of blood ($\sim$0.14 dB.cm^{-1}.MHz$^{1.2}$) is about 3 - 4 times lower than that of cardiac tissue (0.52 dB.cm^{-1}.MHz^{-1}) (Duck, 1990). Therefore, the axial pulse-echo pressures reported here are a worst case scenario.

The MI is defined as the derated peak negative pressure divided by the square root of the frequency (Cobbold, 2007). However, in this article the peak negative pressure was not derated for the calculation of the MI. If the derated peak negative pressure was used for the MI calculation, the axial profiles for fundamental and second harmonic imaging would shift up by $\sim$11 dB. However, the superharmonic is made up from the third - fifth harmonic. The third harmonic component would also shift up by $\sim$11 dB, but the fourth and fifth harmonics would shift up by $\sim$15 dB and $\sim$19 dB respectively. Thus backscattered superharmonic intensity would effectively increase somewhat compared to the intensities obtained using the fundamental and second harmonic imaging modalities.

In these simulations the backscattered energy in the direction of receiving aperture is equal to the incident power. Thus, the frequency dependent character of the backscattering was ignored. This hypothesis is valid for the fundamental of 3.5 MHz, second and third harmonics of 3.6 MHz, as those frequencies are of the same order of magnitude. However, for forth and fifth harmonic backscattering is expected to be larger taking into account the power frequency dependency of biological tissue. Hence we consider a worst-case scenario with respect to the superharmonic. It is important to mention that the contribution of those harmonics to the superharmonic imaging is much lower than the one of the third. Therefore, it was a good approximation to assume a frequency independent character of the backscattering.

10.6 Conclusion

The optimal superharmonic beam is considerably more narrow than the optimal fundamental and second harmonic beams, except at focus where the optimal fundamental beam is the most narrow. Also, the roll-off of the superharmonic beam is superior to that of the fundamental and second harmonic beams. At large depths the superharmonic pulse-echo peak intensity is equal to that of the second harmonic. Therefore, *in-vivo* superharmonic imaging is not only feasible but is expected to improve the image quality of echocardiography compared to the current standard of second harmonic imaging.

CHAPTER 11

Postprocessing methods for superharmonic imaging[1]

Paul L.M.J. van Neer

Abstract Second harmonic imaging is currently the de-facto standard in commercial echographic systems for diagnosis because of its improved resolution and contrast-to-tissue ratio. An emerging technique called superharmonic imaging is based on a combination of multiple frequency components generated during the propagation of sound in tissue. This combination of third to fifth harmonic has the potential to further enhance resolution and image quality of echographic pictures. In this chapter the characteristics of the superharmonics are discussed from an imaging viewpoint using various postprocessing methods. We show that the use of these postprocessing methods alone will be insufficient for the production of high quality *in-vivo* superharmonic images.

[1]Based on nonpublished work performed in cooperation with G.M. Matte, J.M.G. Borsboom, M. Danilouchkine and N. de Jong.

11.1 Introduction

Superharmonic imaging (SHI) was introduced as the combination of the third, fourth and fifth harmonics. The modality improves on second harmonic imaging by combining the third to fifth harmonics arising from nonlinear wave propagation or contrast agent response (Bouakaz et al., 2002). Tissue SHI suppresses near-field artifacts and reverberations better than tissue second harmonic imaging, since the distance at which the energy in a harmonic band becomes significant increases with the harmonic number (Bouakaz and de Jong, 2003). Also, SHI has increased lateral and axial resolution compared to second harmonic imaging (Bouakaz and de Jong, 2003). And finally, SHI suppresses off-axis artifacts better than second harmonic imaging, due to the increased lateral roll-off of the higher harmonics compared to the second harmonic (Bouakaz and de Jong, 2003). Therefore, the resulting images showed more details than those produced by second harmonic imaging (Bouakaz and de Jong, 2003). SHI is also promising for UCA enhanced imaging. It has been demonstrated by Bouakaz et al. (2002) that the contrast-to-tissue ratio (CTR) increases as a function of the harmonic number. Thus, SHI in combination with contrast agents produces a higher CTR than second harmonic imaging, while at the same time minimizing shadowing effects (Bouakaz et al., 2002).

11.2 Imaging using multiple harmonics: ripple artifacts

The standard image processing used for medical ultrasound imaging consists of filtering the relevant frequency band and subsequently taking the Hilbert transform to obtain the envelope data. Ideally, the envelope of a pressure signal produced by a single reflector should monotonically increase before its maximum and monotonically decrease afterwards. Thus a single reflector is indicated by a single reflection in a B-mode image.
If the pressure signal originally transmitted is short (a single cycle), the demodulation of the propagated pressure signal over the superharmonic band dramatically improves the axial resolution. However, in practice the pressure signals transmitted by commercial transducers are usually longer due to the limited bandwidth of the transducer and attached circuitry. In this case the envelope of the propagated pressure signal filtered over the superharmonic band contains ripples as shown in Fig. 11.1. The ripples in the time domain representation lead to ghost reflections in B-mode images: single reflectors appear as multiple overlapping reflectors. The ripples are caused by the troughs between the harmonics, as these troughs break up the superharmonic band (see Fig. 11.2). The troughs are deeper and wider - and the ripples thus more pronounced -, if the signal transmitted by the transducer is more narrowband. Fig. 11.3 shows the relation between transmission signal length/bandwidth versus the ripple depth versus the ripple depth of the time signal at focus filtered at the superharmonic band. The data was obtained using 3D-KZK simulations (Voormolen, 2007). Gaussian apodized sine bursts of varying length with amplitude 1.7 MPa were transmitted using the dual frequency transducer presented in chapter 8 as a source (van Neer et al., 2010). The propagation medium was water. Using 3 cycle transmissions the KZK simulation predicts a 4 dB ripple in the envelope of the time signal filtered at the superharmonic band. This is equal to the experimentally obtained envelope shown in Fig. 11.1. The simu-

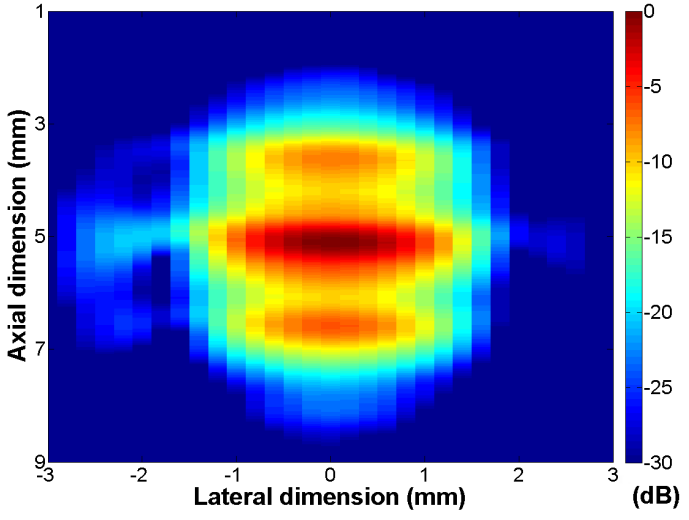

Figure 11.1: The envelope of a pressure signal, which has propagated 6 cm, filtered over the superharmonic band. The pressure signal was produced by the interleaved array combined with the OPEN system and recorded using a hydrophone setup. The propagation medium was water. In transmission three cycle 1 MHz Gaussian apodized sine bursts with amplitude 60 V were used.

lations predict that transmissions with 65% or more -6 dB bandwidth - 1.5 cycle Gaussian apodized sine bursts and shorter - will not result in ripples in the envelope of the time signal filtered at the superharmonic band.

11.2.1 Minimizing ripple artifacts by adding filtered harmonics

Perhaps the most simple solution to the ripple issue is to filter each harmonic band separately, to take the Hilbert transform of each and then to add them in the time domain. The result would have the lateral characteristics expected for SHI, but would have disappointing length in the axial dimension. The reason is that the time length of the signal is determined by the -6 dB bandwidth of a single harmonic in stead of the whole superharmonic band.
A problem of this method is the phase difference between the harmonics. These differences lead to the blurring of the echoes due to the misalignment of the B-mode images produced by each harmonic. This effect becomes more pronounced for short time signals. Phase differences between harmonics are produced in the pulse-echo chain of medical imaging equipment by the electronics, the phase transfer function of the transducer, the transducer's electrical impedance, and by nonlinear wave propagation. Furthermore, the filtering of the harmonics in the postprocessing will modify the phase of the signals.

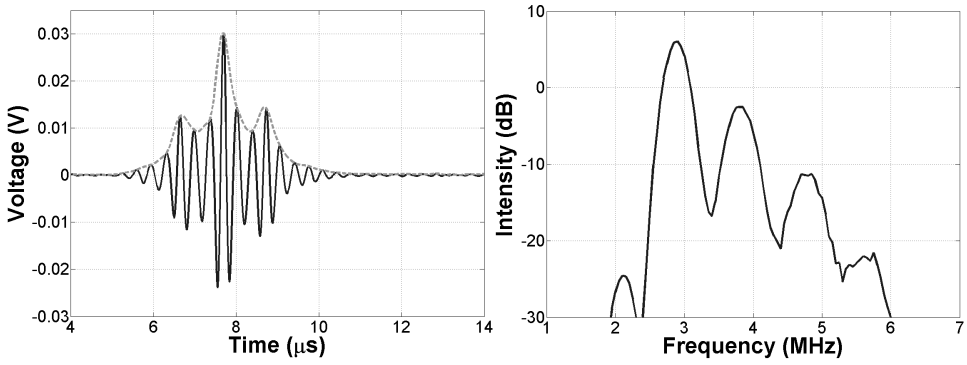

Figure 11.2: On the left the on-axis time signal and its envelope from Fig. 11.1 is displayed. On the right the associated magnitude spectrum of its Fourier transform is shown.

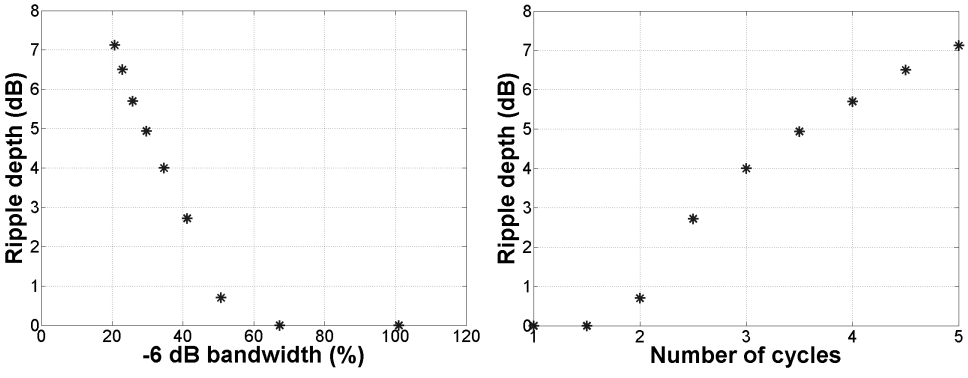

Figure 11.3: On the left the -6 dB bandwidth of the signal transmitted by the transducer versus the ripple depth of the time signal at focus filtered at the superharmonic band. On the right the length of the signal transmitted by the transducer versus the ripple depth of the time signal at focus filtered at the superharmonic band. The data is obtained using 3D-KZK simulations (Voormolen, 2007). The transmitted pulses were Gaussian apodized sine bursts of varying length with amplitude 1.7 MPa. The dual frequency transducer presented in chapter 8 was modeled as a source (van Neer et al., 2010). The propagation medium was water.

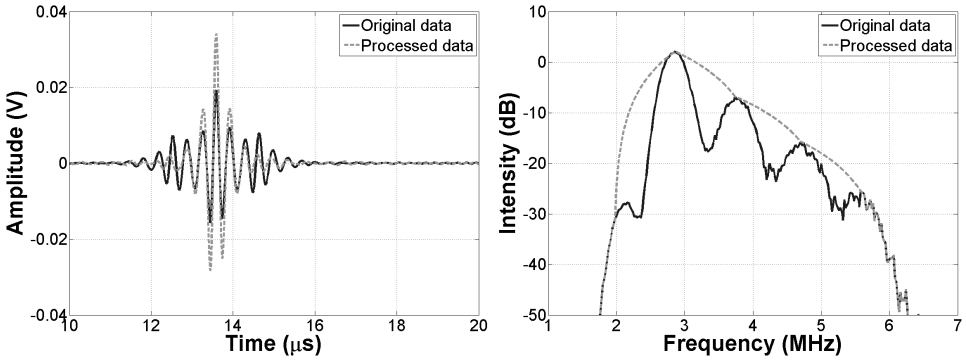

Figure 11.4: The effect of inverse filtering on a nonlinearly propagated pressure signal filtered at the superharmonic band. The original (solid black line) and processed (dashed gray line) time signals and their associated Fourier spectra are displayed on the left and right respectively. The pressure signal was produced by the interleaved array combined with the OPEN system and recorded at an axial distance of 6 cm using a hydrophone setup. The propagation medium was water. In transmission 2.5 cycle 1 MHz Gaussian apodized sine bursts with amplitude 60 V were used.

11.2.2 Minimizing ripple artifacts by 'inverse filtering'

Another option to reduce the ripples associated with SHI is to perform 'inverse filtering'. This method amplifies the frequencies which are low in energy to obtain a smooth band from the third to the fifth harmonic. There are various 'inverse filters' possible, but to highlight the method's advantages and disadvantages a simple implementation is used. A nonlinearly propagated pressure wave is recorded and a Fourier transform is taken of the signal. The maxima of the third, fourth and fifth harmonics are detected in the magnitude spectrum. Between these three maxima the magnitude spectrum is linearly interpolated. The phase spectrum remains unaltered. The new time signal is obtained by taking the inverse Fourier transform.

Some results produced using this method (dashed gray lines) are shown in Figs. 11.4 and 11.5. The original pressure signal filtered over the superharmonic band (solid black line) propagated over 6 cm. The pressure signal was produced by the dual frequency array in combination with the OPEN system and recorded using a hydrophone setup. The propagation medium was water. To obtain the signal displayed in Fig. 11.4 2.5 cycle Gaussian apodized bursts of center frequency 1 MHz with amplitude 60 V were transmitted. To obtain Fig. 11.5 similar signals were transmitted, but 8 cycles in length and with amplitude 30 V. On the left of Figs. 11.4 and 11.5 the recorded pressure signals filtered at the superharmonic band are shown and on the right of these figures the magnitude spectra of the associated Fourier transforms are shown. As can be observed in Fig. 11.4 the envelope of the original pressure signal (solid black line) would contain ripples and a resulting B-mode image would contain ghosting artifacts. The troughs between the harmonics causing these

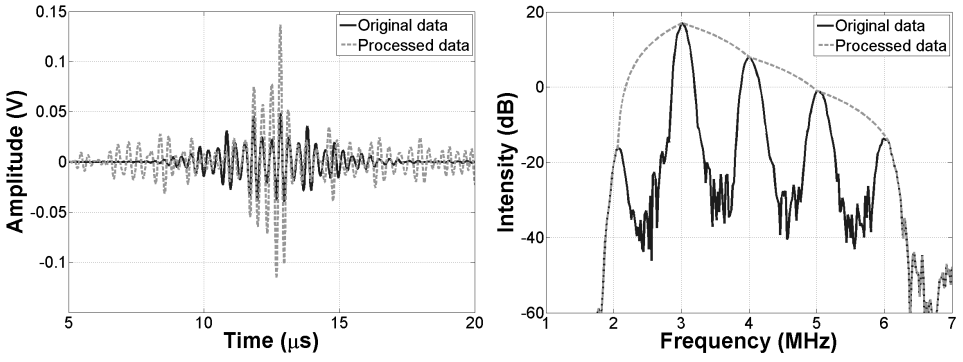

Figure 11.5: The effect of inverse filtering on a nonlinearly propagated pressure signal filtered at the superharmonic band. The original (solid black line) and processed (dashed gray line) time signals and their associated Fourier spectra are displayed on the left and right respectively. The pressure signal was produced by the interleaved array combined with the OPEN system and recorded at an axial distance of 6 cm using a hydrophone setup. The propagation medium was water. In transmission 8 cycle 1 MHz Gaussian apodized sine bursts with amplitude 30 V were used.

ripples can be observed in the corresponding graph on the right of the figure. The 'inverse filtered' pressure signal (dashed gray line) on the other hand has a smooth band from the third to the fifth harmonic. Therefore, the envelope of the time signal displayed on the left of Fig. 11.4 is short and ripple free. The original pressure signal of Fig. 11.4 is ideal for the 'inverse filtering' approach in the sense that the signal-to-noise-ratio (SNR) is sufficient at every relevant frequency - even at the frequencies between the harmonics. In the case of an 8 cycle transmission the result of the inverse filtering approach is different (see Fig 11.5). Although the magnitude of the Fourier spectrum of the processed signal shows a smooth band from the third to the fifth harmonic, the envelope of the processed signal would be worse than the original signal for imaging purposes. The reason is related to the phase associated with each frequency component of the signal.

Fig. 11.6 shows the phase spectra of the Fourier transformed 2.5 cycle (solid black line) and 8 cycle (dashed gray line) bursts displayed in Figs. 11.4 and 11.5. The phase spectrum of the 2.5 cycle burst has a fairly constant slope, the value of which is related to the distance in wavelengths between the start of the window and the location of the reflection in the window. The phase spectrum of the 8 cycle burst has an almost constant first derivative on the frequencies with high SNR - the harmonic bands -, but is semi-random on the frequencies with low SNR between the harmonics. If the frequency components with semi-random phase are amplified using the 'inverse filtering' method, signal is produced at locations in the pressure time signal where no reflector was located and the method breaks down.

The 'inverse filtering' approach is simple and provides good results in *in-vitro* experiments with high SNR. However, it will only lead to a useful result, if the SNR of each frequency component is high enough to ensure that the associated phase of each frequency component

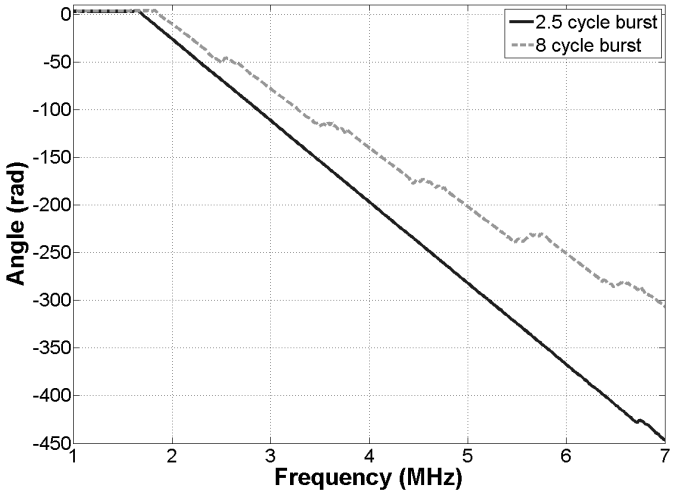

Figure 11.6: The phase spectra of the Fourier transformed 2.5 (solid black line) and 8 cycle (dashed gray line) bursts displayed in Figs. 11.4 and 11.5.

in the superharmonic band is nonrandom. In the case of narrowband transmission signals or at the low SNRs associated with *in-vivo* imaging this condition does not always hold. Therefore, the 'inverse filtering' method is deemed unsuitable for *in-vivo* superharmonic imaging.

11.3 Conclusion

The use of these postprocessing methods alone will not produce high quality *in-vivo* superharmonic images reliably. More complicated transmission schemes are needed. A dual pulse pulsing scheme and a chirp based method are introduced in the following chapters.

CHAPTER 12

A new frequency compounding technique for superharmonic imaging[1]

Guillaume M. Matte, Paul L.M.J. van Neer, Jerome M.G. Borsboom, Martin D. Verweij, Nico de Jong

Abstract Second harmonic imaging is currently the de-facto standard in commercial echographic systems for diagnosis because of its improved resolution and contrast-to-tissue ratio. An emerging technique called superharmonic imaging is based on a combination of multiple frequency components generated during the propagation of sound in tissue. This combination of third to fifth harmonic has the potential to further enhance resolution and image quality of echographic pictures. In order to fulfill the bandwidth requirements of superharmonic imaging, a special interleaved phased array transducer has been developed (Bouakaz et al., 2004b). Currently, the achievable bandwidth for phased array elements used in transmission is close to 80%, but the total system bandwidth in transmission is often lower. Thus harmonics generated during wave propagation will be separated by gaps in the frequency domain. That will introduce specific artifacts visible as ripples in the echo image. We propose a dual pulse method for superharmonic imaging that reduces the ripple artifacts and recovers the axial resolution. This technique consists in firing two lines with a 15% frequency shift for the second firing. Summing the echoes of those two lines will result in filling the gaps in the frequency band of the distorted signal. The optimal choice for the frequency of the second pulse can be derived analytically. Standard detection methods applied to this dual pulse technique will strongly minimize artifacts encountered with envelope detection on superharmonic signals. Theoretical calculations show an improvement in axial resolution by a factor of 2.1 at the -15 dB level compared to the third harmonic. Experimentally, this method shortens the pulse by a factor 2.0 at the -15 dB level compared to the third harmonic. Superharmonic imaging quality can be further improved by frequency compounding techniques such as the dual pulse method described here.

[1]Based on G. M. Matte, P.L.M.J. van Neer, J.M.G. Borsboom, M.D. Verweij, N. de Jong, 'A new frequency compounding technique for super harmonic imaging', Proc. IEEE Ultrasonic Symp., 2008, 357-360.

12.1 Introduction

Superharmonic imaging was introduced as the combination of the third, fourth and fifth harmonics. Its aim was to further improve image resolution and to reduce reverberations compared to second harmonic imaging (Bouakaz et al., 2002; Bouakaz and de Jong, 2003; Bouakaz et al., 2004b). If the transmitted pulse would have a single cycle length, the demodulation of the signal received over the superharmonic band would dramatically improve the axial resolution. The choice to combine the third to fifth harmonics was made to integrate the energy over a large frequency band to gain in terms of amplitude of the received pulse compared to a single harmonic. Another viewpoint is to consider the fourth harmonic as the center of this band of interest. The band of the neighboring harmonics is then used to enlarge the receiver frequency band and thus to increase the axial resolution.
Contemporary transducers made of PZT piezoceramics have up to 80% -6 dB bandwidth with good transmit efficiency, but the transmission system bandwidth is often lower due to electrical tuning. If a pulse with low bandwidth propagates nonlinearly in a thermoviscous medium such as water or tissue, the resulting distorted pulse will show distinct troughs in its frequency spectrum. This separation between the harmonics becomes problematic, if a Hilbert transform is taken of the superharmonic band to obtain the envelope data - a standard method to obtain the signal envelope. In this case the resulting envelope signal will contain ripples.
We propose a solution consisting of transmitting two pulses with the second pulse of slightly different frequency. The sum of these two pulses in the time domain produces a smooth frequency spectrum and the ripple artifacts are minimized. In the time domain, the sum of the two distorted pulses and the wideband filtering around the fourth harmonic is analogous to destructive interference on the ripples of the superharmonic signal. This effect sharpens the superharmonic point spread function (PSF). The PSF used here combines the convolution of the electrical excitation (the pulsing scheme), the transmit transfer function and the spatial impulse response with the effects of nonlinear propagation and postprocessing. Firstly, an analytic method to calculate the optimal frequency of the second pulse based on nonlinear wave propagation is described. Secondly, the performance of the dual pulse method will be explored using a modified Fubini solution, KZK simulations and experiments with single element transducers.

12.2 Theory

An estimate for the optimal frequency of the second transmitted pulse is calculated using the Fubini solution. To this end we modify this equation to hold for Gaussian apodized sine bursts. Although the Fubini solution is strictly speaking only valid for monochromatic signals, this modification will provide insight in the dual pulse method.

The Fubini solution for weakly shocked plane waves produced by a monofrequency source is valid in the preshock region ($\sigma < 1$) (Hamilton and Blackstock, 1998). If a Gaussian

envelope is added to the Fubini solution, we obtain

$$p(\sigma,\tau) = p_0 \sum_{n=1}^{\infty} B_n e^{\left[-n\left(\frac{\omega_0 \tau}{n_c \pi}\right)^2\right]} e^{i(n\omega_0\tau+\varphi)}, \tag{12.1}$$

with n the number of harmonics, n_c the number of cycles, τ the time, ω_0 the angular frequency of the fundamental, φ a phase offset, $B_n = \frac{2}{n\sigma} J_n(n\sigma)$, σ the normalized shock formation distance for monofrequency excitation defined as $\sigma = \frac{z}{\overline{z}}$, z the axial distance, $\overline{z}$ the shock wave distance defined as $\overline{z} = \frac{\rho_0 c_0^3}{\beta \omega_0 p_0}$, ρ_0 the ambient density, c_0 the small-signal acoustic wavespeed and β the nonlinearity parameter.

Using distributions for $\omega \in [0; +\infty]$ (12.1) can be written in the frequency domain as

$$p(\sigma,\omega) = p_0\sqrt{2\pi} \sum_{n=1}^{\infty} \frac{B_n}{\sqrt{2\mu_n}} e^{\left[-\frac{(\omega - n\omega_0)^2}{4\mu_n}\right]}, \tag{12.2}$$

with ω the angular frequency and $\mu_n = n\left(\frac{\omega_0}{n_c\pi}\right)^2$.
A nonlinearly propagated pressure pulse with limited transmission bandwidth will show distinct peaks in its frequency spectrum and the resulting superharmonic PSF contains ripples. The easiest method to minimize this effect by transmitting a second pulse is to locate the third harmonic peak of the second pulse at the minimum between the third and fourth harmonics of the first transmission pulse. The fourth harmonic of the second pulse will then be located between the fourth and fifth harmonic of the first pulse leading to a smooth frequency spectrum of the summed pulse. Thus, we can limit ourselves to the third and fourth harmonics and write (12.2) as

$$p_{SH}(\sigma,\omega) = p_0\sqrt{\pi}\frac{n_c\pi}{\omega_0}\left[\frac{B_3}{\sqrt{3}} e^{-\frac{\left(\frac{\omega}{\omega_0}-3\right)^2\left(\frac{\pi n_c}{2}\right)^2}{3}} + \frac{B_4}{\sqrt{4}} e^{-\frac{\left(\frac{\omega}{\omega_0}-4\right)^2\left(\frac{\pi n_c}{2}\right)^2}{4}}\right]. \tag{12.3}$$

To find the frequency of the minimum between the third and fourth harmonic we need to solve $\frac{dp_{SH}(\sigma,\omega)}{d\omega} = 0$ around $\omega = 3.5\omega_0$. To this end (12.3) is developed in a Taylor series around $\omega = 3.5\omega_0$. A second order Taylor series provides sufficient accuracy (a third order expansion improves the accuracy by only 0.05%) and leads to

$$\frac{\omega_{min}}{\omega_0} = \frac{\frac{B_3}{6\sqrt{3}} e^{\frac{-(n_c\pi)^2}{48}} - \frac{B_4}{8\sqrt{4}} e^{\frac{-(n_c\pi)^2}{64}}}{\left[\frac{(n_c\pi)^2}{24} - 1\right]\frac{B_3}{3\sqrt{3}} e^{\frac{-(n_c\pi)^2}{48}} + \left[\frac{(n_c\pi)^2}{32} - 1\right]\frac{B_4}{4\sqrt{4}} e^{\frac{-n_c\pi}{64}}} + 3.5, \tag{12.4}$$

with ω_{min} the angular frequency of the minimum between the 3^{rd} and 4^{th} harmonics.

The optimum frequency of the second pulse is then given by $\omega_2 = \frac{\omega_{min} - 3\omega_0}{3}$.

12.3 Materials and methods

Firstly, a simulation program was made using Matlab (The Mathworks, Inc., Natick, MA, USA) based on (12.1). As described in the theory section the second optimal frequency

was calculated using (12.4) and a numerical fitting procedure. The transmitted signal p_0 was a gaussian apodized sine burst with center frequency 2.25 MHz, 3 cycles in length and with 450 kPa amplitude. Water was used as the propagation medium, with ρ_0 = 1000 kg/m^3, c_0 = 1490 m/s and β = 3.5. The pressure wave propagated 8 cm.
Secondly, the influence of this dual pulse method on the PSF was studied using the KZK equation (Lee and Hamilton, 1995). The KZK equation was solved in the time domain using a finite difference method (Lee and Hamilton, 1995) using an algorithm programmed in the C and Matlab languages. The simulations were performed for an axisymmetric unfocused transducer 12.7 mm in diameter, which transmitted Gaussian apodized sine bursts with a center frequency of either 1 MHz or 2.25 MHz. Water was used as the propagation medium.
And finally, experimental PSFs were obtained using lateral beam profile measurements of two transducers. One transducer had a resonance frequency of 1 MHz (AS303, Panametrics, Waltham, MA, USA) and the other a resonance frequency of 2.25 MHz (V306, Panametrics, Waltham, MA, USA). Both were unfocused and had diameters of 12.7 mm. The transmitting transducer was excited using gaussian apodized 3 cycle sine bursts of amplitude 65 mV produced by an arbitrary waveform generator (32250A, Agilent, Santa Clara, USA) and amplified by a power amplifier of 56 dB (AR, Southerton, PA, USA). The transmitting transducer was mounted in the sidewall of a water filed tank. The beam profiles were measured using a hydrophone (diameter 0.2 mm, Precision Acoustics, Dorchester, UK) mounted in a xyz-system. For the experiment using the 1 MHz transducer the lateral beam profiles were recorded at an axial distance of 0.3 cm. The axial distance was 8 cm for the experiment using the 2.25 MHz transducer.

12.4 Results and discussion

12.4.1 Fubini solution versus experiment

The optimum frequency of the second pulse for the dual pulse method was calculated to be 15% higher than the frequency of the first pulse.
Axial PSFs were studied using simulations based on the modified Fubini solution and using experiments based on the 2.25 MHz transducer. The peak pressure produced by the 2.25 MHz transducer was 450 kPa at an axial distance of 8 cm. This pressure was used as the input for the Fubini equation. Fig. 12.1 shows the axial PSFs of the third harmonic, single pulse superharmonic and dual pulse superharmonic as calculated using the modified Fubini solution. The axial lengths at the -15 dB level were 1.8 mm, 1.6 mm and 0.84 mm for the third harmonic, single pulse superharmonic and dual pulse superharmonic respectively. Fig. 12.2 details the axial PSFs of the third harmonic, single pulse superharmonic and dual pulse superharmonic as measured experimentally. The measured axial lengths at the -15 dB level were 2.2 mm, 2.0 mm and 1.1 mm for the third harmonic, single pulse superharmonic and dual pulse superharmonic respectively. The axial profiles of the single and dual pulse superharmonics are asymmetric, in contrast to the profiles produced using the modified Fubini solution (Fig. 12.1). This asymmetry is caused by the phase shift between the harmonics and is not modeled by the modified Fubini equation. Superharmonic

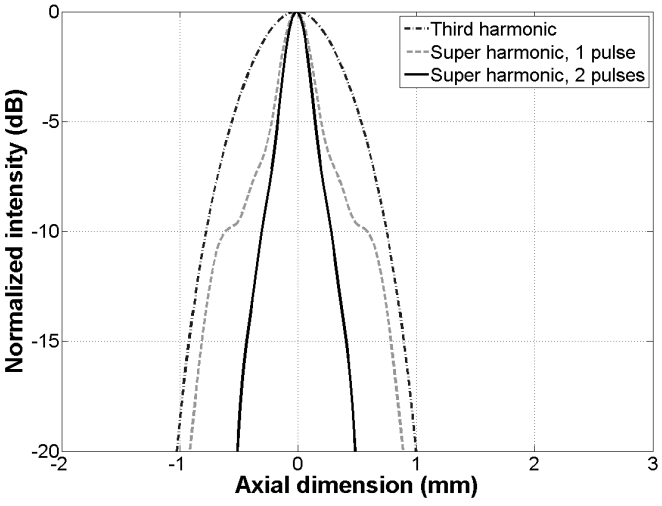

Figure 12.1: Axial PSFs calculated using the modified Fubini solution for the third harmonic, superharmonic single pulse and superharmonic dual pulse. The fundamental frequency was 2.25 MHz.

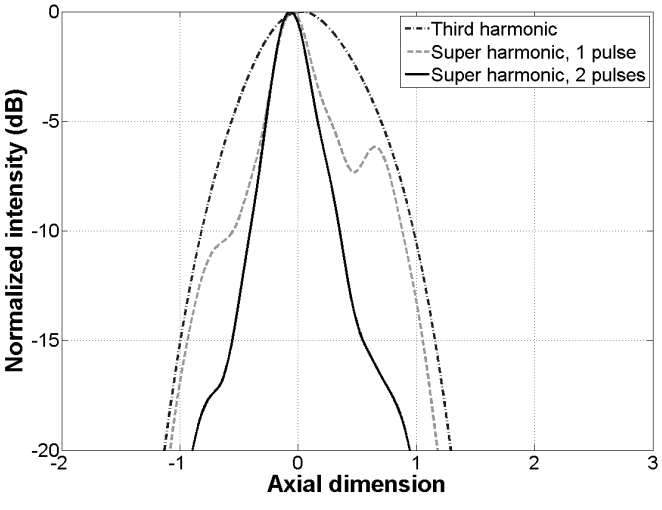

Figure 12.2: Experimentally determined axial PSFs, obtained using a 2.25 MHz transducer as a transmitter and a hydrophone setup for the recording of pressure. The axial distance between transducer and hydrophone was 8 cm. Gaussian apodized 3 cycle sine bursts of amplitude 65 mV which were amplified by 56 dB were used in transmission.

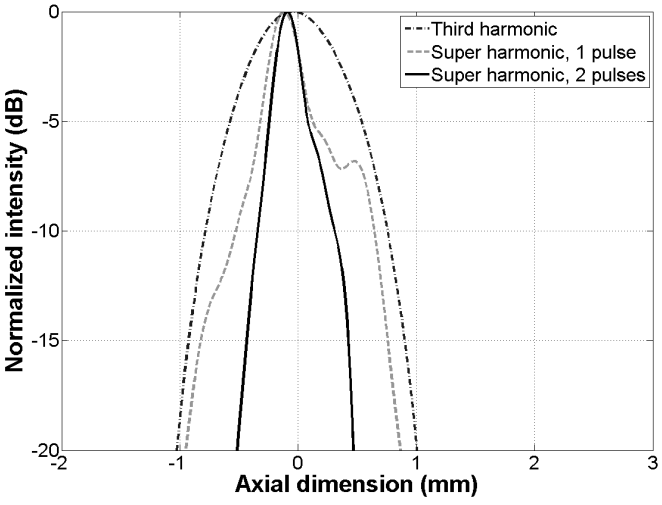

Figure 12.3: Axial PSFs calculated using the modified Fubini solution to calculate the third harmonic, the single pulse superharmonic and the dual pulse superharmonic. A 60° phase shift was added between the harmonics. The fundamental frequency was 2.25 MHz.

axial profiles with similar asymmetry as the experiments can be obtained by phase shifting each harmonic produced by the Fubini equation by 60° relative to its predecessor. The axial lengths at the -15 dB level remain very similar at 1.8 mm, 1.6 mm and 0.86 mm for the third harmonic, single pulse superharmonic and dual pulse superharmonic respectively. The differences between the simulations and the experiments are likely caused by the (unmodeled) transfer functions and impedances of the measurement system and the limited validity of the the modified Fubini solution.

12.4.2 KZK simulations versus experiments

Full two dimensional PSFs were studied using simulations based on the KZK equation and using experiments based on the 1 MHz transducer. Fig. 12.4 shows the single and dual pulse superharmonic PSFs obtained using KZK simulations. The left part of the figure shows the single pulse superharmonic PSF and the right part displays the dual pulse superharmonic PSF. The simulated PSF produced using the dual pulse method is considerably shorter than the single pulse PSF, with excellent cancelation of the ripples. Only a slight remainder of the first ripple is visible at -10 dB. The main lobe increased by 2 dB. Fig. 12.5 details the experimentally obtained single and dual pulse superharmonic PSFs. The experimentally produced PSF shows a reduction of the first ripple by 3 dB and of the second ripple by 15 dB. The main lobe decreases by 3 dB. This in contrast to the simulation results, where this lobe increased by 2 dB. The differences are likely caused by unmodeled parts of the experimental setup: the KZK simulation is a wave propagation simulation and as such does not take into account features such as the amplitude and phase transfer of the hydrophone

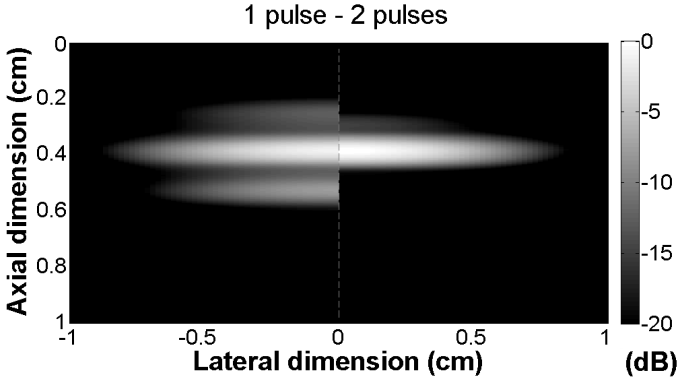

Figure 12.4: Two dimensional PSFs produced using KZK simulations of a 1 MHz transducer at a distance of 9.3 cm. On the left side the single pulse superharmonic PSF is displayed and on the right side the dual pulse superharmonic PSF is displayed. The x-axis displays the lateral dimension and the y-axis the axial dimension. The pressure intensity is denoted by the colorbar using a 20 dB dynamic range.

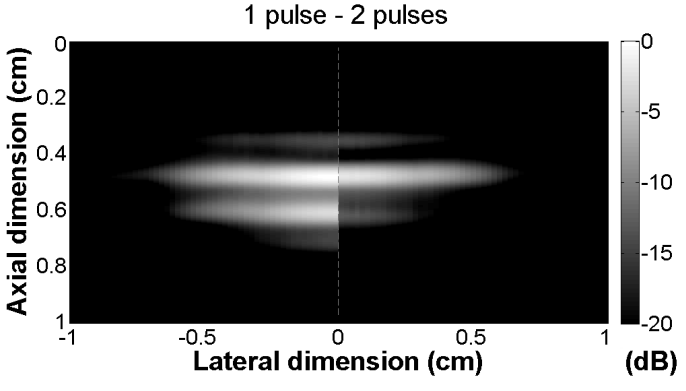

Figure 12.5: Two dimensional experimentally produced PSFs obtained using a 1 MHz transducer at a distance of 9.3 cm. On the left side the single pulse superharmonic PSF is displayed and on the right side the dual pulse superharmonic PSF is displayed. The x-axis displays the lateral dimension and the y-axis the axial dimension. The pressure intensity is denoted by the colorbar using a 20 dB dynamic range.

or the transmitting transducer. In the simulated single pulse superharmonic PSF three ripples are visible, while there are four ripples in the corresponding experimental PSF. This is explained by the effect of the transducer bandwidth on the excitation pulse: the effective bandwidth of the transmitter is more narrow than the excitation pulse causing extra ringing of the transducer in the experiment.

12.5 Conclusion

The dual pulse method significantly shortens the length of the superharmonic signal. It provides a way to minimize the artifacts in the envelope data induced by demodulating a multiple frequency signal.
The calculations based on the Fubini solution show an improvement in axial resolution by a factor of 2.1 of the dual pulse superharmonic compared to the third harmonic at the -15dB level. The experimentally determined axial profiles showed a factor 2.0 improvement at the -15 dB level compared to the third harmonic.
The KZK simulations showed almost complete suppression of the ripples in the dual pulse method at equal lateral resolution. The experiments showed considerable suppression of the ripples, but less than the simulations.
The extension of the proposed method to a phased array imaging system is the next step of this study.

Acknowledgements The author would like to thank the Dutch technology foundation STW which is supporting this work (grant number 7734) and Charles Lancée for his suggestions.

CHAPTER 13

Dual pulse frequency compounded superharmonic imaging for phased array transducers[1]

Paul L.M.J. van Neer, Mikhail G. Danilouchkine, Guillaume M. Matte, Martin D. Verweij, Nico de Jong

Abstract Second harmonic imaging is currently the standard in commercial echographic systems. A new modality, superharmonic imaging (SHI), is based on combining the 3rd to 5th harmonic generated during sound propagation in tissue. This emerging modality could further enhance the resolution and quality of echographic images. To meet the bandwidth requirement for SHI an interleaved phased array was developed. Array elements used in transmission generally have bandwidths of $\sim$80%. However, the transmission system bandwidth is often lower due to electrical tuning leading to gaps between harmonics in the spectral domain. This causes ripple artifacts in the echo image. Last year we introduced a new dual pulse frequency compounding method to reduce these artifacts and showed initial single element results (Matte et al., 2008). In this work we implement and optimize the dual pulse method for an interleaved array on an ultrasound system and research its imaging characteristics, i.e. point spread functions (PSF). In the dual pulse SHI method each trace is constructed by the summing of two firings, the second slightly frequency shifted compared to the first. To study the dual pulse method's performance an interleaved array (44 1 MHz and 44 3.7 MHz elements, optimized for echocardiography) was used in combination with a fully programmable ultrasound system. Initial estimates for the frequencies of the first and second pulses as well as the pulse duration were optimized experimentally. Our findings confirm that the transfer functions of both transducer and system have to be taken into account to determine the optimal transmission frequencies for the dual pulse SHI method. Moreover, a trade-off exists between dual pulse signal length and peak intensity. The optimal results with the dual pulse technique were achieved using a transmission length of 2.5 cycles and transmission frequencies of 0.87 MHz and 1.12 MHz. The lateral beam widths of the optimal dual pulse signal are 1.2 times smaller at the -6 dB level and equal at the -20 dB level compared to the third harmonic. The axial beam widths of the optimal dual pulse signal are 3.1 times

[1]From P.L.M.J. van Neer, M.G. Danilouchkine, G.M. Matte, M.D. Verweij, N. de Jong, 'Dual Pulse Frequency Compounded Super harmonic Imaging for Phased Array Transducers', Proc. IEEE Ultrasonic Symp., 2009, 381-384.

smaller at the -6 dB level and 1.6 times smaller at the -20 dB level compared to the third harmonic. Not only does the dual pulse method solve the ripple artifacts associated with imaging using multiple harmonic bands, dual pulse SHI has markedly improved axial and lateral resolutions compared to the third harmonic at higher than second harmonic intensities.

13.1 Introduction

The idea of using the nonlinear properties of the medium to generate harmonics of the incident ultrasound field dates back to the work of Kompfner and Lemons (1976) on acoustic microscopy. The relevance of this phenomenon in the context of medical applications was later shown by Muir and Carstensen (1980) and experimentally validated by Starritt et al. (1986). These two discoveries spawned the new era of harmonic imaging in medical ultrasound. To date this technique has become the standard for studying the nonlinear behavior of ultrasound contrast agents (UCAs). From a medical point of view it allows to detect areas of perfused or non-perfused tissue and, hence, to assess the function of anatomic organs. Until recently however, the quantitative analysis was limited to the second harmonic only.

A few years ago a new method for tissue and UCA imaging was proposed by Bouakaz et al. (2002). It was based on the selective imaging of the combined harmonics (from the third up to the fifth) and was dubbed superharmonic imaging (SHI). SHI inherits the benefits of second harmonic imaging, but further improves the spatial resolution and reduces the level of the sidelobes. Indeed, the first experimental comparison of the B-mode scans of the bladder cavity, obtained with second and superharmonic imaging, proved the superiority of the latter method (Bouakaz and de Jong, 2003). The inner fluid-filled cavity appeared not only more hypoenhanced, but also exhibited a less visible granular pattern. Moreover, the simulation results showed that the energy content of the second and superharmonic components are similar in the far-field (Bouakaz and de Jong, 2003; Ma et al., 2006).

In spite of the apparent advantages of SHI, there exists a fundamental problem associated with this technique. It is related to the fact that the amplitude of the higher harmonics is progressively lower than the one of the fundamental (Starritt et al., 1986). Each individual component of the superharmonic band has an inherently low signal-to-noise ratio and would thus not be suitable for imaging. Hence, it is imperative to utilize the information from the entire superharmonic band. The spectrum of a nonlinearly propagated acoustic signal is shown in Fig. 13.1. The global maximum corresponds to the fundamental frequency of the transmitted pulse. The local maxima at multiples of the fundamental frequency are the high order harmonics. The existence of the local minima in between the harmonics causes ripples in the point spread function (PSF), which give rise to ghost reflections along the direction of the wave propagation in practical imaging situations. A proper solution to this problem requires the development of dedicated imaging methods. In this paper we demonstrate the feasibility of such a SHI technique with a medical phased array transducer.

13.2 Background

To make SHI possible, a dual pulse frequency compounding technique was proposed by Matte et al. (2008). The main idea is summarized in Fig. 13.1. The imaging protocol makes use of two transmitting pulses with the second pulse of slightly different frequency. Consequently, the time traces are summed together for imaging purposes. The choice of the frequency difference is of the utmost importance for dual pulse SHI. Namely, the loca-

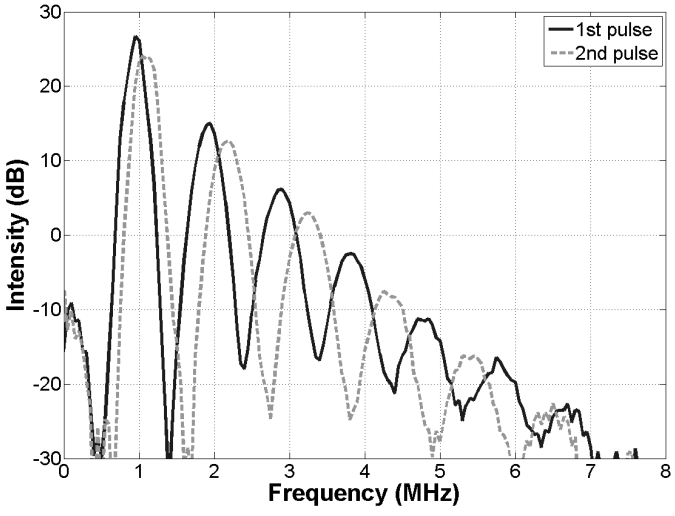

Figure 13.1: The concept of the dual pulse frequency compounding method for SHI.

tion of the higher harmonics in the second pulse should fill the gaps in the spectrum of the first pulse as shown in Fig. 13.1. The spectrum of the cumulative time trace exhibits less prominent minima and have a relatively smooth appearance of the superharmonic band. In terms of imaging characteristics that would yield a better PSF. The PSF used here combines the convolution of the electrical excitation (the pulsing scheme), the transmit transfer function and the spatial impulse response with the effects of nonlinear propagation and postprocessing. The frequency shift was theoretically predicted with the Fubini solution and experimentally validated with the simulation and measurement on a single element transducer (Matte et al., 2008). Although a good agreement between the predicted shift and the simulation was observed, the measurement demonstrated that the suppression of the ripple artifacts for the single element transducer was somewhat suboptimal.
This fact evoked our interest in finding the nature of such behavior. Therefore, the main objectives can be formulated as follows:

1. shed the light on the discrepancies between the experimental and simulation results, reported previously.

2. Optimize the dual pulse frequency compounding protocol with respect to the pulse duration and frequencies.

In this paper we will show that the proposed SHI method is feasible and suitable for application to medical phased array transducers.

13.3 Methods

The optimal frequency shift is calculated theoretically using the Fubini solution describing nonlinear wave propagation in a medium (Matte et al., 2008). However, in general transducers show frequency dependent behavior, as does the system driving the transducer. Usually, the transfer function of a transducer is approximately Gaussian in shape, which influences the frequency difference between the first and second pulses for dual pulse SHI. Moreover, for maximum efficiency in transmission the frequencies of the first and second pulses should be around the resonance frequency of the transducer. Maximum transmit efficiency is desirable because of the limited peak voltage of the transmitters used in ultrasound imaging systems. Therefore, for the practical application of dual pulse SHI, the center frequencies of the first and second pulses have to be optimized for the transducer and the system used.
The shape of the optimal time trace produced by the method is determined by two competing requirements imposed on the transmitted pulses. On one hand the cumulative time trace of two transmitted pulses with slightly different frequencies is used for imaging. The summation fills the troughs between the harmonics of each pulse and results in a smooth frequency spectrum, which in turn leads to a narrow time signal. The smoothness of the spectrum after summation depends on the bandwidth of both pulses. If both pulses are more wideband the spectrum of the summed pulse is smoother. Thus, the shortest possible transmitted pulse would appear to be optimal. On the other hand SHI depends on the combination of the third to fifth harmonics, the generation of which heavily depends on pressure. The obtained peak pressure is determined by the transducer efficiency and the driving system - both in signal length and amplitude. As the peak voltage of the imaging system is limited the remaining free parameter is the length of the signal. The length of the signal should be sufficiently long to achieve the pronounced level of the higher harmonics. Therefore, for a given transducer and system there is an optimal transmission signal length providing the best trade-off between peak pressure and the smoothness of the summed time signal.
Thus, to implement dual pulse SHI for a given transducer and system the optimal frequencies of the first and second pulses have to be determined as well as the optimal length of the transmitted signal.

13.4 Experimental setup

The experimental setup consisted of a water-filled tank, which featured a hydrophone (diameter 0.2 mm, Precision Acoustics, Dorchester, UK) mounted in an xyz-system. A special dual frequency transducer was attached to the tank's sidewall. The elements of the low frequency subarray were excited by Gaussian apodized sine bursts of varying length and frequency with an amplitude of 120 V_{pp}. The excitation signals were produced by a multi channel programmable ultrasound system (OPEN system, Lecoeur Electronique, Chuelles, France, first reported in (Vignon et al., 2005)). The signals received by the hydrophone were digitized by an oscilloscope (9400A, Lecroy, Geneva, Switzerland) with a sampling frequency of 100 MHz and transferred to a computer for further processing. The experi-

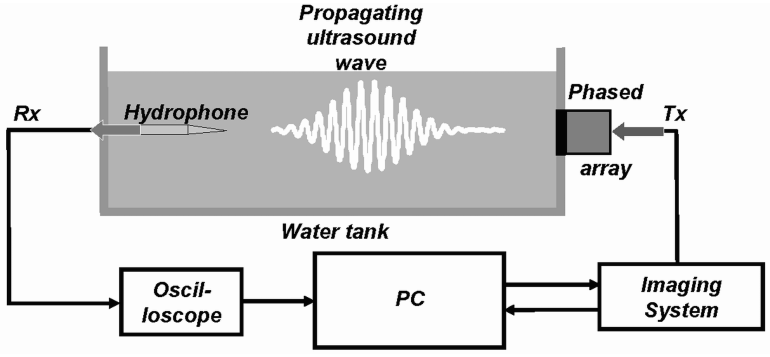

Figure 13.2: The experimental setup.

mental setup is shown in Fig 13.2.
The frequencies of the transmitted pulses were varied between 0.8 and 1.3 MHz and the length of the transmitted signal was varied between 2, 2.5 and 3 cycles.

13.5 Results

The energy intensity in the axial dimension versus the frequency of the second pulse is shown in Fig. 13.3 for 3 cycle transmissions, demonstrating the dependency of the summed pulse on the frequencies of the original pulses. The frequency of the first pulse was 0.89 MHz. In this case the optimal frequency of the second pulse was 1.15 MHz - this results in the summed pulse with the best profile: narrow, smooth and with the lowest amount of ripples. The frequencies of both the first and second pulses were varied for 2, 2.5 and 3 cycle transmissions. For 2 cycle transmissions the optimal transmission frequencies of the first and second pulse were 0.85 MHz and 1.12 MHz respectively. For 2.5 cycle transmissions these frequencies were 0.87 MHz and 1.12 MHz respectively and for 3 cycle transmissions the optimal frequencies were 0.9 MHz and 1.15 MHz. For the remainder of this work it holds that, if reference is made to 2, 2.5 or 3 cycle transmissions, the optimal transmission frequencies mentioned above were used.
Fig. 13.4 details the intensity versus the length of the signal at the transducer's focus (axial and lateral focus both at 6 cm) for 2, 2.5 and 3 cycle transmissions. As a reference the second, third and superharmonic components of a single pulse are also displayed. From the figure, we see that the top 20 dB of the 2, 2.5 and 3 cycle dual pulse transmissions had approximately equal length. However, at lower intensities (-55 dB) the dual pulse signal length becomes considerably larger as the number of cycles increased. Also, the peak intensity reached became higher as the number of cycles increased: -31 dB, -28 dB and -26 dB for 2, 2.5 and 3 cycles respectively. The peak intensities of the second and third harmonics and superharmonic component using a 2.5 cycle transmission were -30 dB, -38 dB and -34 dB respectively. In Fig. 13.5 the dual pulse PSFs, expressed as the intensity versus the axial and lateral dimensions, are displayed for 2, 2.5 and 3 cycle transmissions.

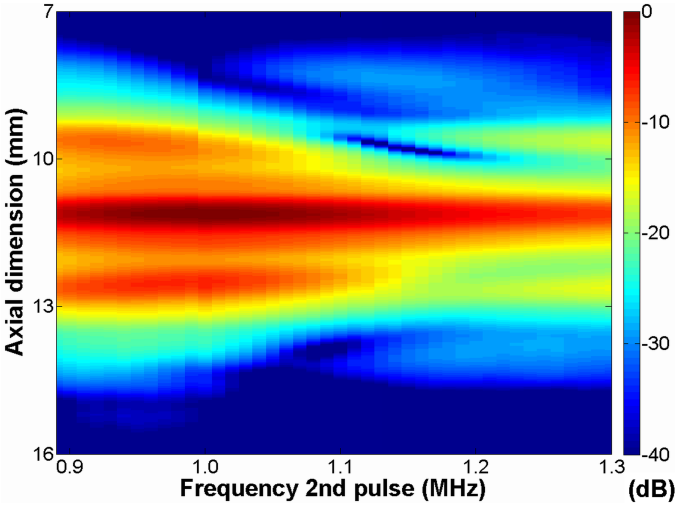

Figure 13.3: The axial intensity profiles (vertical axis) versus the frequency of the second pulse (horizontal axis) for a 3-cycle transmission. The intensity is color coded using a dynamic range of 40 dB. The frequency of the first pulse was fixed at 0.89 MHz.

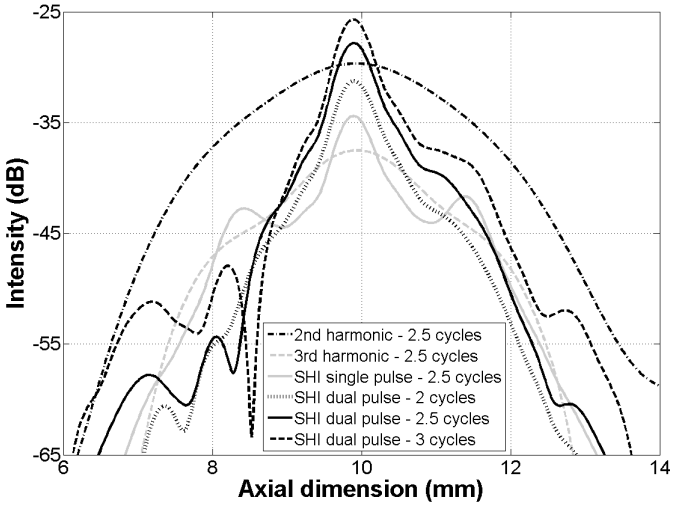

Figure 13.4: The axial intensity profiles for the second, third and superharmonic components. Several profiles of the superharmonic component, obtained using the single pulse protocol as well as the proposed dual pulse methods with different transmission durations, are shown.

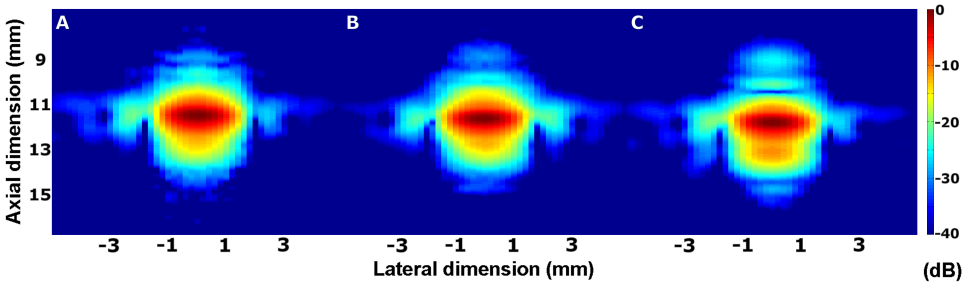

Figure 13.5: PSF for different pulse lengths: 2-cycles (A); 2.5-cycles (B); 3-cycles (C). The relative intensity is color coded using a dynamic range of 40 dB.

The intensities were normalized to their respective maxima. The PSFs were very similar in the lateral dimension. For 2 and 2.5 cycles the PSFs were similar in the axial dimension as well. However, the dual pulse PSF for 3 cycle transmission was considerably longer with regions at -25 to -30 dB before and after the main pulse. Also, there was an intensity plateau at -12 dB.
A comparison between the third harmonic PSF and the optimal dual pulse SHI PSF is shown in Fig. 13.6. The dual pulse SHI lateral beam widths at -6 dB and -20 dB were 1.8 mm and 3.4 mm respectively, whereas for the third harmonic these were 2.2 mm and 3.4 mm respectively. The axial beam widths at -6 dB and -20 dB were 0.8 mm and 3.4 mm respectively for dual pulse SHI and 2.5 mm and 5.3 mm for the third harmonic.

13.6 Discussion

The optimal frequency shift between first and second pulse varied between 0.25 and 0.27 MHz. Those numbers are somewhat is higher than the theoretically predicted value of 0.15 MHz reported previously (Matte et al., 2008). This can be attributed to the transfer functions of both transducer and system. Concerning the ripples, 3 cycles is the upper limit for obtaining a smooth envelope. At higher number of cycles the Fourier spectrum of the summed pulse becomes insufficiently smooth to yield short time pulses. We did not show the results for shorter pulse durations (eg., 1 and 1.5 cycles) as in these cases the transducer is the limiting bandwidth factor. The pulses produced by the transducer do not become shorter, only lower in energy. Since the generation of harmonics depends heavily on pressure, these short pulse lengths were deemed unsuitable for nonlinear imaging in combination with our transducer and system.
The results show that dual pulse SHI solves the ripple artifact associated with single pulse SHI. Moreover, the intensity of the optimal dual pulse signal is higher than the second harmonic. Considering the resolution, the lateral beam widths of the optimal dual pulse signal are 1.2 times smaller at the -6 dB level and equal at the -20 dB level compared to the third harmonic. The axial beam widths of the optimal dual pulse signal are 3.1 times smaller at the -6 dB level and 1.6 times smaller at the -20 dB level compared to the third

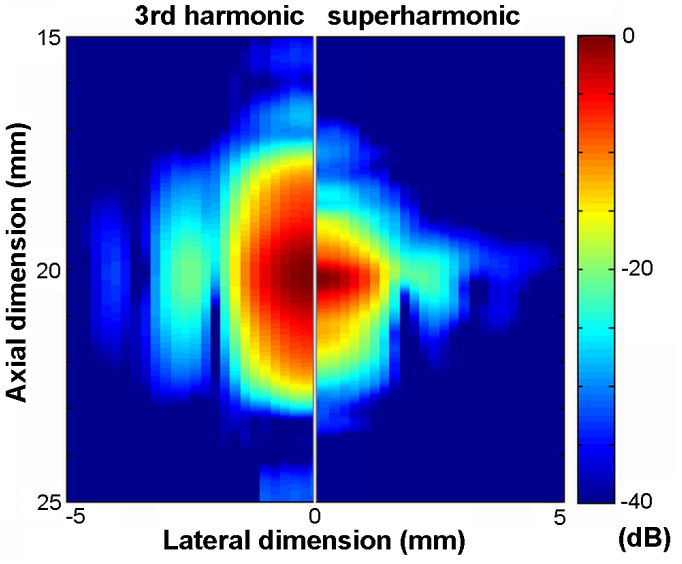

Figure 13.6: Comparison of the 3rd harmonic (left panel) and superharmonic (right panel) PSF's. The relative intensity is color coded using a dynamic range of 40 dB and 2.5 cycle transmissions were used.

harmonic.

13.7 Conclusion

Our findings confirm that the transfer functions of both transducer and system have to be taken into account to determine the optimal transmission frequencies for the dual pulse SHI method. Moreover, a trade-off exists between dual pulse signal length and peak intensity. The optimal results with the dual pulse technique were achieved using a transmission length of 2.5 cycles and transmission frequencies of 0.87 MHz and 1.12 MHz.
Not only does the dual pulse method provide a solution to the ripple artifacts associated with imaging using multiple harmonic bands, dual pulse SHI has markedly improved axial and lateral resolutions compared to the third harmonic at higher than second harmonic intensities.

Acknowledgements The financial support of the Dutch Foundation for Technical Sciences is greatly appreciated.

CHAPTER 14

Chirp based superharmonic imaging for phased array transducers[1]

Paul L.M.J. van Neer, Mikhail G. Danilouchkine, Guillaume M. Matte, Marco M. Voormolen, Martin D. Verweij, Nico de Jong

Abstract Second harmonic imaging has become the de-facto standard for commercial ultrasound systems. Superharmonic imaging (SHI), which targets a combination of the 3rd to 5th harmonics, has certain advantages in comparison to the established standard. The new technique is expected to enhance spatial resolution and, thus, the quality of echographic images. On the other hand, those images are susceptible to so-called ripple artifacts, stemming from the gaps in between harmonics in the frequency domain. The recently proposed dual-pulse frequency compounding protocol suppresses the aforementioned artifacts at the cost of a reduced frame rate (Matte et al., 2008; van Neer et al., 2009). In this work, we employ the chirp protocol for SHI without sacrificing the acquisition speed and investigate its characteristics, i.e. point spread function (PSF). The chirp protocol was implemented on a superharmonic interleaved phased array probe (44 elements tuned at 1 MHz, 44 elements at 3.7 MHz), connected to a fully programmable ultrasound system. A linear chirp with a center frequency of 0.95 MHz and bandwidth of 40% was used as the excitation pulse. The RF traces were recorded at the focal plane along the lateral axis and convolved with the decoding signal to obtain the PSF's. For decoding the pressure signal in focus, computed using a KZK simulation, was used. The lateral beam width of the superharmonic chirp signal is 0.8 and 0.9 times the lateral beam width of the third harmonic at the -6 dB and -20 dB levels respectively. With regard to the axial beam width, the superharmonic chirp signal is 0.9 and 0.8 times the axial beam width of the third harmonic at the -6 dB and -20 dB levels respectively. The PSFs produced using the superharmonic chirp protocol are virtually free from ripples. The superharmonic PSFs show increased spatial resolution in comparison to the third harmonic.

[1]Reprinted with permission from Paul L.M.J. van Neer, Mikhail G. Danilouchkine, Guillaume M. Matte, Marco M. Voormolen, Martin D. Verweij, Nico de Jong, POMA, Vol. 9 - 159th Meeting ASA Baltimore, (2010).

14.1 Introduction

Second harmonic imaging is currently the de-facto standard in commercial echographic systems for diagnosis because of its improved resolution and contrast-to-tissue ratio. An emerging technique called superharmonic imaging (SHI) is based on a combination of multiple frequency components generated during the propagation of sound in tissue (Bouakaz et al., 2002). This combination of third to fifth harmonic has the potential to further enhance resolution and image quality of echographic pictures. Tissue SHI efficiently suppresses near-field artifacts, reverberations, and off-axis artifacts in addition to the enhanced lateral and axial resolution. The resulting images showed more details than those produced by second harmonic imaging (Bouakaz and de Jong, 2003).
In spite of the apparent advantages of SHI, there exists a fundamental problem associated with this method. The bandwidth of contemporary electrically tuned transducers is limited. If a pulse with limited bandwidth propagates nonlinearly in a thermoviscous medium, the resulting distorted pulse will show distinct troughs in its frequency spectrum. These troughs between the harmonics lead to ripples in the point spread function (PSF), which give rise to ghost reflections along the propagation direction in practical imaging situations. In previous work we introduced a dual pulse method to solve the ripple issue and showed its feasibility for phased array transducers (Matte et al., 2008; van Neer et al., 2009). The imaging protocol is based on the transmission of two pulses with the second pulse of slightly different frequency. The echoes produced by each transmission pulse are summed to create an image. The methodology produced good results, but it does have a few drawbacks. Firstly, it is based on transmitting two pulses per A-line and thus the maximum attainable frame rate is reduced by a factor of two - quite a compromise to make when imaging fast moving structures such as heart valves. Secondly, the total amount of energy transmitted into the tissue is limited. It was shown in previous work that an optimum exists between the method's ability to suppress the ripples and the length of the transmitted pulses (van Neer et al., 2009). Thus, the time-bandwidth product of the signals involved in this method is low. To improve the time-bandwidth product coded excitation could be used, which has been shown to improve the SNR by the time-bandwidth product (Misardis and Jensen, 2005b). The improved SNR leads to an increased penetration depth. This is especially useful for higher harmonic imaging, since the signal amplitudes of the higher harmonics are generally low.

In this work we employ a chirp protocol for SHI without sacrificing the acquisition speed. Its characteristics in terms of point spread functions (PSF) are investigated. The PSF used here combines the convolution of the electrical excitation (the pulsing scheme), the transmit transfer function and the spatial impulse response with the effects of nonlinear propagation and postprocessing.

14.2 The chirp protocol

The chirp protocol is based on coded excitation. It is based on the transmission of a pulse train with certain properties (a code). In reception the pulse train is compressed using a

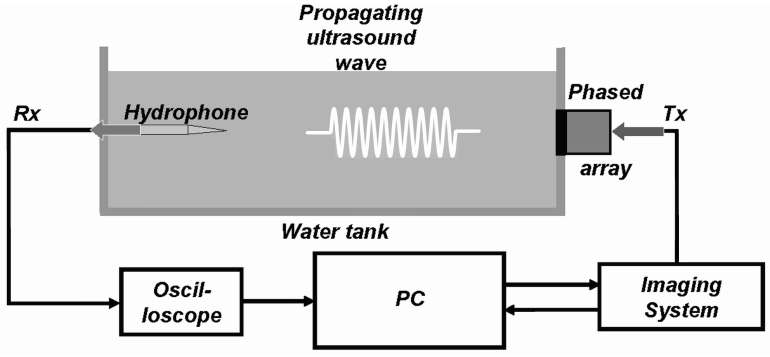

Figure 14.1: The experimental setup.

decoding filter to obtain an image. The first report on coded excitation in medical literature dates back to 1979 (Takeuchi, 1979). Since then a sizable volume of literature has been dedicated to imaging using coded excitation - an excellent overview is given by Misardis and Jensen (2005b,a). Among the codes investigated were chirps (Pollakowski and Ermert, 1994), orthogonal Golay codes (Chiao and Thomas, 2000) and binary sequences (Shen and Ebbini, 1996). Recently, coded excitation using linear chirps was also used for second harmonic imaging of ultrasound contrast agents (Borsboom et al., 2003).
The chirp protocol for SHI consists of transmitting a frequency modulated signal and receiving the third to fifth harmonic. The recorded echo is compressed using a decoding signal. Linear chirps were used because of their higher SNR gain at large imaging depths relative to pulsed excitation compared to the SNR gain reported for nonlinear chirps and Golay codes (Misardis and Jensen, 2005b). The filtered superharmonic band of the on-axis pressure signal in focus computed with the KZK method was used for decoding.

14.3 Materials and methods

14.3.1 Experimental setup

The experimental setup consisted of a water-filled tank featuring a hydrophone (diameter 0.2 mm, Precision Acoustics, Dorchester, UK) mounted in an xyz-system. A special dual frequency transducer (van Neer et al., 2010) was mounted in the tank's sidewall. The elements of the low frequency subarray were excited by linear 0.95 MHz chirps with a -6 dB bandwidth of 40%, amplitude 24 V and length 15 μs. The excitation signals were produced by a multi channel programmable ultrasound system (OPEN system, Lecoeur Electronique, Chuelles, France, first reported in (Vignon et al., 2005)). The signals received by the hydrophone were digitized by an oscilloscope (9400A, Lecroy, Geneva, Switzerland) with a sampling frequency of 100 MHz and transferred to a computer for further processing. The experimental setup is shown in Fig. 14.1.

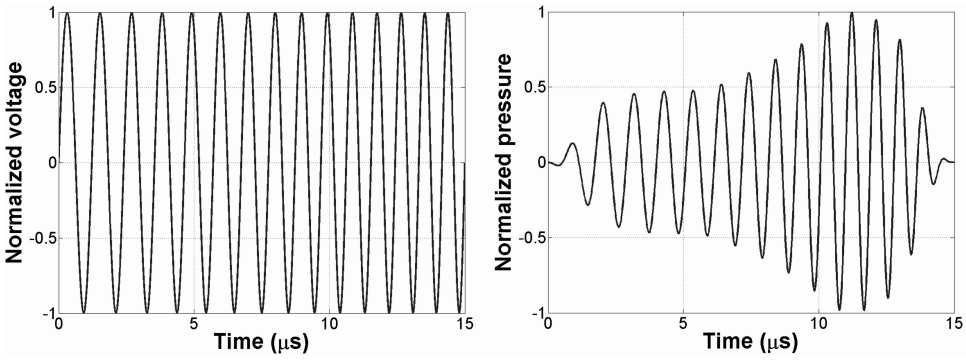

Figure 14.2: On the left the normalized chirp produced by the AWGs of the OPEN system. On the right the actual normalized chirp transmitted by the transducer, calculated using the transfer function.

14.3.2 KZK simulations

The decoding pulse was generated using simulations based on the KZK equation. The KZK equation was solved in the time domain. The nonlinearity and absorption terms were solved using the numerical methods developed by Lee (1993) (Lee and Hamilton, 1995). The diffraction term was solved in the near-field using an implicit backward finite difference method and in the far field using an alternating direction implicit method. The first method is more effective in damping numerical oscillations and the latter method is more accurate allowing for larger step sizes (Voormolen, 2007). A complete description of the algorithms can be found in the PhD-thesis of Voormolen (2007). The algorithm was implemented in the C and Matlab languages. The simulations were performed in full 3D. The low frequency subarray of the dual frequency array was used as the source: the subarray consisted of 44 elements with size 16 mm x 0.2 mm and pitch 0.5 mm (van Neer et al., 2010). The subarray was modeled as a rectangular aperture of 16 x 22 mm. The transmitted pressure was scaled to take into account the kerf between the elements. Lateral and elevation foci at 6 cm were implemented to model the elevation lens and the electronic focusing. As the input for the simulations a voltage chirp similar to the one used for the experiments was used. The voltage chirp was converted to the output pressure pulse of the low frequency subarray using the transmit transfer function (van Neer et al., 2010). The effect of the electrical impedance of the transmitter circuits was neglected as the electrical impedance of the arbitrary waveform generator outputs (5 Ω) was low compared to the electrical impedance of the transducer elements (minimum magnitude of tuned impedance 100 Ω). Both the normalized chirp produced by the AWGs and the normalized chirp transmitted by the transducer are shown in Fig. 14.2.

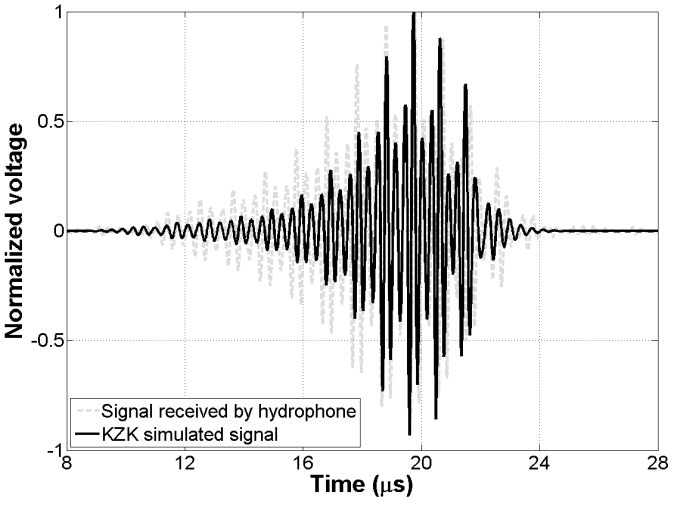

Figure 14.3: The on-axis pressure signal at focus. The dashed gray line displays the experimentally obtained data, the solid black line shows the KZK simulated signal.

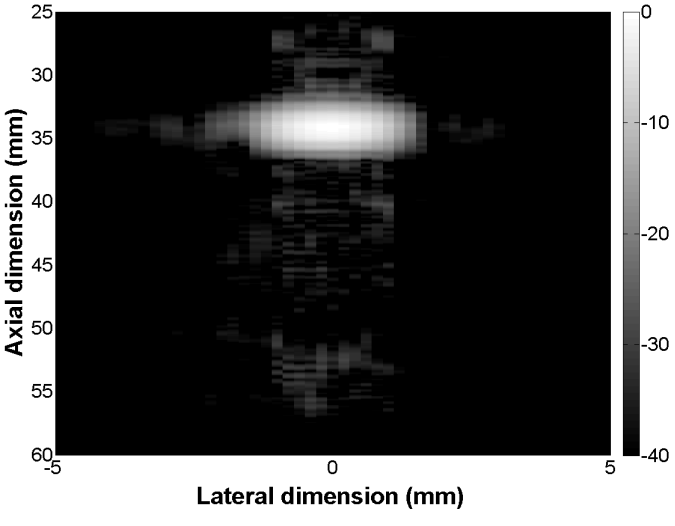

Figure 14.4: Decoded superharmonic chirp PSF. The relative intensity is color coded using a dynamic range of 40 dB. The transmitted signal was a 40% chirp with a 0.95 MHz center frequency and length 15 μs.

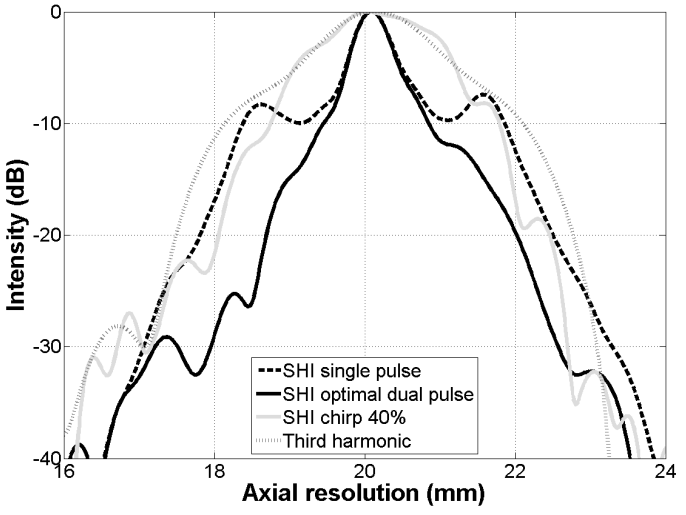

Figure 14.5: The normalized axial intensity profiles for the third harmonic and various superharmonic methods. The third harmonic, the optimal dual pulse (van Neer et al., 2009) and single pulse superharmonic profiles are obtained using 2.5 cycle Gaussian apodized sine bursts with amplitude 60 V. The superharmonic chirp intensity profile was obtained using a 40% chirp with a 0.95 MHz center frequency and length 15 μs.

14.4 Results

In Fig. 14.3 both the measured (dashed gray line) and the simulated (solid black line) on-axis pressure signals are shown. The data presented in the figure clearly shows the similarity between both pulses allowing for the use of the simulated signal for decoding of the experimental signals.

Fig. 14.4 shows the decoded superharmonic chirp PSF. The result presented in the figure shows a smooth and distinct peak with low compression artifacts. The obtained SNR is $\sim$35 dB.

Fig. 14.5 details the normalized axial intensities of the third and superharmonic components. The dual pulse superharmonic profile was obtained using the optimal settings as reported by Matte et al. (2008) and van Neer et al. (2009) and was obtained using Gaussian apodized 2.5 cycle sine bursts with amplitude 60 V. This was also the case for the single pulse superharmonic and third harmonic profiles. The superharmonic chirp profile was obtained using a 40% chirp with a 0.95 MHz center frequency and length 15 μs. From the figure, we see that the superharmonic chirp profile is reasonably smooth but does contain minor ripples. The axial lengths at the -6 dB level are 0.88 mm, 0.81 mm, 2.3 mm and 2.5 mm for the single pulse, optimal dual pulse and chirp superharmonic components and for the third harmonic component respectively. At the -20 dB level the axial lengths increase to 4.7 mm, 3.3 mm, 4.4 mm and 5.3 mm respectively.

Fig. 14.6 displays the third harmonic PSF obtained using a 2.5 cycle Gaussian apodized

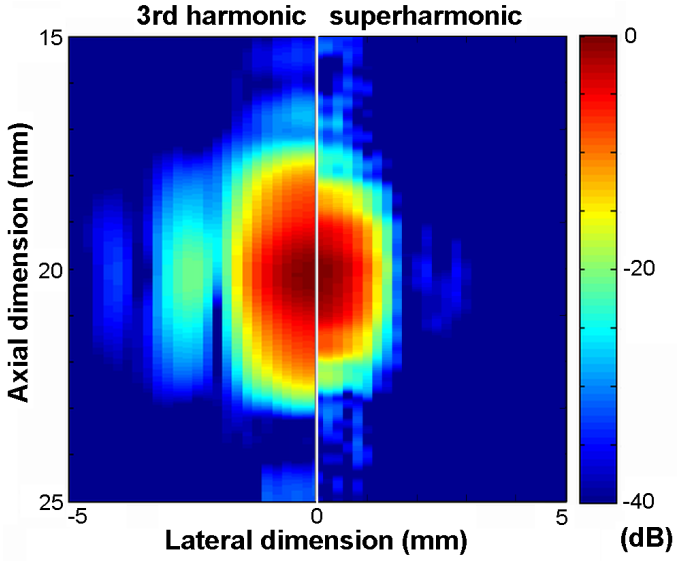

Figure 14.6: Comparison of the 3rd harmonic PSF obtained using 2.5 cycle transmissions (left panel) and the superharmonic chirp PSF (right panel). The relative intensity is color coded using a dynamic range of 40 dB. The third harmonic was obtained by exciting the transducer using a Gaussian apodized 2.5 cycle sine burst with amplitude 60 V.

sine burst on the left and the superharmonic chirp PSF on the right using a dynamic range of 40 dB. The superharmonic chirp lateral beam widths at -6 dB and -20 dB were 1.8 mm and 3 mm respectively, whereas for the third harmonic these were 2.2 mm and 3.4 mm respectively. The axial beam widths at -6 dB and -20 dB were 2.3 mm and 4.4 mm respectively for chirp SHI and 2.5 mm and 5.3 mm for the third harmonic.

14.5 Discussion

The superharmonic PSF produced by the chirp protocol is smooth and almost completely free of ripples. However, as can be seen in Fig. 14.3, the decoding signal can still be improved - especially at the start of the signal there are significant differences between the experimentally recorded signal and the KZK simulated signal. The amplitude differences are likely caused by nonnegligible circuit effects and the phase differences are caused by the phase transfer functions of the circuitry and the transducer.
The relative increase in the axial resolution obtained using the superharmonic chirp protocol amounts to 8% at the -6 dB level and 17% at the -20 dB level compared to the third harmonic. Whereas the relative increase in the lateral resolution obtained using the superharmonic chirp protocol is 18% and 17% at the -6 dB and -20 dB levels respectively compared to the third harmonic. If the axial resolution of the chirp superharmonic protocol is compared to the dual pulse superharmonic method reported previously (Matte et al.,

2008; van Neer et al., 2009), we find a 65% decrease in resolution at the -6 dB level and a 25 % decrease at the -20 dB level. The lateral resolution produced by the superharmonic chirp method is equal to the lateral resolution of the dual pulse method at the -6 dB level and 12% higher at the -20 dB level. The intensity of the superharmonics is equally high (or higher) for the chirp excitation compared to the short burst excitation, but at 40% of the excitation voltage. Comparing the chirp and dual pulse protocols, there is a trade-off between the achievable resolution and the number of transmitted pulses per A-line. However, both imaging schemes produce a considerably better resolution than the third harmonic. It is expected that these resolutions will deteriorate somewhat in *in-vivo* situations, due to the imperfectness of the generated decoding signal (chirp method) and the influence of tissue attenuation (dual pulse method).

14.6 Conclusion

The PSFs produced by the superharmonic chirp protocol are virtually free from ripple artifacts and have increased spatial resolution compared to the third harmonic. However, the spatial resolution is lower compared to the dual pulse superharmonic method (van Neer et al., 2009). Thus there exists a trade-off between the attainable spatial resolution and the frame rate in superharmonic imaging.

Acknowledgements The financial support of the Dutch Foundation for Technical Sciences is greatly appreciated.

CHAPTER 15

Discussion and conclusions

15.1 Harmonic imaging

15.1.1 Clinical significance

Approximately a decade ago it became possible to improve ultrasound image quality by exploiting the nonlinear nature of wave propagation. The method is based on the selective imaging of the second harmonic frequency and is called tissue second harmonic imaging. The technique produces images which have a higher resolution compared to fundamental imaging. Moreover, the resulting images are less sensitive to near-field artifacts, clutter and off-axis scatterers (Bouakaz and de Jong, 2003). This means that the ultrasound images are sharper and cleaner. More important perhaps for clinicians is the fact that the use of nonlinear ultrasound specifically improves the imaging of the patient subgroup considered to be technically challenging to image (Tranquart et al., 1999). The application of second harmonic imaging substantially reduces artifacts and noise in liquid cavities, which appear cleaner and darker on images. Therefore, the abdominal and pelvic masses can be more confidently assessed - particularly in obese patients - allowing for the better differentiation of hypoechoic solid masses and cystic lesions (Tranquart et al., 1999). For example the detection of focal liver lesions is often complicated by the presence of fat or cirrhosis in the liver, or by reverberation in the abdominal wall or the intercostal spaces. Second harmonic imaging improves the liver-lesion contrast, which leads to improved detection of hepatic lesions. The method also facilitates the evaluation of the gallbladder wall and content, and allows for the better detection of gallbladder stones. In obstetric imaging imaging the second harmonic mode provides a better depiction of the fetal anatomy lessening the requirement for transvaginal imaging in the detection of uterine processes (Tranquart et al., 1999). Transthoracic echocardiography (TTE) particularly benefited from the application of second harmonic imaging. The quality of TTE using fundamental imaging was often limited by the presence of various skin and fat layers and the ribs, which all contributed to the degradation of the image quality due to clutter and artifacts. Harmonic

imaging is particularly efficient in reducing these artifacts. Its application has been shown to improve the delineation of the endocardial border of every cardiac wall and perfusion territory, especially in patients technically difficult to image (Kasprzak et al., 1999). The optimal visualization of the endocardial border is important because of the increasing role of stress echocardiography and the prognostic value of left ventricular function. A comparison between an apical four chamber view obtained using fundamental and second harmonic imaging is shown in Fig. 15.1.

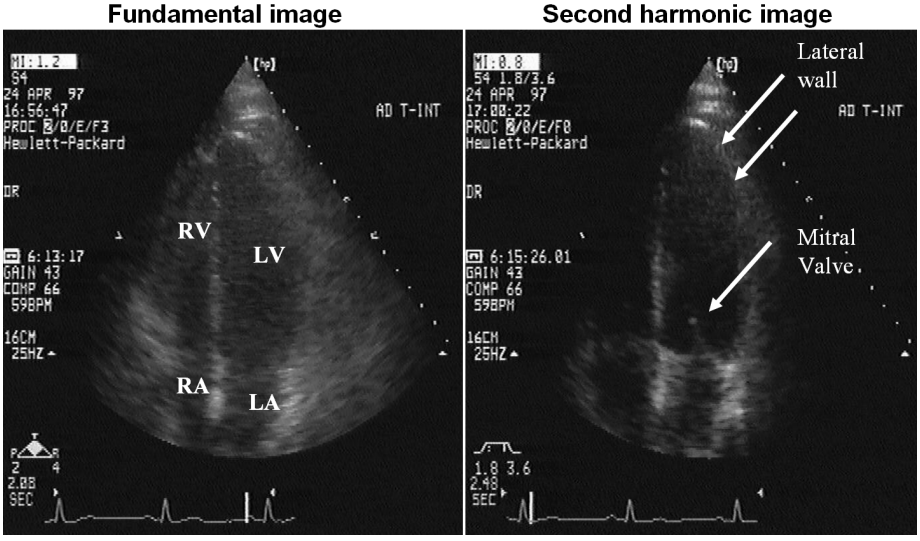

Figure 15.1: Typical apical four chamber view using fundamental imaging (left) and second harmonic imaging (right), made using a late 90s scanner. Image obtained from the 'Medical Acoustics' course by Nico de Jong, with permission.

15.1.2 Transesophageal second harmonic imaging

Although second harmonic imaging is the standard in TTE for several years, it has not yet been applied to transesophageal imaging (TEE). Part of the explanation is that some of the technical challenges of TTE - reverberation due to skin layers and the ribs - are circumvented by using the esophagus as an acoustic window. Also, it is more difficult to construct a second harmonic TEE transducer compared to a TTE transducer, since the device has to fit inside the esophagus. However, it is our opinion that the improved resolution and the reduced sensitivity to clutter and off-axis scatterers brought by second harmonic imaging will considerably improve TEE image quality. Therefore, we are working on a TEE 3D matrix transducer and the development of its topology is reported in part in chapter 5. The preparatory work on the FEM model used is reported in chapter 4.

15.2 Superharmonic imaging

Superharmonic imaging (SHI) has emerged few years ago as an alternative modality to second harmonic imaging, currently adopted as a clinical standard in a variety of medical ultrasound applications. SHI improves on second harmonic imaging by combining the third to fifth harmonics arising from nonlinear wave propagation or contrast-agent response (Bouakaz et al., 2002). SHI faces similar hurdles on the way to becoming an accepted technique as second harmonic imaging did: before the feasibility of the latter was accepted, it was widely assumed that nonlinear distortion was not a significant factor in medical imaging due to its low energy content (Averkiou et al., 1997). Similarly, in the case of SHI it is currently commonly perceived that the energy level of the harmonics higher than the second one is too low to be useful. The superharmonic beam has however even more favorable characteristics compared to the second harmonic beam. Therefore, tissue SHI is expected to suppress near-field artifacts, reverberations, and the reflections from off-axis scatterers more efficiently than second harmonic imaging. Also, the obtained lateral and axial resolutions are expected to increase.
The work presented in this thesis covers the aspects required to implement SHI: a systematic study researching and proving its feasibility (chapters 9 and 10), the development of the necessary hardware (chapters 7 and 8) and the required image processing methods (chapters 11 - 14). The work on each of these subjects is summarized and discussed in the sections below. Also, hints for future work are given.

15.2.1 Feasibility

The work presented in this thesis (chapters 9 and 10) shows that the energy of the higher harmonics could be sufficient for imaging - even at large depths -, but that it is critical to use the optimal transmission frequency. Since the level of these harmonics is determined by two competing phenomena - the progressive build-up of harmonics by nonlinear propagation and their attenuation -, the optimal transmit frequency for SHI depends on the level of the third to fifth harmonics at the distances determined by the application. The optimal transmit frequency for SHI applied to echocardiography was found to be 1.1 - 1.2 MHz and for abdominal imaging 1.7 - 1.9 MHz.
The simulation results presented in chapter 9 showed a third harmonic SNR of 22 dB at 13 cm, a value below the 30 - 40 dB dynamic range required for ultrasound imaging. Assuming that the third and fourth harmonic add in phase this SNR would increase slightly for the superharmonic, but the available dynamic range at this distance would still be limited. However, these simulations were performed using very conservative material and system properties based on the nonoptimized prototype transducers and imaging platform available at the time:

1. the receive sensitivity used in the simulations was based on the measurements of custom arrays presented in chapters 7 and 8. However, these arrays were not electrically tuned to the receiving circuitry nor did they feature acoustic matching. As such the receive sensitivity used in the simulations is rather low. For example, the peak receive sensitivity of the tuned interleaved array transducer presented in chapter 8 was

50% higher.

2. The noiselevel used for the simulations was based on a measurement of the noise produced by the available programmable ultrasound system used in combination with the interleaved array presented in chapter 8. The noiselevel of the prototype ultrasound system alone was $\sim$ 2.7 nV/$\sqrt{Hz}$ - considerably higher than the 1 nV/$\sqrt{Hz}$ specified by the manufacturer. The noise level may be reduced by optimizing the layout and the shielding of the internal components of the ultrasound system. It is expected that the noiselevel of commercial scanners will be considerably lower.
   Also, it may be preferable to create an image by combining only the third and fourth harmonics, as the simulations of chapter 9 showed that the fifth harmonic was below the noisefloor at large depths. Then the bandwidth used in reception could be reduced, thus lowering the noise level.

3. The simulations reported in chapter 9 were performed for a homogeneous medium using the material properties reported for liver. However, the human body has a heterogeneous structure with considerable variation in tissue properties. For example in the case of echocardiography, most of the propagation medium would consist of blood and cardiac tissue. The range of reported B/A and attenuation values for cardiac tissue are approximately equal to those reported for liver. But the attenuation reported for blood is up to four times lower than that of liver tissue, while the B/A is similar (Duck, 1990). To simulate the mix of cardiac tissue and blood encountered in echocardiography some researchers, e.g. Frijlink and Torp (2009), use the average attenuation of those tissue types. This considerably increases the SNR for the higher harmonics.

4. The simulations of chapter 9 were performed using an MI of 1.5, while the regulatory limit is an MI of 1.9. An MI of 1.9 would increase the SNR of the third and fifth harmonics by $\sim$6 dB and $\sim$10 dB respectively.

5. The simulations in chapter 9 suggest that the overall sensitivity in reception could be improved by 5 dB by optimizing the transducer geometry. This is treated in more detail in the next section.

Based on the above discussion, *in-vivo* SHI applied to echocardiography appears feasible for diagnostic pressures. *In-vivo* experiments should determine wether the contribution of the fifth harmonic is sufficient to compensate for the increase in noiselevel compared to imaging using the third and fourth harmonics alone.

15.2.2 Hardware - interleaved transducer design

Next to proving the feasibility of SHI, the development of the hardware required for SHI - notably the transducer - was reported in this thesis. The interleaved array reported in chapter 8 possesses quite optimal characteristics for tissue and UCA enhanced SHI applied to echocardiography. Also, it is suitable for a wide range of other experimental and clinical

imaging modalities, such as second harmonic, subharmonic, and SURF imaging. However, there is always room for improvement:

1. the simulations presented in chapter 9 suggest that a transmission frequency of 1.0 - 1.2 MHz is optimal for echocardiography using SHI. Therefore, the resonance frequency of the transmit subarray of the interleaved array (chapter 8) could be increased slightly improving the attainable resolution. The resonance frequency of the receive subarray should be increased accordingly.

2. Those same simulations in chapter 9 suggest that the system SNR could be improved by 5 dB by changing the ratio of transmit to receive elements of the dual frequency array. The flip side of this optimization is that the voltages exciting the transducer should be scaled accordingly by a factor of 3.3. This modification will make the array less suitable for subharmonic imaging though, as the roles of the low frequency subarray and receive subarrays are reversed for this modality.

3. The bandwidth of the low frequency subarray and the receive sensitivity of the high frequency subarray could be improved by replacing the PZT by single crystal or piezocomposite material. The increase in the transmit bandwidth will improve the axial resolution. More importantly, the simulation results shown in Fig. 11.3 indicate that if the -6 dB bandwidth of the entire transmission chain is 65% or higher, SHI could be performed using standard image processing methods. Moreover, the best compromise between resolution and sidelobe suppression is obtained using transmission pulses with -6 dB bandwidths in the 60 - 80% range (Szabo, 2004).
   Although we did not find an improvement in the peak transmit and receive transfer of the custom arrays based on single crystal or piezocomposites (chapters 7 and 8), this is likely due to dicing difficulties. Single crystal materials are known for being difficult to process (Ming Lu and Proulx, 2005), but the specified material properties indicate that optimizing the manufacturing process may be worth the effort. This is corroborated by the work of Frijlink and Torp (2009), who used FEM simulations to compare the effect of using single crystal versus PZT piezomaterial on the transmit transfer functions of phased arrays intended for echocardiography. In the untuned case the array based on single crystal had a $\sim$4 dB higher transmit transfer with 17% more -6 dB fractional bandwidth compared to the array based on PZT.
   The bandwidth of the entire transmission chain could also be improved by electrically tuning the interleaved transducer off-resonance or by using a multiple-resonance-tuning-circuit. Both methods exchange transmit efficiency for bandwidth, resulting in a lower peak pressure at focus at the same excitation voltage - and, consequently, less energy in the higher harmonics. However, this is not a feasible proposition with the current combination of transducer and imaging system, due to the limited output voltage of the latter.

The concept of separating the transmit and receive chains was also successfully applied to other applications requiring a broad bandwidth. This was demonstrated in chapter 6, where a multilayer single element transducer was developed to measure the volume of liquid filled cavities on the basis of nonlinear wave propagation. This transducer was capable of trans-

mitting a fundamental signal and receiving up to the third harmonic with good sensitivity.

15.2.3 Feasibility of single pulse SHI

Next to the development of hardware for SHI, the signal processing aspects were considered in detail in this thesis. The standard image processing used for medical ultrasound imaging consists of filtering the relevant frequency band and subsequently taking the Hilbert transform to obtain the envelope data. Ideally, the envelope of a pressure signal produced by a single reflector should be a unimodal function, so that a single reflector is indicated by a single reflection in a B-mode image. This is usually the case in fundamental or second harmonic imaging, since the frequency content of the signal is concentrated in a single continuous band. However, in SHI the bands of the third to fifth harmonics are combined. If the original transmission was fairly narrowband, local minima exist in between the harmonics. These minima may cause ripples in the envelope of a nonlinearly propagated signal filtered over the superharmonic band (chapter 11). The ripples could lead to ghost reflections in B-mode images: single reflectors appear as multiple overlapping reflectors.
The simulations presented in this thesis (see Fig. 11.3) indicate that more broadbanded transmissions (-6 dB bandwidth $> 65\%$) would yield ripple-free superharmonic PSFs using standard signal processing methods. However, there is a practical upper limit to the bandwidth of the transmitted pulse. For very wideband signals the second harmonic component generated by the high frequencies in the transmit signal will coincide with the third harmonic component generated by the low frequencies in the transmit signal. This will deteriorate the quality of the superharmonic beam: the second harmonic component has a lower roll-off and increased sidelobes compared to the third harmonic leading to increased clutter in the image. One solution would be to fully remove the second harmonic component by filtering, but that would also remove a part of third harmonic, which is the component of the superharmonic band containing the most energy.
Performing ripple-free SHI using standard signal processing methods would be ideal. However, with our combination of transducer and imaging system it is impossible to transmit pressure signals with the required bandwidth and with sufficient amplitude to perform high quality SHI. Therefore, to minimize the ripples in the superharmonic PSF associated with a narrowband transmission, two pulsing schemes were developed: a dual pulse method and a chirp method.

15.2.4 Dual pulse SHI

The dual pulse method aims at removing the ripple artifacts associated with imaging using multiple harmonic bands. Dual pulse SHI has markedly improved axial and lateral resolutions compared to the third harmonic, but at the expense of a reduced frame rate (see chapters 12 and 13). A considerable advantage of the dual pulse method for practical *in-vivo* SHI is that it produces a smooth time signal without ripples regardless of the level of the fourth or fifth harmonic.
In the future the dual pulse method can be improved in the following ways:

1. the optimization of the frequencies of the transmitted pulses as presented in chapter 13 only takes the transmit subarray into account. In an imaging situation the system will operate in pulse-echo mode and the frequencies of the transmitted pulses will also have to be optimized for the transfer functions of the subarray used in reception and the receive circuitry. To determine these transfer functions the methods presented in chapters 2 and 3 could be used.

2. The pulsing scheme should be corrected for attenuation effects. The transmitted pulse with the highest center frequency will experience more attenuation compared to the low frequency transmission. To correct for this effect the amplitudes of both pulses have to be scaled. The scaling of both pulses is primarily determined by the ratio of the highest and lowest frequency.
   Another attenuation effect to be taken into account is the frequency downshift of the pulses. This depends on the transmission frequency band and the imaging depth. The best strategy would be to optimize the transmission pulses for the expected downshift in the middle of the imaging domain. It is expected that the PSFs in the near and far field will remain acceptable: even though there is an optimal choice of transmission frequencies, transmission frequencies close to the optimal ones will still yield good PSFs (see Fig. 13.3). In the future this will be investigated using simulations.

15.2.5 Chirp SHI

An alternative for dual pulse SHI could be chirp SHI. The PSFs produced by the superharmonic chirp protocol are virtually free from ripple artifacts and have increased spatial resolution compared to the third harmonic. However, the obtained spatial resolution is lower compared to the dual pulse method. Therefore, a trade-off exists between the attainable spatial resolution and the frame rate in superharmonic imaging (see chapter 14).
In the future the chirp SHI protocol can be improved in a number of ways:

1. the decoding pulse used in the chirp protocol can be improved by correcting for the phase transfer function of the transmit subarray and the attached circuitry. The decoding pulse is obtained using KZK simulations; in these simulations the phase transfer of the transducer and transmit circuitry was assumed to be flat over the bandwidth of the transmitted chirp. This is however not the case. By obtaining the amplitude and phase transfer functions of the transmit subarray using the methods described in chapters 2 and 3 and modifying the input for the KZK simulations a more suitable decoding pulse could be obtained. Future work will include these effects in the calculation of the decoding pulse. For a pulse-echo imaging situation the decoding pulse should also be corrected for the amplitude and phase transfer functions of the receive subarray and the attached circuitry.

2. To implement *in-vivo* chirp SHI a depth dependent decoding pulse should be calculated, as the shape of the decoding pulse depends on the effects of two depth dependent phenomena - nonlinear wave propagation and attenuation. All parameters influencing the shape of the decoding pulse - transducer geometry, transfer functions, etc. - can be measured or calculated, except the parameters of the tissue through which

the pressure wave propagates. However, we make the observation that in the case of echocardiography the majority of the propagation medium consists of either cardiac tissue or blood. The B/A of cardiac tissue and blood are approximately equal (Duck, 1990). The attenuation coefficient (α) varies by a factor 3 - 4 between those tissues (Duck, 1990). Thus, it may be possible to obtain an estimate of the optimal decoding pulse by creating a look up table consisting of pressure waveforms produced using KZK simulations with different attenuation values. Then, the estimated decoding pulse could be finetuned using statistical methods, such as the ones used for point spread function deconvolution (Jirik and Torfinn, 2008). In this manner the maximum amount of apriori information would be used to obtain the decoding pulse. A useful decoding pulse may also be obtained by combining chirps with center frequencies at the third, fourth and fifth harmonics of the transmitted chirp. An algorithm could be implemented to maximize the cross correlation coefficients at each depth by varying the relative amplitudes and phases of the $3*f_0$, $4*f_0$ and $5*f_0$ chirps used for the decoding chirp.

The merits of using superharmonic chirps versus the difficulty of obtaining a satisfactory decoding pulse should be compared to the selective filtering at the third harmonic band and decoding using a $3*f_0$ chirp.

15.3 Conclusions

This work demonstrates that SHI is feasible. Our simulations show that the SNR is sufficient for *in-vivo* SHI - even at large imaging depths. It is expected that SHI leads to a considerable improvement in image quality, as the beam produced by the superharmonics has even more favorable characteristics than the second harmonic beam.
The implementation of SHI is a delicate balance encompassing the entire engineering chain from transducer design to signal processing techniques. We developed the necessary hardware to perform *in-vivo* SHI. Additionally, we demonstrated the possibility of imaging with multiple harmonics using dedicated imaging protocols for the first time. In developing these protocols we found that the amplitude and phase transfer functions play an increasingly important role. Therefore, the methods to measure those functions in a simple laboratory setting have been also developed within the scope of this thesis.
Thus, it seems that the major engineering hurdles for SHI have been solved. The main priority for follow-up research should be to investigate whether the image quality improvement outweighs the practical difficulties of implementing SHI by studying *in-vivo* images.

References

I. Akiyama, S. Saito, and A. Ohya. Development of an ultra-broadband ultrasonic imaging system: Prototype mechanical sector device. *J. Med. Ultrasonics*, 33(2):71–76, 2006.

M.A. Averkiou, D.N. Roundhill, and J.E. Powers. A new imaging technique based on the nonlinear properties of tissues. In *Proc. IEEE Ultrasonic Symp.*, pages 1561–1566, 1997.

P.Y. Barthez, R. Leveille, and P.V. Scrivani. Side lobes and grating lobes artifacts in ultrasound imaging. *Veterinary Radiology & Ultrasound*, 38(5):387–393, 1997.

E. Biagi, L. Breschi, E. Vannacci, and L. Masotti. Stable and transient subharmonic emissions from isolated contrast agent microbubbles. *IEEE Trans. Ultrason. Ferroelect. Freq. Control*, 54(3):480–497, 2007.

S. Blaak, Z. Yu, G.C.M. Meijer, C. Prins, C.T. Lancée, J.G. Bosch, and N De Jong. Design of a micro-beamformer for a 2d piezoelectric ultrasound transducer. In *Proc. IEEE Ultrasonic Symp.*, Rome, Italy, 2009.

D. T. Blackstock. Transient solution for sound in a viscous fluid. *Journal of the Acoustical Society of America*, 38(5):931–931, 1965.

R.J. Bobber. General reciprocity parameter. *J. Acoust. Soc. Am.*, 39(4):680–687, 1966.

J.M.G. Borsboom, C.T. Chin, and N. de Jong. Nonlinear coded excitation method for ultrasound contrast imaging. *Ultrasound Med. Biol.*, 29:277–284, 2003.

A. Bouakaz and N. de Jong. Native tissue imaging at superharmonic frequencies. *IEEE Trans. Ultrason. Ferroelectr. Freq. Control*, 50(5):496–506, 2003.

A. Bouakaz, S. Frigstad, F.J. ten Cate, and N. de Jong. Super harmonic imaging: a new imaging technique for improved contrast detection. *Ultrasound Med. Biol.*, 28(1):59–68, 2002.

A. Bouakaz, E.J.W. Merks, C.T. Lancée, and Bom N. Noninvasive bladder volume measurements based on nonlinear wave distortion. *Ultrasound Med. Biol.*, 30(4):469–476, 2004a.

A. Bouakaz, F.J. ten Cate, and N. de Jong. A new ultrasonic transducer for improved contrast nonlinear imaging. *Phys. Med. Biol.*, 49(16):3515–3525, 2004b.

A. Bouakaz, M. Versluis, and N. de Jong. High-speed optical observations of contrast agent destruction. *Ultrasound Med. Biol.*, 31(3):391–399, 2005.

F.P. Branca, F. Bini, and F. Mariozzi. Optimum choice of acoustic properties of filling materials using optical measurement. In *Proc. IEEE Ultrasonic Symp.*, pages 1663–1665, Hawaii, USA, 2004.

A. Briggs. *Acoustic Microscopy*. Oxford University Press, New York, 1992.

A. Caronti, D. Fiasca, G. Caliano, E. Cianci, and M. Pappalardo. Experimental study of acoustic coupling in cmut arrays by optical interferometry. In *Proc. IEEE Ultrasonic Symp.*, pages 1960–1964, Hawaii, USA, 2003.

A. Caronti, A. Savoia, G. Caliano, and M. Pappalardo. Acoustic coupling in capacitive microfabricated ultrasonic transducers: Modeling and experiments. *IEEE Trans. Ultrason. Ferroelectr. Freq. Control*, 52(12):2220–2234, 2005.

X. Chen and K.Q. Schwarz. Acoustic coupling from a focused transducer to a flat plat and back to the transducer. *J. Acoust. Soc. Am.*, 95(6):3049–3054, 1994.

X. Chen, K.Q. Schwarz, and K.J. Parker. Radiation pattern of a focused transducer: A numerically convergent solution. *J. Acoust. Soc. Am.*, 94(5):2979–2991, 1993.

R.Y. Chiao and L.J. Thomas. Synthetic transmit aperture imaging using orthogonal golay coded excitation. In *Proc. IEEE Ultrasonics Symp.*, pages 1677–1680, 2000.

J. Chomas, P. Dayton, D. May, and K. Ferrara. Nondestructive subharmonic imaging. *IEEE Trans. Ultrason. Ferroelect. Freq. Control*, 49(7):883–892, 2002.

T. Christopher. Source prebiasing for improved second harmonic bubble-response imaging. *IEEE Trans. Ultrason. Ferroelectr. Freq. Control*, 46(3):556–563, 1999. Journal Article United States.

J. Chung. Echocardiography in 2009: State of the art. *J. Invasive Cardiol.*, 21:346–351, 2009.

R.S.C. Cobbold. *Foundations of Biomedical Ultrasound*. Oxford University Press, Inc., Oxford, New York, 2007.

M.P. Cooling and V.F. Humphrey. A nonlinear propagation model-based phase calibration technique for membrane hydrophones. *IEEE Trans. Ultrason. Ferroelectr. Freq. Control*, 55(1):84–93, 2008.

P.J. Currie. Transesophageal echocardiography. new window to the heart. *Circulation*, 80: 215–217, 1989.

C. Dang, L.W. Jr. Schmerr, and A. Sedov. Ultrasonic transducer sensitivity and model-based transducer characterization. *Res. Nondestr. Eval.*, 14(4):203–228, 2002.

P. Dawson, D.O. Cosgrove, and R.G. Grainger, editors. *Textbook of Contrast Media*. Isis Medical Media Ltd., Oxford, 1999. Williams R. Microbubble dynamics. In:.

F.A. Duck. *Physical Properties of Tissues*. Academic Press, Inc, San Diego, 1990.

A. Eller and H.G. Flynn. Generation of subharmonic of the order one-half by bubbles in a sound field. *J. Acoust. Soc. Am.*, 46(3B):722–727, 1969.

M. Emmer. *The onset of bubble vibration*. Ph.d. dissertation, Erasmus Univ. Rotterdam, 2009.

T.J. Esward and S.P. Robinson. Extending the frequency range of the npl primary standard laser inteferometer for hydrophone calibration to 60 mhz. *IEEE Trans. Ultrason. Ferroelectr. Freq. Control*, 46(3):737–744, 1999.

H. Feigenbaum. *Echocardiography*. 4th edition edition.

G. Ferin, M. Legros, N. Felix, C. Notard, and L. Ratsimandresey. Ultra-wide bandwidth array for new imaging modalities. In *Proc. IEEE Ultrasonic Symp.*, pages 204–207, New York, USA, 2007.

F. Forsberg, W.T. Shi, B. Jadidian, and A.A. Winder. Multi-frequency harmonic arrays: Initial experience with a novel transducer concept for nonlinear contrast imaging. *Ultrasonics*, 43:79–85, 2004.

M.E. Frijlink and H. Torp. Simulation of acoustic fields from arbitrary transducer stacks using a fem transducer model and nonlinear wave propagation. In *Proc. IEEE Ultrasonic Symp.*, pages –, Roma, Italy, 2009.

P. Frinking, E. Gaud, and M. Arditit. Compression only behavior and subharmonic scattering of phospholipid-shell microbubbles. In *The 14'th European symposium on ultrasound contrast imaging (abstract)*, pages 80–87, Rotterdam, the Netherlands, 2009.

P.J. Frinking, N. de Jong, and E.I. Céspedes. Scattering properties of encapsulated gas bubbles at high ultrasound pressures. *J. Acoust. Soc. Am.*, 105(3):523–533, 1999.

T.W. Galema, M.L. Geleijnse, W.B. Vletter, L. de Laat, and F.J. ten Cate. Clinical usefullness of sonovue contrast echocardiography: the Thorax Centre experience. *Neth. Heart J.*, 15(2):55–60, 2007.

P. Gatta. *Interferometric Characterization of Planar Vibrating Structures*. Ph.d. dissertation (italian), Universitȧ Roma Tre, 2008.

R. L. Goldberg, M.J. Jurgens, D.M. Mills, C.S. Henriquez, D. Vaughan, and S.W. Smith. Modeling of piezoelectric multilayer ceramics using finite element analysis. *IEEE Trans. Ultrason. Ferroelectr. Freq. Control*, 44(6):1204–1214, 1997.

A. Goldstein, D.R. Gandhi, and W.D. O'Brien. Diffraction effects in hydrophone measurements. *IEEE Trans. Ultrason. Ferroelectr. Freq. Control*, 45(4):972–979, 1998.

J.F. Guess, C.G. Oakley, S.J. Douglas, and R.D. Morgan. Cross-talk paths in array transducers. In *Proc. IEEE Ultrasonic Symp.*, pages 1279–1282, 1995.

F. Guidi, H.J. Vos, R. Mori, N. De Jong, and P. Tortoli. Microbubble characterization through acoustically-induced deflation. *IEEE Trans. Ultrason. Ferroelectr. Freq. Control*, 57(1):193–202, 2010.

M.F. Hamilton and D.T. Blackstock. *Nonlinear acoustics*. Academic Press, Inc., San Diego, California, 1998.

T.S. Hart and M.F. Hamilton. Nonlinear effects in focused sound beams. *J. Acoust. Soc Am.*, 84(4):1488–1496, 1988.

J.A. Hossack and B.A. Auld. Improving the characteristics of a transducer using multiple piezoelectric layers. *IEEE Trans. Ultrason. Ferroelectr. Freq. Control*, 40(2):131–139, 1993.

J.A. Hossack, P. Mauchamp, and L. Ratsimandresy. A high bandwidth transducer optimized for harmonic imaging. In *Proc. IEEE Ultrasonic Symp.*, pages 1021–1024, San Juan, Puerto Rico, 2000.

H.A. Hubert, K. Chambers, J. Clifton, and J. Tasaka. Clinical utility of a portable ultrasound device in intermittent catheterization. *Archives of Physical Medicine and Rehabilitation*, 79:172–175, 1998.

J. Huijssen. *Modeling of Nonlinear Medical Diagnostic Ultrasound*. PhD thesis, Delft University of Technology, 2008.

J. Huijssen and M.D. Verweij. An iterative method for the computation of nonlinear, wide-angle, pulsed acoustic fields of medical diagnostic transducers. *J. Acoust. Soc. Am.*, 127: 33–44, 2010.

J. Huijssen, M.D. Verweij, and N. de Jong. 3d time-domain modeling of nonlinear medical ultrasound with an iterative greens function method. In *proc. IEEE Ultrasonics symp..*, Vancouver, Canada, 2006.

J. Huijssen, M.D. Verweij, and N. de Jong. Comparison of an angular spectrum method and a greens function method for nonlinear propagation of pulsed acoustic fields from medical phased array transducers. In *proc. IEEE Ultrasonics symp.*, New York, USA, 2007.

J. Huijssen, M.D. Verweij, and N. de Jong. Greens function method for modeling nonlinear three-dimensional pulsed acoustic fields in diagnostic ultrasound including tissue-like attenuation. In *proc. IEEE Ultrasonics symp.*, Beijing, China, 2008.

V.F. Humphrey. Nonlinear propagation in ultrasonic fields: measurements modelling and harmonic imaging. *Ultrasonics*, 38:267–272, 2000.

J.A. Jensen. Field: A program for simulating ultrasound systems. *Paper presented at the 10th Nordic-Baltic Conference on Biomedical Imaging Published in Medical & Biological Engineering & Computing*, 34(Supplement 1 Part 1):351–353, 1996.

J.A. Jensen and N.B. Svendsen. Calculation of pressure field from arbitrarily shaped, apodized and excited ultrasound transducers. *IEEE Trans. Ultrason. Ferroelectr. Freq. Control*, 39(2):262–267, 1992.

J. Jeong, C. Seo, and J.T. Yen. Dual-layer transducer array for 3-d imaging. In *Proc. IEEE Ultrasonic Symp.*, pages 2371–2374, New-York, USA, 2007.

R. Jirik and T. Torfinn. Two-dimensional blind bayesian deconvolution of medical ultrasound images. *IEEE Trans. Ultrason. Ferroelectr. Freq. Control*, 55(10):2140–2153, 2008.

J.D. Kasprzak, B. Paelinck, F.J. Ten Cate, W.B. Vletter, N. De Jong, D. Poldermans, A. Elhendy, A. Bouakaz, and J.R.T.C. Roelandt. Comparison of native and contrast-enhanced harmonic echocardiography for visualization of left ventricular endocardial border. *Amer. J. Cardiol.*, 83(2):211–217, 1999.

J.A. Kisslo, D.B. Adams, and G.J. Leech. Two-dimensional echocardiography in the normal heart. In *Echo in Context - 21st Annual Satellite Video Teleconference*, 2006.

C. Koch. Amplitude and phase calibration of hydropohones by heterodyne and time-gated time-delay spectrometry. *IEEE Trans. Ultrason. Ferroelectr. Freq. Control*, 50(3):344–348, 2003.

C. Koch and W. Molkenstruck. Primary calibration of hydrophones with extended frequency range 1 to 70 mhz using optical interferometry. *IEEE Trans. Ultrason. Ferroelectr. Freq. Control*, 46(5):1303–1314, 1999.

R. Kompfner and R. A. Lemons. Nonlinear acoustic microscopy. *Applied Physics Letters*, 28(6):295–297, 1976.

T. Kondo and M. Kitatuji. Medical transducer arrays using composite materials for acoustic matching layers. In *Proc. IEEE Ultrasonic Symp.*, pages 1318–1321, Montreal, Canada, 2004.

K. Kooiman, M.R. Böhmer, M. Emmer, H.J. Vos, C. Chlon, W.T. Shi, C.S. Hall, S.H. de Winter, K. Schroën, M. Versluis, N. de Jong, and A. van Wamel. Oil-filled polymer microcapsules for ultrasound-mediated delivery of lipophilic drugs. *J. Contr. Release*, 133(2):109–118, 2009.

B.J. Krenning, M.M. Voormolen, and J.R. Roelandt. Assessment of left ventricular function by three-dimensional echocardiography. *Cardiovasc. Ultrasound*, pages 1–12, 2003.

S. Krishnan, J.D. Hamilton, and M. O'Donnell. Suppression of propagating second harmonic in ultrasound contrast imaging. *IEEE Trans. Ultrason. Ferroelectr. Freq. Control*, 45(3):704–711, 1998.

V. P. Kuznetsov. Equations of nonlinear acoustics. *Soviet Physics - Acoustics*, 16(4):467–470, 1971.

C. Labuda, J.L. Raymond, and C.C. Church. Reciprocity calibration of hydrophones in the megahertz frequency range. In *Proc. IEEE Ultrasonic Symp.*, pages 1595–1597, 2004.

C.T. Lancée. *A transesophageal phased array transducer for ultrasonic imaging of the heart*. Phd-thesis, Erasmus University Rotterdam, 1987.

C.T. Lancée, J. Souquet, H. Ohgashi, and N. Bom. Transducers in medical ultrasound: Part one. ferro-electric ceramics versus polymer piezo-electric materials. *Ultrasonics*, 23(3): 138–142, 1985.

C.T. Lancée, N. de Jong, and N. Bom. Design and construction of an esophageal phased array probe. *Med. Prog. Technol.*, 13(3):139–148, 1988.

Y.S. Lee. *Numerical solution of the KZK equation for pulsed finite amplitude sound beams in thermoviscous fluids.* Phd-thesis, The University of Texas, 1993.

Y.S. Lee and M.F. Hamilton. Time-domain modeling of pulsed finite-amplitude sound beams. *J. Acoust. Soc. Am.*, 97(2):906–917, 1995.

D.A. Leedom, R. Krimholtz, and G.L. Matthaei. Equivalent circuits for transducers having arbitrary even- or odd-symmetry piezoelectric excitation. *IEEE Trans. Sonics Ultrason.*, SU-18(3):128–141, 1971.

T.G. Leighton. *The acoustic bubble*. Academic Press Limited, London, United Kingdom, 1994.

H. Li, Y.C. Li, D. Zhou, J. Peng, H.S. Luo, and J.Y. Dai. Application of pmnpt single crystal in a 3.2 mhz phased-array ultrasonic medical imaging transducer. In *Proc. IEEE Int. Symp. App. Ferroelec.*, pages 572–574, Nara-city, Japan, 2007.

A.L. Lopez-Sanchez and W. Schmerr. Determination of an ultrasonic transducer's sensitivity and impedance in a pulse-echo setup. *IEEE Trans. Ultrason. Ferroelectr. Freq. Control*, 53(11):2101–2112, 2006.

G. Ludwig and K. Brendel. Calibration of hydrophones based on reciprocity and time delay spectrometry. *IEEE Trans. Ultrason. Ferroelectr. Freq. Control*, 35(2):168–174, 1988.

L.D. Luker and A.L. van Buren. Phase calibration of hydrophones. *J. Acoust. Soc. Am.*, 70 (2):516–519, 1981.

X. Lurton, editor. *An introduction to underwater acoustics: principles and applications*. Praxis Publishing Ltd, Chichester, UK, 2002.

H.T. Lutz and H.A. Gharbi. *Manual of diagnostic ultrasound in infectious tropical diseases*. Springer-Verlag, Berlin Heidelberg, Germany, 2006.

Q. Ma, D. Zhang, X. Gong, and Y. Ma. Investigation of superharmonic sound propagation and imaging in biological tissues in-vitro. *J. Acoust. Soc. Am.*, 119(4):2518–2523, 2006.

W.P. Mason and H.J. McSkimin. Attenuation and scattering of high frequency sound waves in metals and glasses. *J. Acoust. Soc. Am.*, 19(3):463–473, 1947.

S.E. Masoy, O. Standal, P. Nasholm, T.F. Johansen, and B. Angelsen. Surf imaging: In-vivo demonstration of an ultrasound contrast agent detection technique. *IEEE Trans. Ultrason. Ferroelectr. Freq. Control*, 55(5):1112–1121, 2008. Evaluation Studies Journal Article Research Support, Non-U.S. Gov't United States.

G. Matte, P.L.M.J. van Neer, J.M.G. Borsboom, M.D. Verweij, and N. de Jong. A new frequency compounding technique for super harmonic imaging. In *Proc. IEEE Ultrasonic Symp.*, pages 357–360, New York, NY, 2008. IEEE.

G.M. Matte, P.L.M.J. van Neer, J. Huijssen, M. Verweij, and N. de Jong. Parameter optimization of interleaved phased arrays for transthoracic and abdominal applications of super harmonic imaging. 2010.

R.E. McKeighen. Design guildelines for medical ultrasonic arrays. In *Proc. SPIE*, volume 3341, pages 2–18, San Diego, USA, 1998.

G.J. McMorrow, H. Baartmans, N. Bom, and C.T. Lancée. Instanteneous ultrasonic measurement of bladder volume. patent: Pct wo 2004/017834 a1, diagnostic ultrasound europe b.v., lage dijk 14, 3401 rg ijsselstein, the netherlands. 2002.

E.J.W. Merks, C.T. Lancée, N. Bom, A.F.W. van der Steen, and de Jong N. Comparison of three different transducer concepts for acoustic bladder volume measurements. In *Proc. IEEE Ultrasonic Symp.*, pages 2239–2242, Rotterdam, the Netherlands, 2005.

E.J.W. Merks, J.M.G. Borsboom, M.M. Voormolen, N. Bom, A.F.W. van der Steen, and N. de Jong. A klm-circuit model of a multi-layer transducer for bladder volume measurements. *Ultrasonics*, 44(Suppl. 1):705–710, 2006a.

E.J.W. Merks, A. Bouakaz, N. Bom, C.T. Lancée, A.F.W. van der Steen, and N. de Jong. Design of a multi-layer transducer for acoustic bladder volume assessment. *IEEE Trans. Ultrason. Ferroelect. Freq. Control*, 53(10):1730–1738, 2006b.

D.M. Mills. Medical imaging with capacitive micromachined ultrasound transducer (cmut) arrays. In *Proc. IEEE Ultrasonic Symp.*, pages 384–390, Montreal, Canada, 2004.

X. Ming Lu and T.L. Proulx. Single crystals vs. pzt ceramics for medical ultrasound applications. In *Proc. IEEE Ultrasonic Symp.*, pages 227–230, Rotterdam, the Netherlands, 2005.

T. Misardis and J.A. Jensen. Use of modulated excitation signals in medical ultrasound. part ii: design and performance for medical imaging applications. *IEEE Trans. Ultrason. Ferroelectr. Freq. Control*, 52(2):192–207, 2005a.

T. Misardis and J.A. Jensen. Use of modulated excitation signals in medical ultrasound. part i: basic concepts and expected benefits. *IEEE Trans. Ultrason. Ferroelectr. Freq. Control*, 52(2):177–191, 2005b.

T.G. Muir and E.L. Carstensen. Prediction of nonlinear acoustic effects at biomedical frequencies and intensities. *Ultrasound Med. Biol.*, 6(4):345–357, 1980.

S.L. Mulvagh, A.N. DeMaria, S.B. Feinstein, P.N. Burns, S. Kaul, M. Miller, J.G. Monaghan, T.R. Porter, L.J. Shaw, and F.S. Villanueva. Contrast echocardiography: current and future applications. *J. Am. Soc. Echocardiogr.*, 13(4):331–342, 2000.

K. Nathanail, M. van Stralen, C. Prins, F. van den Adel, P.J. French, N. De Jong, A.F.W. van der Steen, and J.G. Bosch. Rapid 3d transesophageal echocardiography using a fast-rotating multiplane transducer. In *Proc. IEEE Ultrasonics Symp.*, pages 848–851, Beijing, China, 2008.

J. Ord, D. Lunn, and J. Reynard. Bladder management and risk of badder stone fomation in spinal cord injured patients. *Journal of Urology*, 170(5):1734–1737, 2003.

M. Pollakowski and H. Ermert. Chirp signal matching and signal power optimization in pulse-echo mode ultrasonic nondestructive testing. *IEEE Trans. Ultrason. Ferrorelect. Freq. Control*, 41(5):655–659, 1994.

E.G. Radulescu, P.A. Lewin, A. Goldstein, and A. Nowicki. Hydrophone spatial averaging corrections from 1 to 40 mhz. *IEEE Trans. Ultrason. Ferroelectr. Freq. Control*, 48(6): 1575–1580, 2001.

E.G. Radulescu, P.A. Lewin, J. Wojcik, and A. Nowicki. Calibration of ultrasonic hydrophone probes up to 100 mhz using time gating frequency analysis and finite amplitude waves. *Ultrasonics*, 41:247–254, 2003.

P.W. Rehrig, W.S. Hackenberger, and X. Jiang. Status of piezoelectric single crystal growth for medical transducer applications. In *Proc. IEEE Ultrasonic Symp.*, pages 766–769, Hawaii, USA, 2003.

S.M. Rhim and H. Jung. Piezoelectric single crystal for medical ultrasound transducer. In *Proc. IEEE Ultrasonic Symp.*, pages 300–304, New York, USA, 2007.

S.M. Rhim, H. Jung, J. S. Jun, and J.S. Hwnag. A 6.0 mhz 0.15 mm pitch phased array ultrasonic probe using pmn-pt single crystal. In *Proc. IEEE Ultrasonic Symp.*, pages 219–222, Rotterdam, the Netherlands, 2005.

J.R.T.C. Roelandt. Three-dimensional echocardiography: the future today! *Comput. Graph.*, 24(5):715–729, 2000.

B.A. Schrope and V.L. Newhouse. Second harmonic ultrasonic blood perfusion measurement. *Ultrasound Med Biol*, 19(7):567–79, 1993.

B.A. Schrope, V.L. Newhouse, and V. Uhlendorf. Simulated capillary blood flow measurement using a nonlinear ultrasonic contrast agent. *Ultrasonic Imaging*, 14(2):134–158, 1992.

A.R. Selfridge. Approximate material properties in isotropic materials. *IEEE Trans. Sonics Ultrason.*, SU-32(3):381–394, 1985.

J.B. Seward. Transesophageal echocardiography: Technique, anatomic correlations, implementation and clinical applications. *Mayo Clin. Proc.*, 63:649–680, 1988.

P.M. Shankar, P.D. Krishna, and V.L. Newhouse. Advantages of subharmonic over second harmonic backscatter for contrast-to-tissue echo enhancement. *Ultrasound Med. Biol.*, 24:395–399, 1998.

R.S. Shapiro, J. Wagreich, R.B. Parsons, A. Stancato-Pasik, H.C. Yeh, and R. Lao. Tissue harmonic imaging sonography: evaluation of image quality compared with conventional sonography. *AJR*, 171:1203–1206, 1998.

H.H. Shariff, P. Bevan, R. Karshafian, R. Williams, and P.N. Burns. Radial modulation imaging: Raising the frequency for contrast imaging. In *Proc. IEEE Ultrasonic Symp.*, pages 104–107, Vancouver, Canada, 2006.

C.C. Shen and Y.C. Hsieh. Optimal transmit phasing on tissue background suppression in contrast harmonic imaging. *Ultrasound Med. Biol.*, 34(11):1820–1831, 2008.

C.C. Shen, Y.C. Wang, and Y.C. Hsieh. Third harmonic transmit phasing for tissue harmonic generation. *IEEE Trans. Ultrason. Ferroelect. Freq. Control*, 54(7):1370–1381, 2007.

J. Shen and E.S. Ebbini. A new coded-excitation ultrasound imaging system - part i: basic principles. *IEEE Trans. Ultrason. Ferroelect. Freq. Control*, 43(1):131–140, 1996.

S. Sherrit, H.D. Wiederick, and B.K. Mukherjee. A complete characterization of the piezoelectric dieelectric and elastic properties of motorola pzt 3203 hd including losses and dispersion. In *Proc. SPIE*, volume 3037, pages 158–169, Newport Beach, 1997.

W.T. Shi and F Forsberg. Ultrasonic characterization of the nonlinear properties of contrast microbubbles. *Ultrasound Med. Biol.*, 26(1):93–104, 2000.

J. Sijl, E. Gaud, P.J.A. Frinking, M. Arditi, N. De Jong, D. Lohse, and M. Versluis. Acoustic characterization of single ultrasound contrast agent microbubbles. *J. Acoust. Soc. Am.*, 124(6):4091–4097, 2008.

D.M. Skyba, R.J. Price, A.Z. Linka, T.C. Skalak, and S. Kaul. Direct in vivo visualization of intravascular destruction of microbubbles by ultrasound and its local effects on tissue. *Circulation*, 98:290–293, 1998.

R. Slappendel and E.W. Weber. Non-invasive measurement of bladder volume as an indication for bladder catheterization after orthopaedic surgery and its effect on urinary tract infections. *Eur. J. Anaesthesiol.*, 16(8):503–506, 1999.

H.C. Starritt, F.A. Duck, A.J. Hawkins, and V.F. Humphrey. The development of harmonic distortion in pulsed finite-amplitude ultrasound passing through liver. *Physics in Medicine and Biology*, 31(12):1401–1409, 1986.

L. Sugeng, S.K. Shernan, I.S. Salgo, L. Weinert, D. Shook, J. Raman, V. Jeevanandam, F. DuPont, S. Settlemier, B. Savord, J. Fox, V. Mor-Avi, and R.M. Lang. Live 3-dimensional transesophageal echocardiography: Initial experience using the fully-sampled matrix array probe. *JACC*, 52(6):446–449, 2008.

T.L. Szabo. Time-domain wave-equations for lossy media obeying a frequency power-law. *Journal of the Acoustical Society of America*, 96(1):491–500, 1994. Nw521 Times Cited:88 Cited References Count:59.

T.L. Szabo. *Diagnostic Ultrasound Imaging: Inside Out*. Elsevier Academic Press, San Diego, 2004.

Y. Takeuchi. An investigation of a spread energy method for medical ultrasound systems - part one: theory and investigation. *Ultrasonics*, 17(4):175–182, 1979.

J.D. Thomas and D.N. Rubin. Tissue harmonic imaging: Why does it work? *Journal of the American Society of Echocardiography*, 11(8):803–808, 1998.

J.N. Tjotta, S. Tjotta, and E.H. Vefring. Propagation and interaction of 2 collinear finite-amplitude sound beams. *Journal of the Acoustical Society of America*, 88(6):2859–2870, 1990. El603 Times Cited:27 Cited References Count:32.

J.N. Tjotta, S. Tjotta, and E.H. Vefring. Effects of focusing on the nonlinear-interaction between 2 collinear finite-amplitude sound beams. *Journal of the Acoustical Society of America*, 89(3):1017–1027, 1991. Fa701 Times Cited:48 Cited References Count:13.

F. Tranquart, N. Grenier, V. Eder, and L. Pourcelot. Clinical use of ultrasound tissue harmonic imaging. *Ultrasound Med. Biol.*, 25(6):889–894, 1999.

S. Umchid, R. Gopinath, K. Srinivasan, P.A. Lewin, A.S. Daryoush, L. Bansal, and M. El-Sherif. Development of calibration techniques for ultrasonic hydrophone probes in the frequency range from 1 to 100 mhz. *Ultrasonics*, 49:306–311, 2009.

P.L.M.J. van Neer, G. Matte, J. Sijl, J.M.G. Borsboom, and N. de Jong. Transfer functions of us transducers for harmonic imaging and bubble responses. *Ultrasonics*, 46(4):336–340, 2007.

P.L.M.J. van Neer, M.G. Danilouchkine, G.M. Matte, M.D. Verweij, and N. de Jong. Dual pulse frequency compounded super harmonic imaging for phased array transducers. In *Proc. IEEE Ultrasonic Symp.*, pages –, Rome, Italy, 2009.

P.L.M.J. van Neer, G. Matte, M.G. Danilouchkine, C. Prins, F. van den Adel, and N. de Jong. Super harmonic imaging: development of an interleaved phased array transducer. *IEEE Trans. Ultrason. Ferroelectr. Freq. Control*, 57(2):455–468, 2010.

A. van Wamel, K. Kooiman, M. Harteveld, M. Emmer, F.J. ten Cate, M. Versluis, and N. de Jong. Vibrating microbubbles poking individual cells: Drug transfer into cells via sonoporation. *J. Contr. Release*, 112:149–155, 2006.

M.D. Verweij and J. Huijssen. A filtered convolution method for the computation of acoustic wave fields in very large spatiotemporal domains. *J. Acoust. Soc Am.*, 125(1):1868–1878, 2009.

F. Vignon, J.-F. Aubry, M. Tanter, A. Margoum, M.Fink, and J.M. Lecoeur. Dual-arrays brain imaging prototype: Experimental in vitro results. In *Proc. IEEE Ultrasonic Symp.*, pages 504–507, Rotterdam, the Netherlands, 2005.

M.M. Voormolen. *3D Harmonic Echocardiography*. PhD thesis, Erasmus University Rotterdam, 2007.

H.J. Vos. The modelling, design and prototyping of a 20 mhz - 40 mhz harmonic intravascular ultrasound transducer. MSc thesis, 2004.

H.J. Vos. *Single Microbubble Imaging*. PhD thesis, Erasmus University Rotterdam, 2010.

B. Ward, A.C. Baker, and V.F. Humphrey. Nonlinear propagation applied to the improvement of resolution in diagnostic medical ultrasound. *J. Acoust. Soc. Am.*, 101(1):143–154, 1996.

V. Wilkens and C. Koch. Amplitude and phase calibration of hydrophones up to 70 mhz using broadband pulse excitation and an optical reference hydrophone. *J. Acoust. Soc. Am.*, 115(6):2892–2903, 2004.

J.S.K. Woo. A short history of the development of ultrasound in obstetrics and gynecology. *Website: http://www.ob-ultrasound.net/history1.html*, 2002.

J. Wu. Determination of velocity and attenuation of shear waves using ultrasonic spectroscopy. *J. Acoust. Soc. Am.*, 99(5):2871–5, 1996.

G. G. Yaralioglu, B. Bayram, and B.T. Khuri-Yakub. Finite element analysis of cmuts: Conventional vs. collapse operation modes. In *Proc. IEEE Ultrasonic Symp.*, pages 586–589, Vancouver, Canada, 2006.

E.A. Zabolotskaya and R.V. Khokhlov. Quasi-plane waves in the nonlinear acoustics of confined beams. *Soviet Physics - Acoustics*, 15:3540, 1969.

R.J. Zemp, J. Tavakkoli, and R.S.C. Cobbold. Modeling of nonlinear ultrasound propagation in tissue from array transducers. *J. Acoust. Soc. Am.*, 113(1):139–152, 2003.

S. Zhou and J.A. Hossack. Investigation of digital filtering for stacked, phased ultrasound transducers. In *Proc. IEEE Ultrasonic Symp.*, pages 1201–1204, Munich, Germany, 2002.

S. Zhou, P. Reynolds, and J.A. Hossack. Improving the performance of capacitive micromachined ultrasound transducers using modified membrane and support structures. In *Proc. IEEE Ultrasonic Symp.*, pages 1925–1928, Rotterdam, the Netherlands, 2005.

M.J. Zipparo, C.G. Oakley, D.M. Mills, A.M. Dentinger, and L.S. Smith. A multirow single crystal phased array for wideband ultrasound imaging. In *Proc. IEEE Ultrasonic Symp.*, pages 1025–1029, Montreal, Cananda, 2004.

Summary

Medical ultrasound is one of the most prevalent radiological modalities used for diagnostic purposes. The technique allows for the visualization of tissues in the human body and is used in a diverse range of medical fields. In the field of clinical cardiology echocardiography is the main diagnostic technique. However, despite many advances in the recent years echocardiography remains technically challenging. A considerable subgroup of patients (10 - 20%) is considered difficult to image due to tough acoustic windows and inhomogeneous skin layers. Especially for obese patients or patients with lung disease the echo image quality could compromise the diagnosis.

Up to the late 90s medical ultrasound was linear - the transmitted frequency was equal to the received frequency. About a decade ago, it became possible to improve the quality of ultrasound images by exploiting the nonlinear nature of wave propagation. The technique is called 'tissue harmonic imaging' and was originally limited to the selective imaging of the second harmonic frequency. The harmonic beam is narrower and has an increased roll-off in combination with reduced sidelobes compared to the fundamental beam. Also, the harmonic beam builds up progressively. Therefore, second harmonic imaging is less sensitive to near-field artifacts, clutter and off-axis reflectors, in combination with a higher lateral resolution. These characteristics considerably improved ultrasound image quality, especially for the patient subgroup considered challenging to scan. The main drawback of using the second harmonic band for imaging lies in the fact that it contains significantly less energy than the fundamental band. That imposes considerable demands on the design of the entire ultrasound system including the transducer.

Recently, a new imaging technique dubbed 'superharmonic imaging' (SHI) was proposed. It takes advantage of the higher - third to fifth - harmonics arising from nonlinear propagation or ultrasound contrast agent response. Next to its better suppression of near-field artifacts, tissue SHI is expected to improve axial and lateral resolutions resulting in clearer images than second harmonic imaging. The benefit of SHI applied to UCAs comprises a better contrast-to-tissue ratio. The drawback of using these higher harmonics for imaging is that they contain even less energy than the second harmonic.

This thesis focuses on the development of transducers and signal processing methods for imaging and diagnosis based on nonlinear effects due to wave propagation (or ultrasound contrast agent response), with a particular emphasis on SHI. The presented work covers the aspects required to implement SHI - from proving its feasibility, the design of the necessary hardware, to the required image processing methods.

The first part of the thesis is concerned with the characterization and modeling of transducers. The developed methods and models are applied on the development of a transducer intended for 3D second harmonic transesophageal echocardiography and a transducer used to noninvasively measure bladder volumes based on the harmonic content of the echos.
An important part of transducer and system design is the measurement of a transducer's performance, for their assessment or the optimization of pulsing schemes or postprocessing. Therefore, we developed three methods to measure the absolute amplitude transfer function of a transducer, these are treated in chapter 2. A complete description of transducer behavior should also entail the phase between the driving signal and the surface oscillation of the transducer. Chapter 3 reports on a practical method to measure the phase transfer function of a transducer using a simple laboratory setup.
One of the crucial steps in the development of high performance transducers is their modeling. The models are based on a set of assumptions on transducer geometry and material behavior. Therefore, it is of the utmost importance to realize how accurate these models are. In chapter 4 we compare the surface vibration of a single array element as calculated by a 3D finite element model (FEM) with measurements obtained using a laser interferometer system. A good agreement was obtained between the model and the experiments.
The validated FEM model in combination with laser interferometer measurements is used in chapter 5 to determine the optimal geometry and element make-up for a matrix transducer intended for 3D second harmonic transesophageal echocardiography (TEE). TEE uses the esophagus instead of the thorax as an imaging window to the heart. The use of this window circumvents artifacts due to the ribs or fat layers in the skin. Moreover, it allows for the use of a higher transmission frequency. The current 3D TEE probes use fundamental imaging, but we expect that 3D TEE image quality may also benefit from second harmonic imaging. A TEE transducer consists of a flexible endoscope with the array transducer located at the tip. As the device has to fit in the esophagus, the size constraint is the main challenge for the design of a TEE transducer. To have the most efficient layout of the acoustic stacks and electronics in the limited 3D space of the endoscope tip the transducer was split in a 1.5D subarray for transmission and a 2D subarray for reception. The proposed geometry and element make-up for the transducer fulfills or exceeds all of the requirements for 3D second harmonic TEE.
Within the scope of this thesis a multilayer transducer concept was developed in chapter 6 for the noninvasive measurement of bladder volume. The measurement method is based on the fact that the amount of generated harmonics present within the echoes received from a region of interest behind the posterior bladder wall are highly correlated to the amount of urine present within the propagation path. This is caused by the much stronger nonlinear behavior of urine compared to that of tissue. The main challenge was to design a transducer

capable of efficiently transmitting the fundamental and receiving up to the third harmonic with high sensitivity. This challenge was met by a multilayer design, which used a PZT layer for transmission and a copolymer layer for reception. By locating the copolymer layer inside the structure, the developed inverted multilayer transducer also optimized the signal-to-noise ratio (SNR).

The second part of this work focuses on the development of a special transducer and signal processing methods for SHI. The use of SHI implies a large dynamic range and requires a sufficiently sensitive array transducer over a frequency range from the transmission frequency up to its fifth harmonic (bandwidth $> 130\%$). This is a considerably larger bandwidth than that offered by conventional array transducers. To obtain this bandwidth a dual frequency interleaved phased array transducer was developed. The transducer was optimized for echocardiography. The rationale behind the design choice, frequencies and aperture used is reported in chapter 8. The research track on the piezomaterials used is reported in chapters 7 and 8. The developed dual frequency design featured alternately interleaved transmit and receive elements. The main drawback of this design is the intrinsically reduced sensitivity as only half the elements are used in reception. Since the level of the higher harmonics generated by nonlinear propagation is low, it is important to find ways to boost the receive sensitivity. Chapter 9 presents a systematic study to optimize the distribution of the transmit and receive elements in order to maximize the receive sensitivity. The optimal topology for superharmonic echocardiography was the mixed transducer configuration with 1 transmit element per 6 receive elements. This configuration considerably improved the SNR compared to the regular interleaved design, while a high quality ultrasound beam was retained.
One of the most important parameters to influence SHI is the transmission frequency. This strongly affects the levels of the third to fifth harmonics at the distances determined by the application and therefore the obtainable SNR and quality of the resulting superharmonic image. An investigation of the optimal transmission frequency for SHI depending on the imaging application by simulation of the entire imaging chain is reported in chapter 9. The optimal transmission frequency for superharmonic echocardiography was found to be 1.0 - 1.2 MHz. For superharmonic abdominal imaging the optimal frequency was 1.7 - 1.9 MHz. Next, the characteristics of the optimal superharmonic beam were compared in chapter 10 to those of the optimal fundamental and second harmonic beams. The superharmonic beam is in the far field more narrow than the fundamental and second harmonic beams and has a sharper roll-off. Moreover, the pulse-echo intensity of the superharmonic beam is in the far field equal to that of the second harmonic. Thus, *in-vivo* superharmonic imaging is not only feasible but is expected to improve the image quality of echocardiography compared to the current standard of second harmonic imaging.
It is important in an ultrasound image that a single reflector is indicated by a single reflection. If the transmitted pressure wave is short (e.g. one cycle), the demodulation of the propagated wave over the superharmonic band dramatically improves the axial resolution. However, in practice the pressure signals transmitted by commercial transducers are often longer leading to ripples in the filtered superharmonic signals. These ripples in the time domain representation lead to ghost reflections in B-mode images: single reflectors appear

as multiple overlapping reflectors. The cause of the ripples are the troughs in between the harmonics in the frequency domain representation of the propagated pulse. A more thorough explanation for this effect is given in chapter 11. Two solutions to prevent ghost reflections and to preserve the axial resolution of SHI are given in this thesis. The first is treated in chapters 12 and 13 and consists of two transmissions per trace, with the second slightly frequency shifted compared to the first. The responses of both transmissions are then summed leading to a filling of the troughs in the frequency domain. The second solution is based on coded excitation. In this method a linear chirp is transmitted. The received signals are then decoded and the aforementioned ripples are compressed out of the result. The decoding pulse is obtained using simulations. Both solutions can be used to obtain superharmonic images and predict a considerable gain in axial resolution.
Thus, it appears that the major engineering hurdles for SHI have been solved. The main priority for follow-up research should be to investigate whether the image quality improvement outweighs the practical difficulties of implementing SHI by studying *in-vivo* images.

Samenvatting

Echografie is een van de meest gebruikte radiologische modaliteiten voor het stellen van medische diagnoses. Met deze techniek kunnen weefsels in het menselijke lichaam gevisualiseerd worden en ze wordt daarom in een breed scala aan medische applicaties toegepast. Zo is echocardiografie de belangrijkste diagnostische beeldvormende techniek in het veld van de klinische cardiologie. Ondanks de grote vooruitgang van de laatste jaren blijft echocardiografie echter technisch uitdagend. Een behoorlijke groep van patiënten (10 - 20%) is technisch moeilijk om te scannen door problematische akoestische 'ramen' en inhomogene huidlagen. Vooral bij mensen met overgewicht of patiënten met longziekten kan de echokwaliteit onvoldoende zijn voor een diagnose.
Tot het eind van de jaren 90 was de implementatie van medische echografie linear - de uitgezonden frequentie was gelijk aan de ontvangen frequentie. Ongeveer 10 jaar geleden werd het mogelijk om de kwaliteit van ultrageluid beelden te verbeteren door gebruik te maken van het feit dat golfpropagatie niet-lineair is. De nieuwe techniek werd 'tissue harmonic imaging' genoemd en was oorspronkelijk beperkt tot beeldvorming gebaseerd op de tweede harmonische component. De bundel van de harmonischen is nauwer, valt off-axis sneller weg en heeft lagere zijlobben in vergelijking met de fundamentele bundel. Ook bouwt de tweede harmonische zich progressief op. Daarom is beeldvorming gebaseerd op de tweede harmonische minder gevoelig voor artefacten in het nabije veld en voor off-axis reflectoren. Ook is de laterale resolutie hoger. Deze eigenschappen zorgden voor een significante verbetering in de beeldkwaliteit, vooral voor de groep patiënten die technisch moeilijk te scannen was. Het belangrijkste nadeel van de tweede harmonische is het feit dat deze minder energie bevat in vergelijking met de fundamentele band. Dat verhoogt significant de eisen waaraan een ultrageluidsysteem - inclusief de transducent - moet voldoen. Recentelijk is een nieuwe beeldvormende techniek, genaamd 'superharmonische beeldvorming' (SHI), geïntroduceerd. Deze methode maakt gebruik van de derde tot en met de vijfde harmonischen, die ontstaan door niet-lineaire propagatie van drukgolven of door het gedrag van ultrageluid contrast middelen. Naast een betere onderdrukking van artefacten in het nabije veld, is de verwachting dat de toepassing van SHI zal leiden tot beelden

met hogere axiale en laterale resoluties in vergelijking met beeldvorming gebaseerd op de tweede harmonische. Het voordeel van het toepassen van SHI in combinatie met ultrageluid contrast middelen ligt in een verhoogde contrast-to-tissue ratio. Het nadeel van het gebruik van deze hogere harmonischen is dat deze nog minder energie bevatten dan de tweede harmonische.

Dit proefschrift richt zich op de ontwikkeling van transducenten en signaalverwerkingstechnieken voor beeldvorming en diagnoses gebaseerd op de niet-lineariteit van golfpropagatie (of het gedrag van ultrageluid contrast middelen), met een specifieke nadruk op SHI. Het ge-presenteerde werk beslaat de aspecten die nodig zijn om SHI te implementeren - van het aantonen van de haalbaarheid van de techniek, het ontwerp van de vereiste hardware, tot de benodigde beeldvormende technieken.

Het eerste gedeelte van dit proefschrift is gewijd aan de karakterisatie en de modellering van ultrageluid transducenten. De ontwikkelde methodes en modellen worden vervolgens toegepast op de ontwikkeling van een transducent voor 3D tweede harmonische transesophagale echocardiografie (TEE) en op een transducent die gebruikt wordt om noninvasief het blaasvolume te meten gebaseerd op het niveau van de gegenereerde harmonischen.
Een belangrijk onderdeel van het ontwerpproces van transducenten en ultrageluidssytemen is het meten van de prestaties van transducenten, zodat dit gebruikt kan worden om transducenten te beoordelen of om zendtechnieken en postprocessing te optimaliseren. Hiertoe hebben we drie methodes ontwikkeld om de absolute amplitude overdracht van een transducent te meten, deze worden behandeld in hoofdstuk 2. Een volledige karakterisatie van een transducent dient ook het faseverschil tussen de oscillatie van het oppervlak en de excitatie te beschrijven. Hoofdstuk 3 behandelt een praktische methode om de fase overdrachtsfunctie van een transducent te meten met behulp van een eenvoudige laboratorium opstelling.
Een van de cruciale stappen in de ontwikkeling van hoogwaardige transducenten is het modelleren ervan. De modellen zijn gebaseerd op een set aannames van de transducentgeometrie en het materiaalgedrag. Daarom is het uiterst belangrijk om te weten hoe accuraat deze modellen zijn. In hoofdstuk 4 vergelijken we de oppervlaktetrillingen van een transducent element zoals berekend met een 3D eindige elementen model met metingen die verkregen zijn met behulp van een laserinterferometer. De overeenkomst tussen de uitkomsten van het model en de metingen was goed.
Het gevalideerde eindige elementen model wordt in hoofdstuk 5 in combinatie met laserinterferometermetingen gebruikt om de optimale geometrie en opbouw van de elementen van een matrix transducent bedoeld voor 3D TEE te bepalen. TEE gebruikt de esophagus in plaats van de thorax als een akoestisch ‘raam’ naar het hart. Het gebruik van dit raam voorkomt artefacten door de ribben of vetlagen in de huid. Ook laat het een hogere zendfrequentie toe. De huidige 3D TEE transducenten zijn gemaakt voor fundamentele beeldvorming, maar onze verwachting is dat de beeldkwaliteit van 3D TEE een flinke sprong voorwaarts maakt met de toepassing van tweede harmonische beeldvorming. Een TEE transducent bestaat uit een flexibele endoscoop met de feitelijke transducent aan het

uiteinde gemonteerd. Omdat het apparaat in de esophagus moet passen, zijn de ruimtelijke limitaties de grootste uitdaging voor het ontwerp. Om de akoestische elementen en de electronica zo efficiënt mogelijk te verdelen over de beschikbare ruimte, is het transducent ontwerp opgedeeld in een 1.5D subarray voor transmissie en een 2D subarray voor ontvangst. De geoptimaliseerde geometrie en elementopbouw voldoet aan alle eisen voor 3D tweede harmonische TEE.
In hoofdstuk 6 van dit proefschrift is verder een multilaags transducent concept ontwikkeld om noninvasief het blaasvolume te kunnen meten met behulp van akoestiek. De meetmethode is gebaseerd op het feit, dat de harmonische energie in de echo's afkomstig van een gebied na de achterste blaaswand sterk gecorreleerd is met de hoeveelheid urine in het propagatiepad. Dit wordt veroorzaakt door het sterkere niet-lineaire gedrag van urine in vergelijking met dat van weefsel. De voornaamste uitdaging was om een transducent te ontwerpen die efficiënt kan zenden op de fundamentele frequentie en tot en met de derde harmonische kan ontvangen met een hoge gevoeligheid. De oplossing was een multilaag ontwerp, waarbij een PZT-laag voor transmissie gebruikt werd en een copolymeer-laag voor ontvangst. Door het copolymeer binnen de transducent achter het PZT aan te brengen werd de signaal-ruis-verhouding geoptimaliseerd.

Het tweede deel van dit proefschrift draait om de ontwikkeling van zowel een speciale transducent als de benodigde signaalverwerking voor SHI. Om SHI te kunnen realiseren is een systeem met een groot dynamisch bereik nodig. Verder dient men te beschikken over een voldoende gevoelige transducent over het benodigde frequentiebereik van de fundamentele frequentie tot en met de vijfde harmonische (bandbreedte $> 130\%$). Deze vereiste bandbreedte is aanzienlijk hoger dan die van conventionele transducenten. Om de benodigde bandbreedte te verkrijgen is een array transducent ontwikkeld die bestaat uit twee in elkaar geschoven array transducenten met verschillende resonantiefrequenties (het zogeheten dubbele frequentie ontwerp). De verkregen transducent was geoptimaliseerd voor echocardiografie. De motivatie voor het ontwerp, de resonantiefrequenties en de apertuur staat omschreven in hoofdstuk 8. Het onderzoek naar de optimale piezomateriaalkeuze staat beschreven in de hoofstukken 7 en 8. In de aldus ontworpen dubbele frequentie transducent zijn de zend- en ontvangstelementen om en om gerangschikt. Het grootste nadeel van dit ontwerp is de intrinsiek gereduceerde gevoeligheid, omdat maar de helft van de elementen in ontvangst gebruikt worden. Het niveau van de harmonischen gegenereerd door niet-lineaire propagatie is echter laag, dus het is belangrijk om manieren te vinden om de ontvangstgevoeligheid te verhogen. Hoofdstuk 9 draait om het verhogen van de ontvangstgevoeligheid door de distributie van de zend- en ontvangstelementen te optimaliseren. De optimale topologie voor superharmonische echocardiografie was een configuratie waarbij 1 zendelement werd afgewisseld met 6 ontvangstelementen. Deze configuratie verhoogde de behaalde signaal-ruis-verhouding aanzienlijk, terwijl de kwaliteit van de bundel op hetzelfde hoge niveau bleef.
Een van de meest belangrijke parameters die een rol spelen bij SHI is de transmissiefrequentie. Deze beïnvloedt hoeveel derde tot en met de vijfde harmonischen er op een bepaalde afstand gegenereerd wordt. Dat bepaalt de te behalen signaal-ruis-verhouding en de kwaliteit van de resulterende superharmonische beelden. Een onderzoek naar de

optimale transmissiefrequentie voor SHI afhankelijk van de toepassing staat beschreven in hoofdstuk 9. Hiervoor werd de gehele beeldvormingsketen gesimuleerd. De optimale transmissiefrequentie voor superharmonische echocardiografie is vastgesteld op 1.0 - 1.2 MHz. Voor superharmonische abdominale beeldvorming verandert deze frequentie in 1.7 - 1.9 MHz. In hoofdstuk 10 worden de karakteristieken van de optimale superharmonische bundel vergeleken met die van de optimale fundamentele en tweede harmonische bundels. De superharmonische bundel is smaller in het verre veld en valt off-axis sneller weg in vergelijking met de fundamentele en tweede harmonische bundels. Verder is de puls-echo intensiteit in het verre veld van de superharmonische bundel net zo hoog als die van de tweede harmonische bundel. Superharmonische beeldvorming is daarom niet alleen haalbaar, maar zal ook de beeldkwaliteit van echocardiografie verbeteren in vergelijking met tweede harmonische beeldvorming - de huidige standaard.
Het is belangrijk dat een enkele reflector in een ultrageluid beeld aangegeven wordt door een enkele reflectie. Als de uitgezonden drukgolf kort is (bijvoorbeeld een enkele periode), verbetert de axiale resolutie dramatisch door de demodulatie van de gepropageerde golf over de superharmonische band. Echter, in de praktijk zijn de signalen, die door commerciële transducenten uitgezonden worden, langer. Dit leidt tot rimpels in het gefilterde superharmonische signaal. Deze rimpels in de tijddomein-representatie leiden tot zogenaamde spookreflecties in ultrageluidbeelden: de reflectie van een enkele reflector ziet er uit alsof deze van meerdere reflectoren komt. De oorzaak van deze rimpels zijn de troggen tussen de harmonischen in de frequentiedomein-representatie van de gepropageerde golf. Een meer uitgebreide verklaring voor dit effect wordt gegeven in hoofdstuk 11. In dit proefschrift worden twee oplossingen gepresenteerd om spookreflecties te voorkomen en zo de axiale resolutie van SHI te behouden. De eerste oplossing wordt behandeld in de hoofdstukken 12 en 13 en bestaat uit twee transmissies per beeldlijn (A-lijn), waarbij de tweede een frequentie heeft die een klein beetje hoger is. De ontvangen signalen van beide transmissies worden bij elkaar opgeteld, wat leidt tot het opvullen van de troggen in het frequentiedomein. De tweede oplossing is gebaseerd op gecodeerde transmissies. In deze methode wordt een lineaire chirp uitgezonden. De ontvangen signalen worden dan gedecodeerd, waardoor de rimpels uit deze signalen worden verwijderd. Het decodeersignaal wordt verkregen met behulp van simulaties. Beide oplossingen kunnen gebruikt worden om superharmonische beelden te maken en leiden tot een significante verbetering in de axiale resolutie.
Het lijkt er dus op dat de grootste uitdagingen voor SHI zijn opgelost. In een vervolgonderzoek zou de nadruk moeten liggen op de vraag of de verbetering in de beeldkwaliteit opweegt tegen de praktische problemen bij het implementeren van SHI. Dit zou het beste vastgesteld kunnen worden door *in-vivo* beelden te bestuderen.

Dankwoord

Dat is het dan, mijn proefschrift is af: de bekroning op iets meer dan 4 jaar werk. Toen ik met mijn afstuderen begon op deze afdeling in april 2004, had ik zeker niet verwacht hier ook mijn promotie af te ronden. Als ik terugkijk, valt me vooral de enorme ontwikkeling op die ik heb doorgemaakt - zowel op professioneel als op persoonlijk vlak. De keuze om hier te gaan promoveren was dan ook duidelijk een goede.
Een promotietraject doe je niet alleen, velen dragen daar op een grote of kleine manier aan bij. Als eerste wil ik mijn promotoren, Prof. dr. ir. Ton van der Steen en Prof. dr. ir. Nico de Jong, bedanken voor hun enthousiasme en begeleiding. Zij zijn de stuwende krachten die ervoor zorgen dat de afdeling van wereldniveau is en blijft. Ton, ik wil je bedanken voor de mogelijkheid om mijn promotie onderzoek uit te voeren bij deze uitstekende vakgroep. Nico, je stond altijd klaar om met een frisse en kritische blik mee te denken. Als ik jou kon overtuigen van de juistheid van mijn onderzoek, dan wist ik zeker dat dat met de reviewers ook wel ging lukken.
Verder zou ik de leden van mijn promotiecommissie willen bedanken voor hun inzet en de bereidheid om mijn proefschrift te beoordelen.
Hans, ik wil je bedanken voor je enthousiasme en interesse voor mijn onderzoek, ook al was je daar officieel niet bij betrokken. Dat geldt ook voor Annemieke: we hebben uiteindelijk niet zo veel samengewerkt, maar je was altijd hulpvaardig en bereid tot meedenken. Groot respect heb ik voor Charles, de man bij wie we aankloppen als we echt een ingewikkeld probleem hebben. Bedankt voor je advies!
Er zijn een aantal mensen met wie ik veel heb samengewerkt gedurende mijn promotie onderzoek. Guillaume, it has been a pleasure working with you. Our different takes on solving problems was a great asset to our work. Although you moved on to a new job before the project was finished, you continued to work on your PhD. That is not an easy feat and I respect you for it. Cardiovasculaire! Mike, het was niet alleen gezellig, ik heb ook veel van je geleerd - met name met betrekking tot het schrijven van artikelen. Ook heb ik genoten van onze discussies over politiek en cultuur. Verder wil ik Egon, Rik, Sandra en Jerome bedanken voor de goede samenwerking. Onze vele discussies waren (meestal)

erg plezierig en leidden vaak tot nieuwe inzichten en oplossingen - zelfs als (of misschien doordat) we het niet eens waren.
Het projectteam beperkte zich niet alleen tot de afdeling Biomedische Technologie. Zo was er ook coöperatie met de TU Delft in de vorm van Martin Verweij en Koos Huijssens. Martin en Koos, bedankt voor de interessante discussies over niet-lineaire verschijnselen. Ook zou ik de mensen van Oldelft Ultrasound - o.a. Christian Prins, Franc van den Adel, Ruud 't Hoen, Rob Smallenburg, Roelof Hardenberg en Ruud van Went - willen bedanken voor de prettige samenwerking en de fabricage van de 'interleaved' transducent prototypes.
Verder zou ik speciaal de mensen van de werkplaats willen bedanken. Leo, Wim, Geert en Michiel, jullie zijn cruciaal in het realizeren van onze ideeën. De samenwerking was erg productief, vooral doordat jullie aktief meedenken bij het vinden van oplossingen. Ik verbaas me er iedere keer weer over wat jullie kunnen maken. Er zijn nog meer mensen die met hun ondersteuning het doen van onderzoek mogelijk maken. In het bijzonder wil ik Mieke vermelden, die een onmisbare rol speelt in het reilen en zeilen van de afdeling. Ook wil ik Robert noemen, die altijd klaar staat om te helpen of - als dat niet mogelijk is - om je probleem te relativeren. Bedankt, niet alleen voor de hulp, maar ook voor de gezelligheid!
De sfeer op de afdeling Biomedische Technologie is uitstekend en een belangrijke reden daarvoor zijn de mensen die er werken. Ik wil mijn (oud) collega's van de afdeling Biomedische Technologie, o.a. (in willekeurige volgorde) David, Marijn, Esther, Cees, Marco, Klazina, Jan, Hans, Roland, Marcia, Frits, Xavier, Margreet, Gijs, Krista, Marianne, Martijn, Dave, Miranda, Anja, Gerard, Guillaume R. en nog vele anderen, bedanken voor hun hulpvaardigheid, interesse en voor de gezelligheid tijdens en na het werk (meestal met een biertje). De gespreksonderwerpen en interesses bleven daarbij gelukkig niet beperkt tot het vakgebied, vooral met Cees heb ik menig museum bezocht de afgelopen jaren! Er is ook goed contact tussen onze afdeling en de afdeling Physics of Fluids van de Universiteit Twente. Jeroen, Sander, Marlies en anderen, het was altijd gezellig om elkaar weer te zien op congressen en tijdens werkbezoeken!
Zonder de steun en aanmoediging van mijn ouders en broer was ik nooit zover gekomen. Van alles wat ik van jullie heb meegekregen, waren de belangrijkste eigenschappen wel optimisme, doelgerichtheid en doorzettingsvermogen. Ik ben ontzettend blij dat we zo'n hechte band hebben, bedankt voor alles!
Gedurende mijn tijd in Rotterdam ben ik een geweldige vrouw tegengekomen, met wie ik inmiddels samenwoon. Suzana, toen je naar Nederland kwam om te studeren, had je nooit kunnen denken dat je hier zou blijven. Die keuze resulteerde in een spannende en onzekere tijd, maar dat is gelukkig helemaal goed gekomen. Ieder moment met jou is nog net zo geweldig als in het begin! Bedankt voor je liefde en je steun!

Paul van Neer
Rotterdam, april 2010

About the author

Paul L.M.J. van Neer was born in Heerlen, the Netherlands on August 10, 1982. He followed secondary school (VWO) at the Stella Maris College (Meerssen, the Netherlands) and graduated in 1999. He went on to study Biomedical Engineering at the Eindhoven University of Technology (Eindhoven, the Netherlands). After obtaining his BSc. degree he continued his master studies at the 'Biomechanics & Tissue Engineering' (BMTE) division. During his master he went for an externship at San Diego State University (San Diego, California, USA), where he worked on the development of an *in-vitro* pulse duplicator for the modeling of the left ventricle and the systemic circulation of humans. His MSc. graduation project was a collaboration between the department of Biomedical Engineering of the Erasmus Medical Center (Rotterdam, the Netherlands) and the department of Biomedical Engineering of the Eindhoven University of Technology. The project focused on the development of a noninvasive method to detect broken outlet struts of Björk-Shiley convexo concave heart valves. He obtained his Master of Science degree in 2005 with the judicium 'Met grote waardering'.
After his graduation he was employed as a junior researcher to publish on his graduation work. Next, he worked as a junior researcher for the Signal Processing Systems Group, Department of Electrical Engineering, Eindhoven University of Technology on ultrasound contrast agent applications. From 2006 onwards he was detached by the Interuniversity Cardiology Institute of The Netherlands (part of the Royal Dutch Academia of Sciences) at the Erasmus Medical Center in Rotterdam. There he joined the Department of Biomedical Engineering at the Thoraxcenter to pursue his PhD. degree. His research focused on the development of ultrasound transducers and signal processing techniques for nonlinear ultrasound imaging.
Paul L.M.J. van Neer lives in Rotterdam with his partner Suzana Habe.

List of publications

Papers in preparation

P.L.M.J. van Neer, M.G. Danilouchkine, M.M. Voormolen, N. de Jong, Comparison of fundamental, second harmonic and superharmonic imaging: a simulation study, in preparation.

G.M. Matte, **P.L.M.J. van Neer**, M.G. Danilouchkine, N. de Jong, Dual pulse method for superharmonic imaging, in preparation.

Peer-reviewed articles

P.L.M.J. van Neer, S. Blaak, H. Bosch, C.T. Lancée, C. Prins, N. de Jong, Optimal geometry and element make-up for a transesophageal matrix transducer intended for second harmonic imaging, submitted.

G.M. Matte, **P.L.M.J. van Neer**, M.G. Danilouchkine, J. Huijssen, M. Verweij, N. de Jong, Parameter optimization of a superharmonic phased array transducer for transthoracic applications, submitted.

P.L.M.J. van Neer, H.J. Vos, N. de Jong, Reflector-based phase calibration of ultrasound transducers, *Ultrasonics*, accepted.

D. Maresca, M. Emmer, **P.L.M.J. van Neer**, H.J. Vos, M. Versluis, M. Muller, N. de Jong, A.F.W. van der Steen, Acoustic sizing of an ultrasound agent, *Ultrasound Med. Biol.*, under revision.

P.L.M.J. van Neer, G. Matte, M.G. Danilouchkine, C. Prins, F. van den Adel, N. de Jong,

Super-harmonic imaging: development of an interleaved phased-array transducer, *IEEE Trans. Ultrason. Ferroelectr. Freq. Control*, 57(2):455-468, 2010.

T.V. Schohy, G. Matte, **P.L.M.J. van Neer**, A.F.W. van der Steen, J. McGhie, A. Bogers, N. de Jong, A new transesophageal probe for newborns, *Ultrasound Med. Biol.*, 35(10):1686-1689, 2009.

E.J.W. Merks, **P. van Neer**, N. Bom, A.F.W. van der Steen, N. de Jong, Multilayer transducer for acoustic bladder volume assessment on the basis of nonlinear wave propagation, *Ultrasound Med. Biol.*, 35(10):1690-1699, 2009.

G.M. Matte, J.M.G. Borsboom, **P. van Neer**, N. de Jong, Estimating acoustic peak pressure generated by ultrasound transducers from harmonic distortion level measurement, *Ultrasound Med. Biol.*, 34(9):1528-1532, 2008.

P.L.M.J. van Neer, G. Matte, J. Sijl, J.M.G. Borsboom, N. de Jong, Transfer functions of US transducers for harmonic imaging and bubble responses, *Ultrasonics*, 46:336-340, 2007.

P.L.M.J. van Neer, A. Bouakaz, E. Vlaanderen, J. de Hart, F.N. van de Vosse, A.F.W. van der Steen, N. de Jong, Detecting broken struts of a Björk-Shiley heart valve using ultrasound: a feasibility study, *Ultrasound Med. Biol.*, 32(4):503-512, 2006.

Conference proceedings

P.L.M.J. van Neer, M.G. Danilouchkine, G.M. Matte, M.M. Voormolen, M.D. Verweij, N. de Jong, Chirp based superharmonic imaging for phased array transducers, *POMA, 159th Meeting ASA Baltimore*, Vol. 9, 2010.

P.L.M.J. van Neer, M.G. Danilouchkine, G.M. Matte, M.D. Verweij, N. de Jong, Dual pulse frequency compounded super harmonic imaging for phased array transducers, *Proc. IEEE Ultrasonics Symp., Rome, Italy*, 381-384, 2009.

M. Pasovic, M. Danilouchkine, **P. van Neer**, O. Basset, C. Cachard, A.F.W. van der Steen, N. de Jong, Angular spectrum method for the estimation of the lateral profile of the ultrasound pressure field of the third harmonic, *Proc. IEEE Ultrasonics Symp., Rome, Italy*, 2801-2804, 2009.

G.M. Matte, **P.L.M.J. van Neer**, J.M.G. Borsboom, M.D. Verweij, N. de Jong, A new frequency compounding technique for super harmonic imaging, *Proc. IEEE Ultrasonics Symp., Beijing, China*, 357-360, 2008.

P.L.M.J. van Neer, G. Matte, P. Gatta, M. Pappalardo, N. de Jong, A comparison of array

element surface vibration calculated by finite element modelling and laser interferometer measurements, *Proc. IEEE Ultrasonics Symp., Beijing, China*, 788-791, 2008.

M. Emmer, G. Matte, **P. van Neer**, A. van Wamel, N. de Jong. Improved ultrasound contrast agent detection in a clinical setting. *Proc. IEEE Ultrasonics Symp., New York, NY, USA*, 2235-2238, 2007.

P.L.M.J. van Neer, G. Matte, J.M.G. Borsboom, M.D. Verweij, N. de Jong, Development of a phased array for tissue and contrast super harmonic imaging. *Proc. IEEE Ultrasonics Symp., New York, NY, USA*, 200-203, 2007.

P.L.M.J. van Neer, G. Matte, J. Sijl, J.M.G. Borsboom, N. de Jong, Transfer functions of US transducers for harmonic imaging and bubble responses, *Proc. International Congress on Ultrasonics, Vienna, Austria*, Paper ID 1713, 1-4, 2007.

P.L.M.J. van Neer, F.N. van de Vosse, N. de Jong, A.F.W. van der Steen, E. Vlaanderen, A. Bouakaz, J. de Hart, *In-vitro* development of a novel method to noninvasively establish BScc valve integrity, *Proc. IEEE Ultrasonics Symp., Rotterdam, the Netherlands*, 1109-1112, 2005.

Presentations without paper

D. Maresca, M. Emmer, **P.L.M.J. van Neer**, H.J. Vos, M. Versluis, M. Muller, N. de Jong, A.F.W. van der Steen, Acoustic sizing of an ultrasound agent (O), *15^{th} European Symposium on Ultrasound Contrast Imaging, Rotterdam, the Netherlands*, 2010.

P.L.M.J. van Neer, M.G. Danilouchkine, G.M. Matte, M.D. Verweij, N. de Jong, Super harmonic imaging methods: an overview, *SUGB fall meeting, Nijmegen, the Netherlands*, 2009.

G.M. Matte, **P.L.M.J. van Neer** (duo-presentation), J.M.G. Borsboom, N. de Jong, Super harmonic imaging, *14^{th} New England Doppler Conference, Maastricht, the Netherlands*, 2007.

P.L.M.J. van Neer, A. Bouakaz, E. Vlaanderen, J. de Hart, F.N. van de Vosse, A.F.W. van der Steen, N. de Jong, *In-vitro* development of a novel method to noninvasively establish BScc valve integrity, *SUGB spring meeting, Maastricht, the Netherlands*, 2006.

Academic reports

P.L.M.J. van Neer, Ultrasonic superharmonic imaging, PhD. Thesis, Erasmus University Rotterdam, the Netherlands, 2010.

P.L.M.J. van Neer, The Björk-Shiley valve: Detecting broken struts using standard diagnostic ultrasound instruments, MSc. Thesis, Eindhoven University of Technology, the Netherlands, 2005.

PhD portfolio

Name PhD Student: Paul van Neer	PhD period: January 2006 - Jun 2010
Erasmus MC Dep.: Biomed. Engineering	Promotors: N. de Jong/A.F.W. van der Steen
Research School: Coeur	Supervisor: -

Courses	Year	ECTS
Biomedical English writing and communication (NIHES)	2008	4
Classical Methods for Data-analysis (CC02) (NIHES)	2008	6
Medical Imaging - 1, Principles, ultrasound and magnetic resonance, (ESMP, Archamps, France)	2006	1.5
Mastercourse Medical Acoustics (Biomedical Engineering, University of Twente)	2006	5

International conferences	Year	ECTS
159'th meeting of the Acoustical Society of America (Baltimore, Maryland, USA)	2010	1.5
The fifteenth European Symposium on Ultrasound Imaging (Rotterdam, the Netherlands)	2010	0.6
IEEE International Ultrasonics Symposium (Rome, Italy)	2009	0.9
The fourteenth European Symposium on Ultrasound Imaging (Rotterdam, the Netherlands)	2009	0.6
IEEE International Ultrasonics Symposium (Beijing, China)	2008	0.9

International conferences (continued)	Year	ECTS
The thirteenth European Symposium on Ultrasound Imaging (Rotterdam, the Netherlands)	2008	0.6
IEEE International Ultrasonics Symposium (New York, NY, USA)	2007	0.9
14'th New England Doppler Conference (Maastricht, the Netherlands)	2007	1.2
International Congress on Ultrasonics (Vienna, Austria)	2007	1.2
The twelfth European Symposium on Ultrasound Imaging (Rotterdam, the Netherlands)	2007	0.6
The eleventh European Symposium on Ultrasound Imaging (Rotterdam, the Netherlands)	2006	0.6

Seminars and workshops	Year	ECTS
Zooming into the Near Field (IEEE course, Rome, Italy)	2009	0.15
Ultrasonic Signal Processing for Detection, Estimation & Imaging (IEEE course, Rome, Italy)	2009	0.15
Therapeutic and diagnostic use of microbubbles and ultrasound	2009	0.4
CMUTs: Theory, Technology, and Applications (IEEE course, Beijing, China)	2008	0.15
Acoustic Microscopy (IEEE course, Beijing, China)	2008	0.15
Conservative Finite Difference Method & Allied Topics (IEEE course, New York, NY, USA)	2007	0.15
Ultrasound Imaging Systems (IEEE course, New York, NY, USA)	2007	0.15
MUI Medical ultrasound imaging (ICU course, Vienna, Austria)	2007	0.15
HIFU High intensity focused ultrasound (ICU course, Vienna, Austria)	2007	0.15
NDT Non-destructive testing (ICU course, Vienna, Austria)	2007	0.15

Supervising activities	Year	ECTS
Bachelor project (4 months)	2010	1.5